Cassini Observations of Saturn's Magnetospheric Cusp

Jamie Matthew Jasinski

Thesis submitted for the degree of Doctor of Philosophy

July 2015

Mullard Space Science Laboratory
Department of Space and Climate Physics
University College London

I, Jamie Matthew Jasinski, confirm that the work presented in this thesis is my own. Where information has been derived from other sources, I confirm that this has been indicated in the thesis.

Abstract

The magnetospheric cusp is a funnel-shaped region where shocked solar wind plasma is able to enter the high latitude magnetosphere via the process of magnetic reconnection. The first in-situ analysis of the cusp region at Saturn is presented using data from the Cassini spacecraft, primarily from particle instruments and magnetic field observations. The analysis is presented in three sections.

Firstly, two high-latitude spacecraft crossings are confirmed to be cusp observations by: (i) comparing the observed plasma with that of the magnetosheath and the adjacent magnetosphere, (ii) investigating the direction of the observed ions and (iii) analysing the composition of the plasma. The ion observations are shown to be a result of 'bursty' reconnection occurring at the dayside magnetopause. The field-aligned distances to the reconnection site are calculated from the observed energy-pitch angle dispersions.

Secondly, all the observations of the cusp are presented for the high latitude spacecraft orbits between 2007 and 2013. A comparison of the observations is made as well as classification into groups due to varying characteristics. The locations of the reconnection site are calculated and compared to the literature. The events are also compared to solar wind propagation models to investigate any correlations.

Finally, the magnetic field observations of the cusps are analysed, focusing on the diamagnetic depressions. This characteristic is not observed in all of the cusps, and the possible explanations for this are discussed. The data are subtracted from a magnetic field model, and the calculated magnetic pressure deficits are compared to the particle pressures. A high plasma pressure layer in the magnetosphere adjacent to the cusp is discovered to also depress the magnetic field.

A summary of the consequences of this work is discussed specifically regarding the ongoing debate of the role of reconnection at Saturn and its influence on magnetospheric dynamics.

" *Modern science has been a voyage into the unknown, with a lesson in humility waiting at every stop.*"

Carl Sagan

Acknowledgements

The first thanks must go to all my supervisors; Dr. Chris Arridge, Prof. Andrew Coates and Dr. Geraint Jones. I've always joked that being graced with three supervisors must be the greatest of all compliments as everyone wants to get in on my genius; or it's the gravest of insults: I need so much supervision that the workload must be spread out amongst 3 great academics. Jokes aside, nothing would have been possible without the help of the 'Big Three'.

Chris, you have been at the forefront of my supervision and have always been awesome at explaining stuff, even when my questions start with "This is probably a stupid question, but...". Without your depth of knowledge and wide expertise of the subject matter this work would not have come to fruition. Your infectious passion for physics has provided me with a thirst to continue my time in science. Andrew, you have been the wise guide through this journey, with an extraordinary availability for someone so senior. Your constant positive attitude and support has always made me feel more confident about my work and my abilities. Your encyclopaedic knowledge of all things planetary related has been really inspiring. Geraint, you have always been present and willing to meet up and help out when it was needed, and for that I thank you. Your calmness has been contagious over the course of the four years, and you have always been a pillar of encouragement. I thank all of you for sharing your time with me.

If there ever was a fourth supervisor, a 'Spiritual' supervisor of the university world, then it would have been Dr. David Williams, for guidance in everything academia-ish except for the actual science. Specifically your patience in the final year when stress of thesis and job searching produced ramblings from a person on the brink (of madness) of finishing, thank you.

The next mentions are to Neville Shane(ski), Lin Gilbert, and Gethyn Lewis. Neville, you were always willing to help out with IDL. The hours you sat with me going through error reports was fantastic, and I don't think I would have been able to accomplish anything in those early days without you. You left half way through for America, and you will be proud that I won the croquet championship in your team name, 'The Planetary A-team'. Gethyn 'Bread Machine' Lewis, I never knew anyone could eat a whole loaf of bread before an all you can eat breakfast, until I met you. I thank you for helping me with IDL, specifically polyfills, I can't remember

how many times you wrote it out for me! Lin, you have been amazing with helping out with all things CAPS and IDL related! I thank all of you!

Tom 'T-bone' Nordheim, I feel like we have gone through this PhD process together, and I have always been happy that we could help each other out. You were always ready to explain Saturn's moon processes to me, and I am sure our friendship and collaboration will continue, even though we are leaving for different institutes. William Dunn, I have enjoyed our football chats on the way to work in the morning, as well as the attempt of naming discoveries after ourselves. The car journeys would definitely have been a lot more dull without you or Nadine (and her ridiculous stories) and Yudish's constant 'banter'. Leonardo Regoli, the lab became a sadder place when you left for Germany. I will particularly remember your croquet championship winning point with me and Will. I enjoyed our metal discussions, and seeing Metallica was awesome! A shout out to William Poole (for help with LaTeX), and members of office 108, including Annie, Kim and Marianna. Jason, Kirthika and Ailsa, we started upon this road together, living at the lab at the start. It has been great to get to know you guys over these last few years. Jason, now that we have finished, we have time to save the galaxy.

I would also like to thank other academics at the lab and overseas. Adam Masters you helped in the first months in office 108, and have always been ready to discuss ideas. Jonny Rae, Chris Owen and Andrew Fazakerley, you have always been available with your open door policy to help when I didn't understand something. Todd Smith, you have made international conferences a lot more fun, and I enjoyed San Antonio after MOP with you. I would also like to thank Prof. Jim Slavin for inviting me out to Michigan in the last year of my PhD. I really enjoyed my time in Ann Arbor working with you and Jim. Dr. David Kipping, for getting me into the research game during my undergraduate days, for the early inspiration and being a role model as well as for the introduction to Carl Sagan.

A thank you to all the collaborators over the years, who have helped out at critical moments: Michelle Thomsen, Laurent Lamy, Jared Leisner, Nick Sergis, Aikaterina Radioti and Elias Roussos. I would also like to thank STFC for funding my PhD, and the RAS and MSSL Student Travel Fund, for financing some of my travels abroad.

To all the people who kept me sane over the last few years. Henio Polus, 'my-brother-from-another-mother', thank you for the support, the constant stream of ridiculous jokes, the times you told people that I study 'Star Wars' and all the good moments watching Polska play football. I will never forget that awesome victory over Germany, that was spectacular. I should also thank you for mixing many of the setlists that have accompanied me during my work ("in the mix, with Henryk P"). Shout out to the Ockley Boys, the Streatham Social Crew and the Peckham Posse, for all the pub outings, barbecues, and general nights in and out.

Finally a big thank you to my parents Renata and Krzyś, my brother Przemek and my girlfriend Mary. Przem you have always been the cool big brother throughout my life, and your support and encouragement over the years have made me a better person. You also provided me with a big pair of headphones at the start of my PhD (they are still working) to help me listen to 'choons' whilst trying to do IDL. To Mama and Tata; saying that you have been supportive is a massive understatement, but you have supported me emotionally and financially throughout the last four years and the other twenty-two before that. You have always been a rock in my life, whether it was to push me at the correct times or to take the pressure off and make me feel more confident. And Mary, your unwavering belief in me has kept me going these last few years. You have put up with all my madness and the floors strewn with science papers. Thank you for being there to tell me off when I was watching films when I should have been working, and for telling me to watch films when I was working too much. The fact you moved to Dorking with me (the driest place in the Solar System) shows your unfaltering support and love. I know I said I wouldn't write anything clichéd, but...You are my light in dark places when all other lights go out.

"As children we fear the dark.
The unknown troubles us.
Anything might be out there.
Ironically, it's our fate to live in the dark.
Head out from the Earth in any direction you choose
and after an initial flash of blue, you are surrounded by blackness, punctuated
only here and there by the faint and distant stars.
There are 400 billion stars in the Milky Way galaxy, of this immense multitude,
could it be that our hum-drum Sun, is the only one with an inhabited planet?
Maybe?
Maybe the origin of life or intelligence is exceedingly improbable or maybe
civilisations arise all the time but wipe themselves out as soon as they are able.
Or, here and there, peppered across space, maybe there are worlds
something like our own.
On which other beings gaze up and wonder as we do
about who else lives in the dark.
Life is a comparative rarity, you can survey dozens of worlds and find that
only on one of them does life arise, and evolve, and persist.
In our time, we have crossed the solar system and sent four ships to the stars.
But we continue to search for inhabitance.
Life looks for life."

Carl Sagan

Contents

List of Figures

List of Tables

Chapter 1

Introduction

Plasma is the fourth state of matter; a gas whose atoms are dissociated into electrons and ions. Plasmas can be found in stellar interiors, the Corona, the Solar Wind, planetary magnetospheres, accretion discs, and they can also be found on Earth in lightning bolts, the ionosphere and in a fluorescent light tube. It is said that 99% of the Universe is in the form of a plasma; this makes it an important field of physics to study.

Since the dawn of spacecraft exploration, space plasma research has increased in popularity due to the possibility of spacecraft travelling through plasma allowing for observations of the conditions *in situ*. The first explorations took place at Earth, the terrestrial magnetosphere being the easiest to access. However in 1973 and 1974, Pioneer 10 and Mariner 10 made the first visits to the magnetospheres of Jupiter and Mercury respectively. The first Saturn flyby took place five years later in 1979 by Pioneer 11. As technology improves, the instrumentation onboard spacecraft becomes more sophisticated, so more advanced investigations can occur. Coordinated spacecraft missions such as ISEE 1/2 and Cluster II have led to a very detailed analysis of the terrestrial magnetosphere. Many missions aimed at observing the Sun (e.g. Stereo A/B, ACE) have propelled the understanding of the solar wind, as well as its source.

Saturn is the second largest planet (Figure 1.1), and has the second largest magnetosphere in the solar system. Saturn's magnetosphere is seen as an intermediate between Earth and Jupiter in terms of its dynamics. Before the arrival of the Cassini-Huygens mission, Saturn was visited by three spacecraft. However it is the Cassini orbiter, which has been at Saturn since 2004, that has provided the most

Figure 1.1: A mosaic of Saturn from Cassini images (Credit: NASA/APOD/Cassini Imaging Team).

information about the Saturnian system. This thesis investigates a region in the magnetosphere at Saturn, a magnetic funnel known as the cusp, which allows the direct entry of solar wind plasma into the system. The terrestrial cusp, as we shall see later, has been the source of many investigations. However, this thesis provides the first analysis of this interesting region at Saturn, using many years of data from the Cassini mission.

First of all, the different approaches of describing plasma physics must be explained, starting with the definition of a plasma. The equations and figures are mostly sourced from the following textbooks unless otherwise specified: *Chen* (1974); *Kivelson and Russell* (1995); *Baumjohann and Treumann* (1996); *Gombosi* (1999) and *Cravens* (2004).

1.1 Plasma

An ionised gas is not automatically defined as a plasma. So what is the definition of a plasma?

> *"A plasma is a quasineutral gas of charged and neutral particles which exhibits collective behaviour."* *Chen* (1974)

The criteria: "quasineutral" and "collective behaviour", now need to be defined for this to make sense, and so the three conditions that make a plasma will be explained. For a plasma to be quasineutral, there must be nearly equal numbers of electrons and positively charged ions (n_e and n_i respectively), so it can be assumed that $n_e \simeq n_i \simeq n$, where n is the plasma density. So overall the net charge is zero.

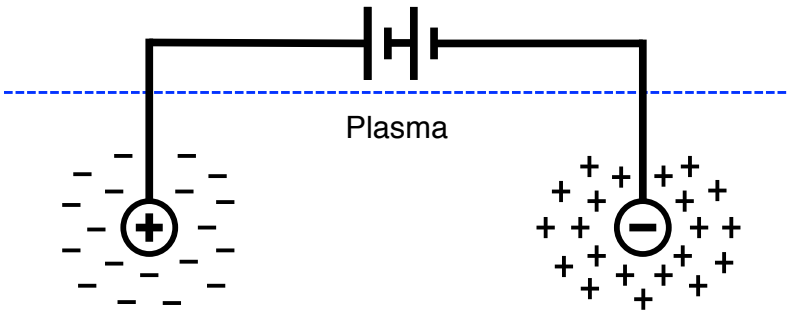

Figure 1.2: An example of Debye shielding. Adapted from *Chen* (1974).

A charged particle however, will exert an electrostatic potential called the *Coulomb potential* defined as ϕ_C:

$$\phi_C = \frac{1}{4\pi\epsilon_0}\frac{q}{r} \tag{1.1}$$

where q and r are the charge and distance from the particle, and ϵ_0 is the permittivity of free space. One of the characteristics of a plasma is that it can shield out these potentials via the attraction of oppositely charged particles. If two oppositely charged spheres are submerged into a plasma in order to create an electric field (Figures 1.2) then the electrons in the plasma will be attracted to the positively charged sphere, and ions to the negatively charged sphere. These charges therefore 'shield' the rest of the plasma from the electric field (so that it can maintain quasineutrality) and the spheres will have a Debye potential, ϕ_D:

$$\phi_D = \frac{1}{4\pi\epsilon_0}\frac{q}{r}e^{-\frac{r}{\lambda_D}} \tag{1.2}$$

where the Debye length (λ_D) is the distance that the Debye potential reduces the Coulomb potential by a factor e. The Debye length is dependant on the plasma density:

$$\lambda_D = \left(\frac{\epsilon_0 k_B T_e}{n q_e^2}\right)^{1/2} \tag{1.3}$$

where k_B is the Boltzmann constant, T_e is the electron temperature, and q_e is the charge of an electron. The temperatures and charge of the electrons are considered

(instead of the ions) because the electrons have a lower mass, and so the electrons 'do the moving'.

This introduces the first and second conditions of the definition of a plasma. Firstly, if the scale length of a plasma is taken to be L, then in order for there to be quasineutrality, the Debye length must be significantly smaller than L. Secondly, for Debye shielding to occur then the density of the plasma must be sufficient in order for a Debye sphere to be created. The number of electrons inside a Debye sphere is: $\Lambda{=}n\frac{4\pi}{3}\lambda_D^3$, and so the requirement for collective behaviour is that Λ must be significantly larger than 1, so that the sphere contains enough particles to shield the charge. Λ is known as the *plasma parameter*.

The final condition for a plasma relates to collisions between particles. If the charged particles collide too frequently with neutral atoms then their behaviour is no longer dictated by electromagnetic forces, but by hydrodynamic forces (which govern ideal gases). If the electron frequency oscillation of a plasma is w_{pe}, and the average time between collisions is τ_n then in order for a gas to behave like a plasma, τ_n must be larger compared with the inverse of w_{pe}.

Therefore the three conditions for a plasma are:

$\lambda_D \ll L$

$\Lambda \gg 1$

$w_{pe}\tau_n > 1$

The weakly ionised gas of a jet engine exhaust is not classified as a plasma because the number of collisions between the ionised particles and neutral atoms results with the gas being governed by hydrodynamic forces and not electromagnetic forces.

1.2 Single Particle Motion

To understand the motion of a charged particle in the presence of electric and magnetic fields ($\boldsymbol{E}$ and $\boldsymbol{B}$, respectively), the equations of motion of the particle must be solved. A particle with mass m, charge q, and velocity $\boldsymbol{v}$, will have the following equation of motion:

$$m\frac{d\mathbf{v}}{dt} = q(\mathbf{E} + \mathbf{v} \times \mathbf{B}) \tag{1.4}$$

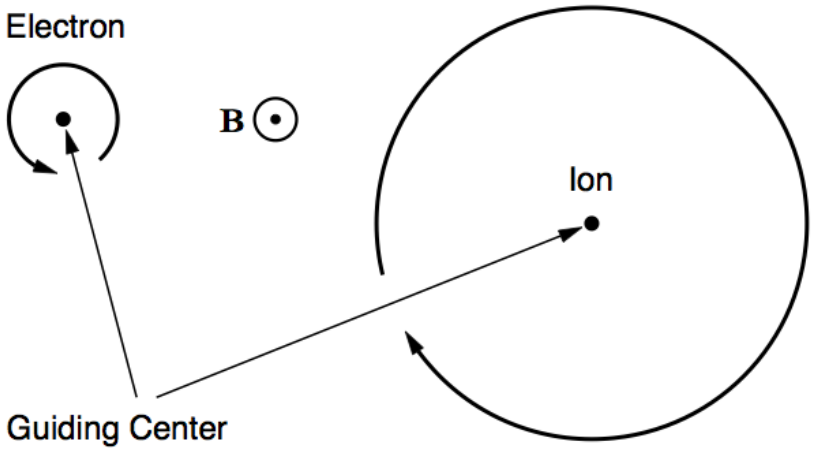

Figure 1.3: The gyration of charged particles around the guiding centre (*Baumjohann and Treumann* 1996).

where the right-hand side is the Lorentz force. If the electric field is taken away ($\boldsymbol{E}= 0$) and $\boldsymbol{v}$ is perpendicular to $\boldsymbol{B}$, the above equation is reduced to:

$$m\frac{d\mathbf{v}}{dt} = q\mathbf{v} \times \mathbf{B} \tag{1.5}$$

Differentiating this with respect to time gives:

$$\frac{d^2\mathbf{v}}{dt^2} = -\left(\frac{qB}{m}\right)^2 \mathbf{v} \tag{1.6}$$

which describes the motion of a simple harmonic oscillator. The particle's motion is that of a circle around the magnetic field in the plane perpendicular to $\boldsymbol{B}$ (see Figure 1.3). The frequency of this simple harmonic oscillator, known as the gyrofrequency is given by:

$$w_g = \frac{qB}{m} \tag{1.7}$$

The radius of this motion is the gyroradius (known also as the Larmor radius) is given by r_g:

$$r_g = \frac{v_\perp}{w_g} = \frac{mv_\perp}{qB} \tag{1.8}$$

The gyration of the particles is shown in Figure 1.3. Positively and negatively charged particles gyrate in opposite directions, due to the dependance on the sign

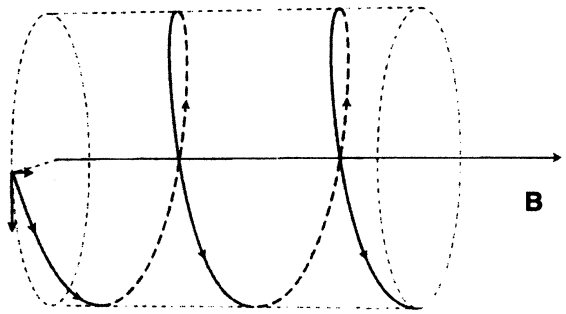

Figure 1.4: A helical orbit of an electron in a uniform magnetic field (*Gombosi* 1999).

of q. The centre of gyration is known as the guiding centre. From Equation 1.8 it can be seen that the gyroradii will increase for more massive particles, so ions of the same $v_\perp$ will have a larger r_g than electrons. Furthermore, a doubly ionised ion will have a smaller gyroradius than a singularly charged ion of the same species. A particle that is gyrating also represents a circular current that generates its own magnetic field. This field is oppositely orientated to the background field, and therefore reduces the local magnetic field. This is called the 'diamagnetic effect'.

Up until now charged particles only with a velocity perpendicular to the magnetic field have been considered. If a charged particle has a non-zero field-aligned velocity component, then the trajectory of the particle now becomes a helical one, whereby gyration around the field line occurs whilst travelling along $\boldsymbol{B}$; this can be seen in Figure 1.4.

The ratio between the perpendicular ($v_\perp$) and the parallel ($v_{||}$) components of the velocity is the tangent of what is called the *pitch angle* (α), the angle between the velocity vector and the magnetic field:

$$\alpha = \tan^{-1}\left(\frac{v_\perp}{v_{||}}\right) \tag{1.9}$$

This means that pitch angles of 0° and 180° ($v_\perp$ =0) represent particles travelling directly parallel and anti-parallel to the field line, respectively. Pitch angles of 90° define particles where $v_{||}$ =0 and the motion is entirely orthogonal to $\boldsymbol{B}$ (Figure 1.3).

To further describe the behaviour of single-particle motion, the scenario will become progressively more complicated, and will explore how the motion of a particle changes under different influences. This discussion will start with the inclusion of an electric field.

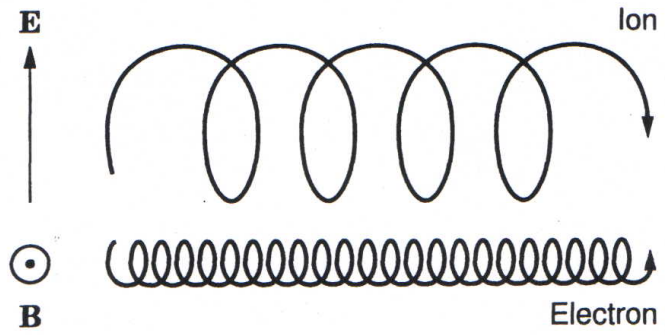

Figure 1.5: An illustration of the $\boldsymbol{E} \times \boldsymbol{B}$ drift (*Baumjohann and Treumann* 1996).

1.2.1 Motion under a uniform electric and magnetic field

The presence of an electric field $\boldsymbol{E}$ perpendicular to $\boldsymbol{B}$ causes a superimposed motion in the direction both perpendicular to $\boldsymbol{E}$ and $\boldsymbol{B}$ (Figure 1.5). This is done (with the assumption that $v_\perp$ is orthogonal to $\boldsymbol{B}$) by differentiating Equation 1.4 with respect to time to give the velocity of the guiding centre drift, $\boldsymbol{v}_E$:

$$\frac{d^2\mathbf{v}}{dt^2} = -w_g^2(\mathbf{v} - \mathbf{v}_E) \tag{1.10}$$

where

$$\mathbf{v}_E = \frac{\mathbf{E} \times \mathbf{B}}{B^2} \tag{1.11}$$

In Figure 1.5 the effect of the electric field can be seen. Electric fields do the work necessary to accelerate particles, whilst magnetic fields only change the direction of a moving charge (i.e. magnetic fields do no work on the particles). As the electric field accelerates the particle in the direction of $\boldsymbol{E}$ this increases the gyroradius of the particle when motion is in the same direction (i.e. in the same direction as $\boldsymbol{E}$). When the particle travels in the opposite direction to $\boldsymbol{E}$, the electric field opposes the motion and the gyroradius decreases. This causes a drift orthogonal to both $\boldsymbol{E}$ and $\boldsymbol{B}$ (see Figure 1.5). However the drift is not dependant on charge, therefore both ions and electrons drift in the same direction.

1.2.2 Motion in a spatially varying magnetic field

If a particle is gyrating in a magnetic field that increases in strength ($\nabla \boldsymbol{B}$), in a direction perpendicular to the magnetic field $\boldsymbol{B}$, then the gyroradius decreases whilst in the stronger magnetic field (Equation 1.8). This means that a drift occurs in a direction perpendicular to both $\nabla \boldsymbol{B}$ and $\boldsymbol{B}$ (see Figure 1.6). The velocity of

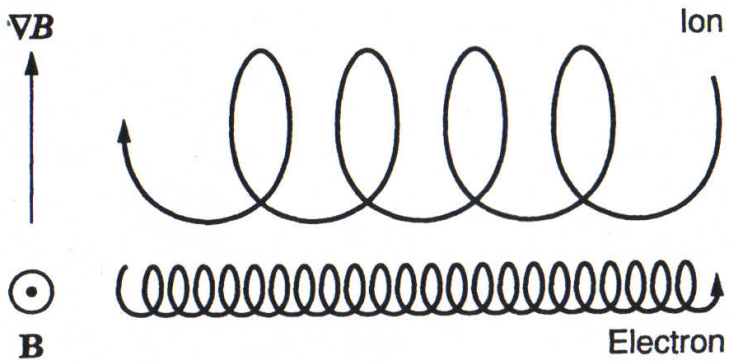

Figure 1.6: An illustration showing the behaviour of particles under the magnetic gradient drift (*Baumjohann and Treumann* 1996).

the gradient drift is:

$$\mathbf{v}_\nabla = \frac{mv_\perp^2}{2qB^3}(\mathbf{B} \times \nabla \mathbf{B}) \tag{1.12}$$

Another drift occurs when magnetic field lines are curved, such as in a magnetosphere. Due to the particle having a velocity component parallel to the magnetic field $v_{||}$, the particle experiences a centrifugal force. The drift direction of the particle is perpendicular to both the radius of curvature $\boldsymbol{R}_C$ (See Figure 1.7) and $\boldsymbol{B}$, so in an azimuthal direction. The resulting velocity of the drift is:

$$\mathbf{v}_R = \frac{mv_{||}^2}{q}\frac{\mathbf{R}_C \times \mathbf{B}}{R_C^2 B^2} \tag{1.13}$$

There is a general pattern to particle drifts. If a general force $\boldsymbol{F}$ is applied instead of $q\boldsymbol{E}$ to the equation of motion shown in Equation 1.4, then the drift of the guiding centre has a velocity $\boldsymbol{v}_F$:

$$\mathbf{v}_F = \frac{1}{q}\frac{\mathbf{F} \times \mathbf{B}}{B^2} \tag{1.14}$$

In the previous examples, both the gradient drift and the curvature drift are dependant on charge, and so they act in opposite directions for electrons and ions. The differential flow of charge causes a current to form. A combination of both the curvature drift and the magnetic gradient drift contribute to the magnetospheric ring current.

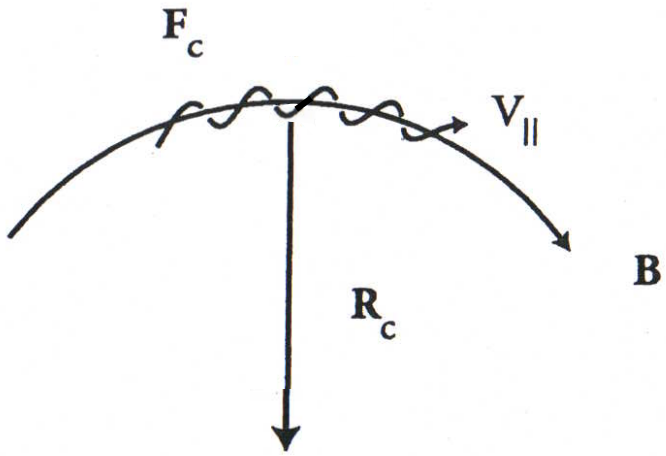

Figure 1.7: The centrifugal force $\boldsymbol{F}_C$ acting on a particle on a curved magnetic field line. Adapted from *Cravens* (2004).

1.2.3 The magnetic moment and bounce motion

A gyrating charged particle represents a current loop, and so a gyrating particle will have an associated magnetic moment. Since the magnetic moment μ is associated with gyration, it is related to the perpendicular velocity of the particle by the equation:

$$\mu = \frac{mv_\perp^2}{2B} = \frac{W_\perp}{B} \tag{1.15}$$

where $W_\perp$ is the perpendicular energy of the particle. As was discussed earlier, a magnetic field cannot accelerate particles, and so during gyration, as long as no other force is applied to the particle, μ is conserved, so that energy is conserved (when the magnetic field is not varying significantly in comparison to the period of gyration). This conserved quantity is called the first adiabatic invariant.

If a particle is travelling along a field line (whilst gyrating), and the magnetic field is increasing in the direction of $\boldsymbol{B}$, then for μ to be conserved, the perpendicular energy must also increase. This happens on field lines in a planetary dipole field, where the magnetic field converges at the poles. As a particle travels towards a pole, $v_\perp$ will increase. This also means that for kinetic energy to be conserved, $v_{||}$ decreases, causing the particle to experience an effective force known as the *mirror force* in the opposite direction to that which it is travelling. The mirror force $\boldsymbol{F}_{||}$,

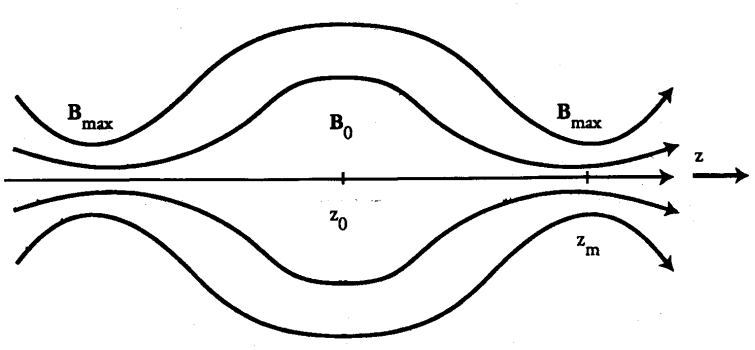

Figure 1.8: A magnetic bottle with a local minimum field strength B_0 in the centre of two local field strength maxima (B_{max}). Taken from *Cravens* (2004).

can be written as:

$$\mathbf{F}_{||} = -\mu \frac{dB}{d\mathbf{s}} = -\mu \Delta_{||} B \tag{1.16}$$

where $d\boldsymbol{s}$ is a line element along $\boldsymbol{B}$. This means that particles gyrating along the field line will reach a point where $v_{||}$ becomes zero, and the particle will then start to travel in the opposite direction due to the effect of $\boldsymbol{F}_{||}$. This effect is known as *magnetic mirroring*, and causes particles to be trapped on a field line in a 'magnetic bottle', and to 'bounce' between the mirror points of a dipole. An example of converging field lines of a magnetic bottle can be seen in Figure 1.8.

If the velocity of the particle is substituted into Equation 1.15, using $v_\perp = v \sin \alpha$, then:

$$\mu = \frac{m v^2 \sin^2 \alpha}{2B} \tag{1.17}$$

If a particle moves along a field line and the field strength changes, this causes the pitch angle to change, so that μ is conserved. If a particle labelled '0' (located where the magnetic field strength is B_0 and its pitch angle is α_0) moves to another area of the field line (where the pitch angle and magnetic field strength are α_1 and B_1 respectively), then the pitch angles of the particle are related by the following equation:

$$\sin^2 \alpha_1 = \frac{B_1}{B_0} \sin^2 \alpha_0 \tag{1.18}$$

If a particle is at $z = z_0$ in Figure 1.8, the pitch angle is α_0. The particle mirrors

when the magnetic field becomes strong enough for $v_{||}$=0 and α=90°. This occurs when B=B_{mirr}:

$$B_{mirr} = \frac{B_0}{\sin^2 \alpha_0} \tag{1.19}$$

B_{mirr} increases with lower values of α_0. As shown in Figure 1.8, a bottle exists between two points with field strengths equal to B_{max}. From the above equation, particles with a larger $v_\perp$ (i.e. pitch angles closer to 90°) at the equator (z_0) will mirror before they reach B_{max}, as their B_{mirr} is lower by comparison (i.e. their pitch angle becomes 90° closer to z_0). This also means that for particles with larger $v_{||}$ (i.e. pitch angles closer to 0°) at the equator, their B_{mirr} will be greater than B_{max}. This means that B_{max} does not mirror all the particles (especially for particles with a α_0=0). For any magnetic bottle there is a range of values of α_0 that are not confined. For a particle to be confined:

$$\sin^2 \alpha_0 > \left(\frac{B_0}{B_{max}}\right)^{\frac{1}{2}} = \frac{1}{R_{mirr}^{\frac{1}{2}}} \tag{1.20}$$

where R_{mirr} is the 'mirror ratio' defined as:

$$R_{mirr} = \frac{B_{max}}{B_0} \tag{1.21}$$

Particles that do not mirror, 'escape' the magnetic bottle. If there is a distribution of particles that is isotropic at $z = z_0$, and then the particles are observed at some later time, then the missing particles have 'escaped' the system through a *loss cone*; a cone or a small range of very low pitch angles.

Particles that do not pass through the loss cone are confined to the magnetic bottle and bounce back and forth. The time taken to bounce from z_0 to each B_{mirr} and back to z_0 is characterised by the bounce period T_b where:

$$T_b = \oint \frac{dz}{v_{||}(z)} = 4 \int_{z_0}^{z_{max}} \frac{dz}{v\left[1 - \frac{B(z)}{B_0} \sin^2 \alpha_0\right]^{\frac{1}{2}}} \tag{1.22}$$

1.2.4 Application to the Magnetosphere

The simplest model of the magnetic field in a planetary magnetosphere is that of a dipole. The coordinate system that is usually used is spherical coordinates, where

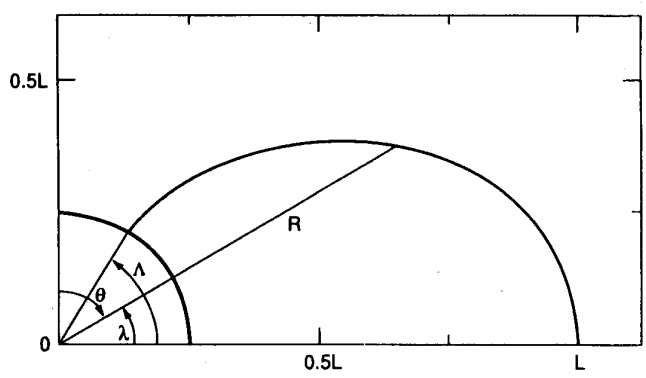

Figure 1.9: A sketch showing the physical quantities R, Λ, θ and λ (*Kivelson and Russell* 1995).

R is the radial distance to a point on the field line and λ is the magnetic latitude at that point (see Figure 1.9). L is the "L-shell" value of a field line, which defines the radial distance of a field line where it crosses the equator (see Figure 1.9). The magnetic latitude of the footprint on the surface of the planet of a magnetic field line is given as the invariant latitude, Λ. The radial distance R, to any particular point of a magnetic field line is described as:

$$R = L\cos^2\lambda \tag{1.23}$$

The magnetic field strength at any point in a dipole field distribution is given by:

$$B(R,\lambda) = \frac{M}{R^3}(1+3\sin^2\lambda)^{1/2} \tag{1.24}$$

where M is the dipole magnetic moment. The values of the individual components of the magnetic field are defined as:

$$B_R(R,\lambda) = -\frac{M}{R^3}2\sin\lambda \tag{1.25}$$

$$B_\lambda(R,\lambda) = \frac{M}{R^3}\cos\lambda \tag{1.26}$$

Looking at Equation 1.24 it can be seen that the magnetic field is weakest at the equator, and as the latitude is increased at a constant R then the magnetic field strength also increases. This is why planetary magnetospheres act as magnetic bottles, and why trapped particles in the magnetosphere bounce.

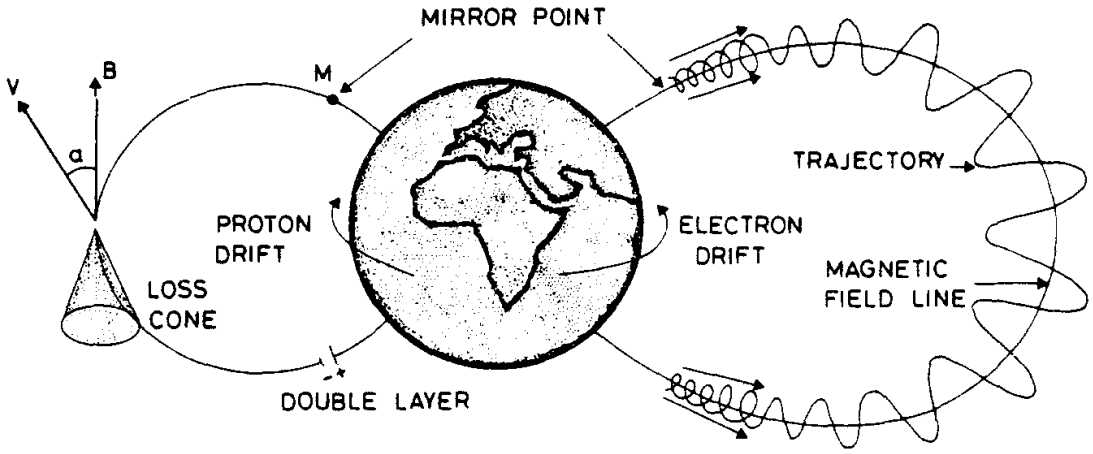

Figure 1.10: The motions of particles in a magnetosphere due to different drifts which have been defined above in the text. The bouncing of trapped particles between two mirror points is shown (*Lemaire* 1982).

A summary of some of the effects described in this chapter so far can be seen in Figure 1.10, with the application to the Earth's magnetosphere. The gyration of particles around the magnetospheric field line as well as the bouncing of trapped particles between mirror points (due to the magnetic field lines converging towards the poles) can be seen in the magnetosphere. The loss cone of particles with closely field-aligned pitch angles that do not mirror (and therefore penetrate the ionosphere and are 'lost') is shown. The drifting of electrons and protons in different directions is due to the gradient and curvature drift forces. The 'double layer' is a representation of the field-aligned electric potential drop that occurs near the planet, which accelerates the particles to produce the aurora.

1.3 Magnetohydrodynamics

The previous section discussed the behaviour of singly charged particles in electric and magnetic fields. However, from the definition of a plasma, there are many more particles present, and so a different approach to account for this is necessary. Instead of computing the single particle motions of many particles (which would take a lot of computational power), the single particle approach can be neglected in exchange for treating the motion of particles in a plasma as a collective fluid. In hydrodynamics, a particle's motion is part of a fluid due to constant collisions with neighbouring particles. A plasma is treated as an electrically conducting fluid which is then affected by internal and external magnetic fields. This approach is called *magnetohydrody-*

namics (*Alfvén* 1942), or 'MHD' for short. MHD is therefore a combination of fluid conservation equations combined with equations of electromagnetism. Similarly to single-particle motion, certain conditions of the plasma fluid must be met for MHD to be valid. Firstly, the scale sizes of the fluid must be significantly larger than the gyroradius of the particles. Secondly, the timescales of the changes in the plasma fluid must be much larger than w_g^{-1} (the typical gyroperiod) of the plasma.

Maxwell's equations are used to describe the relationship between electric and magnetic fields, and are written as follows, starting with Ampere's Law:

$$\nabla \times \mathbf{B} = \mu_0 \mathbf{j} + \frac{1}{c^2} \frac{\partial \mathbf{E}}{\partial t} \tag{1.27}$$

where μ_0 is the permeability of free space, c is the speed of light, and $\mathbf{j}$ is the current density. This equation states that changes in a magnetic field can be produced by either a current or a time-varying electric field (or both).

Faraday's Law:

$$\nabla \times \mathbf{E} = -\frac{\partial \mathbf{B}}{\partial t} \tag{1.28}$$

represents changes in an electric field which can be produced by a time-varying magnetic field.

Gauss' Law for magnetic fields is given by:

$$\nabla \cdot \mathbf{B} = 0 \tag{1.29}$$

implies that there is no divergence in a magnetic field and therefore magnetic monopoles cannot exist.

Gauss' Law for electric fields is:

$$\nabla \cdot \mathbf{E} = \frac{\rho}{\epsilon_0} \tag{1.30}$$

where ρ is the charge density and ϵ_0 is the permittivity of free space. The equation states that the divergence of an electric field is related to the density of electric charge.

In MHD, it is assumed that the fluid is quasineutral (the number of electrons and positively charged ions both equal n). If it is assumed that there are no source

or loss processes occurring then the total charge and mass is conserved during the fluid's motion, and so the mass conservation equation is:

$$\frac{\partial n}{\partial t} + \nabla \cdot (n\mathbf{v}) = 0 \tag{1.31}$$

The second equation for MHD is the equation of motion (or the momentum equation). Here it is written for the one-fluid case.

$$nm\left[\frac{\partial \mathbf{v}}{\partial t} + (\mathbf{v} \cdot \nabla)\mathbf{v}\right] = qn(\mathbf{E} + \mathbf{v} \times \mathbf{B}) - \nabla P \tag{1.32}$$

In an unmagnetised fluid the only acting forces are viscous and pressure forces, whilst for a plasma there is an added electromagnetic component, the Lorentz force, which acts on the charged particles. Equation 1.32 describes the change in fluid velocity in relation to the density and electromagnetic forces acting on the fluid.

As well as the above Maxwell's and MHD equations, Ohm's Law is also used. For many parts of the magnetosphere, Ohm's Law can be simplified to be written as:

$$\mathbf{j} = \frac{1}{\eta}(\mathbf{E} + \mathbf{v} \times \mathbf{B}) \tag{1.33}$$

where η is the resistivity of the plasma (which can be written as the inverse of the conductivity, σ^{-1}). This shows that the current density $\mathbf{j}$, is related to the rest electric and motional electric fields. The plasma resistivity η, is proportional to the collisional frequency, and in a (almost) collisionless plasma, this value becomes extremely low, which means the plasma is highly conducting. Therefore the limit of Equation 1.33 as η tends to zero becomes:

$$\mathbf{E} = -\mathbf{v} \times \mathbf{B} \tag{1.34}$$

which shows that in an infinitely conducting plasma, the electric field is the motional (or convective) electric field. This gives rise to the MHD concept of 'frozen-in' flux, whereby the magnetic field is frozen to the particles. This means that if the particles in a plasma fluid move, the magnetic field will also move so that the particles remain on the same field line.

1.3.1 Frozen-in Flux and the Magnetic Reynolds Number

Ohm's law (Equation 1.33), can be written with conductivity instead of resistivity, $\sigma = 1/\eta$. Using Ampere's Law and Faraday's Law, the following equation can be written:

$$\frac{\partial \mathbf{B}}{\partial t} = \nabla \times (\mathbf{v} \times \mathbf{B}) + \frac{1}{\mu_0 \sigma} \nabla^2 \mathbf{B} \tag{1.35}$$

where μ_0 is the permeability of free space. This is known as the induction equation (or the dynamo or hydromagnetic equation). The first term on the right side of the equation shows how the magnetic field varies due to convection of the plasma. The second term represents how the magnetic field diffuses through a plasma. The value $(\mu_0 \sigma)^{-1}$ is called the magnetic diffusivity. For a fully convective collisionless plasma, the magnetic field is advective and the second term is zero, causing the magnetic field to move with the plasma. If there are collisions, the resistivity increases and the diffusion of the magnetic field occurs.

The ratio between the two terms of the above equation is known as the magnetic *Reynolds number* (R_m):

$$R_m = \frac{\mu_0 \sigma}{\nabla^2 \mathbf{B}} \nabla \times (\mathbf{v} \times \mathbf{B}) \tag{1.36}$$

and measures which of the two terms is more important. Rewritten using simple dimensional terms, where L is the length scale and V is the velocity of convection, the equations becomes:

$$R_m = \mu_0 \sigma L V \tag{1.37}$$

If $R_m \gg 1$, then the plasma is convective and the magnetic field is frozen into the plasma. For a collisionless plasma the convective term is usually the dominant one. For a plasma where the magnetic field varies over large spatial scales, the plasma is said to follow ideal MHD conditions (i.e. when $R_m \gg 1$).

1.3.2 Magnetic Tension, Pressure and Plasma-β

Combining Ampere's Law and the momentum equation we can obtain:

$$\mathbf{j} \times \mathbf{B} = -\nabla \left(\frac{B^2}{2\mu_0} \right) + \frac{(\mathbf{B} \cdot \nabla)\mathbf{B}}{\mu_0} \tag{1.38}$$

From this equation, the first component on the right hand side shows the force exerted by a gradient in the square of a magnetic field strength. The first term is effectively the gradient of a pressure p_B which is written as:

$$p_B = \frac{B^2}{2\mu_0} \tag{1.39}$$

This is the magnetic pressure of a plasma. The last term of Equation 1.38 is the magnetic tension force. This force may arise when a magnetic field is bent and becomes distorted, and the tension force acts to return it to a lower energy configuration.

The total effective pressure of a plasma is thus the sum of the plasma pressure (P) and the magnetic pressure (p_B). The ratio of these two pressures provides the the plasma β ('beta') parameter:

$$\beta = \frac{2\mu_0 P}{B^2} \tag{1.40}$$

The plasma β determines which pressure is more important in determining the dynamics of the plasma. A low-β plasma where $\beta \ll 1$ occurs when the magnetic pressure dominates and it is said that the 'fluid follows the magnetic field'. In a high-β plasma of $\beta \gg 1$, the plasma pressure dominates and it is said that the 'magnetic field follows the fluid'. When $\beta \sim 1$ then neither of the two pressures dominate.

1.3.3 Diamagnetic Drift

A plasma fluid is made up of particles, and if the individual particles have drifts which are directed perpendicular to the magnetic field direction, then one would expect a plasma fluid to also have drifts. The pressure term ∇P however does not appear in the single-particle motion equations, and therefore the drift associated with it can only be found in fluids. If the left hand side of the equation of motion (Equation 1.32) is taken to equal zero (due to the assumption that that the direction of the drift is perpendicular to the gradient), and a cross product is taken with $\boldsymbol{B}$, the following result is obtained:

$$qn[\mathbf{E} \times \mathbf{B} + (\mathbf{v}_\perp \times \mathbf{B}) \times \mathbf{B}] - \nabla p \times \mathbf{B} = 0$$
$$qn[\mathbf{E} \times \mathbf{B} + \mathbf{B}(\mathbf{v}_\perp \cdot \mathbf{B}) - \mathbf{v}_\perp B^2] - \nabla p \times \mathbf{B} = 0$$

Rearranging gives:

$$\mathbf{v}_\perp = \frac{\mathbf{E} \times \mathbf{B}}{B^2} - \frac{\nabla p \times \mathbf{B}}{qnB^2} \tag{1.41}$$

It can be seen that the first term on the right hand side of the equation is the $\boldsymbol{E} \times \boldsymbol{B}$ drift, found in Equation 1.11. The second term is the velocity of a new drift known as the *diamagnetic drift*. Due to opposite directions of gyration, in a quasineutral plasma the diamagnetic drift is associated with the motion of electrons and ions in opposite directions. This will cause an effective drift current to flow in the plasma. This current is written as:

$$\mathbf{j}_{dia} = \frac{\mathbf{B} \times \nabla p}{B^2} \tag{1.42}$$

It is called a diamagnetic current as it will decrease the external magnetic field. This drift can be explained physically. Figure 1.11 shows a positive density gradient directed from right to left. On the left side of the figure, more particles are gyrating than on the right. For a specific volume element in the gradient, there are more particles moving down than up, due to the higher density. This results in a drift in the plasma perpendicular to the gradient and the magnetic field, and an effective drift current flow. The current is detectable because it generates a magnetic field which can be measured.

1.4 Plasma in the Solar System

Plasmas are found throughout the Universe as well as in the Solar System. The Solar System is full of plasma that has a magnetic field embedded in it, and the different regions important to this thesis will be described.

1.4.1 The Solar Wind

The solar wind is a constant stream of plasma that is highly variable, and travels radially outward from the Sun with a magnetic field threaded through it. It consists mainly of electrons and protons, as well as a very small percentage ($\sim$ 5 % by

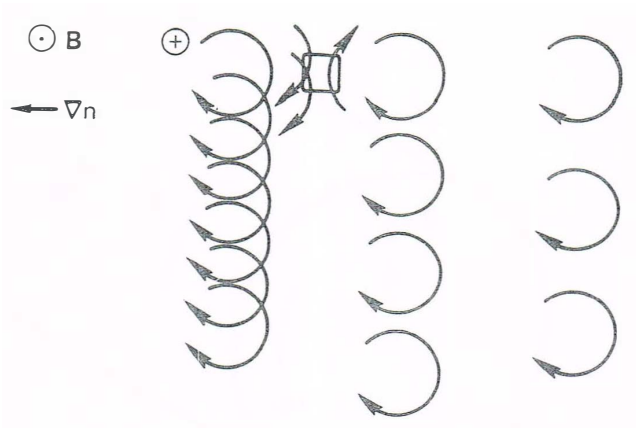

Figure 1.11: An illustration of the diamagnetic drift (*Chen* 1974).

number) of helium ions (*Baumjohann and Treumann* 1996). It was first suggested to exist due to the observations of the anti-sunward direction of cometary tails (*Biermann* 1951).

An explanation for the cause of the solar wind came later. The Sun's atmosphere is not confined to its surface like that of a planet, due to the very high thermal conductivity of the Sun's corona. Due to hydrostatic equilibrium not being maintained, the Corona is actually expanding outwards, causing a constant outflow of particles and radiation into interplanetary space. This idea was first proposed by *Chapman and Zirin* (1957) and later expanded upon by *Parker* (1959). This causes all of the planets to be bathed in the Sun's outflowing atmosphere (i.e the solar wind).

The solar wind is a highly conductive fluid with a Reynold's number of $R_m > 10^6$ (*Kivelson and Russell* 1995), so the magnetic field that originates deep in the Sun is dragged out into interplanetary space by the outflowing plasma. Therefore, pervading throughout the solar wind plasma there is a magnetic field of solar origin, known as the Interplanetary Magnetic Field (IMF). Combining the frozen-in approximation with the rotation of the Sun results in the IMF being 'wound up' into an Archimedean spiral, known as the Parker Spiral.

The spiral configuration produces an angle between the sun-planet radial vector and the direction of the IMF. This angle increases with distance from the Sun, and therefore differs for each of the planets (see Table 1.1). At an infinite distance from the Sun, the angle would be 90°.

The solar wind is variable, however it is usually grouped into two types; the

Table 1.1: The average IMF strength and direction (*Owen, C. J. priv. com*)

Planet	Angle	Strength
Mercury	21°	35 nT
Earth	45°	7 nT
Mars	56°	4 nT
Jupiter	80°	1nT
Saturn	85°	0.5 nT
Neptune	88°	0.2 nT

slow solar wind, with speeds of 300-400 km s^{-1}, and the fast solar wind, with speeds of up to 700 km s^{-1} (*Kivelson and Russell* 1995). The fast solar wind originates from open coronal holes found at the high latitudes of the Sun. The slow wind originates from closed coronal streamers found at lower latitudes. These velocities vary with the solar cycle (11 years), and are affected by the complex variations of the solar magnetic field.

At times of higher solar activity coronal holes can exist at all latitudes leading to ejection of high speed solar wind nearer the ecliptic. In addition, during the declining phase of the solar cycle, the Suns dipole axis is significantly tilted from its spin axis such that the sources of high speed solar wind cross the near-equatorial region twice per solar rotation. When fast streams of solar wind are emitted at this location, due to their higher velocity they are able to overtake the slow streams, causing an interaction between the two. A compression of the plasma and magnetic field takes place, resulting in large increases of the magnetic field strength. As these regions rotate with the Sun, they are called *corotating interaction regions* or 'CIRs'. An example of a CIR is shown in Figure 1.12. In this figure, the Parker spiral can also be seen with the curved IMF.

At the boundaries of a CIR, shocks can form where particles can be accelerated. On the leading side of the CIR a forward shock forms and propagates outwards from the CIR. On the trailing side, the shock is called the reverse shock and propagates into the fast solar wind. These CIRs can persist throughout many solar rotations.

1.4.2 Magnetospheres

The solar wind and the IMF dominate the majority of the space in the Solar System, however the magnetic field of a planet acts as an obstacle. The solar wind interacts with all the planets, however the focus of this discussion is on planets with intrinsic magnetospheres. Two of the eight planets (Venus and Mars) have flow-induced

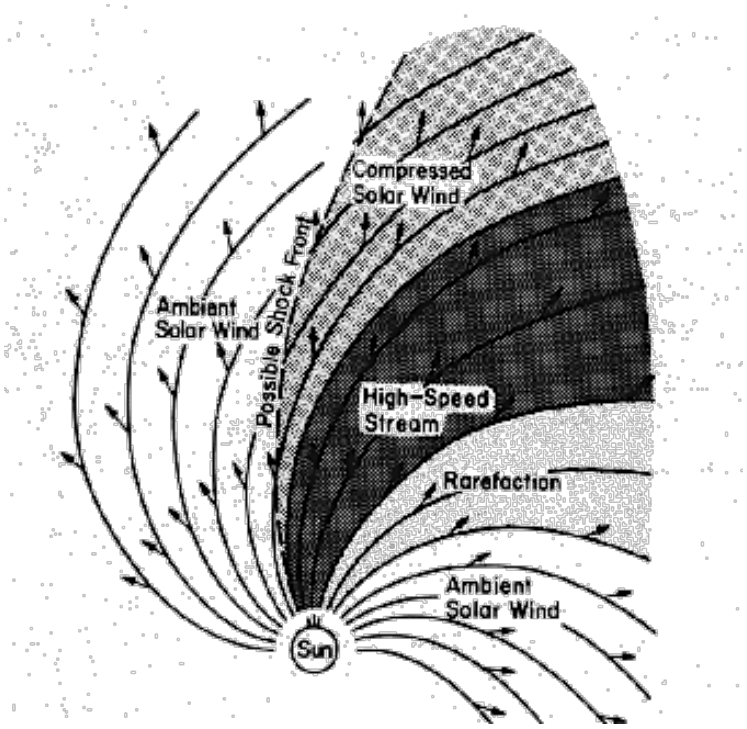

Figure 1.12: A corotating interaction region of the fast and slow solar wind (*Hundhausen* 1972). The shape of the Parker spiral can also be seen in the curved field lines originating from the Sun.

magnetospheres, with the rest having intrinsic magnetospheres. An induced magnetosphere occurs when the IMF induces a current in the unmagnetised planet's atmosphere, which due to Lenz's law results in a magnetic field being produced that opposes the IMF. This creates a magnetic barrier between the planet and the solar wind, and therefore an 'induced magnetosphere' forms.

Chapman and Ferraro (1931a,b) were the first to suggest that the Earth's magnetic field would create a low-density cavity within the solar wind. We call the low-density cavity the Earth's magnetosphere. The magnetosphere is defined as the region of space around Earth where plasma behaviour is dominated by the Earth's magnetic field. Chapman & Ferraro initially thought that the Sun ejected matter on a transient basis, however as discussed previously, the solar wind is continuous, but highly variable.

Most of the studies in the past and present have focused on the Earth's magnetic field which, in a vacuum (with no internal or external plasma or external magnetic fields present) would represent a magnetic dipole. However, due to the pressure exerted by the impinging solar wind, the dayside of the magnetosphere is

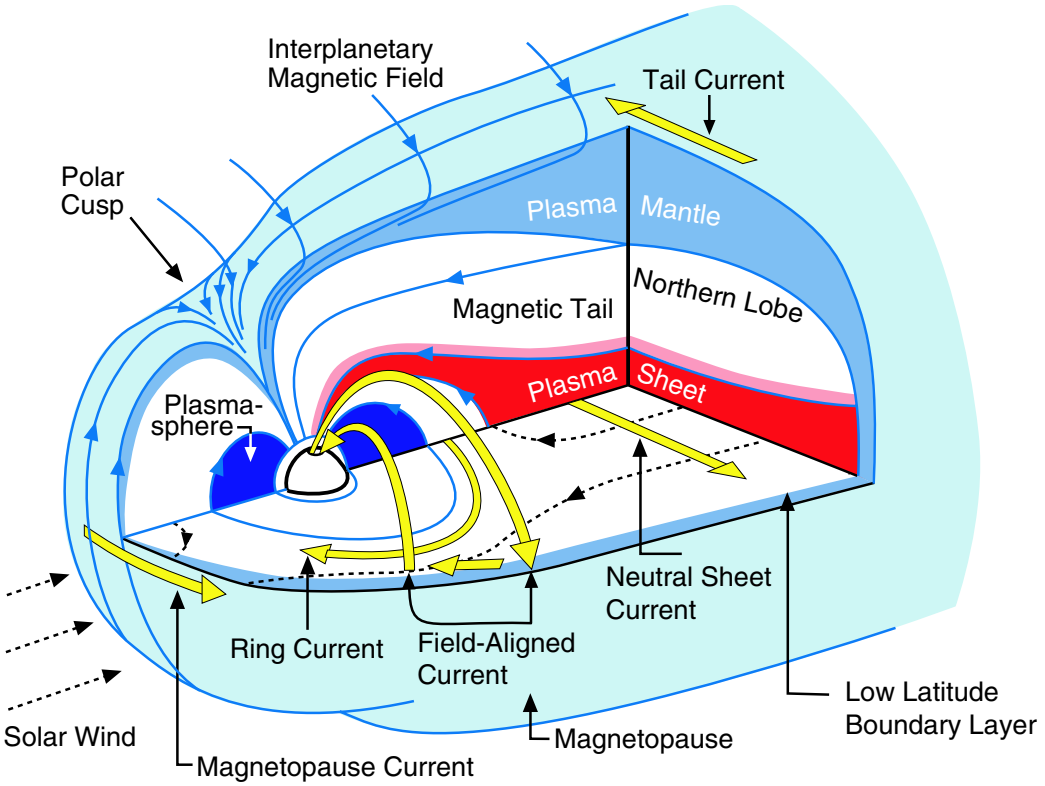

Figure 1.13: A diagram of the magnetosphere with its various regions and currents highlighted (*de Keyser et al.* 2005).

compressed. The nightside of the magnetosphere is stretched out into a long tail, called the *magnetotail*. The exact consequence of the frozen-in condition results in the inability of magnetised plasmas to mix (i.e. the plasma from the solar wind and the magnetosphere cannot mix), and therefore the magnetosphere becomes 'closed' to the solar wind. This is known as the *closed* magnetospheric model. A diagram of the terrestrial magnetosphere is shown in Figure 1.13. The different regions common to all magnetospheres are described below, with the aid of the diagram.

1.4.2.1 The Bow Shock and the Magnetosheath

The magnetosonic speed (c_{ms}) can be calculated for the solar wind according to:

$$c_{ms} = \sqrt{c_S^2 + v_A^2} \tag{1.43}$$

where c_s is the sound velocity, and v_A is the *Alfvén velocity*. The Alfvén velocity describes the speed at which waves can propagate (longitudinally) along the direction

of a magnetic field line in a plasma, and is described by the following equation:

$$v_A = \sqrt{\frac{B^2}{\mu_0 \rho}} \tag{1.44}$$

where ρ is the density of the plasma.

The magnetosonic Mach number (M_{ms}) can be calculated as the ratio of the velocity of the fluid to the magnetosonic velocity. A *supermagnetosonic* plasma is defined by $M_{ms} > 1$, and a shock occurs when the plasma encounters a non-moving obstacle because the plasma is unable to divert around the obstacle.

The solar wind is supermagnetosonic, so when it encounters a planetary magnetosphere as an obstacle in its path, a shock is formed upstream of the planet. The shocked material has two boundaries. The first being the bow shock, which is the boundary between the supermagnetosonic solar wind (upstream of the bow shock) and the shocked, disturbed solar wind plasma called the *magnetosheath*. The second boundary is between this shocked plasma and the magnetosphere (the magnetopause).

When the solar wind is shocked, it is slowed down and most of its kinetic energy is converted into thermal and magnetic energy. Therefore the magnetosheath is hotter and denser than the solar wind. The magnetic field strength is also higher in the magnetosheath because it is still frozen in to the plasma which has become denser. The subsolar magnetosheath is subsonic near the subsolar point of the magnetosphere and so the plasma is able to divert around the magnetosphere. Further down the flanks of the magnetosphere the magnetosheath will no longer be subsonic.

The magnetosheath is an important region as it is the 'border' between the magnetosphere and the IMF in the upstream solar wind. The IMF drapes around the magnetosphere along the magnetopause, and its orientation can influence the behaviour of the magnetospheric dynamics.

1.4.2.2 Magnetopause

Due to the frozen-in approximation of MHD, the plasma from the magnetosheath and magnetosphere cannot mix, and so a boundary between the two regimes exists, called the *magnetopause*. This boundary is highlighted in sky-blue in Figure 1.13.

There is a gradient and a curl in the magnetic field across the magnetopause due to the usually weak field in the magnetosheath and the strong field in the

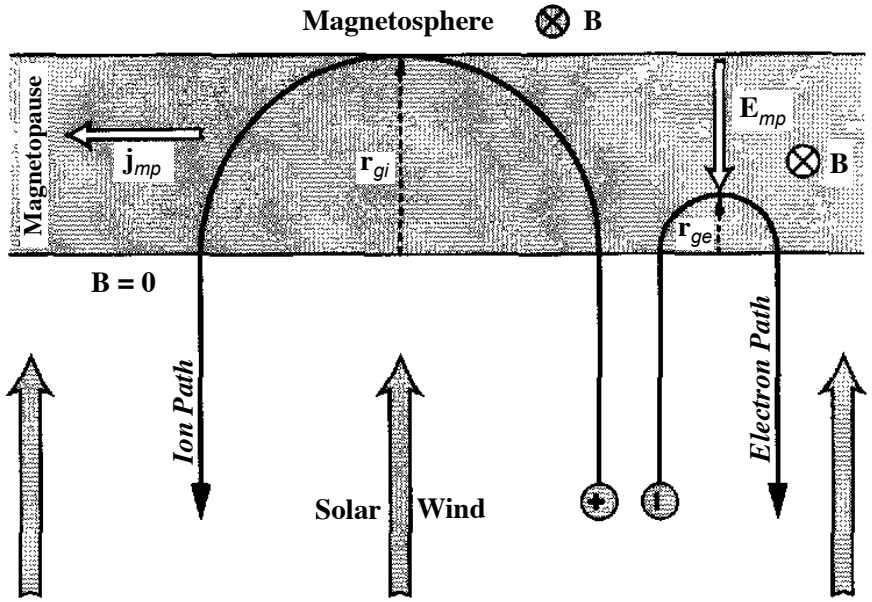

Figure 1.14: A schematic of the magnetopause surface current layer (*Baumjohann and Treumann* 1996).

magnetosphere. From Ampere's Law this curl is supported by a surface current layer. Therefore, in reality the magnetopause is not a line in space, but a current sheet with a distinct thickness. Figure 1.14 explains this current layer.

Particles enter the magnetospheric side of the magnetopause and, due to the increased magnetic field, their gyroradii decrease. After a half-orbit, the particles re-enter the magnetosheath with a reversed velocity. The thickness of the current layer is therefore of the order of the ion gyroradii. Electrons and ions gyrate in opposite directions, so there is a differential motion of the charge which gives rise to the current. This is a diamagnetic current caused by the density gradient and so it decreases the external magnetic field in the magnetosheath. The dayside current (see Figure 1.13) runs across the magnetopause from dawn to dusk, and then closes via the tail current, which is also 'fed' by the cross-tail current inside the magnetosphere. The tail current is divided into a northern and southern component, crossing over the lobes (dusk to dawn).

The location of the magnetopause maybe evaluated using a pressure balance across the boundary. The magnetopause is found where the dynamic, magnetic and plasma pressures of the solar wind and the magnetosphere are in equilibrium. Within the solar wind, the plasma pressure (thermal and dynamic) is more dominant, with the dynamic pressure more significant than the thermal component. In

the magnetosphere the magnetic pressure is more dominant. Therefore, by taking a (simplified) balance between the dynamic pressure of the solar wind and the magnetic pressure of the magnetosphere, the location of the magnetopause can be calculated. The subsolar position of the magnetopause is the location taken at its subsolar point, and at Earth this distance (between the planet centre and the subsolar point, usually measured in planetary radii) is proportional to $P_{dynamic}^{-1/6}$, whilst for the Jovian magnetosphere, the power in this relationship has been found to be between -1/4 and -1/5 (*Huddleston et al.* 1998), resulting in the terrestrial magnetosphere being less responsive to compression. This magnetopause standoff distance is usually considered when comparing different planetary magnetospheres. At Earth it is ∼10 Earth radii from the planet centre (R_E), whilst at Saturn it is ∼20 Saturn radii (R_S).

1.4.2.3 The Inner Magnetosphere

The inner terrestrial magnetosphere is marked by a cold, dense region of plasma in the shape of a toroid known as the *plasmasphere* (highlighted in dark blue in Figure 1.13). This plasma is of ionospheric origin and co rotates with the planet. Located at a similar distance from the planet are also the radiation belts (at Earth known as the Van Allen belts). These belts are areas of high energy particles. The proton belt extends all the way across the radiation belts, whilst the electron belt is divided into two regions, an inner and outer belt. These two regions are separated by the slot region, which is formed due to wave-particle gyroresonant interactions (whistler-mode and electromagnetic ion cyclotron wave) which can pitch-angle scatter the particles into the loss cone, causing them to be lost into the ionosphere (e.g. *Lyons and Thorne* 1973; *Spence et al.* 2013).

1.4.2.4 The Magnetotail

The nightside of the magnetosphere is stretched out into a tail-like configuration due to viscous interactions between the planetary magnetic field and the solar wind flow. The tail can extend for hundreds of planetary radii downstream of the planet.

The magnetotail has different regions which can be found in another diagram of the magnetosphere (Figure 1.15) with the magnetotail labelled. The plasma sheet contains high-density hot plasma (n∼0.5 cm^{-3}), with a relatively low magnetic field strength (B∼10 nT, from *Lui* 1987). A neutral sheet is found at its centre which has

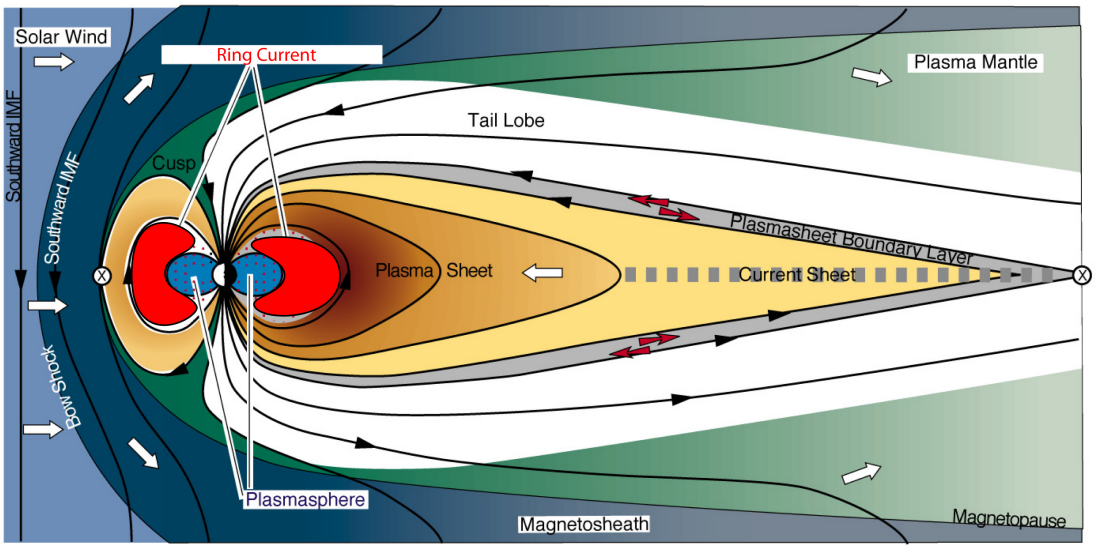

Figure 1.15: A diagram of the terrestrial magnetosphere with the magnetotail regions labelled (*Wang* 2008).

an extremely low magnetic field (B∼2 nT and n∼1 cm^{-3}). This is due to the change in the field orientation from a planetward directed magnetic field in the northern part, and anti-planetward in the southern part (for the terrestrial magnetosphere). The next region is the plasma sheet boundary layer, which is a transition layer between the plasma sheet and the tail lobes (n∼0.1 cm^{-3} and B∼20 nT). The tail lobes are regions with lower density plasma (n∼0.01 cm^{-3}) and higher magnetic field strengths (B∼25 nT) compared to the plasma sheet. Approximations of the number density and magnetic field strength were taken from *Lui* (1987).

1.4.2.5 Currents

Currents in the magnetosphere are associated with the variations or deformations of the magnetic field, which (mentioned previously) is summarised by Ampere's Law. The magnetosphere is deformed from a dipole due to the solar wind, and so several current systems arise. These currents can be seen in Figure 1.13, as yellow arrows. The magnetopause current occurs due to the field gradient between the magnetosphere and the magnetosheath, and travels from dawn to dusk, and in the tail over the lobes. It is also connected to the cross-tail current, which is associated with the oppositely orientated magnetic fields in the tail neutral sheet. When viewed from the Sun, these two currents are shaped into a theta symbol, Θ.

Near the Earth, there is a ring current which occurs partly due to the gradient and curvature drift of particles along the magnetospheric field lines. The ring current

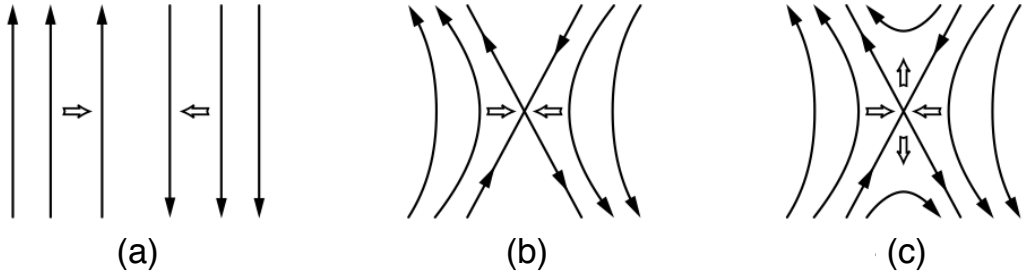

Figure 1.16: A simple schematic of oppositely aligned magnetic field lines reconnecting to form a new configuration (*Baumjohann and Treumann* 1996).

can also be partially diverted through the ionosphere along field-aligned currents, called *Birkeland* currents. Birkeland currents form at the inner edge of the plasma sheet, and the ring current is diverted along the field lines towards and away from the planet.

1.5 Magnetospheric dynamics

In this section the different processes contributing to magnetospheric dynamics will be presented. One of the drivers of dynamics is the process of magnetic reconnection, which will be discussed first.

1.5.1 Magnetic reconnection

Magnetic reconnection occurs when field lines are oppositely orientated, and interact to form a new configuration. From MHD, the magnetic Reynolds number gives a measure of whether the magnetic field advects with the plasma or not. For a high Reynolds number, MHD is an appropriate assumption of the rules that govern a plasma. However, when R_m is low, the magnetic field can diffuse through the plasma, and the frozen-in approximation is no longer valid. This may occur in current layers such as the magnetopause.

A simple reconnection model is shown in Figure 1.16. Two field lines approach each other due to plasma flow (a). Then the two magnetic field lines will reconnect to form two different field lines (b). As magnetic tension forces act to straighten the field lines which are curved, the field lines will move away from the reconnection region (c) and allow the next field line to undergo the same process. During reconnection, magnetic energy can be released and transferred to the plasma. Where previously two bodies of plasma could not interact due to ideal MHD, the new configuration of the magnetic field line allows for the plasmas to mix.

In the Sweet-Parker model of reconnection (*Parker* 1957), the diffusion region is long and narrow and the reconnection rate depends on the plasma inflow rate (v_{inflow}) through this region. This is written as:

$$v_{inflow} = \frac{v_A}{R_m^{1/2}} \tag{1.45}$$

This shows that the reconnection rate is dependant on the Alfvén velocity and the magnetic Reynolds number, which usually results in a low reconnection rate due to most plasmas having a high R_m. The Petschek reconnection model (*Petschek* 1964) is an improvement on this model, and does not require all of the material that is to be reconnected to pass through a diffusion region. Instead, the material is accelerated by shocks at the reconnection site. This decreases the size of the diffusion region, and increases the inflow velocity, and subsequently the reconnection rate is found to be more realistic in comparison to observed Solar System reconnection rates (e.g. *Priest* 2014).

1.5.2 The Dungey Cycle

Closed magnetospheric field lines that are opened via reconnection at the dayside magnetopause, map from the ionosphere into interplanetary space. Due to reconnection, the field lines become kinked and magnetic tension acts to 'straighten' them. This tension, along with the antisunward flow in the magnetosheath, drag the field lines poleward. These open field lines convect until they reach the tail, whereby the process of reconnection occurs again with other open field lines at a new location in the nightside of the magnetosphere. This causes the open field lines to become closed once again, and magnetic tension causes the now-closed field lines to become dipolarised. The energisation from reconnection and dipolarisation heats the plasma which creates the main emission in the auroral oval. Eventually the field lines will move through the flanks of the magnetosphere and reach the dayside where they may reconnect with the IMF at the magnetopause again. Reconnection must occur in the tail in order to replenish the field lines at the dayside, otherwise there would be a net erosion of magnetic flux on the dayside, and the Earth would be completely naked to the solar wind. This cycle is named after the author *Dungey* (1961) who first proposed it.

A representation of the Dungey cycle can be seen in Figure 1.17. In panel (a)

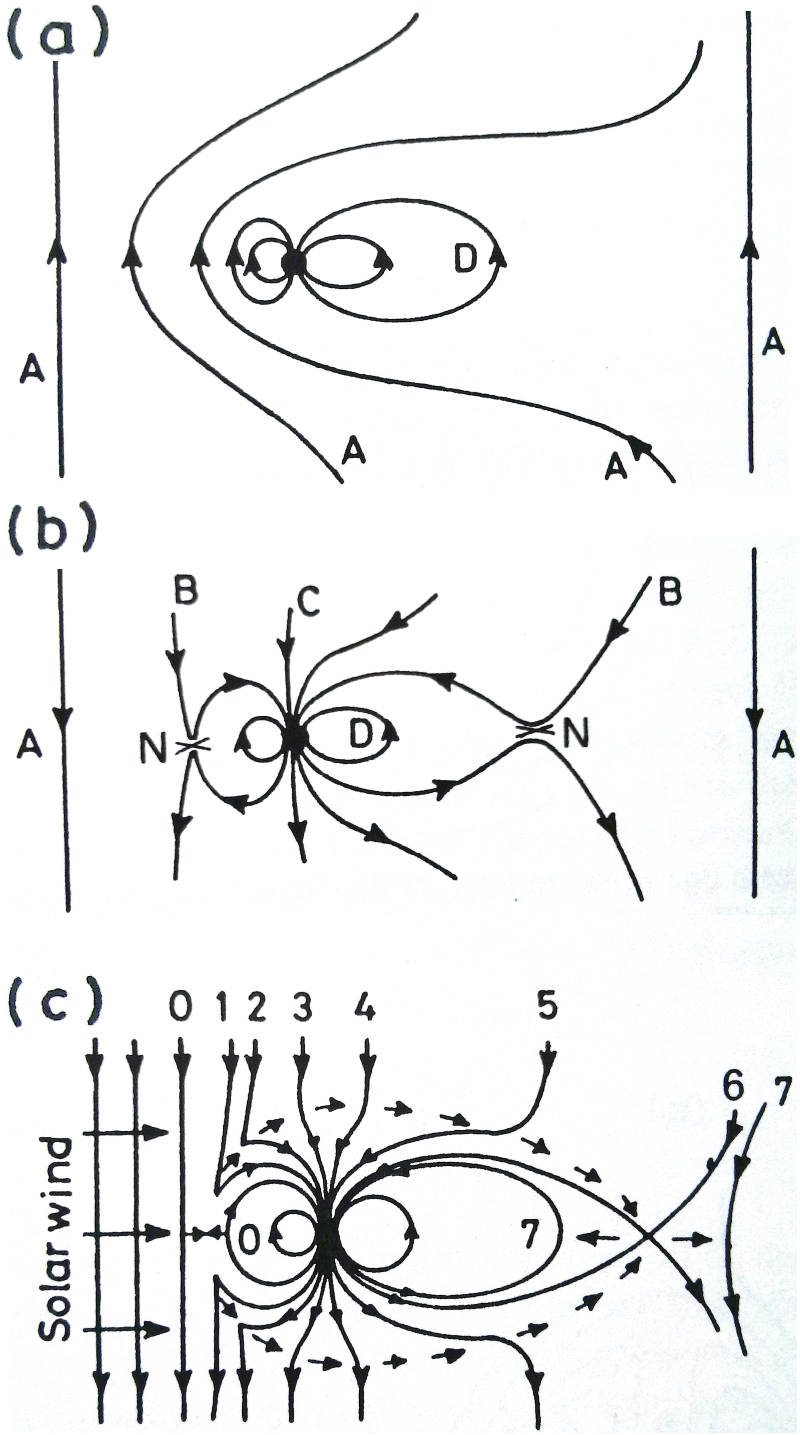

Figure 1.17: Field lines in the solar wind and the magnetosphere: a) when the IMF is parallel to the magnetospheric dayside field (i.e closed magnetosphere), b) for anti-parallel IMF (an open magnetosphere), the individual lines labelled A: IMF-line, B: IMF-line connecting or disconnecting to a geomagnetic field line, C: Open geomagnetic field line, D: a closed geomagnetic field line and N: the neutral point. Finally (c), the circulation of the magnetospheric field lines due to the Dungey cycle. The field lines labelled from 0−7 show the positions of the evolution of a magnetic field line during the Dungey cycle (*Hargreaves* 1995).

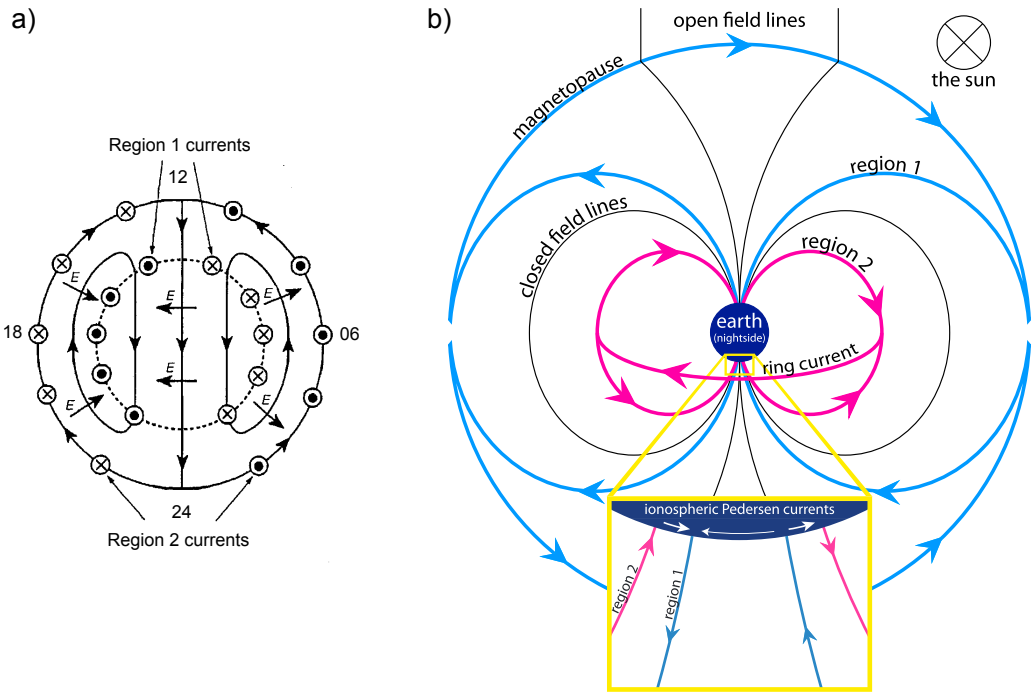

Figure 1.18: On the left in panel a): an illustration of the twin cell convection pattern the Dungey cycle produces in the ionosphere, with noon at the top, dawn to the right and dusk to the left. Also shown are the region 1 and 2 field-aligned currents flowing out of and into the ionosphere (dots and crosses). On the outside the local times are labelled. Taken from *Mauk and Bagenal* (2012). Panel b) shows the Region 1 and 2 currents, the Pedersen current and the magnetopause and ring current in the magnetosphere. The Pedersen current across the polar cap is thinner to represent that it is weaker than the currents between the two Regions. The view is from midnight (local time) as if the Earth was eclipsing the Sun. Taken from *Coxon et al.* (2014).

the IMF is northward and the field lines are not anti-parallel, resulting in no reconnection occurring, and the magnetosphere being closed. In panel (b) the different states of a field line are presented (see panel caption). In panel (c) the Dungey cycle is shown with the evolution of a field line before reconnection at '0', until the closure of magnetic field lines at '6' and dipolarisation of closed field lines at '7'. The closed field line returns to the magnetopause to be reconnected again. After reconnection occurs the field line convects poleward and when the field line is at positions 1 and 2, plasma from the magnetosheath is allowed to enter the magnetosphere. These regions are known as the cusps, and are an important region for the entry of plasma, momentum and energy into the magnetosphere from the shocked solar wind. The physics of this region will be discussed later, and is the focus of this thesis at the Saturnian magnetosphere.

In Figure 1.18a) the effect of the Dungey cycle in the northern ionosphere can

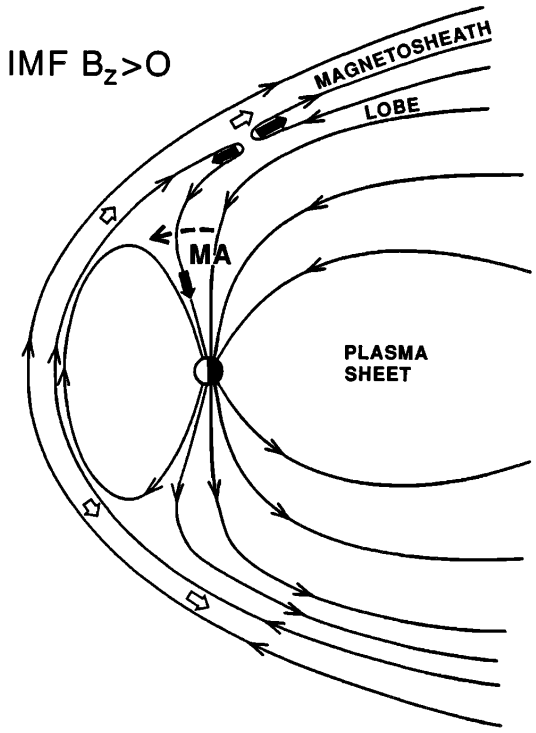

Figure 1.19: An example of lobe reconnection at the terrestrial magnetosphere during positive B_Z of the IMF. The magnetosheath plasma enters through the cusp/mantle region labelled 'MA'. Taken from *Sandholt et al.* (1996).

be seen. A twin cell convection pattern occurs where newly opened field lines move with the solar wind flow across the middle of the polar cap (region of open flux). The return flow of the newly closed field lines occurs on the outside of the polar cap.

The system of field-aligned currents which link the ionosphere, the inner magnetosphere and the magnetopause are also shown in panel a. The system approximately forms two rings in the polar ionosphere. The poleward ring (Region 1) links the currents associated with the magnetopause and the magnetotail to the ionosphere, and flows upward from the planet on the dusk side and downward into the planet on the dawn side. The equatorward ring (Region 2) links the ionosphere to the partial ring current (in the inner magnetosphere). These currents in the magnetosphere are shown in panel b of Figure 1.18. Region 1 and 2 currents are closed through Pedersen currents in the ionosphere, which flow in the direction of the electric field labelled 'E' (in panel a). The Pedersen currents across the polar cap (those linking Region 1 currents) are much smaller than those flowing in the auroral zones (i.e. the currents linking Region 1 with Region 2) (e.g. *Coxon et al.*

2014).

When the IMF is parallel to the planetary magnetic field, reconnection does not occur on the dayside, however the IMF is anti-parallel at a location anti-sunward of the cusp, and reconnection can occur in the lobes, either in one hemisphere or in both (e.g. *Gosling et al.* 1991; *Øieroset et al.* 1997). An example of lobe reconnection can be seen for the terrestrial case in Figure 1.19, where an IMF-line has reconnected with a lobe magnetospheric field line, that then proceeds to move equatorward where plasma can enter the cusp/mantle region (labelled 'MA').

The Dungey cycle is driven by reconnection due to the magnetosphere's interaction with the solar wind, and is the main driver of magnetospheric dynamics at the Earth.

1.5.3 The Vasyliūnas Cycle

The level of significance of the Dungey Cycle at Jupiter and Saturn is still contested. Earth is a slowly rotating magnetosphere in comparison to Jupiter and Saturn. The Vasyliūnas Cycle attempts to describe the plasma flow and role of reconnection in a faster rotating magnetosphere such as Jupiter. Jupiter has a large stretched-out magnetodisk. As field lines and plasma rotate around the magnetosphere, the field lines are compressed at the dayside magnetopause. However once they rotate towards dusk and the tail, the lines are allowed to stretch and expand tailwards. This is shown in the right-hand panel of Figure 1.20. The left panel shows the equatorial view, and the right panel shows the view from dusk of the magnetic field configuration. It can be seen that the field line has stretched between the configuration at 1 and 2.

The part of the flux tube near the planet rotates at a rate closer to that of the planet in comparison to the part which is further out. This can be seen in the bending of the field lines in the left panel. This effect, combined with the elongation of the flux tube causes instabilities to form, as seen by the field lines 2 and 3. Plasmoids form as 'loops' of magnetic field inside the last closed field line, and cannot be released. Eventually at 4, the last closed field line reconnects at the 'Magnetic-X-line' and the plasmoid is finally allowed to be released down the tail. This cycle was first proposed by *Vasyliūnas* (1983).

The plasma and field line dynamics of Saturn's magnetosphere is suggested to be driven by a mix of both the Dungey Cycle and the Vasyliūnas Cycle. This will

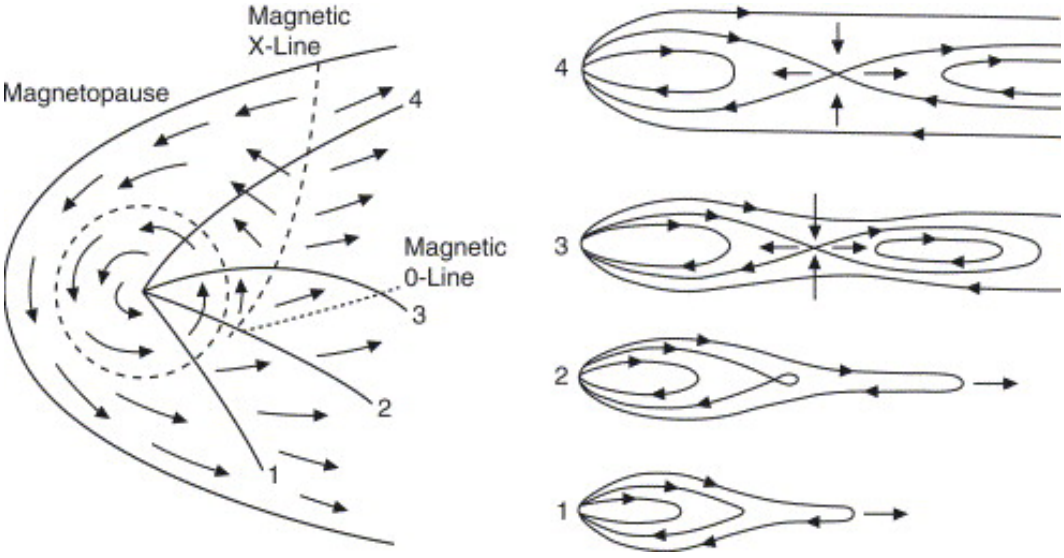

Figure 1.20: A sketch of the Vasyliūnas Cycle. On the left is a sketch of the equatorial view of the magnetosphere with plasma flow labelled and with lines numbered 1−4. On the right are the magnetospheric configurations representing what 1−4 look like as if viewed from dusk (*Vasyliūnas* 1983)

be explained in more detail later.

1.5.4 Differences between Planetary Magnetospheres

Most of the previous concepts have been discussed in terms of the Earth, however they also apply to other magnetised planets. All the other planetary magnetospheres have a magnetopause and a bow shock. However there are some differences between the planetary magnetospheres. The main difference concerns their size. Jupiter and Saturn have by far the largest magnetospheres, whilst Mercury has the smallest (see Fig. 1.21).

The magnetospheres vary in size due to two reasons. Firstly, the strength of the planetary magnetic moment (as well as any contributing magnetic fields from a ring current) will influence the size of the magnetosphere. The subsolar magnetopause occurs at the point where the solar wind dynamic pressure is equal to the magnetospheric magnetic and thermal pressures. Therefore, a stronger magnetic field results in the magnetopause being pushed further into the solar wind, causing a larger magnetosphere. Secondly, the solar wind dynamic pressure decreases radially outwards from the Sun, resulting in a planet with a given magnetic field structure having a larger magnetosphere the further it is away from the Sun (see Table 1.2 for a comparison of properties between Earth, Jupiter and Saturn).

In Table 1.2, we can see that the plasma sources at Jupiter and Saturn are

Table 1.2: Magnetospheric properties of Earth, Jupiter and Saturn compared, taken from *Dougherty et al.* (2009)

Parameter	Earth	Jupiter	Saturn
Heliocentric distance (AU)	1	5.2	9.5
Typical solar wind ram pressure (nPa)	1.7	0.07	0.015
Magnetic moment (Tm^3)	7.75 x 10^{15}	1.55 x 10^{20}	4.6 x 10^{18}
Typical Bow Shock distance	$\sim$13 R_E	$\sim$170 R_J	$\sim$27R_S
Typical magnetopause distance	$\sim$10 R_E	$\sim$90 R_J	$\sim$22 R_S
Magnetospheric Plasma sources (kg/s)	$\sim$1	$\sim10^3$	$\sim$300
Equatorial rotation period (hours)	23.934	9.925	10.53

several orders of magnitude larger than at Earth. This is because Jupiter and Saturn have volatile moons that contribute to the plasma source within the magnetosphere. At Jupiter, the volcanic moon Io is a major source of plasma (e.g. *Spencer and Schneider* 1996). This forms a plasma torus, which adds another aspect to the structure and dynamics at Jupiter's magnetosphere. At Saturn the moons Enceladus, Dione and Tethys are icy and produce a neutral torus, which is the E-ring (*Saur et al.* 2008). This is ionised to produce the E-ring plasma torus. At Jupiter the mass loading is localised near Io's orbit whilst at Saturn it is more evenly distributed. Another feature seen from Table 1.2 is that the giant planets are fast rotators which has an effect on the dynamics of the magnetosphere, causing the formation of a magnetodisk. The fast rotation of Jupiter and Saturn also results in the magnetic field lines in the lobes being twisted (e.g, *Isbell et al.* 1984; *Milan et al.* 2005).

This concludes the general introduction to magnetospheres. The next chapter will explain in more detail the physics and characteristics of the terrestrial cusp which has been the subject of extensive observation.

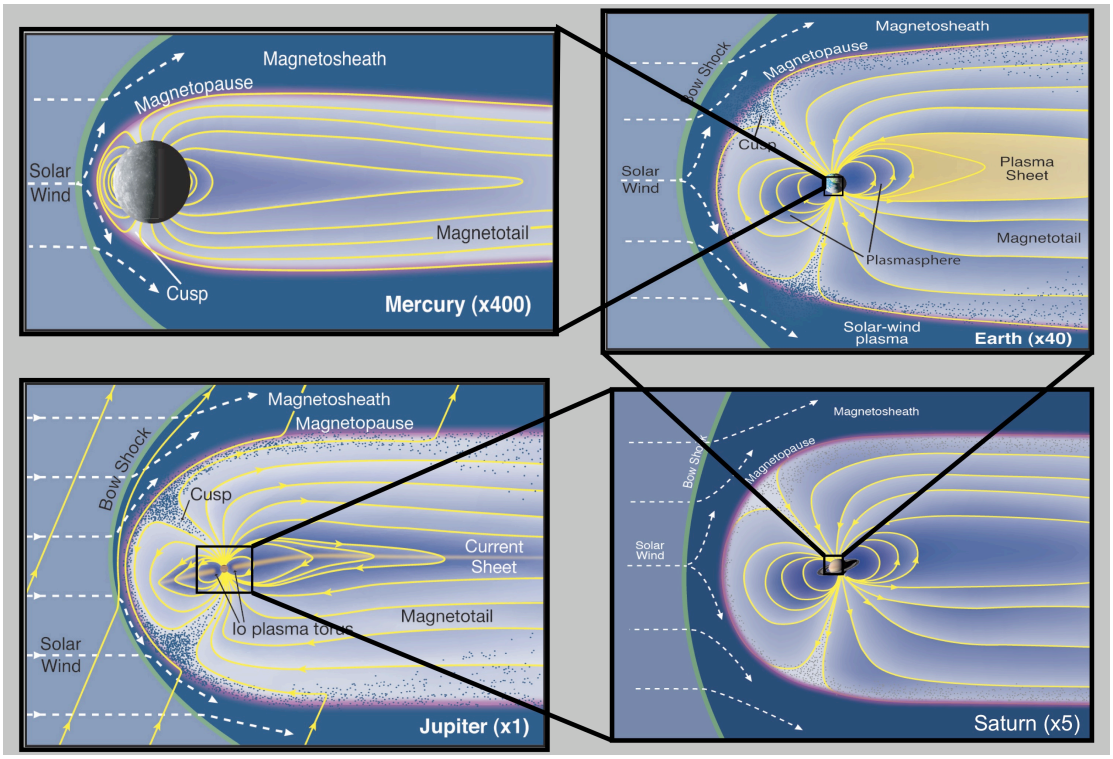

Figure 1.21: A diagram comparing the various sizes of the magnetospheres. Clockwise from top left are: Mercury, Earth, Saturn and Jupiter. The sheer size of Jupiter's magnetosphere can be marvelled at with it being much larger than the Sun (*Bagenal and Bartlett* 2015).

Chapter 2

Earth's Magnetospheric Cusps

The first idea of the magnetospheric cusp was postulated by Chapman & Ferraro in the paper *A new theory of magnetic storms* in 1931. They postulated that within the magnetosphere there would be a pair of magnetic 'null' points, one in the northern hemisphere, and one in the southern. They labelled these points the 'horns' shown in the left panel of Figure 2.1, labelled 'Q'. These are now called the cusps and a more updated diagram with the location of them inside the magnetosphere can be seen in the right panel labelled 'C'. The magnetic funnel-shaped region of the cusp is always present due to the geometry of the field lines in a magnetosphere. However the direct entry of solar wind plasma into this region occurs via the process of reconnection between the IMF and closed magnetospheric field lines. Consequently, the observation of the cusp is usually in regard to the observed (injected solar wind) plasma in the high latitude dayside magnetosphere from the reconnection site. As a result, reconnection is a process that adds open flux to the magnetosphere in addition to being a driver of plasma flow and dynamics. Therefore the cusps are important to study as they are a source of direct entry of matter, energy and momentum into the magnetosphere as well being a proxy for the study of reconnection. Much of the research which has been carried out on the topic of the cusp has been done in regard to the Earth, which this chapter will now summarise.

The magnetic field lines that thread through the cusp map to the ionosphere. Therefore the cusp is a means for direct entry of plasma into the magnetosphere and also the ionosphere. The cusp maps to a very narrow region on the ionosphere, however it extends to a wide range of latitudes and longitudes at higher altitudes. The polar cap is a region poleward of the cusp (at higher latitudes).

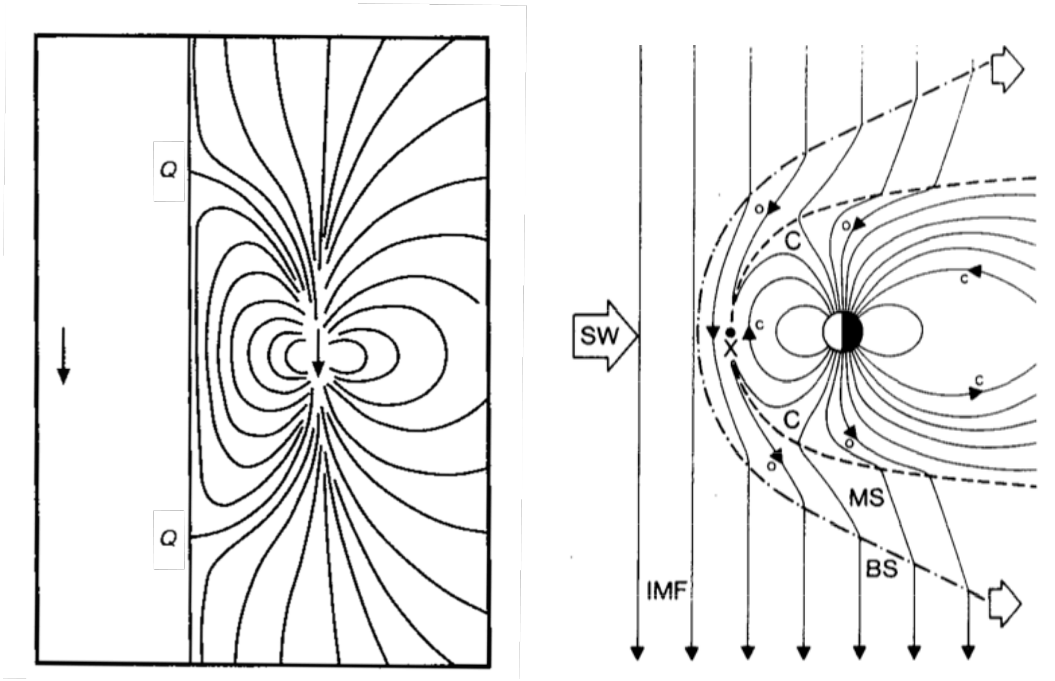

Figure 2.1: Left: A diagram of the first concepts of the magnetosphere which implicitly introduced the ideas of two magnetic 'null points' that *Chapman and Ferraro* (1931a,b) called the 'horns' (labelled Q) which we now call the cusps. Right: An updated schematic of the cusps in the magnetosphere showing a cross-section of the Earth's magnetosphere, from noon to midnight. The Sun is on the left, and the IMF carried by the solar wind (SW) has a southern orientation. The inner dashed line is the magnetopause and the outer dashed line is the bow shock. In between is the mangetosheath (MS). The magnetic field lines of the planet reconnect with the IMF at 'X' and open and closed field lines are labelled 'o' and 'c' respectively. The cusp (C) occurs due to reconnection (*Smith and Lockwood* 1996).

Until the first observations of plasma occurrence in the polar magnetosphere by the satellite *Imp 5*, the possibility of a high-latitude cusp region was debated and this was labelled the 'zone of confusion' (*Axford and Hines* 1961). This confusion ended with the paper *Plasma in the Earth's Polar Magnetosphere* (*Frank* 1971). In the paper the author attempts to answer a very simple question: can plasma enter the magnetosphere through Chapman & Ferraro's proposed magnetic neutral points?

The observations showed an increase in proton intensities in the cusp which are comparable to the magnetosheath, see Figure 2.2. This occured at a magnetic latitude of 68°, an L shell value of $L \simeq 40$ and a radial distance of ∼35 000km. It can also be seen that the polar cap region is observed to be completely empty of all particles (within the detection limit of the instrument). *Frank* (1971) examined 11 consecutive passes of the cusp with Imp 5, and reached the conclusion that the polar cusp (as a magnetic funnel shaped structure) is a permanent feature, and not a

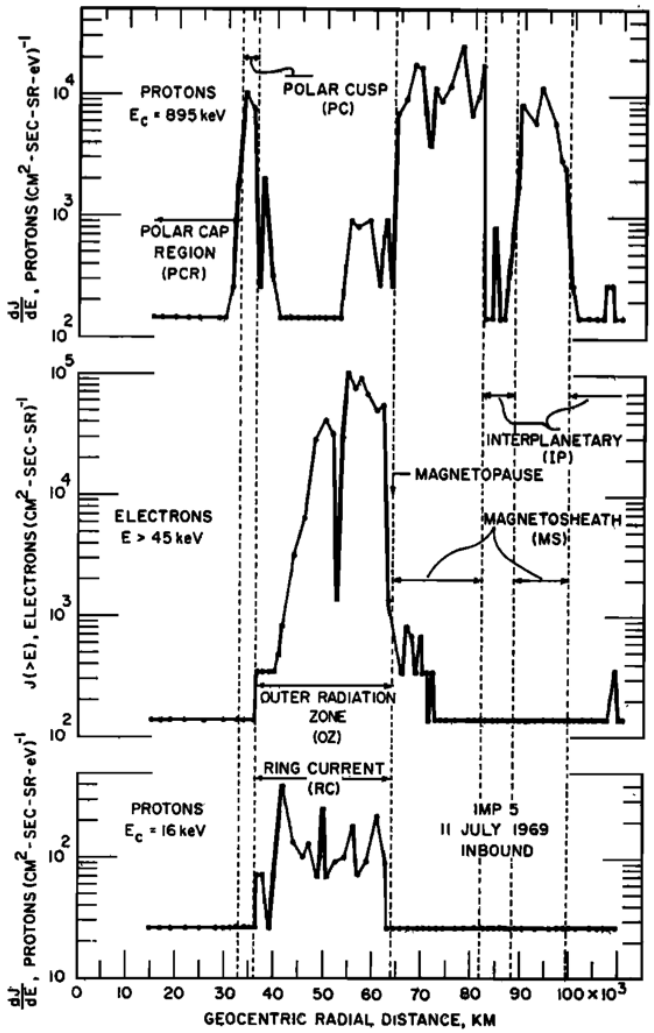

Figure 2.2: An inbound pass of Imp 5 through the polar magnetosphere, passing through the magnetic cusp. The magnetic cusp can be seen by the sharp peak of protons at 35000 km (*Frank* 1971).

transient one. Furthermore, since the cusp occurs at various local times (a couple of hours either side of noon), then the cusp field lines intersect with the magnetopause not at a single point, but along a line of an approximate length $\sim 1R_E$.

The observations also showed that the width of the cusp increases the further away from Earth the satellite is. The open-closed boundary was found to be at Λ =79°. The position of the cusp was found to be variable and dependent on the solar wind interaction with the magnetosphere.

Frank (1971) compares the proton energy spectra of the distant cusp (a radial distance of ∼10 R_E from the planet) and mid-altitude cusp (∼6 R_E) to that of the magnetosheath. At the distant cusp the energy spectrum of the protons is the same

as the magnetosheath, however at the mid-altitude cusp the lower energy protons are depleted.

Further observations were undertaken by the soft particle spectrometer (SPS) onboard the *Isis 1* satellite, which also observed the polar magnetosphere. *Heikkila and Winningham* (1971) reported fluxes of low-energy (<1 keV) electrons and protons observed in the daytime high-latitude region of the magnetosphere. They also reported that the electrons experience a sharp cutoff at high energies. The energy spectrum at the cusp peaks at 100-200 eV, which was shown to be similar to those observed in the magnetosheath. The data from Isis 1 was compared to Imp 5 observations of the cusp, and both were found to be in agreement with one another. It was concluded that the observed particle flux in the cusp is mostly of solar wind origin and that the shape of the cusp is not axially symmetric, but more wedge-shaped.

In 1968, the satellite *Ogo 5* observed the cusp during a magnetic storm (*Russell et al.* 1971). During these observations the cusp was observed at lower magnetic latitudes such as 43°. This is due to an increased reconnection rate occurring at the magnetopause causing increases in erosion of dayside magnetic flux, and thus causing the cusp to move equatorwards. Diamagnetic depressions were measured by the magnetometer whilst in the cusp. The diamagnetic depression coincided with increased fluxes of high energy electrons ($\leq$50 keV), something that was not previously observed. The high energy electrons however did not account for the 'missing' magnetic pressure during the magnetic depression. *Russell et al.* (1971) assumed that the high energy electrons would be accompanied by high energy protons, which would account for this energy discrepancy.

Confusion arose when another region was discovered which occupied a wide swathe of local times, and was located slightly equatorward of the cusp. This area was coined the 'cleft' (*Heikkila* 1972), a term used for the topological boundary of a closed field line. However others argued that direct magnetosheath precipitation into the low altitudes was more likely to occur at a narrow region at noon and not local times outside this range (*Paschmann et al.* 1976; *Haerendel et al.* 1978). *Heikkila* (1985) argued that the cusp was a sublayer of the cleft, occurring slightly more polewards and at noon. The cusp and cleft were used interchangeably for many years, and no real distinction between the two was made until the late 1980's. It was shown that the precipitation of magnetosheath plasma at low altitudes occurred

very close to noon local time, and that this was the cusp layer. The cleft was the high latitude extension of the low latitude boundary layer, with higher energies and lower fluxes, just equatorward of the cusp and at large ranges of local times (*Newell and Meng* 1988, 1989). The two regions are distinguishable due to their different particle energy distributions.

2.1 Energy-Latitude Dispersions – "Velocity Filter Effect"

After reconnection occurs at the magnetopause, particles are able to access the magnetosphere from the magnetosheath whilst the magnetic field line is connected between the two. The properties of the injected particles change as the field line convects poleward and anti-sunward. Ions in the magnetosheath tailward of the cusp will have a larger bulk flow velocity in comparison to their thermal velocities. This results in the ions travelling anti-sunward, and not entering the magnetosphere on open field lines tailward of the cusp. Electrons will flow with the ions in order to maintain quasi-neutrality in the plasma, and so also do not enter tailward of the cusp.

This causes the cusp precipitation to only be seen at certain latitudes, and causes it to be characterised into different "layers" in decreasing levels of precipitation - from the cusp, to the mantle and the polar cap (where there isn't any precipitation occurring). The mantle is a region just poleward of the cusp, where lower density plasma is observed travelling anti-planetward along the magnetospheric field line, representing particles that have mirrored and are travelling tailward (e.g. *Rosenbauer et al.* 1975; *Newell et al.* 1991; *Onsager et al.* 1993)

Upon reconnection, particles enter the newly opened field line from both the magnetosheath and the magnetosphere as indicated by the two large arrows in Figure 2.3. The two field lines that reconnect are labelled S1 and S2 (for separatrix between the magnetosphere and the magnetosheath). Ions and electrons are accelerated by the process of magnetic reconnection into the region and the boundaries labelled E1, E2 and I1, I2 are where a spacecraft would observe the electron and ion edges respectively. The electron edge E2 (in comparison to I2) is closer to the open-closed-field-line boundary due to the electrons having a higher field-aligned velocity than the ions (due to their lower mass). However both ions and electrons

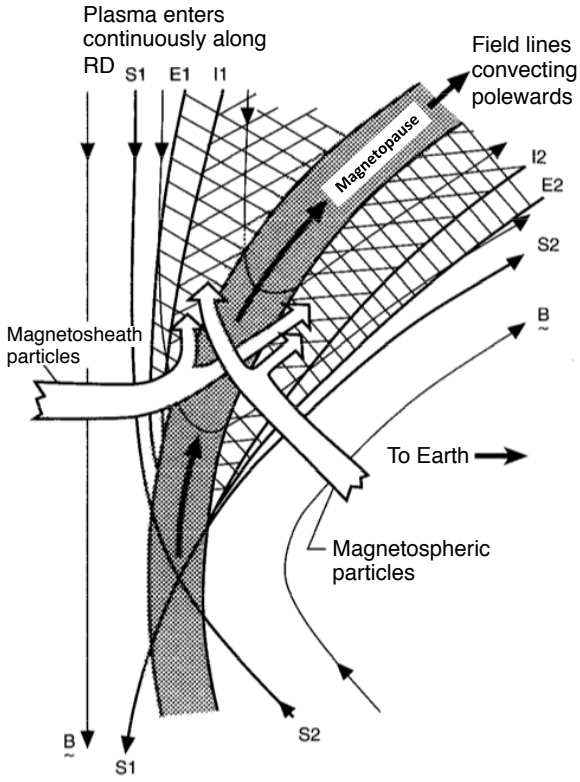

Figure 2.3: An illustration showing the different injection regions of particles occurring at the magnetopause during reconnection. S1 and S2 form the two magnetic field lines that are reconnecting (currently). Particles from the magnetosphere and the magnetosheath are entering. The shaded lines outline the regions were the ions and electrons (I and E) have accessibility (adapted from *Gosling et al.* 1990a).

drift at the same $\boldsymbol{E}\times\boldsymbol{B}$ velocity, in a direction perpendicular to the field.

The particles that are injected have different energies (differing velocities). This means that particles with two different energies will have a different time-of-flight along a field line. As a result, a particle with a higher energy will reach a position on the field line earlier (in time) than the lower energy particle. As the field line convects poleward, the position on that field line will be at a lower latitude for the higher energy particles. This results in lower energy particles reaching higher latitudes later (in time) along the field line than the higher energy particles. Therefore the particles become dispersed amongst different latitudes. This gives rise to the *velocity filter effect* (*Shelley et al.* 1976; *Hill and Reiff* 1977; *Lockwood et al.* 1994) that is observed by a spacecraft, an example of which can be seen in Figure 2.4. A spacecraft that is moving through the cusp from lower to higher latitudes will see an energy-latitude dispersion in the ions, whereby the higher energy ions are observed at lower latitudes. This means that higher energy ions would be seen at the ion edge I2 in

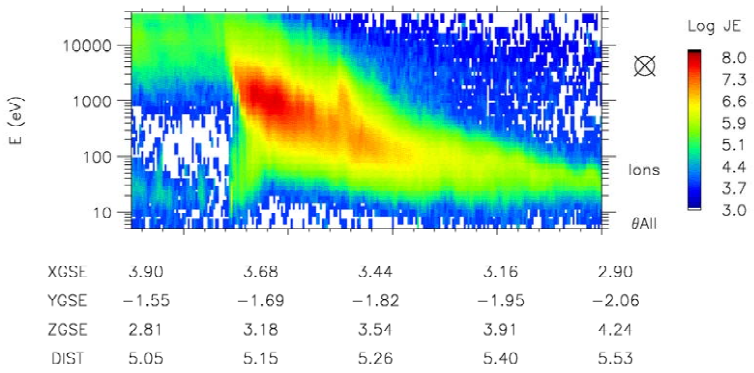

Figure 2.4: An example of an ion energy-latitude dispersion observed by one of the Cluster spacecraft (adapted from *Pitout et al.* 2009).

Figure 2.3, and lower energy ions would be seen at higher latitudes than I2 (i.e. more time needs to pass before lower energy ions appear at a particular point on the convecting field line).

Reiff et al. (1977) explored two possibilities for the existence of cusps: the process of reconnection and cross-field diffusion. It is accepted that magnetic reconnection is the reason for plasma injection into the cusp. *Reiff et al.* (1977) found that reconnection is the more significant process of the two (occurrence frequency of up to 80%). They observed that at altitudes of 1000 km, the cusp has a latitudinal width of a few degrees which is significantly larger than the gyroradius of a typical cusp proton. This observation led to their conclusion that this type of structure is a product of magnetic reconnection injection (see the right panel of Figure 2.5).

Figure 2.5 (left side) is a good representation of the velocity filter effect, where the dashed lines represent ions of different energies. *Reiff et al.* (1977) propose that since an ion energy dispersion is seen, the size of the injection region at the point of reconnection must be less than or comparable to the distance that the ions travel

Figure 2.5: On the left: an open-model magnetosphere illustrating how higher energy ions mirror earlier after injection (with the dashed arrows representing ions of two different energies). On the right: a closed-model magnetosphere illustrating the ions during cross-field diffusion (*Reiff et al.* 1977).

from the reconnection region to the place of observation.

At Earth, electron dispersions are not observed because the difference in time of flight between different typical energies of electrons is negligible. The energy and observation time is related by the following equation (*Lockwood et al.* 1995):

$$d_n(m/2E_n)^{\frac{1}{2}} = t_s - (t_0 + t_n) = t_s\left(\frac{V_S}{V_C}\right) - t_n \tag{2.1}$$

If reconnection occurs at a time t_0 and the newly opened field line moves poleward, the field line reaches a point P_n on the magnetopause where plasma is injected. The time taken for this to occur is a time t_n after reconnection occurs. If ions are observed at a time t_s then the time of flight T is equal to the arrival time minus the combined time of reconnection and the time taken to inject the plasma at the point P_n. The field-aligned distance from P_n to the spacecraft is d_n. E_n is the energy of the ion, and m is the mass of the ion. The right hand side takes into account V_C and V_S which are the convection and satellite speeds normal to the open-closed boundary.

This is derived by calculating the poleward distance the field line has moved (i.e. for the case where injection site P_n is also the reconnection site) which is $V_C(t_s - t_0)$. It should be clarified that the time of reconnection t_0, is not the start time (i.e. $t = 0$) in this model. This means that the distance the field line has moved since reconnection would be equal to the distance the spacecraft has travelled from $t = 0$ until the observation time t_s, so $V_s t_s$. Equating these two distances and substituting for $(ts - t_0)$ (into the middle of Equation 2.1) produces the right hand side of Equation 2.1.

The dispersions have a range of energies which shows that there are a range of locations along the magnetopause from where the ions are injected whilst the field line is convecting (*Onsager et al.* 1993; *Lockwood and Smith* 1993). This also reveals that the cause for the entry of magnetosheath particles into the magnetosphere occurs due to reconnection and not because of the minimum magnetic field associated with the cusp's location.

The idea of 'pulsed' or 'bursty' reconnection driving the cusp observations led to the idea of a pulsating cusp model (*Smith and Lockwood* 1990), which would produce multiple consecutive dispersions to be observed with energy jumps (*Smith*

et al. 1992), as well as ionospheric signatures (*Lockwood et al.* 1993). Other multiple dispersions were reported to have a spatial explanation rather than a temporal one (*Newell et al.* 1991). Using the same data as *Newell et al.* (1991), it was shown that the jumps in energy in the spectrograms were due to changes in reconnection rate, specifically three pulses of reconnection occurring approximately ten minutes apart (*Lockwood and Smith* 1992). The pulsating cusp model is also supported by other high latitude observations (e.g. *Escoubet et al.* 1992; *Onsager et al.* 2001) as well as magnetopause observations of flux transfer events (e.g. *Russell and Elphic* 1979; *McWilliams et al.* 2004). The different morphologies of dispersion 'steps' in the data were outlined by *Lockwood and Smith* (1994), and are now described.

Figure 2.6a-d shows the associated step signature of ion dispersions expected under different conditions for a spacecraft travelling polewards in the mid altitudes. V_C and V_S are the velocities of the convecting field line and the spacecraft respec-

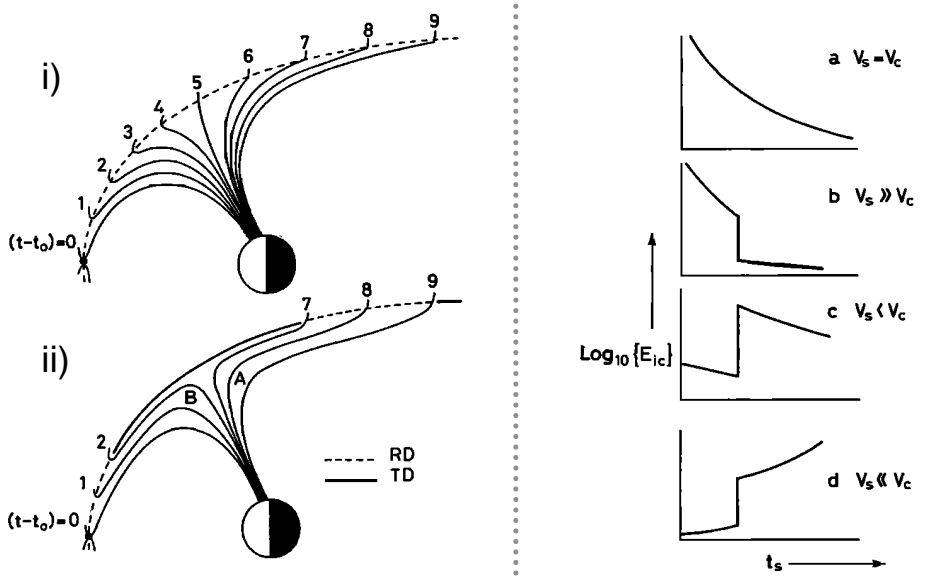

Figure 2.6: On the left hand side: the effect of pulsed reconnection on the magnetic field line topology, (i) the evolution of a field line after reconnection as it travels polewards from the time t =0 until t =9. If steady state reconnection is occurring then this the topology of all the field lines at any given time. (ii) A snapshot of the field lines after pulsed reconnection has occurred at time t =0-2, and at t =7-9 before t_0, which creates the regions labelled A and B. On the right hand side: the variations of the lowest energy ion cutoff of dispersions occurring under different conditions during pulsed reconnection (a) $V_S = V_C$, (b) $V_S \gg V_C$, (c) $V_S < V_C$ and (d) $V_S \ll V_C$, where V_C and V_S are the velocities of the convecting field line and the spacecraft respectively, at the time the observation takes place t_s. The velocities are poleward from the open closed field line boundary and positive. In (b) the spacecraft observes the region B and then A as shown in (ii). Whilst in (c and d) the spacecraft observes region A and then B (adapted from *Lockwood and Smith* 1994).

tively. Both velocities are positive and in the direction normal to the open-closed field line boundary (directed polewards). On the left there is a depiction of the topology of the field line for when, (i) reconnection is occurring steadily, and (ii) when there are bursts of reconnection occurring at time $t = t_0-$(0-to-2) and $t = t_0-$(7-to-9), see caption. If the spacecraft is travelling at the same velocity as the field line (i.e. the spacecraft is stationary in field line rest frame), then it observes a normal steady dispersion (right hand side, graph a). If the spacecrafts velocity is larger than that of the field line (b), then it overtakes the field line where it has been observing a normal dispersion, and observes a different field line which is 'older' (i.e. has reconnected previously), and so the energy drops significantly. This can be visualised with the aid of (ii) − the spacecraft exits region B, and enters A for which reconnection had occured further back in time.

If the spacecraft's velocity is lower than the field line's (c), then the field line overtakes the spacecraft this time. Due to the motion of the field lines, the spacecraft effectively moves from region A to region B. This causes a 'step-up' in the energy, as the second field line to be observed had reconnection occurring more recently, and so the more energetic ions are still present. The final example occurs when the spacecraft velocity is significantly smaller than the field line's. A reverse signature is observed, because the spacecraft is practically at rest in comparison to the large V_C, and so the leading boundary ($t = t_0 - 9$) of region A would be observed first with lower energies, followed by the trailing boundary ($t = t_0 - 7$) with the higher energies. Then the spacecraft would pass into region B, with the same step up as the previous example.

When an energy-latitude dispersion is observed that has higher energies followed by lower energies (spacecraft moving poleward), this is called a 'normal-sense' dispersion. This implies that the reconnection occurred at the dayside magnetopause. If a dispersion is observed in the opposite direction (also with the spacecraft moving poleward), then this means that the field line is convecting equatorward. This is called a 'reverse-sense' dispersion and implies that reconnection occurred in the lobes. Knowing the direction of the spacecraft trajectory and the sense of the dispersion reveals the general location of the reconnection site. An example of an irregular observation of a dispersion can be seen in Figure 2.7. A normal-sense dispersion is observed immediately followed by a reverse sense dispersion.

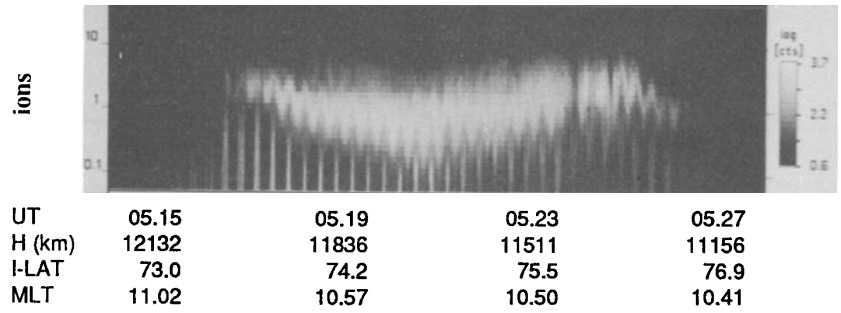

Figure 2.7: Observations from the Viking spacecraft that observed the terrestrial cusp. A normal-sense dispersion is observed first followed immediately by a reverse dispersion (adapted from *Woch and Lundin* 1992).

2.1.1 Temporal and spatial cusp dispersion structures

Energy-latitude dispersions observed in the cusp can be characterised into two groups of structures; temporal and spatial. A structure can be temporal due to the change of a process during the time of the observation. A spatial structure could be due to a feature that is moving relative to the spacecraft. Ambiguities arise in the observations and it is important to discover what the underlying cause is.

As an example, the observation presented in Figure 2.7 could be a spatial or a temporal structure. If it is a temporal structure this means that subsolar reconnection was occurring and halfway through the observation it stopped, and lobe reconnection started. If this is a spatial structure then subsolar and lobe reconnection were occurring at the same time and the spacecraft passes from one region to another. Another unlikely scenario is that it is a spatial structure with a large V_C that caused the region to pass over the spacecraft, and a similar observation is made to a hybrid of Figure 2.6c and d.

In order to determine which is the cause, multiple spacecraft are required to pass through the cusp at the same time but at different locations. If the spacecraft observe the same structures at similar times then it is a temporal structure. If the spacecraft don't observe the same structures, then the structure is spatial. These structures have been studied in detail with the Cluster mission (e.g. *Wing et al.* 2001; *Trattner et al.* 2002, 2005, 2008; *Escoubet et al.* 2006). However, this thesis focuses on single spacecraft observations and therefore the spatial-temporal ambiguities cannot be resolved.

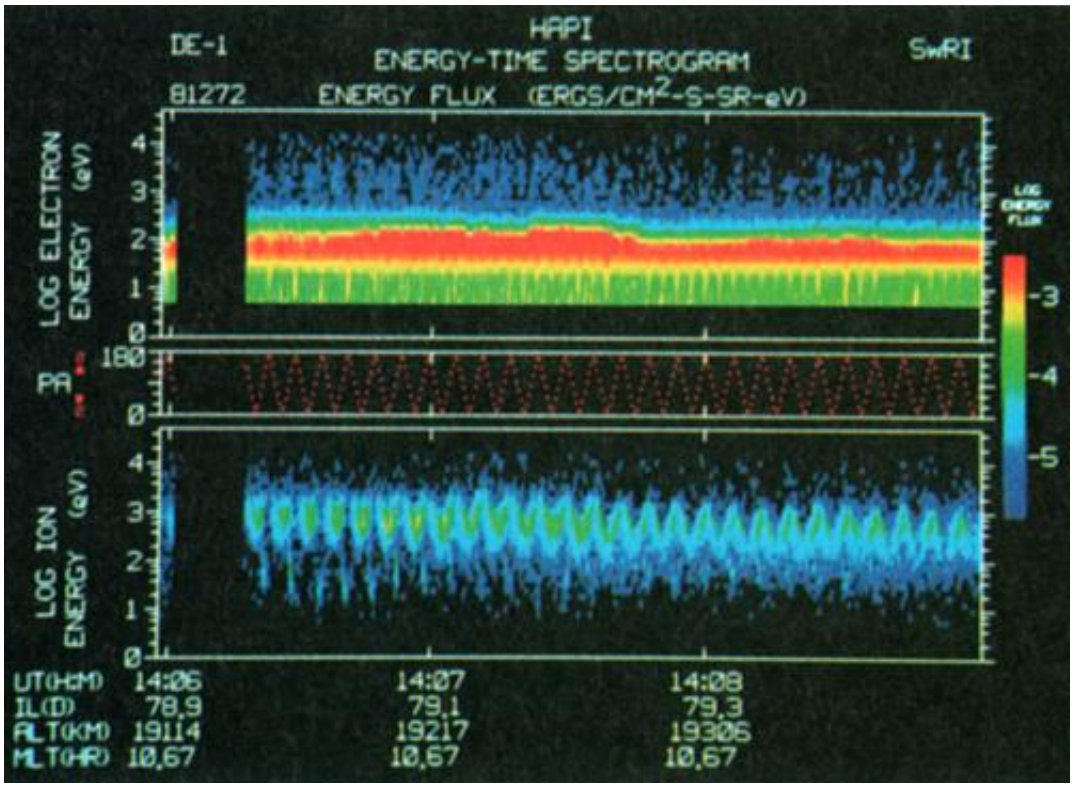

Figure 2.8: Energy-time spectrograms for electrons (top panel), and ions (bottom panel). The middle panel shows the pitch angle look direction which is changing from 0-180◦ periodically. The ion energy-pitch angle dispersion can be see by the repetitive 'V' symbol in the data (*Burch et al.* 1982).

2.2 Energy-Pitch Angle Dispersions

Burch et al. (1982) reported a 'V' shaped ion-energy pattern in the cusp observed during a change of pitch angle coverage, which was observed by the DE-1 spacecraft as is shown in Figure 2.8. For each energy-time spectrogram the electron and ion observations are shown, with the pitch angle look direction (middle panels) corresponding to the particle observations. In the top panels, low energy, dense electrons are observed, similar to the magnetosheath, as one would expect. However the ions show a 'V' signature which is the result of an energy-pitch angle dispersion, where low energies are observed when the instrument looks in the 0° pitch angle direction (and high energies at 180°). In the northern hemisphere at Earth where these observations were made, this means that the higher energy ions are travelling anti-planetwards.

These ions observed in the cusp with anti-planetward pitch-angles (180° in the northern cusp) have already mirrored at low altitudes, and therefore travelled a

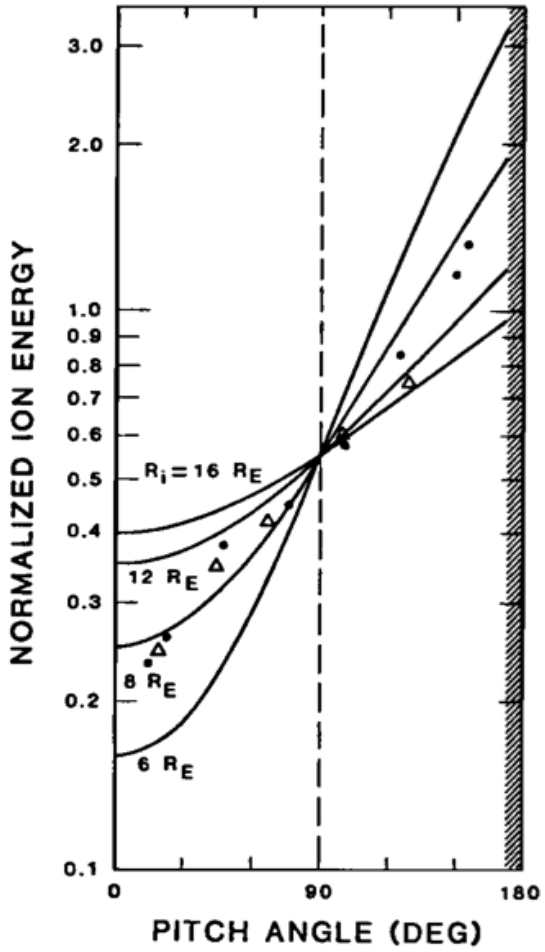

Figure 2.9: The calculated pitch angle/energy relationship for ions injected at different radial distances R_i at the magnetic dipole line of 78°, and later observed at $4R_E$ on the same field line (*Burch et al.* 1982).

larger field-aligned distance from the reconnection site, compared to ions with a planetward pitch-angle which have not yet mirrored. In order for this to occur, the ions with an anti-planetward pitch-angle must have a higher energy so that their parallel velocity is larger, allowing them to be observed simultaneously.

Burch et al. (1982) computed the energy dependance on the pitch angle for ions which had different injection regions along the magnetopause. The result is that the gradient of the dispersion is correlated to the field-aligned distance from where the particles were injected (see Figure 2.9). The model equation that they used to calculate the field aligned distance to the reconnection is:

$$E(\alpha_o, t) = \frac{m}{2t^2}\left[\int_{s_i}^{s_o} ds/\sqrt{1 - sin^2\alpha_o(B(s)/B_o)}\right]^2 \tag{2.2}$$

where ds is the arc length along a model field line, s_o and s_i are the observation and injection points respectively, m is the particle's mass, $B(s)$ is the magnetic field strength along the field line, B_o is the magnetic field strength at the observation point, α_o is the observed pitch angle, and t is the transit time of the particle from the injection site (via the mirror point for ions that have mirrored) to the observation point. The integration is made from the injection point via the mirror point to the point of observation. This equation is a manipulation of the bounce time shown in Equation 1.22.

2.3 Diamagnetic depressions

The gyromotion of high density magnetosheath plasma entering the magnetosphere can induce a diamagnetic depression observed as a decrease in the local magnetic field in the cusp (e.g. *Erlandson et al.* 1988; *Niehof et al.* 2008). An example of a depression is shown in Figure 2.10, where it can be seen that as the ion flux increases during the cusp there is a decrease in the magnetic field. These depressions have been called *cusp diamagnetic cavities* (CDCs). CDCs have also been correlated to occur during energetic particle observations, and have been named *cusp energetic particle* (CEP) events (*Chen et al.* 1998). In this section, this final characteristic of the cusp is described.

Chen et al. (1997, 1998) reported the observation of high energy He^{++} in the cusp up to energies of 2 MeV, with the intensity peaking at 1-200 keV/q. The intensity of this range was also anticorrelated with the depth of the magnetic field depression in the cusp. The authors concluded that although the plasma was of solar wind origin, the high energies of the ions were not similar to those of the magnetosheath and therefore there must be a major acceleration region in the cusp. CDC's have been observed to sometimes be as big as 6 R_E. *Fritz et al.* (2003) observed them with >40 keV ions, which were "more typical...of radiation belt populations than solar wind". The CEPs however could plausibly originate from particles accelerated at the bow shock that are then transported through to the cusp (*Trattner et al.* 1999, 2001, 2003), rather than accelerated locally as was suggested by *Chen et al.* (1998). However, *Nykyri et al.* (2011a) argue that the presence of energetic O^+ ions in the cusp is not consistent with acceleration at the bow shock. The acceleration mechanism for CEPs observed in CDCs is still debated, with the

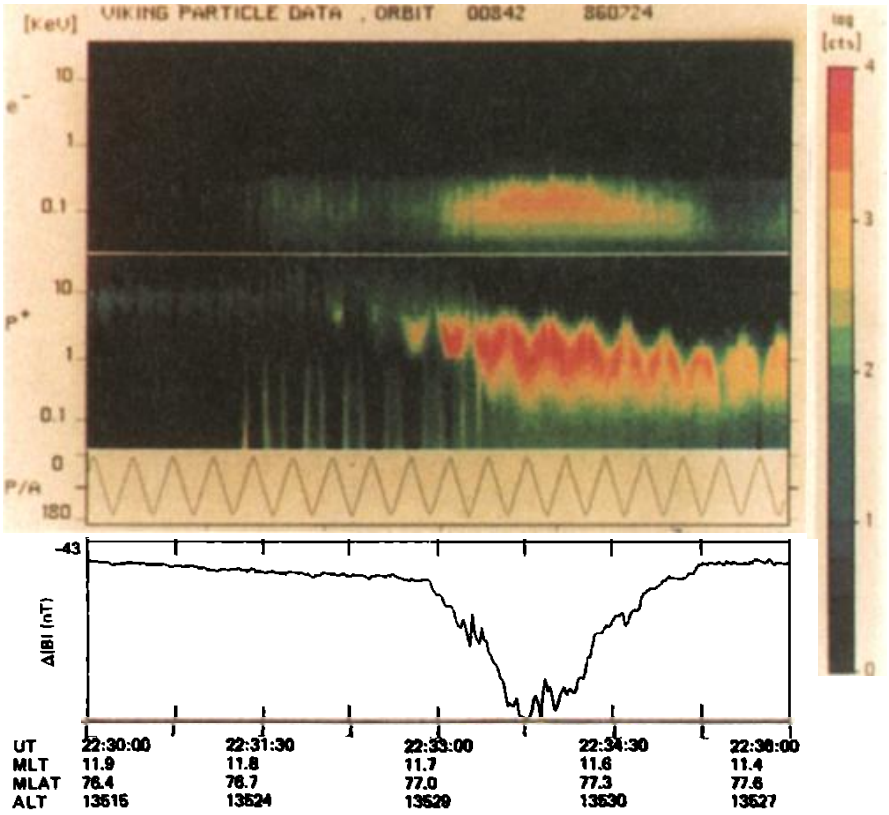

Figure 2.10: An example of a magnetic field depression during a cusp observation. In the top two panels are spectrograms of electron and ion observations respectively. In the bottom panel is the the magnetic field magnitude (adapted from *Erlandson et al.* 1988; *Andre et al.* 1988).

discussion focused solely on the origin on the CEPs.

A survey of observations from the Polar spacecraft (*Zhou et al.* 2000) formed the basis of investigating the diamagnetic depressions in correlation to low energy plasma with ion temperatures of ∼100 eV. *Zhou et al.* (2001) found that the diamagnetic pressure deficit (i.e. the pressure associated with the decrease in magnetic field strength) was greater under larger solar wind dynamic pressures at the magnetopause. The solar wind dynamic pressure was calculated as a function of the angle between the magnetopause normal and the Sun direction. Since the dynamic pressure was dependant on this angle, when the dipole was tilted away from the Sun, the angle (between the magnetopause normal and the Sun direction) was larger and consequently the solar wind dynamic pressure and the resulting cusp magnetic depression were both smaller (*Zhou et al.* 2001). Therefore a correlation between the depression magnitude and this angle was found.

The authors also found that the depression was greatest at local times of $11-13$

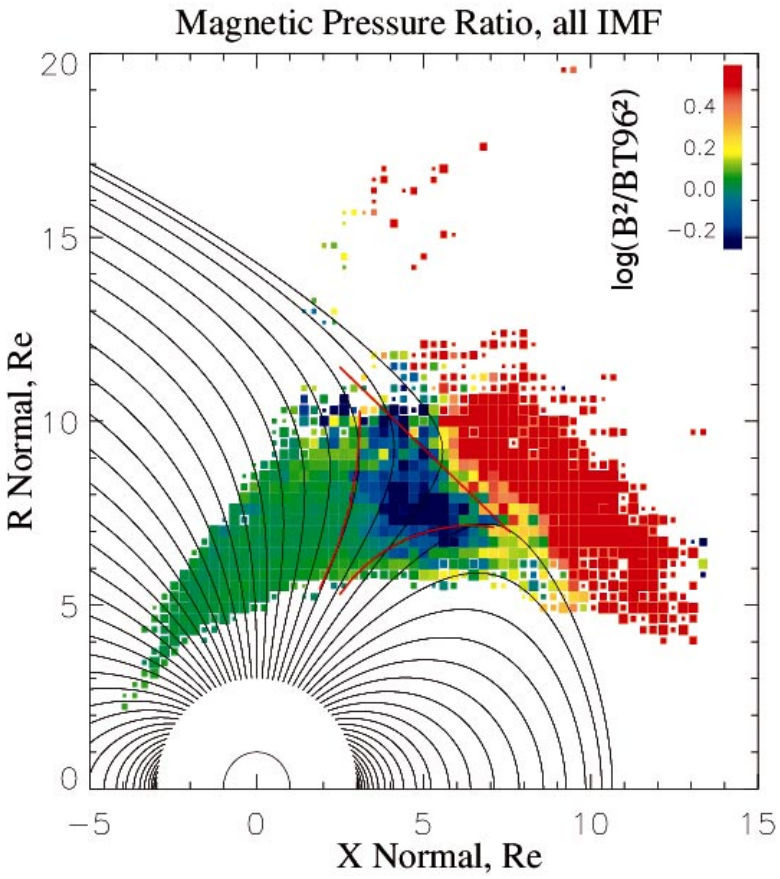

Figure 2.11: The spatial distribution of the diamagnetic depression (the ratio between the magnetic pressure and the *Tsyganenko* (1995) magnetic model) observations at the terrestrial cusp (*Lavraud et al.* 2004). The model can be seen in the background as "reference".

hours. The correlation of observations to magnetospheric tilt towards the Sun was supported by a previous report of a survey of the locations of the cusp (*Eastman et al.* 2000). *Tsyganenko and Russell* (1999) found that the depressions were larger at larger radial distances from the planet, due to the rapid increase of geomagnetic field strength close to the planet. This is supported by the analysis reported by *Lavraud et al.* (2004), who reported the greatest depressions to occur in the exterior cusp (i.e. largest distances from the planet), shown in Figure 2.11. The three boundaries of the exterior cusp are: the closed magnetosphere (equatorward from the cusp), the plasma mantle (poleward from the cusp), and the magnetosheath.

2.4 Solar Wind Dependence

The cusp has been observed to move equatorward during times when the IMF of the solar wind turns to a southward direction (e.g. *Burch* 1973). This is due to an increase in reconnection rate when the shear between the IMF and geomagnetic

field lines increases, so the geomagnetic field is eroded at the dayside and the open-closed field line boundary subsequently moves equatorward. The cusp is observed to move azimuthally depending on the IMF conditions (e.g. *Burch et al.* 1985; *Candidi et al.* 1989). This is described in Figure 2.12. With a large B_y component in the IMF, the newly opened field lines will have a dawnward and duskward flow for the northern and southern hemispheres respectively when $B_y > 0$. The opposite is true for an IMF $B_y < 0$. The corresponding ionospheric flows also behave in a similar fashion (bottom panel of Figure 2.12). This is due to the convection and magnetic tension force acting in an azimuthal direction after reconnection instead of a completely poleward one when the IMF is completely antiparallel to the dayside magnetospheric field interior to the magnetopause.

2.5 Location of the cusp

Pitout et al. (2006, 2009) undertook very large statistical investigations involving cusp observations made by the Cluster mission. They found that the location of the cusp depends on the dynamic pressure of the solar wind as well as its IMF-B_y component (as discussed previously). It was also found that the cusp has a location change response time of $\sim$20 minutes after solar wind conditions changing (the orientation of the IMF), with the response time dependent on the change in the IMF B_z magnitude. A seasonal effect was seen where the cusp is wider (i.e when the cusp 'faces' the solar wind more directly).

Figure 2.13 provides a selection of some of the results presented in the survey. It can be seen that the northern and southern hemisphere cusp observations are centred on 12:00 local time and between $75-80^\circ$ invariant latitude. In (b) the northern cusp is more commonly located in the morning sector for negative B_y and in the afternoon for positive B_y, with an opposite trend observed in the south.

This concludes the discussion on the terrestrial cusp. In the next chapter an introduction to Saturn's magnetosphere is presented.

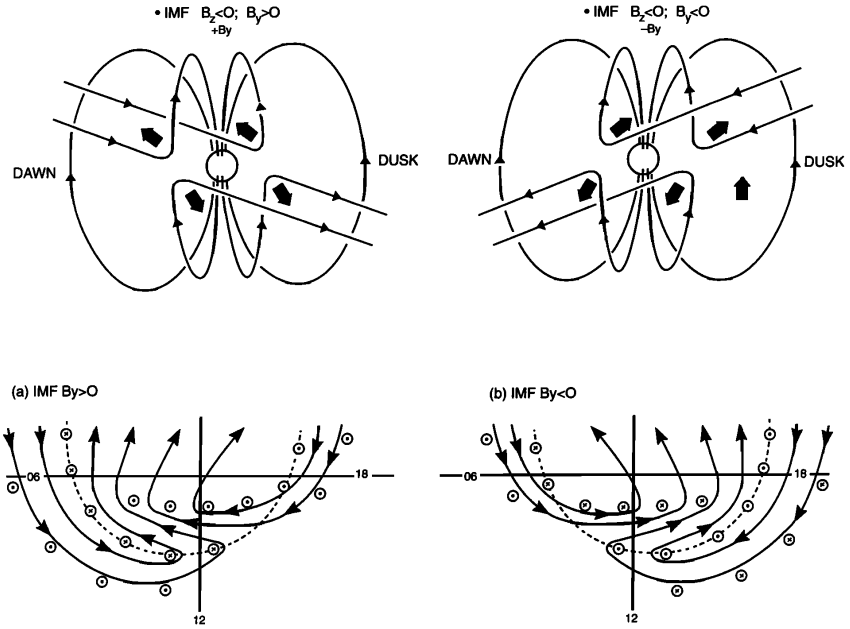

Figure 2.12: Effect of the IMF B_y component on field lines in the magnetosphere. Top: View from the Sun, the newly opened field lines have an azimuthal component in their motion due to the IMF orientation (*Gosling et al.* 1990b). Bottom: Ionospheric flood and the field aligned currents for different IMF B_y. The open-closed field-line boundary is shown as the dashed line (*Cowley et al.* 1991).

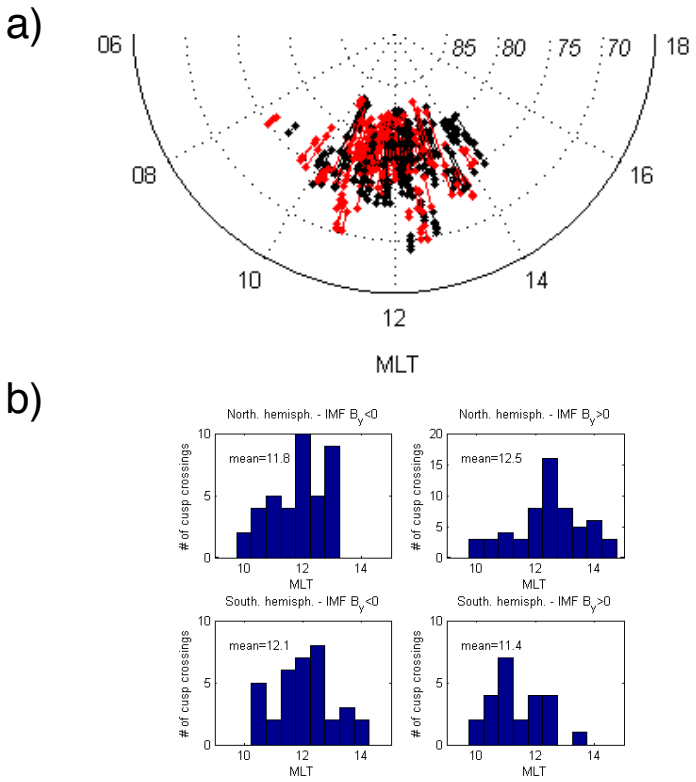

Figure 2.13: A selection of some of the results adapted from *Pitout et al.* (2006): (a) the magnetic local time and invariant latitude locations of cusp crossings with black and red representing northern and southern hemisphere crossings, and (b) the cusp crossings by local time for different B_y components of the IMF.

Chapter 3

Saturn and its Magnetosphere

Saturn has been observed by astronomers since prehistoric times. Saturn (as well as the day called Saturday) takes its name from the Roman god Saturnus, the god of agriculture. Saturnus was the Roman equivalent of the Greek god Kronos, one of the Titans and father of Zeus.

The rings of Saturn were first observed with a telescope by Galileo in 1610 who thought the rings were moons. A photograph of Saturn as seen through a telescope can be seen in Figure 3.1. It was Christiaan Huygens who later discovered that they were in fact rings. Huygens also discovered Saturn's largest moon, Titan. Domenico Cassini later in the same century discovered the moons Iapetus, Rhea, Dione and Tethys, and also a gap in the rings, which is now called the *Cassini division*. 1789 saw the discovery of two other moons, Enceladus and Rhea, by Sir William Herschel.

Saturn is the sixth planet in our solar system and lies approximately 9.5 AU away from the Sun. It has an orbit of $\sim$29.4 years and an equatorial radius (at the 1 bar pressure level) of 60,268 km. Saturn's rotation (spin) axis is tilted at 26° to the orbital plane normal. Its magnetic dipole axis is tilted less than 0.1° from the spin axis (*Burton et al.* 2010). This is very different to the corresponding angle at Earth (11°) and Jupiter (10°), making Saturn unique and very interesting. It is one of the Gas Giants of the Solar System, whose atmosphere is largely composed of 75% hydrogen and 25 % helium (*Fouchet et al.* 2009). Saturn has the most extensive set of rings in the Solar System and has a whole host of moons. A diagram of the planet with its rings and inner moons can be seen in Figure 3.2; the relative distance from the planet of the moons are scaled. Saturn's largest moon Titan is not included as it located much further out from the planet. Saturn and its moons make up their

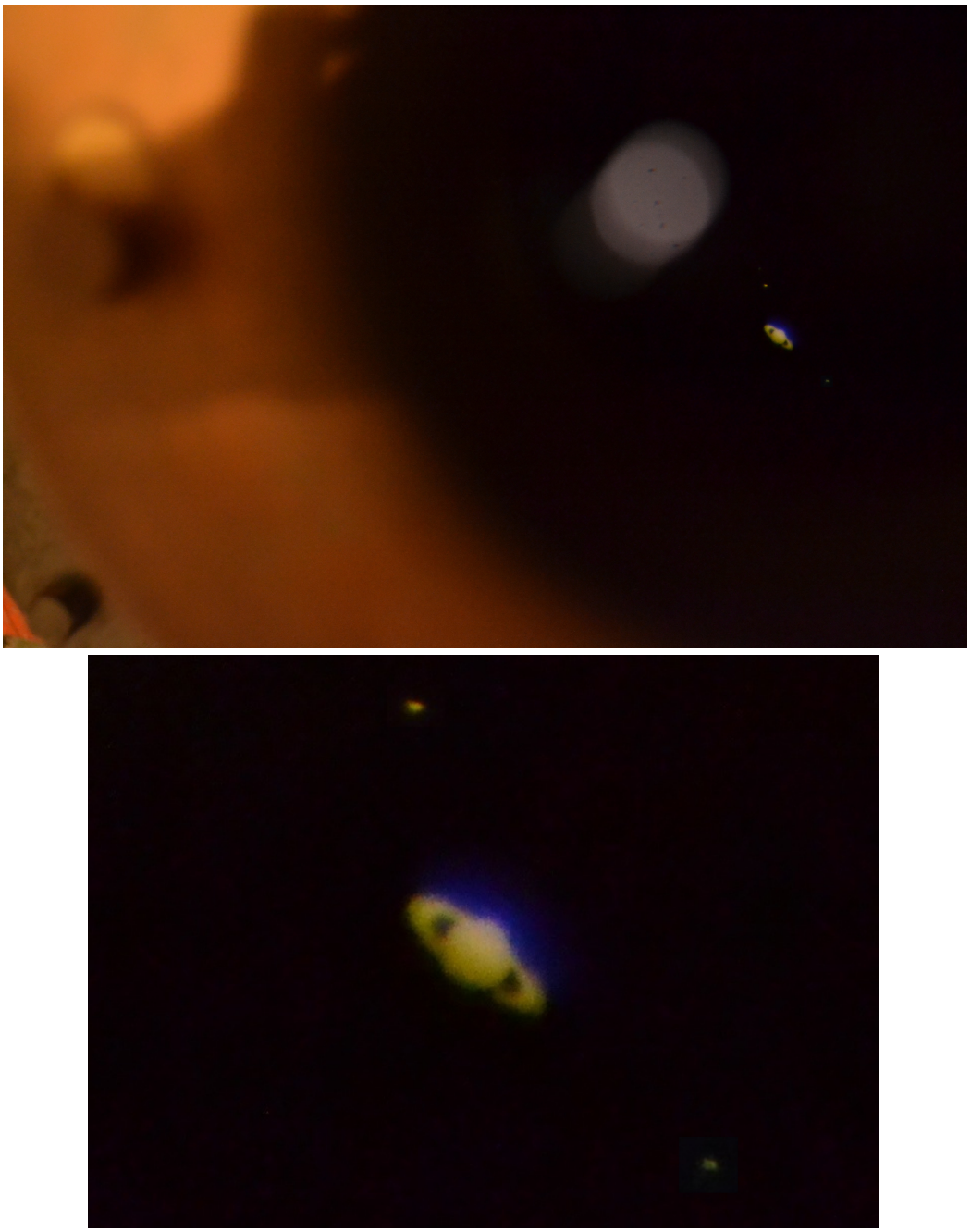

Figure 3.1: This mosaic (bottom panel is a zoomed in version) was taken with my Digital-SLR camera, and shows the eyepiece of the 0.4m Dorides Refracting Telescope at the National Observatory of Athens. Saturn as well as two of its moons: Rhea (left) and Dione (right), can be seen through the eyepiece.

own little system, analogous to the Solar System.

From Tables 1.1 and 1.2 it can be seen that the solar wind conditions at Saturn differ vastly from those observed at the terrestrial magnetosphere. The Parker spiral angle is large (85°) and the IMF strength low (∼0.5 nT) at Saturn. The solar wind ram pressure is also two orders of magnitude lower. The mean solar wind speed is

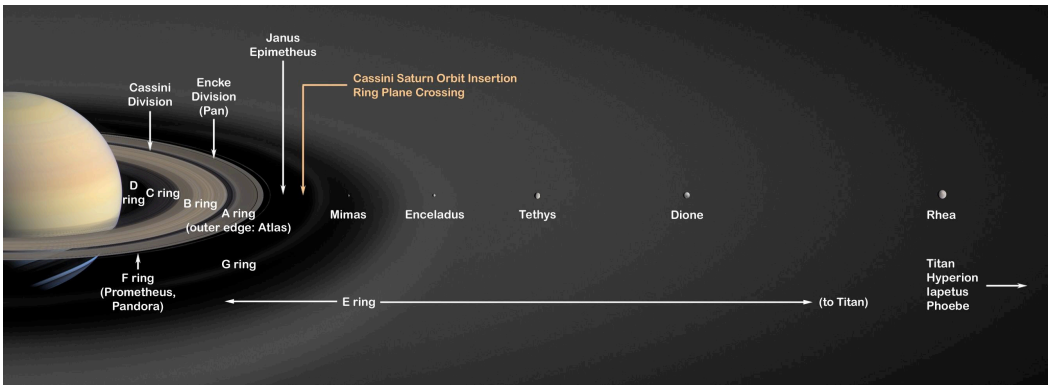

Figure 3.2: Saturn and its inner moons, with the distances between the moons scaled (credit NASA/JPL).

also ∼500 km s^{-1} (*Jackman and Arridge* 2011). The solar wind at Saturn's orbit during the first half of 2004 was found to be dominated by corotating interaction regions, where regions of compression and rarefaction were observed to occur with a period of the solar rotation (*Jackman et al.* 2004).

The solar wind dynamic pressure has been observed to influence the Saturn Kilometric Radiation (e.g. *Desch and Rucker* 1983). The increase in solar wind dynamic pressure is positively correlated to SKR energy. *Badman et al.* (2008) reported observations of the intensification of the SKR power when solar wind compressions arrived at the planet. Also, the occurrence of solar eruptions has been observed to vary the radiation belt (*Roussos et al.* 2008). The stable belts extend up to the orbit of the moon Tethys (see Section 3.1.1.1). During three solar disturbances, the authors reported the observation of increased energetic ion fluxes (MeV) beyond the orbit of Tethys extending to 8 R_S (i.e. beyond the location of the stable belt). This revealed the presence of a transient belt called the 'Dione Belt' (after the moon Dione whose orbit lies in this region).

The only spacecraft to visit Saturn before the Cassini-Huygens Mission which arrived in 2004 were, Pioneer 11 in 1979, and Voyagers 1 and 2, in 1980 and 1981 respectively. The first three were single flybys that only had a relatively brief glimpse of the Saturnian system. Pioneer 11 crossed the bow shock at noon local time, completed a flyby with a perikrone on the duskside and then exited the system through the dawnside magnetopause, all in the equatorial plane (*Acuna and Ness* 1980; *Acuna et al.* 1980). The noon magnetopause was observed at ∼17 R_S from the planet, which means the solar wind dynamic pressure must have been very high, for

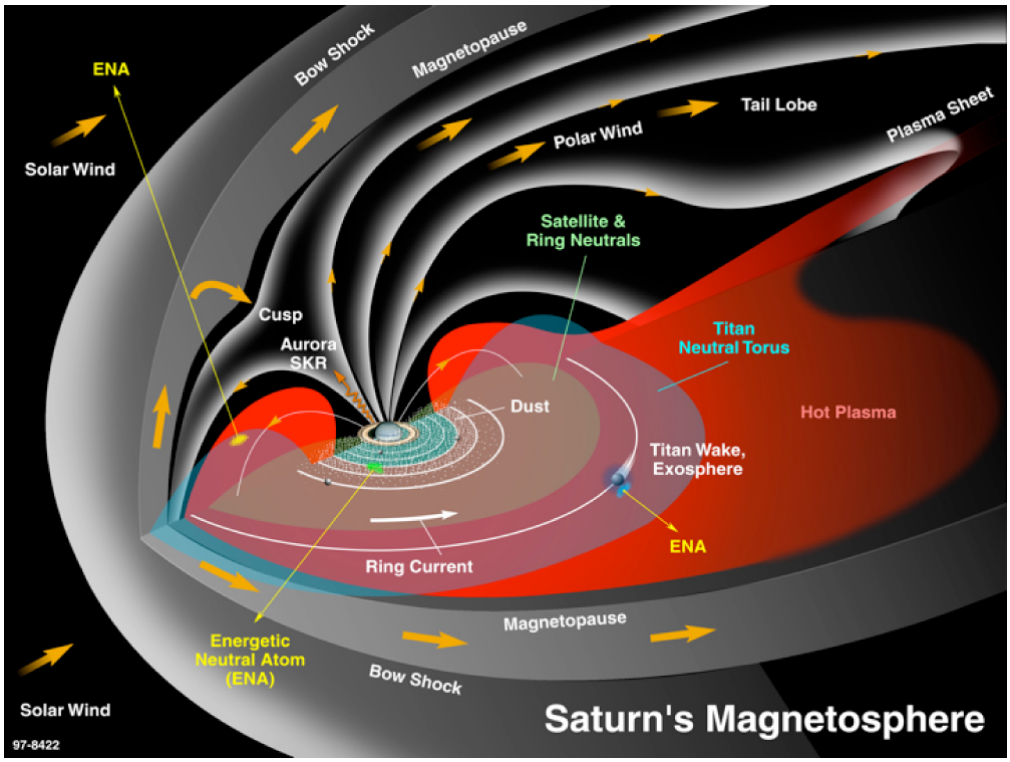

Figure 3.3: A cartoon of Saturn's magnetosphere showing the different regions (*Krimigis et al.* 2004).

such a close-in magnetopause boundary. Voyager 2 performed a similar trajectory during its flyby as Pioneer 11, reaching slightly higher latitudes (30°). Voyager 1, however, went slightly further downtail of the planet (*Ness et al.* 1981). It was not until twenty-three years later that the Cassin-Huygens mission arrived in the form of an orbiter (Cassini) and a probe into Titan's atmosphere (Huygens).

In this chapter, a summary of the Saturnian system is presented, focusing on the planet's magnetosphere largely from results obtained by the Cassini spacecraft.

3.1 Regions of the Magnetosphere

Like at Jupiter, Saturn's magnetic field moment is orientated oppositely to that of Earth, so the north magnetic pole is located in the northern hemisphere. The magnetic moment of Saturn is $\sim$21 μT R_S^3, (which is stronger than Earth's by comparison). As mentioned previously it has a very small magnetic tilt in relation to the spin axis. Saturn's magnetosphere has many regions, with varying dynamical plasma features. A schematic of the magnetosphere can be seen in Figure 3.3. The different regions will now be explained.

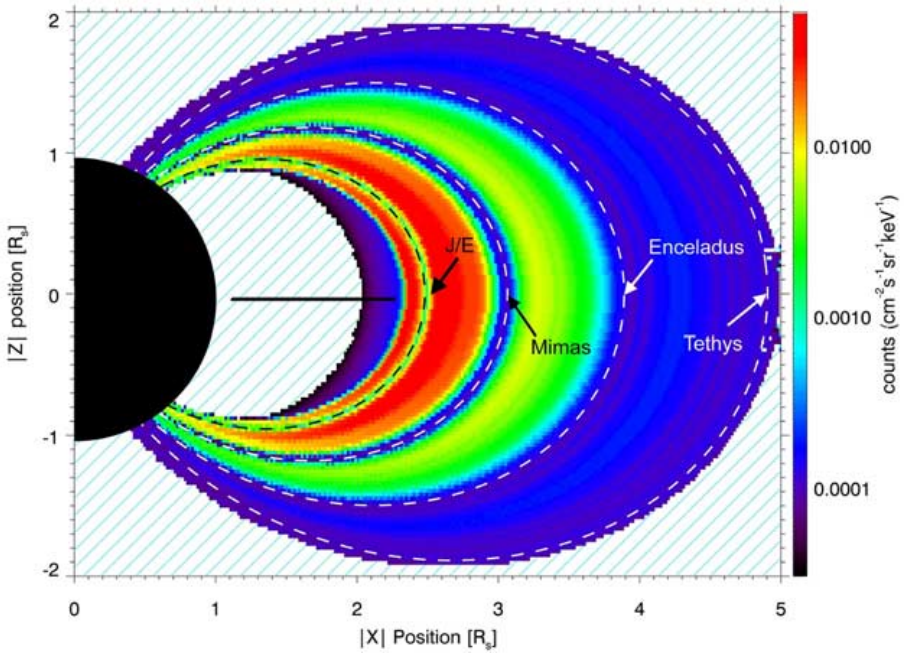

Figure 3.4: The ion radiation belt location observed by the LEMMS instrument up to L-shell values of Tethys' orbit. The shaded region is of fluxes below the colour bar. The moons Janus and Epimetheus are labelled as 'J/E' (*Roussos et al.* 2008).

3.1.1 Inner Magnetosphere

The magnetosphere up to the radial distance 3 R_S from the planet centre, is dominated by Saturn's dense rings. The rings are a plasma source, however they are also a plasma sink, as ion lifetimes are short and this results in low levels of plasma. The magnetic field in this region is strongly dipolar.

The inner magnetosphere is usually taken to extend from ∼3 to ∼6 R_S from the planet, and is home to three of the larger moons, Mimas, Enceladus and Tethys. It is also home to the region with the highest fluxes of low-energy particles as well as the radiation belts, which have the highest intensities of energetic particles in the 1 MeV range (*Krupp et al.* 2009).

3.1.1.1 Radiation Belts

The radiation belts are toroidal areas of energetic electrons and ions (ion energies >1 MeV/nuc and electron energies > 1 MeV). There is a stable as well as a transient belt (*Roussos et al.* 2008, 2011). The proton radiation belt extending up to the orbit of Tethys is shown in Figure 3.4. It can be seen that the moons create decreases in flux at their L-shells, with the most striking observed at Mimas, with the flux dropout called the 'Mimas Gap'. The high fluxes can be seen to begin at the edge of the A-

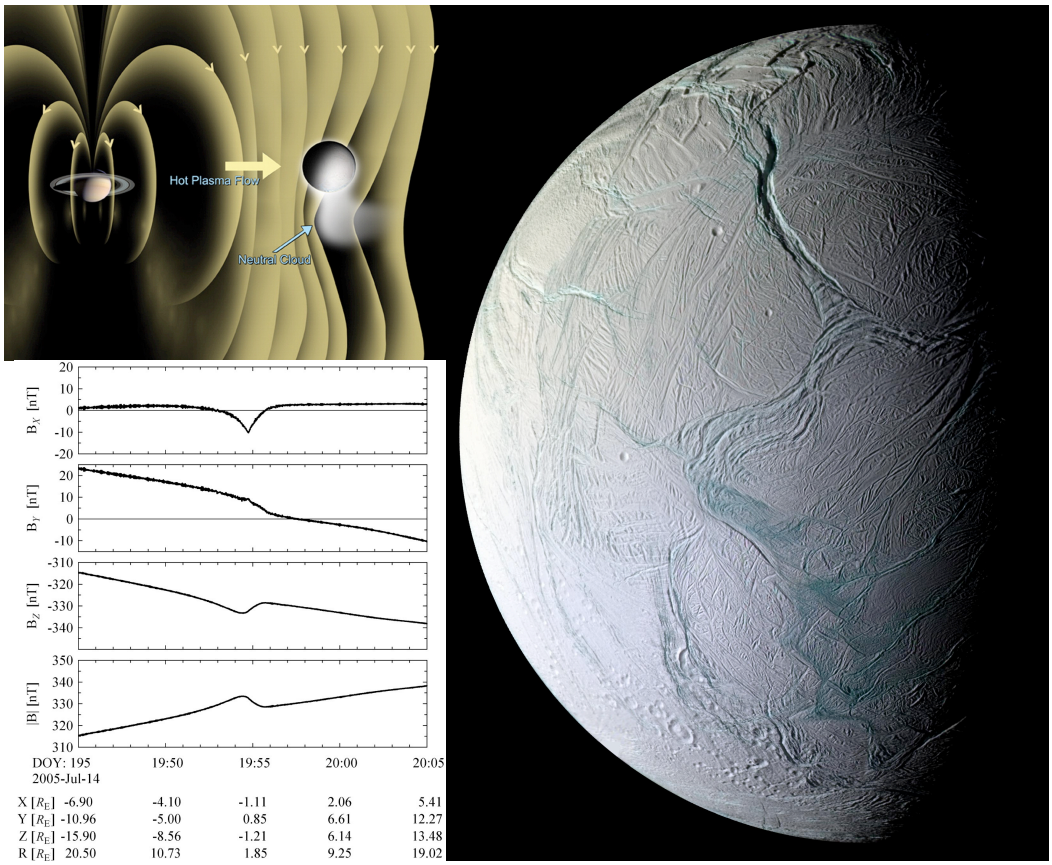

Figure 3.5: Top left: a schematic of the plume's interaction with Saturn's magnetosphere by warping the field lines. Bottom left: magnetometer data discovering the plumes of Enceladus during a flyby presenting observations of the three component of the magnetic field (X is in the direction of corotation, Y is directed toward the planet and Z completes the right hand set), as well as the magnetic field magnitude (*Dougherty et al.* 2006). Right: An image of Enceldaus (Credit Cassini Imaging team/SSI/JPL/ESA/NASA).

ring. Lower fluxes are observed to almost 5 R_S. Beyond this (and at the main rings) the fluxes drop below the instrument threshold except in special circumstances. The radiation belts interact with the moons and are able to release water group ions by sputtering (*Paranicas et al.* 2008). During Cassini orbit insertion a new radiation belt was discovered within the D-ring (*Krimigis et al.* 2005).

3.1.1.2 Enceladus and its plumes

During the first flyby of Enceladus, the magnetometer onboard the Cassini spacecraft observed a perturbation in the magnetic field (*Dougherty et al.* 2006). Ion cyclotron waves were observed at the water group ion frequency, suggesting that Enceladus was a source of plasma. In two subsequent closer flybys of the moon, this was confirmed. Observations from the third flyby are shown in Figure 3.5, with an image of the moon on the right.

The observations shown in the bottom left show the data from the magnetometer centred on the flyby. The clear perturbation of the magnetic field can be seen, with the distinct increase in magnetic field strength shown in the bottom panel. The strongest perturbation of the magnetic field can be seen in the B_X component of the magnetic field (in the direction of corotation), which was consistently observed throughout the three flybys. A schematic of the data is shown in the top left. The plume of water erupting from the moon is being ionised and picked up by the magnetic field and the corotating magnetospheric plasma is being slowed down as well as deflected.

The effective diameter of the obstacle that the eruption of the plumes creates has been modelled to show that it is $\sim$6 R_E (R_E is Enceladus' radius which is equal to 250km) (*Khurana et al.* 2007). The water ice grains are the main source of the E-ring, and the moon is the main source of neutrals in the magnetosphere. Some of the neutrals are ionised and are added to the corotating plasma. The eruptions are estimated to produce $\sim$100 kg/s up to $\sim$300 kg/s of material that is ionised and picked up by the magnetic field (*Tokar et al.* 2006; *Mauk et al.* 2009). Enceladus is therefore a large contributor to the plasma and dust found in Saturn's magnetosphere (e.g. *Jones et al.* 2006; *Waite et al.* 2006; *Hansen et al.* 2006; *Porco et al.* 2006). By comparison, the Jovian moon Io has been found to produce $\sim$1000 kg s^{-1} of ionised mass in Jupiter's magnetosphere (e.g. *Dessler* 1980). However, even though Io produces a larger amount of mass in the Jovian magnetosphere, this does not mean that the Saturnian magnetosphere is any less mass-loaded. Due to the scale quantities (solar wind mass flux and the critical mass flux to prevent corotation) being smaller at Saturn, Enceladus may be more significant in plasma production (and therefore the perturbation of its planet's magnetic field) in Saturn's magnetosphere than Io is in Jupiter's magnetosphere (*Vasyliūnas* 2008).

3.1.2 The middle Magnetosphere

The middle magnetosphere is usually defined to extend from 6 to 15 R_S. The radiation belt intensities drop several orders of magnitude. Generally the densities are decreased in the middle magnetosphere, decreasing with distance from Enceladus. The middle magnetosphere is home to the ring current.

3.1.2.1 Ring current

The ring current is similar to the Earth's ring current in the sense that it is generated by particles undergoing gradient and curvature drift. It is different from Earth's ring current because it is directed in the opposite direction (i.e. Saturn's ring current flows azimuthally along the direction of planetary corotation), due to the oppositely orientated magnetic dipole (e.g. *Krimigis et al.* 1983; *Bunce et al.* 2008a). The ring current is present from 6 R_S outwards to 15 R_S (sometimes 20 R_S depending on the location of the magnetopause) (*Bunce et al.* 2007; *Achilleos et al.* 2010). An image of the intensity of neutral atom emission due to charge exchange within the ring current, is shown in Figure 3.6.

From ∼8 R_S outwards, the magnetic field departs from a dipolar configuration. The ring current decreases the field strength from a dipolar value from the inner edge to some characteristic distance, then enhances the field strength from this location towards the outer edge. At Earth the ring current is a toroidal shape (approximately). The centrifugal stresses acting on the plasma at Saturn act to deform the field outwards of 16 R_S to form a thin disk-like distribution of current and plasma sheet.

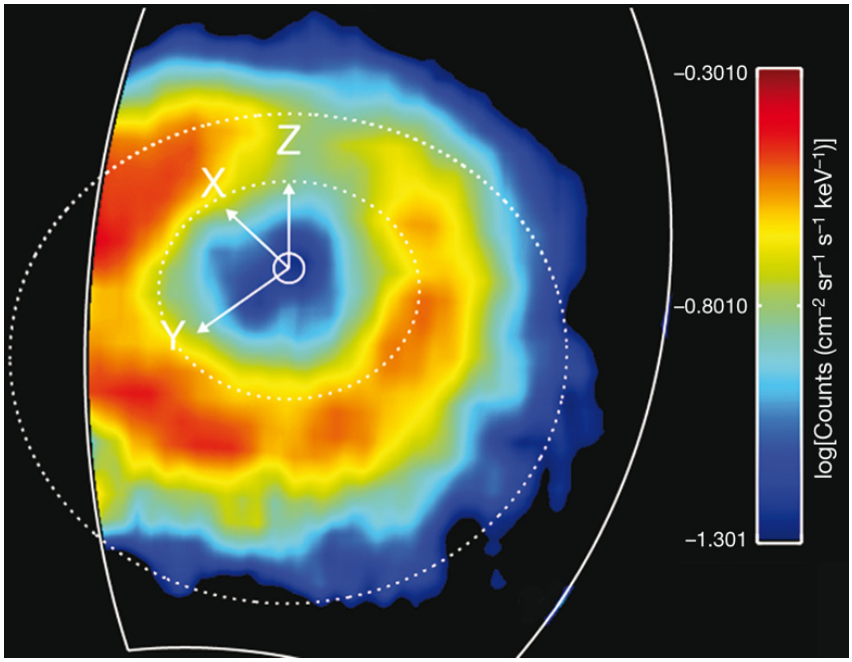

Figure 3.6: An ENA image taken by the MIMI-INCA instrument in the 20-50 keV energy range from above (north) the equatorial plane, looking down. The two dashed lines represent the orbits of Rhea and Titan from Saturn in the centre. (*Krimigis et al.* 2007).

3.1.3 Outer Magnetosphere

The outer magnetosphere is home to the magnetodisk, which was introduced above. Due to the role of the centrifugal force in the overall force balance in the plasma, the plasma adopts a disk-like configuration, as does the magnetic field. The plasma sheet residing within the magnetodisk is saucer-shaped, due to the solar wind impingement being transmitted to the disk and causing the current sheet to be moved out of the rotational equator (*Arridge et al.* 2008). This causes the disk to be 'bowl' or 'saucer' shaped as can be seen in an illustration shown in Figure 3.7.

Due to the negligible tilt between the rotation and the magnetic axis, there should not be an oscillation of the current sheet on a daily basis as at Jupiter. However, *Carbary et al.* (2008) showed a periodic tilting of the plasma sheet to occur at the same period as the SKR emission, which suggests a latitudinal motion of the sheet generated by a mechanism other than the dipole tilt with respect to the rotation axis. The outer magnetosphere is principally formed of hot plasma with particle energies $\geq$100 eV.

3.1.4 Magnetopause

The magnetodisk at Saturn, where the plasma is confined to the equatorial region, affects the shape of the magnetopause. The warping of the magnetodisk is likely to have a seasonal effect on the shape of the magnetopause, with one hemisphere more likely to be confined, and the other relatively inflated (e.g. *Maurice and Engle* 1995; *Pilkington et al.* 2014). *Achilleos et al.* (2008) found the magnetopause standoff distance at Saturn to have a bimodal distribution with two favoured at ∼22 and

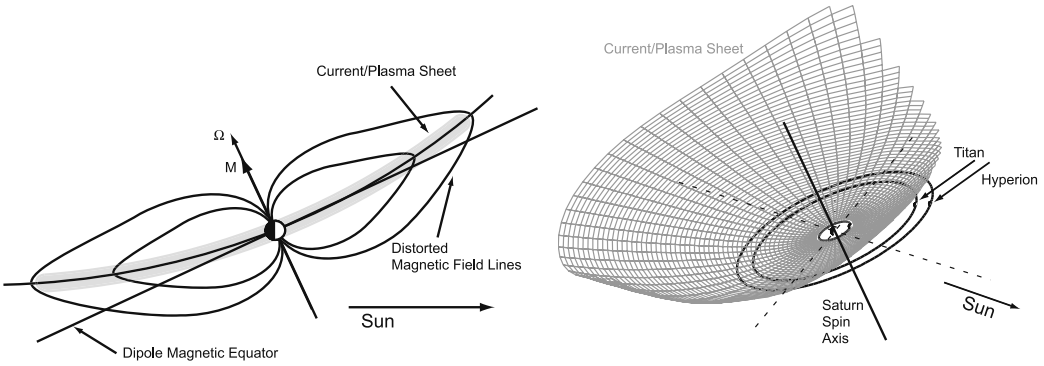

Figure 3.7: Sketches showing the bowl shaped magnetodisk and current sheet. On the left: the view from dawn of the current sheet and deformed magnetic field lines. Right: A 3-D view of the current sheet, highlighting that the moons can be underneath it (*Arridge et al.* 2008).

$\sim$27 R_S, which did not correlate with any corresponding bimodal distribution of solar wind dynamic pressure, suggesting that there must be an internal process influencing the magnetopause position. A similar result was obtained for the Jovian system by *Joy et al.* (2002).

A large equatorial magnetodisk produces a magnetopause shape which departs from symmetry about the planet-Sun line. Specifically the magnetopause is relatively inflated near the equatorial region and thus relatively flattened at the polar regions. *Huddleston et al.* (1998) found a polar flattening effect of the magnetopause at Jupiter. They also found the Jovian magnetosphere to be more compressible (i.e. its relative change in size is larger for a given relative change in the solar wind dynamic pressure) than the terrestrial magnetosphere. *Arridge et al.* (2006) found a similar effect at Saturn by analysing the first six orbits of Cassini and using magnetopause crossings to construct a model of the magnetopause surface and its compressibility. *Kanani et al.* (2010) and *Jia et al.* (2012) both built upon this work with more realistic models, and confirmed that the magnetospheric compressibility is not as pronounced at Saturn, showing the kronian magnetosphere to be an intermediate between Jupiter and Earth in this regard. *Pilkington et al.* (2014) found the kronian magnetopause to exhibit a polar flattening, where the magnetopause is 'flattened' by $\sim$19% approximately along a direction orthogonal to the X-Y plane in the KSM coordinate system (see Section 4.2 for a description of the KSM coordinate system).

3.2 Dynamics

The icy moons of Saturn provide the majority of plasma in the magnetosphere. It is argued that Saturn's magnetospheric dynamics are influenced by the solar wind and that the system has a Dungey Cycle (*Cowley and Bunce* 2003). Saturn has a rotational period of $\sim$10.75 hours. This is extremely fast for a planet of such a large size as Saturn. This classifies Saturn as a 'fast-rotator', whose effects manifest themselves in the dynamics of Saturn's magnetosphere and aurora. Therefore, in terms of the nature of the plasma dynamics, Saturn is treated as a 'middle case' between Jupiter and the Earth. Saturn is therefore thought to be driven by a mix of the Dungey Cycle and the Vasyliūnas Cycle. The description in this section is a theoretical view of the dynamics in a fast-rotating magnetosphere (which also has

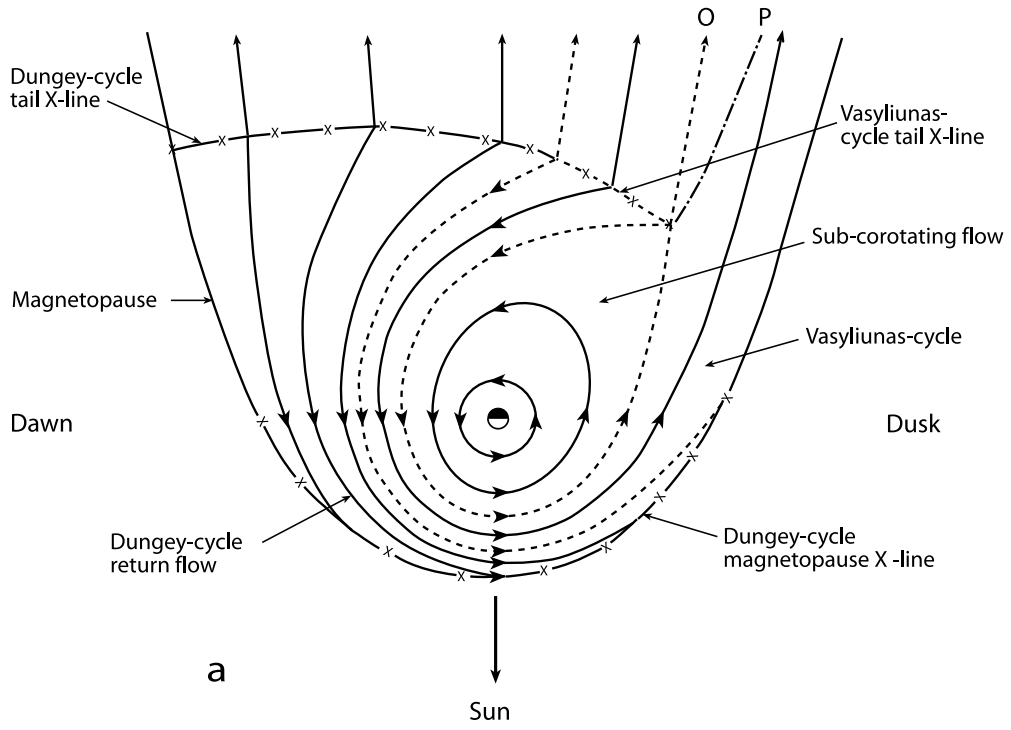

Figure 3.8: A sketch of the equatorial plane of Saturn's magnetosphere. Shown here is the plasma flow. Dawn is to the left, dusk to the right. Arrowed lines show plasma streamlines, dashed lines show the boundaries between different flow regimes. Solid lines with 'X' show the position of reconnection due to the Dungey Cycle, whilst dashed lines with 'X' show reconnection due to the Vasyliūnas Cycle. The 'O' line shows the plasmoid O line from the Vasyliūnas Cycle and the 'P' shows the limit of plasmoid field lines (*Cowley et al.* 2004a).

a solar wind driven Dungey Cycle) presented by *Cowley et al.* (2004a,b, 2005).

Figure 3.8 shows a sketch of the plasma flow in the magnetosphere's equatorial plane extending to ∼20 R_S on the dayside. The inner region shows plasma flow ranging from rigid corotation which falls to ∼50-60% of rigid corotation in the middle magnetosphere. On the outer dusk flank there is plasma loss occurring in the Vasyliūnas Cycle. Just after midnight towards dawn, there are flows of plasma on newly closed magnetic field lines due to the Dungey Cycle. These field lines are then opened on the dayside magnetopause by reconnection, also due to the Dungey Cycle. The flow of the plasma on the outer magnetospheric field lines rotates at ∼50-80% of rigid corotation. Of course these flows in the magnetosphere have an effect on the flows in the ionosphere, since the magnetospheric field lines are rooted there, and particles precipitate into the ionosphere. These ionospheric flows are shown in Figure 3.9. The region of open flux extends to ∼15° colatitude. The ionospheric flows are a combination of the tailward flows of newly opened magnetic field lines

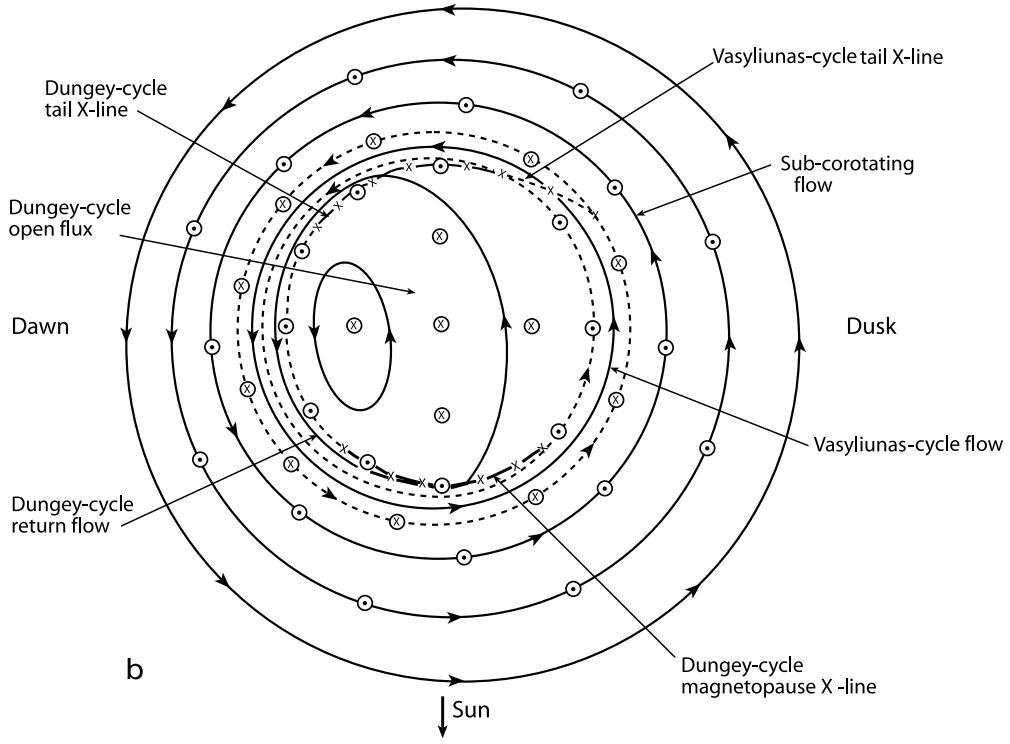

Figure 3.9: A sketch of the ionospheric plasma flow corresponding to the magnetospheric flow from Figure 3.8. The outer circle corresponds to a colatitude of ∼30°, mapping to a radial distance in the equatorial plane of $\sim 3 R_S$. Circles with dots and crosses show place of upward and downward current respectively. (*Cowley et al.* 2004a).

associated with the Dungey Cycle as well as subcorotation of the magnetospheric field lines. It can be seen that in this picture, this produces a one-cell convection pattern centred on the dawn side, and not the twin-cell convection pattern that occurs at Earth.

Field lines in the auroral oval have been shown to rotate at ∼34% of rigid corotation, which correspond to flow velocities of approximately 550 m/s (*Stallard et al.* 2004). The transpolar antisunward flows in the ionosphere of newly opened field lines associated with the Dungey Cyle were found to be ∼200 m/s (*Cowley et al.* 2004a). These field lines are surrounded by much faster flows on closed field lines of the order of ∼2 km/s (*Cowley et al.* 2004a). This rotational flow shear at the open-closed field line boundary produces the associated field aligned currents that drive the main auroral oval at Saturn. During onsets of the Dungey Cycle, the currents are increased, producing enhancements in the dawn side of the aurora, due to the precipitation of hot plasma (from the nightside) on the sunward dawn flows.

Cowley et al. (2005) took a step-by-step approach at using these ideas to deter-

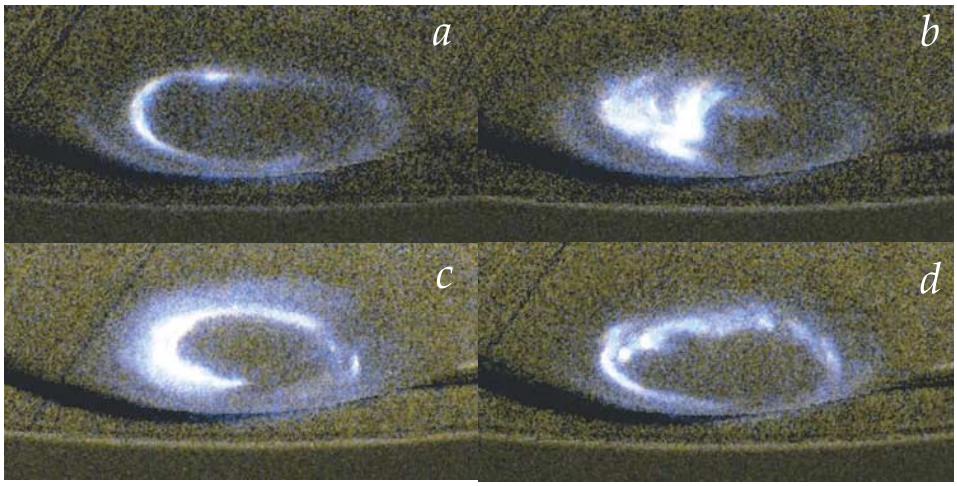

Figure 3.10: Hubble Space Telescope (HST) observations of Saturn's southern UV aurora in January 2004. Images are separated by 2 days. Noon is to the top, dawn to the left and dusk to the right. (a) A large auroral oval is seen during 'quiet' solar wind. (b) A corotating interaction region of the solar wind impinges on the magnetosphere causing the Dungey Cycle to be triggered, filling the dawn region of the oval. (c) The dawn side still has brighter emission, however the Dungey Cycle is decreasing. (d) Return to a unfilled auroral oval *Cowley et al.* (2005).

mine the dynamics of the magnetosphere that produced a set of auroral observations by the Hubble Space Telescope (HST) in January 2004 (see Figure 3.10). During these observations Cassini was measuring the solar wind upstream from Saturn. A forward shock of a corotating interaction region (CIR) in the solar wind was observed ∼17 hours prior to image b (*Jackman et al.* 2004).

The interpretation provided by *Cowley et al.* (2005) about the dynamics of the magnetosphere during these observations is explained in Figure 3.11. Sketches are made of the equatorial plane of the magnetosphere and the corresponding ionosphere. Sketches (a) and (b) occur 2-3 hours after the onset of rapid reconnection in the tail, occurring due to the arrival of the CIR, compressing the magnetosphere and thus triggering tail reconnection. Open field lines have just been closed in the tail, moved planetward and rotated towards dawn causing a bulge (shaded region) in the dawn flank. The effect on the ionosphere is that the newly closed field lines have filled into the polar cap (shaded region) on the dawn/night side, and precipitation of hot plasma has caused emission.

After ∼10 hours, the newly closed field lines have made half a rotation in the magnetosphere. This is represented in (c) and (d) in Fig. 3.11. Solar wind pressure on the dawn side has caused the bulge to move planetward in the magnetosphere. In

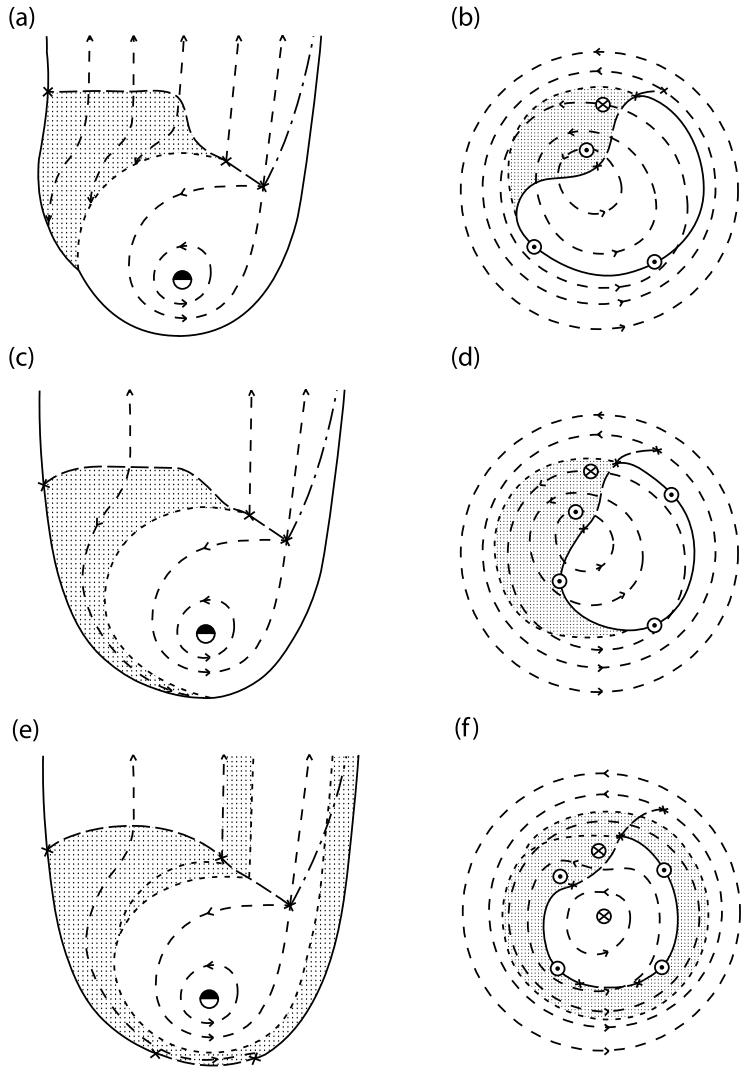

Figure 3.11: Sketches explaining the dynamics of the magnetosphere during the observations of the southern aurora by HST. Sketched are the conditions of the equatorial plane and the corresponding ionospheric behaviour 2-3 hours (a,b), ∼10 hours (c,d) and ∼20 hours (e,f) after the onset of rapid reconnection in the tail. (c,d) are a snapshot intended to be taken at the same time as the 'b' HST observation in Fig. 3.10, whilst (e,f) occur a few hours before the observation of 'c' in Figure 3.10. The circled dots and crosses represent upward (from the planet) and downward field-aligned currents (*Cowley et al.* 2005).

the ionosphere the newly closed field lines have continued rotating and the precipitating plasma causes emission in the shaded region. This shaded region has rotated into the dayside causing a crescent shaped aurora.

After a full rotation of the newly closed field lines (∼20 hours), some of the plasma has been lost down the dusk flank in the magnetosphere (e). In the ionosphere (f) the polar cap has shrunk. Reconnection in the tail is ongoing, however at a much smaller rate than in (a) and (b). This causes a smaller bulge on the

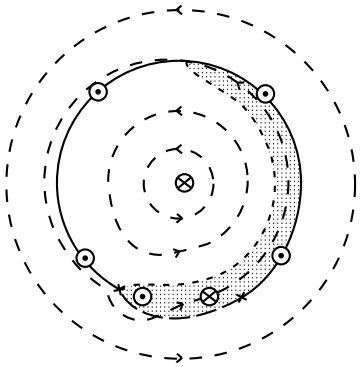

Figure 3.12: A sketch of the ionosphere after ongoing dayside reconnection for approximately a full planetary rotation. The open-closed boundary is pushed equatorward and emission on opened field lines is spread azimuthally (*Cowley et al.* 2005).

dawn/night side in the ionosphere. This explanation by *Cowley et al.* (2004b) is a qualitative explanation of the auroral observations. *Cowley et al.* (2005) mention the cusp as being more likely to be observed in the aurora as a line spread azimuthally from noon onwards for a couple of hours of LT, rather than a spot as seen on Earth. This is better represented in their sketch of dayside reconnection in Figure 3.12. Here we see the state of the ionosphere after dayside reconnection has been continuous for ∼10 hours. Newly opened field lines increase the size of the auroral oval. Due to the rotation of the planet we would expect cusp aurora to be diffuse and spread azimuthally, similarly to what has been shown in Figure 3.12. However *Gérard et al.* (2005) reported a spot in the aurora at noon which they interpreted to be the cusp auroral signature.

3.3 Reconnection at Saturn

The arrival of solar wind shocks at Earth has been shown to be a driver of reconnection at both the dayside magnetopause and the magnetotail, regardless of the orientation of the IMF. However the influence of the shocks on the aurora is more pronounced when the IMF has a southward (i.e. anti-parallel) orientation (*Meurant et al.* 2004). *Crary et al.* (2005) presented an example where the global power of the aurora increased at Saturn during a significant increase in the solar wind dynamic pressure and not a rotation in the orientation of the IMF. *Meredith et al.* (2014) showed that small patchy post-noon aurora coincide with the IMF (observed upstream of the bow shock) having a positive B_Z component, and an absence of these auroral signatures was observed to coincide with the IMF having a negative B_Z com-

ponent. Therefore both the solar wind dynamic pressure and the IMF orientation hold an influence on the aurora at Saturn. However, the degree to which reconnection occurs at Saturn, and its contribution to the magnetosphere's dynamics is still a highly debated topic.

The reconnection rate is reduced when the field lines on either side of the magnetopause are not completely anti-parallel (*Quest and Coroniti* 1981). Theory suggests that the occurrence of reconnection when the magnetic shear between the two magnetic fields is not completely anti-parallel is also dependant on the plasma β (Equation 1.40). *Scurry et al.* (1994) observed that large plasma β values in the magnetosheath reduce the rate of reconnection at Earth. However it has been argued that the difference of the β value between the two regions is more important (*Swisdak et al.* 2010; *Masters et al.* 2012).

When the plasma β is vastly different between the two regions, a gradient in density occurs, and particle diamagnetic drift will act to suppress reconnection from occurring unless the magnetic fields are anti-parallel (*Swisdak et al.* 2003). The theory of reconnection suppression states that the diamagnetic drift disrupts the reconnection jets that are a result of reconnection and are required to conserve the inflow of plasma (into the reconnection region). This can be seen in Figure 3.13. When the magnetic fields are anti-parallel, the drift is perpendicular to the outflow jets and so there is no disruption. However if the fields are not completely anti-parallel (like in the illustration), the drift is no longer completely perpendicular to the outflow jets and suppression can occur. The suppression of the outflow jets and subsequently that of reconnection can be seen in two different planes in Figure 3.13. The condition for reconnection to be suppressed occurs when:

$$|\Delta\beta| > \frac{2L}{d_i} tan\left(\frac{\theta}{2}\right) \tag{3.1}$$

where L is the scale length of the density gradient between the two regions, d_i is the ion inertial length and equals c/w_{pi} (w_{pi} is the ion plasma frequency and c is the speed of light), and θ is the angle between the magnetic field lines (*Swisdak et al.* 2010; *Masters et al.* 2012). This means that for large $|\Delta\beta|$ across the magnetopause, the angle between the magnetic fields must also be large for reconnection to proceed. This β dependence is also supported by observations of reconnection in the solar

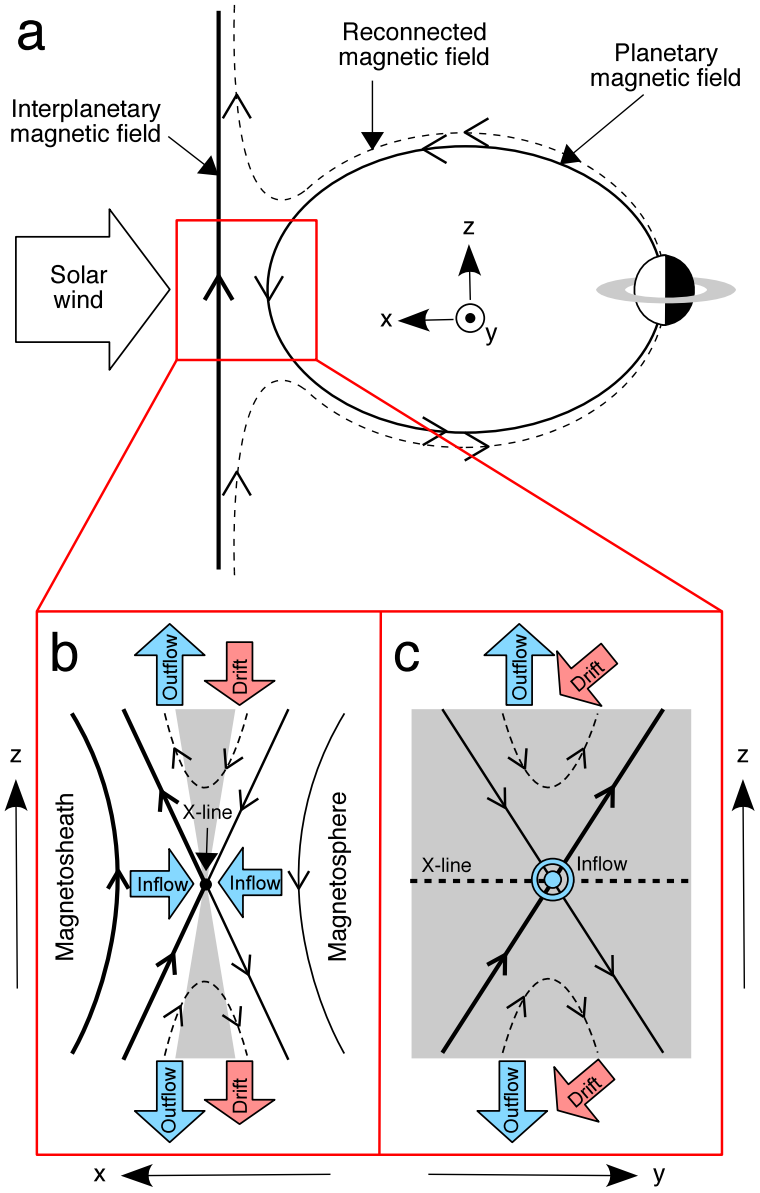

Figure 3.13: (a) An illustration of magnetic reconnection at Saturn's dayside magnetopause. (b and c) Illustrations of the suppression of reconnection when there is a diamagnetic drift that opposes the flow of the reconnection jets. The grey shading represents the magnetopause current layer (*Masters et al.* 2012).

wind (*Phan et al.* 2010).

A difference in plasma β across the reconnection layer at Earth results in reconnection requiring shear angles between $\sim 90° - 270°$, with the highest reconnection rates being observed during southward IMF (*Burton et al.* 1975; *Mozer and Retinò* 2007). A large difference in plasma β across the magnetopause occurs due to high Alfvénic Mach numbers (M_A) in the solar wind, which produce high-β mag-

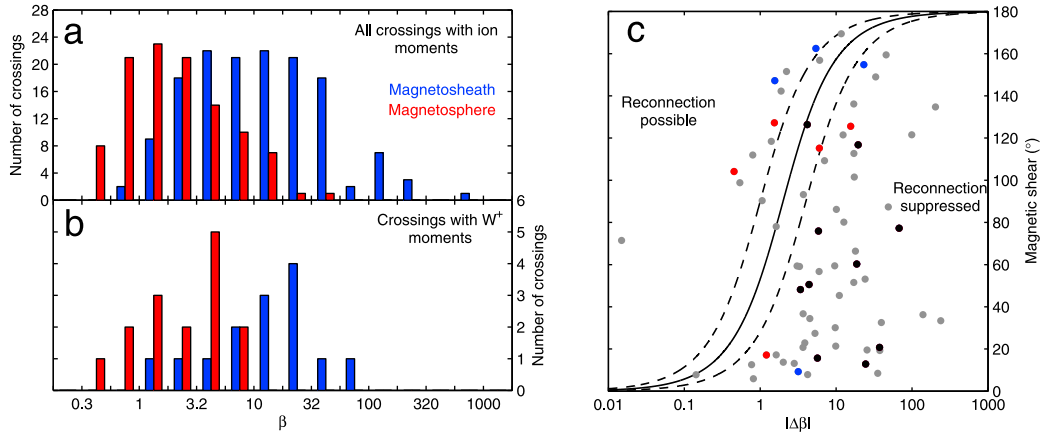

Figure 3.14: The results from magnetopause crossings at Saturn by *Masters et al.* (2012). (a and b) the plasma-β conditions at Saturn's magnetopause, (c) The result of the condition in Equation 3.1 for reconnection suppression for the magnetopause crossings with $|\Delta\beta|$ plotted against θ, and the lines of suppression. The colours show whether reliable plasma pressures for the water group ion species (W^+) were available for both magnetosheath and magnetosphere (black), the magnetosphere only (red), the magnetosheath only (blue) or neither (grey). The dashed lines represent $L = 0.5d_i$ and $L = 2d_i$ for the left and right respectively. The solid line represents $L = d_i$.

netosheaths (*Slavin et al.* 1984). In comparison, M_A in the solar wind (SW) at Mercury is lower, and reconnection is possible for very low shear angles (*Slavin et al.* 2014).

Solar wind M_A increases with increasing distance from the Sun, and so the difference in β across the reconnection layer is very large at Saturn (*Scurry and Russell* 1991). *Masters et al.* (2012) investigated this by analysing 520 magnetopause crossings made by Cassini between June 2004 and August 2007. By measuring the conditions on either side of the magnetopause, the authors were able to calculate the $|\Delta\beta|$ across the boundary. The results from the study are presented in Figure 3.14.

Figure 3.14a) and b) show that the β has a wide range of values for both the magnetosphere and magnetosheath, but the magnetosheath has considerably higher average values. Panel c shows that for many (if not most of the crossings) the conditions for reconnection suppression are satisfied. *Masters et al.* (2012) therefore argue that conditions at Saturn's magnetopause mostly do not allow reconnection to take place and that "*we should not assume that the nature of this coupling* [reconnection between solar wind and magnetosphere] *is always Earth-like*".

This idea is further highlighted with the observational search for flux transfer events (FTEs). FTEs are twisted magnetic field lines in a helical structure, which are produced during reconnection. This phenomenon has often been observed at

Earth (e.g. *Russell and Elphic* 1978; *Fear et al.* 2005, 2008, 2009; *Owen et al.* 2008) and at Mercury (e.g. *Slavin et al.* 2010, 2012). However a study by *Lai et al.* (2012) surveying magnetopause crossings did not confirm any observations of flux transfer events at Saturn during the Cassini era. A limitation of the work of *Lai et al.* (2012), is that their surveyed locations were limited to the equatorial regions and they do not cover higher latitudes. *Huddleston et al.* (1997) found evidence for FTEs at Jupiter, but none at Saturn. They report evidence for reconnection via the observation of a rotational discontinuity at Saturn. The low-latitude boundary layer between the magnetopause and the magnetosphere also has been observed not to vary in thickness for different IMF orientations (*Masters et al.* 2011a,b), unlike at Earth where it is found to be thinner when the IMF is anti-parallel to the magnetospheric field (due to the erosion of the open magnetic field lines) (e.g. *Šafránková et al.* 2007).

However, this is not to say that reconnection does not happen at all, just that it is not as common as at Earth, is not necessarily Earth-like, and that its effect on the dynamics of the kronian magnetosphere is thus not necessarily analogous to the terrestrial system. Modelling of the possible areas where reconnection can occur has shown that reconnection is favoured in regions away from the subsolar regions and located more poleward (*Desroche et al.* 2013). This result is supported by independent global MHD simulations (*Fukazawa et al.* 2007).

Although no FTE signatures have been found, other evidence for reconnection occurring at Saturn has been reported. In situ observations near the magnetopause of heated electrons, suggestive of reconnection occurring, have been reported at Saturn (*McAndrews et al.* 2008).

There is also evidence of reconnection in the auroral observations in the form of ionospheric signatures (*Radioti et al.* 2011, 2013). The reconnection signatures in the aurora take the form of poleward bifurcations of the main auroral oval. The bifurcations occur between 1200-1800 local time (see Figure 3.15). Also reported in more detail is a set of observations from July 13th 2008. In the auroral observations the bifurcations are seen to originate from the main oval, and then depart poleward from it with time. During this time the oval also increases in area suggesting that open flux in the pole is increasing due to ongoing dayside reconnection. The width of the bifurcations suggests that reconnection is occurring along the magnetopause,

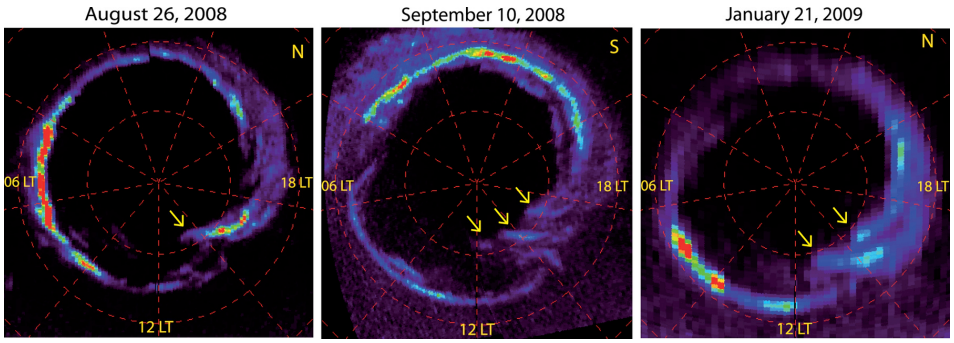

Figure 3.15: Observations by UVIS onboard Cassini of Saturn's northern and southern aurora (labelled, N or S in the top right corner). The arrows show the bifurcations identified by *Radioti et al.* (2011).

along a length of ∼4hours in local time (LT).

Evidence for reconnection in the auroral data have also been supported by simultaneous in situ observations. *Badman et al.* (2013) reported bursts of magnetospheric electrons on reconnected field lines in the magnetosheath, as well as evidence of bifurcation and cusp spots in the aurora. Auroral footprints of the cusp at Saturn were first reported from observations in 2004, during the Hubble Space Telescope (HST)-Cassini campaign, whereby the HST imaged Saturn's poles and Cassini monitored solar wind conditions. This occurred in the months prior to Cassini's Saturn orbit insertion (SOI). *Gérard et al.* (2005) present the HST data and noticed a large spot slightly poleward of the main auroral oval (see Figure 3.16). The spot was attributed to electron precipitation from the cusp resulting in transient aurora being produced.

These investigators imposed strict criteria in order to discriminate between the cusp and possible emission occurring due to subcorotating auroral 'spots' near the main auroral oval. The first criterion is that the cusp emission must stay fixed in the local time over ∼45min of the observing interval, so that it is not confused with subcorotating spots. The second criterion is that the brightness of the emission must be at least twice as intense as that of the background (*Gérard et al.* 2004, 2005). During the time of this observation, Cassini data was used to estimate that the dayside reconnection voltage was high with a southward IMF, resulting in high latitude reconnection which is consistent with the cusp emission seen poleward of the auroral oval.

Reconnection in the magnetotail has also been investigated (*Jackman et al.*

Figure 3.16: A HST image of Saturn's southern pole from the 21 January 2004, as viewed from the northern pole (as if looking through the planet). Noon is located at the bottom of the image with dawn and dusk at the left and right sides of the image respectively. The auroral oval can be seen as a ring, with the bright spot just poleward of the oval at midday being identified as caused by cusp electron precipitation (*Gérard et al.* 2005).

2007, 2008). *Jackman et al.* (2011) showed that the number of plasmoids observed is lower than the expected ∼2.2 plasmoid ejections per day required at Saturn to match a Dungey Cycle timescale of ∼6 to 10 days. *Badman et al.* (2014) calculated open flux estimates from a survey of auroral images. They reported the typical amounts of flux closed (∼13% of the open flux content) between observations is much smaller than at Earth, and there can be a short-term imbalance between open flux creation and closure in the tail. This is due to the large timescales of flux transport. All of the above evidence suggests that the Dungey Cycle at Saturn over large timescales is not as 'enthusiastic' as the *Cowley et al.* (2005) picture may suggest, and that a more dampened cycle combined with the Vasyliūnas Cycle exists at Saturn.

This thesis contributes to the ongoing discussion on magnetic reconnection with the analysis of the cusp observations at Saturn.

Chapter 4

Cassini and its Instrumentation

The Cassini-Huygens Mission is one of the most successful planetary missions ever undertaken. It is an international flagship mission with an estimated cost of over $3 billion. The mission consists of an orbiter (Cassini) and a probe (Huygens). Cassini was built at NASA's JPL and the Italian Space Agency built the radio equipment and the high gain antenna. Although Cassini was mainly built in the USA, many of the instruments were built in Europe through collaborations. The Huygens probe was built by the European Space Agency (ESA) in order to probe the atmosphere of Saturn's largest moon Titan, as well as land on its surface. It is named after Titan's discoverer, Christiaan Huygens. An image of the spacecraft (with the probe attached) during spacecraft vibration and thermal testing can be seen in Figure 4.1. The interplanetary spacecraft is one of the largest and heaviest ever built ($\sim$6 tonnes including propellant), with a height of 6.7 m and width of 4 m.

The mission was launched on the 15th of October 1997. With gravity assists from flybys of Venus (twice), Earth and Jupiter, the Cassini-Huygens mission finally entered Saturn's orbit on the 1st of July 2004 (*Russell* 2003). The Huygens probe successfully landed on Titan on the 14th of January 2005. Cassini completed its initial prime mission in June 2008, and then its first extended mission (the "Cassini Equinox Mission") in 2010. Equinox occurred in August 2009, with the initial mission occurring during southern summer at Saturn. Cassini is currently in its second extended mission ("Cassini Solstice Mission"), which will end in September 2017. The "Grand Finale" will include a set of proximal orbits which will be highly inclined and will cross between the planet and the innermost ring (D-ring), and the mission will end with the spacecraft entering the planet's atmosphere. Many dif-

Figure 4.1: Cassini during spacecraft vibration and thermal testing (Credit: NASA)

ferent scenarios for the end of the mission were proposed, however the use of the spacecraft as a planetary probe was evaluated to be the best for science return as well as the best use of the low levels of propellant (to ensure that there is no risk of collision with Titan or Enceladus). When this occurs, Cassini will have performed the longest observation of a planet (apart from Earth) by a single spacecraft. Saturn's orbital period is ∼29.5 years, and so by the end of the mission, Cassini will have been at Saturn for almost half a Saturnian year. Such a timescale allows for the study of seasonal as well as solar cycle changes (timescales of ∼11 years) at the Saturnian system.

The primary objectives of the mission are: (i) investigate Saturn's atmosphere and weather system, (ii) observe the ring systems and their interaction with the local environment, (iii) make flybys of the many moons, and (iv) study the dynamics and structure of the magnetosphere as well as its coupling to Saturn's ionosphere and interactions with the moons and rings. In order to perform these tasks, Cassini is armed with twelve instruments (and Huygens with six).

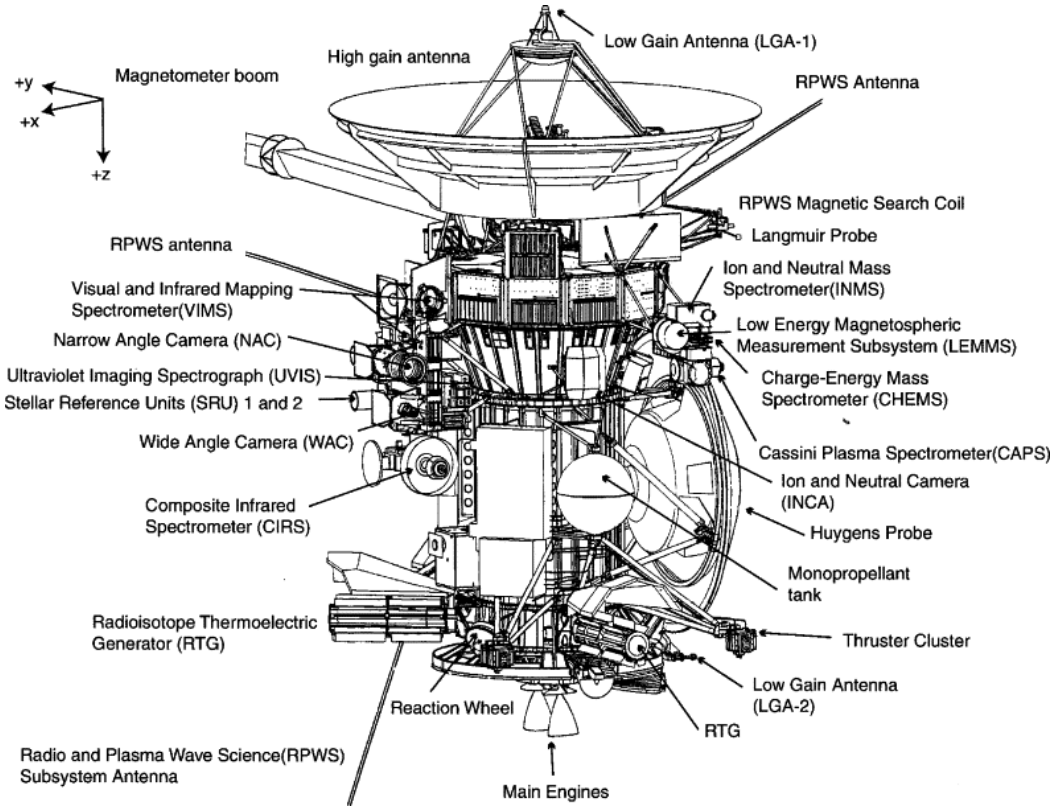

Figure 4.2: A schematic of the Cassini spacecraft with the Huygens probe attached. From *Burton et al.* (2001).

Onboard Cassini is a suite of instrumentation (see Figure 4.2) designed to take in-situ measurements of the local region in space as well as remote sensing instrumentation. The instrument particularly relevant to this thesis is the Cassini Plasma Spectrometer (CAPS). CAPS is formed of three sensors: the Electron Spectrometer (ELS), the Ion Mass Spectrometer (IMS) and the Ion Beam Spectrometer (IBS). The ELS was built at MSSL. Much of the work that is discussed in this thesis involves the ELS and the IMS, whilst IBS is not used and is not discussed further. Observations from the magnetometer (MAG) are also used and discussed in this thesis, with more in-depth analysis discussed in the final research chapter. Finally, data from the following instruments are used to complement CAPS and MAG observations: the Magnetospheric Imaging Instrument (MIMI) and the Radio Plasma Wave Science (RPWS) instrument. MIMI, like CAPS, is composed of three sensors: the low-energy magnetospheric measurement systems (LEMMS), the charge-energy-mass spectrometer (CHEMS) and the ion and neutral camera (INCA). INCA is not used and therefore not discussed further.

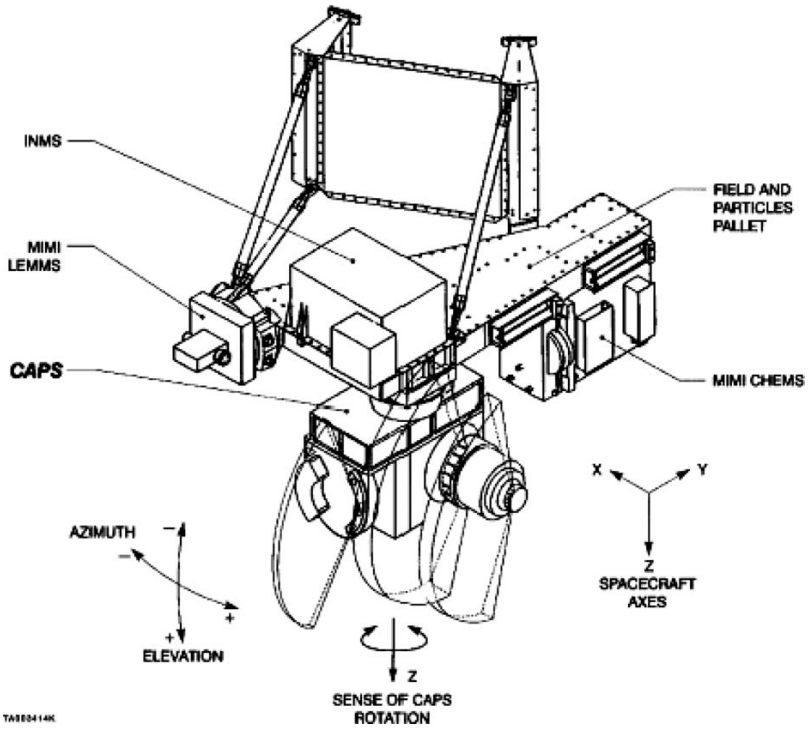

Figure 4.3: A diagram of the 'Fields and Particle Pallet' onboard Cassini. Taken from *Young et al.* (2004).

Cassini is not a spin-stabilised spacecraft. This means that the spacecraft does not spin, and as a result the actual relevant instrumentation onboard does not have a 4π steradian field of view (FOV), i.e. not all the surrounding area is sampled. Cassini is a three-axis stabilised spacecraft. This means it either requires thrusters or reaction wheels to change its attitude. The spacecraft only spins occasionally during periods of downlink connection with the Earth.

4.1 Cassini Plasma Spectrometer (CAPS)

CAPS is located on the 'Fields and Particle Pallet' (FPP) of Cassini (see Figure 4.3), which is located on one of the sides of the spacecraft. The ELS and IMS are mounted on top of each other and are aligned so they look in a similar direction (see Figure 4.4). Ideally CAPS would have a 4π steradian FOV, to observe particles from all directions simultaneously, however it does not. Therefore CAPS is mounted on an actuating platform that moves at 1° per second to increase the angular coverage. The instruments and their instantaneous FOV in relation to the FPP and the spacecraft are highlighted in Figures 4.5 and 4.6, respectively. With the magnetometer boom pointing in the Y_{SC} direction (in spacecraft-centered coordinates), and the

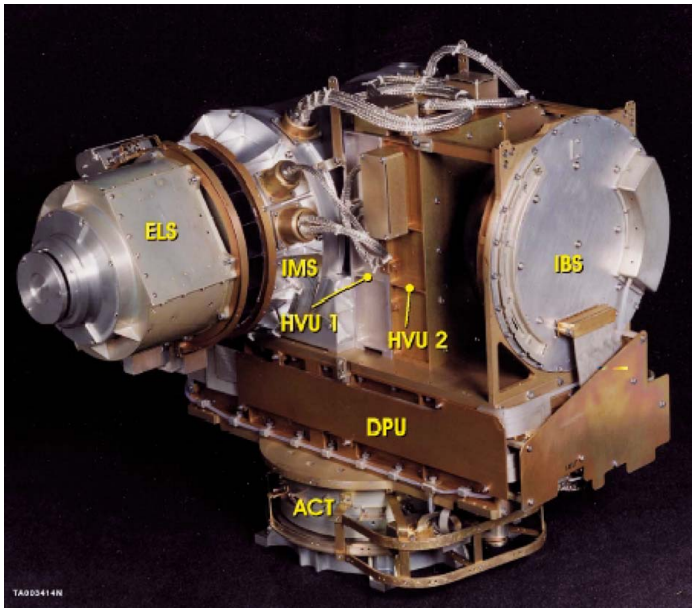

Figure 4.4: The CAPS instrument photographed before launch, taken from *Young et al.* (2004).

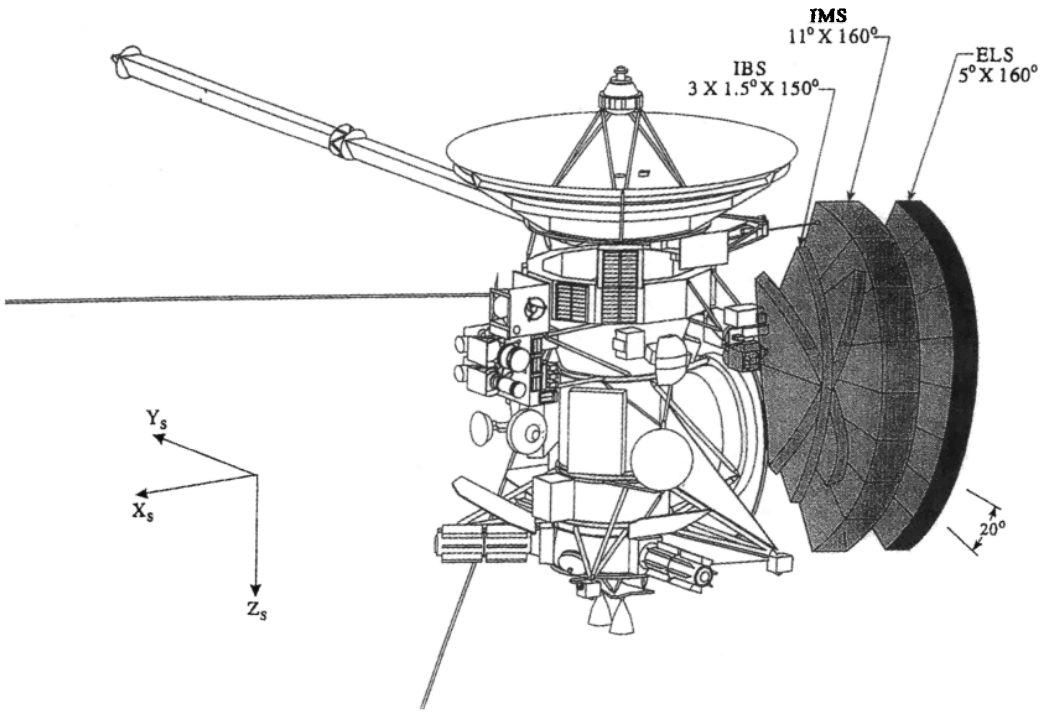

Figure 4.5: Schematic of the location of CAPS onboard Cassini, and the field of view of the instrument (shaded arc). Taken from *Rymer et al.* (2001).

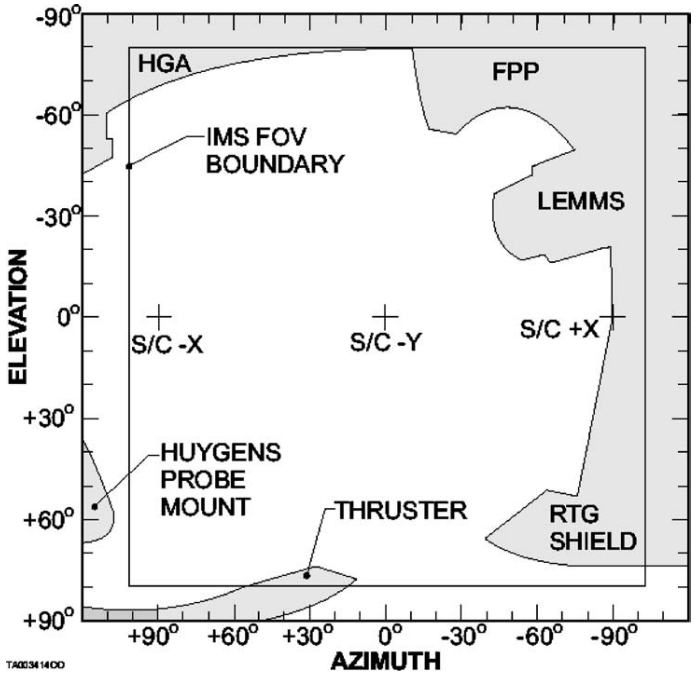

Figure 4.6: The projected FOV of the IMS, and the obscuration by other parts of the spacecraft. Taken from *Young et al.* (2004).

high-gain antenna directed in the $-Z_{SC}$ direction, the FOV of CAPS is in the Y−Z plane, with a maximum actuation angle of $\pm 104°$ possible in the X−Y plane (around Z_{SC}).

The FOV of IMS is shown in Figure 4.6, and presents how parts of the FOV are obscured by other instruments on the FPP, and components of the spacecraft (such as the high-gain antenna [HGA], and the radioisotope thermoelectric generator [RTG] shield). The obstructions are very similar for the ELS FOV.

4.1.1 Electron Spectrometer (CAPS-ELS)

ELS is a hemispherical top-hat electrostatic analyser (ESA) that measures electron flux as a function of energy per charge, and the angle of arrival of the electrons. The energy range that the electrons are observed over is 0.58−28250 eV/q (*Linder et al.* 1998; *Young et al.* 2004). Particles enter the instrument through a baffle, located at the top of the ELS (see Figure 4.7). The baffle and the internal surface of the instrument are covered with a black coating to reduce particle scattering by absorption of photoelectrons and solar photons. The electrons then pass between two concentric electrostatic plates (labelled ESA in Figure 4.7), one which is grounded and the other which is positively charged, creating a potential difference between

the plates. Negatively charged particles with a specific range of energies-per-charge will thus be deflected by the potential difference, whilst particles with other energies will impact the surface of the analyser. The voltage across the plates can be changed to differ the energy-per-charge of the observed particles that exit the analyser and are counted.

The trajectories of the particles (with the correct energies) are then accelerated through a grid and led through to two microchannel plates (MCPs). The accelerated electrons striking the MCP cause a cascade of secondary electrons. The number of secondary electrons produced by the impact of one incident electron is called the 'gain' and is usually of the order of $\sim 10^6$ electrons. The secondary electrons are collected by eight anodes arranged in an arc formation. The anodes each cover a FOV of $20° \times 5°$(the sensitivity of which is not uniform but Gaussian). This provides ELS with a complete instantaneous FOV of $160° \times 5°$. Depending on which anode

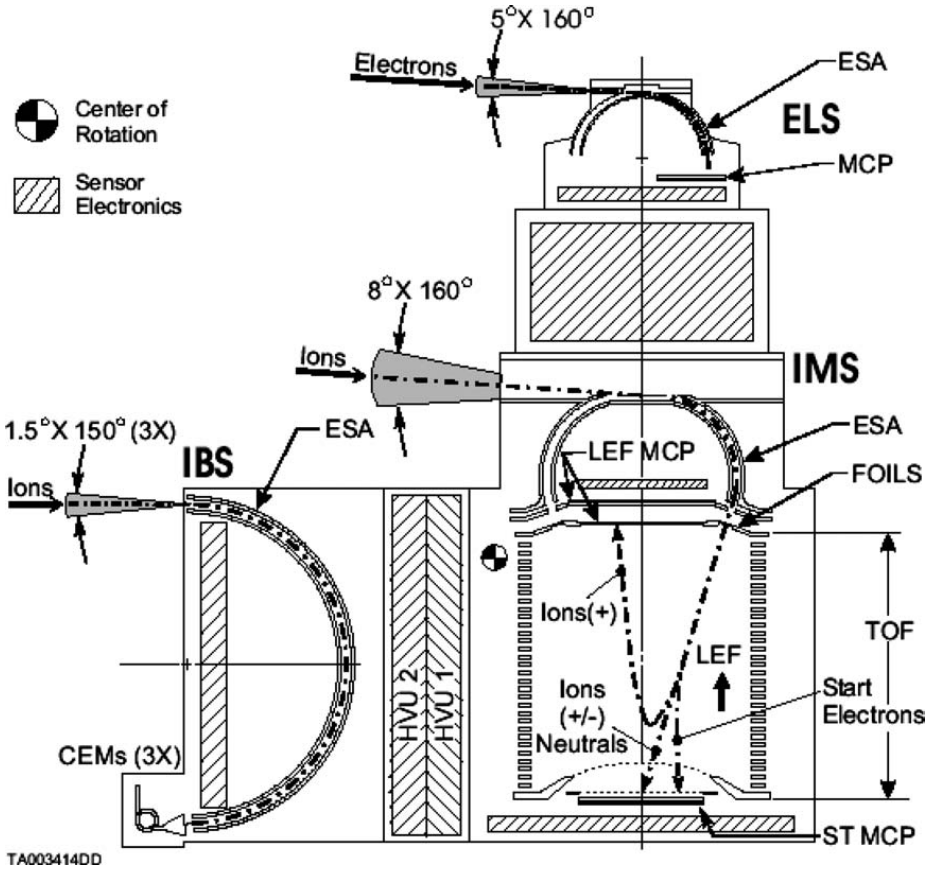

Figure 4.7: The layout of the ELS, IMS and IBS that make up CAPS, shown in the spacecraft X-Y plane. The bold dashed lines represent the particles trajectories within the instruments. Taken from *Young et al.* (2004).

observes the electrons, the direction of the incoming electrons can be registered.

The potential across the analyser plates is varied quasi-logarithmically (it is linear at low energies-per-charge) between 64 energy steps, from the highest energy bin to the lowest (63rd). The 64th bin is used to switch back to the highest energy bin, and is called the 'fly back'. The ELS has a energy passband (i.e an energy resolution) of $\Delta E/E=0.17$. The lower energy bands are closer together, which produces a higher resolution. The total time required to complete a full energy sweep is two seconds (31.25 ms per sample).

The raw counts from the observations are converted into calibrated quantities using the 'geometric factor' (G) which is dependant on the area and solid angle of the instrument aperture, the post-acceleration grid efficiency and the MCP efficiency. The geometric factor is calculated from pre- and post-launch calibration tests as well as simulations, including calibration comparisons with other instruments. A detailed explanation can be found in *Lewis et al.* (2010), who define the geometric factor as:

> "*...the relationship between the number of electrons entering the instrument and the number being measured by the instrument.*"

The electron observations made by the instrument are then passed to the data processing unit (DPU), to be processed and packaged for transmission back to Earth. The data is arranged into 'A' and 'B' cycles. A-cycles contain 16 energy sweeps, so take a total of 32 seconds. B-cycles are (usually) made up of eight A-cycles. For telemetry purposes sometimes several sweeps are summed together resulting in longer time resolutions.

In this thesis the data from the ELS are presented with the background (and spacecraft photoelectrons - explained below) subtracted using a signal-to-noise ratio threshold of 0.5.

4.1.2 Spacecraft Potential

Spacecraft can become positively or negatively charged depending on the plasma environment that they are immersed in (*Whipple* 1981). The spacecraft potential does not change when the net current:

$$I_i + I_e + I_{pe} + I_{se} = 0 \tag{4.1}$$

where I_i and I_e are the ion and electron currents, I_{pe} is the photoelectron current, and I_{se} is the secondary electron current.

Solar irradiation can free electrons from the spacecraft surface via photoemission. Secondary electrons can be produced when electrons from the ambient plasma strike the spacecraft, causing electrons to be emitted from the surface. This creates a potential difference between the spacecraft and the surrounding environment. This means that the electrons observed by the ELS from the plasma environment are accelerated towards the instrument and so are observed with an increased energy, with the increase equivalent to the spacecraft potential (for singly charged particles). Photoelectrons with energies higher than the spacecraft potential (usually $\sim$10 eV) can escape the spacecraft. However, those that do not are observed by the instrument.

The spacecraft can also be negatively charged during eclipses or whilst in very dense plasma environments. This occurs when there are more electrons attaching themselves to the spacecraft than photoelectrons produced, causing the spacecraft to become negatively charged. This results in electrons being decelerated whilst entering the instrument, or altogether repelled from the spacecraft.

4.1.3 Ion Mass Spectrometer (CAPS-IMS)

The IMS observes positively charged ions with energies of $1-50280$ eV/q. The IMS also provides compositional information of the atomic and molecular ions. The information IMS can provide about the ions observed is produced as a function of energy per charge, direction of observation, and mass per charge.

Similar to ELS, ions enter the IMS and pass through an ESA which, in the IMS is toroidal. There is a voltage applied to the inner plate that deflects the ions of particular energies within the toroid. The selected ions then exit the ESA and are accelerated through one of eight carbon foils at the entrance of the time-of-flight (TOF) analyser (see Figure 4.7). On passing through the carbon foil, secondary electrons are produced which are then measured by the straight-through (ST) MCP where the 'start' time is recorded.

The TOF analyser is a cylinder with a linear electric field (LEF) arranged in rings on the outside. Ions with energies-per-charge less than 15.5 keV/q undergo sufficient deflection that their trajectory is bent by almost 180° and are detected by the LEF MCP (located at the top, Figure 4.7). Ions of higher energies per

charge (>15.5 keV/q) pass straight through (ST) to the MCP at the bottom of the instrument and a 'stop' time is recorded. Monatomic ions hit an MCP and their mass-per-charge is calculated from the TOF (IMS is unable to identify the mass or charge seperately). For molecular ions the identification of the mass-per-charge is more complicated. Polyatomic ions break up whilst passing through the foils, and their fragments are detected by either the LEF MCP or ST MCP, or both (and a 'stop' time is recorded). The pattern of detections from the daughter particles is then recorded and passed onto the spectrum analyser module (SAM) which identifies the original ion from a look-up table. TOF accumulation occurs over a period of a B-cycle (256s). However it is usually summed over two or four B-cycles. The data reduction software (presented at COSPAR) written by *Reisenfeld et al.* (2008) is used to produce the ion counts from TOF.

The FOV of the IMS is made up of eight anodes each observing 20°-8.3°, making up a total FOV of 160°−8.3°. Each anode corresponds to a 20° portion of the acceptance of the entry baffle, so the arrival direction of the electron is known as it will be recorded by a specific anode. The ESA voltage is varied to measure energy-per-charge ions in 63 logarithmic bins from 1 to 50280 eV/q, taking four seconds. The energy resolution is the same as the ELS: $\Delta E/E=0.17$.

Recently it has come to light amongst the CAPS team that the timing of the TOF data products do not always match the ion IMS counts. This issue has yet to be resolved, with no clear constant global offset reported. In the work of this thesis, the TOF timings are always compared to the ion spectrogram, and I match the TOF times myself. This is usually done by comparing the time of when the spacecraft is in the cusp (from the spectrogram) and when it enters the polar cap where counts drop to background levels, so the difference in counts is most clear. In all the examples presented for the cusp, the TOF timings appear to be shifted forward by one B-cycle, so the timestamps are not of the start but are of the end of the data product. Therefore, for all the examples used, the timestamp in the data is used for the end of the data product, and the start time is taken as the timestamp from the previous data product.

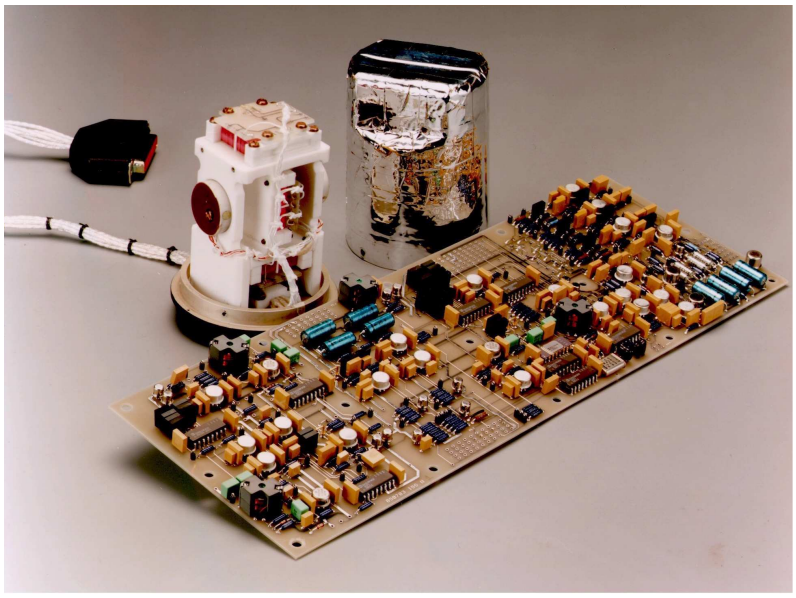

Figure 4.8: A photograph of the MAG fluxgate magnetometer without its casing. Taken from *Dougherty et al.* (2004).

4.2 Magnetometer (MAG)

The Cassini magnetic field investigation (*Dougherty et al.* 2004) is comprised of a scalar/vector helium magnetometer (S/VHM) at the end of an 11m long boom, and a fluxgate magnetometer (FGM) halfway along the same boom. Having two magnetometers allows for the spacecraft-generated magnetic field to be more easily removed from the observations, as well as aiding in calibration of the two instruments as the outputs can be compared. Also, in the event that one of the magnetometers fails, having a second allows for magnetic field observations to continue. This is in fact what happened. The S/VHM failed in 2005, and therefore only data from the FGM is used and further discussed in this thesis.

FGM was built at Imperial College and can be seen in the photograph in Figure 4.8 without its cover before launch. A fluxgate magnetometer is made of a ferromagnetic core that is then surrounded by two sets of coils. A current is driven through one of the coils (the 'drive' coil), which induces an alternating cycle of magnetic field saturation in the core. This alternating cycle drives the core to saturation twice per cycle. The magnetic field in the core induces a current in the second coil (the 'sense winding' coil). The current in the second coil is then compared to that of the drive coil. If there is no external magnetic field present, then the currents in the two coils should match. However if there is an external magnetic field then this

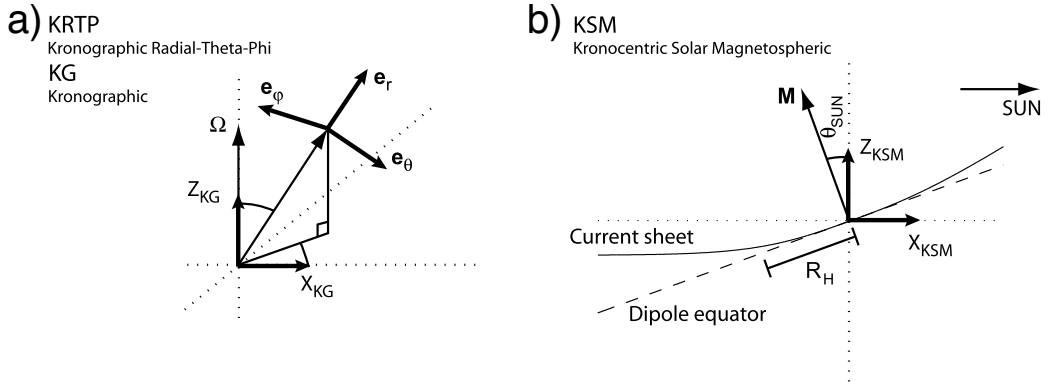

Figure 4.9: Illustration of the KRTP and KSM coordinate systems. Adapted from *Arridge et al.* (2011).

will influence the current induced in the second coil and therefore will not match the current in the drive coil. The difference between the two coils is a function of the strength of the external magnetic field parallel to the core.

The FGM is made of three single-axis fluxgate sensors, which are aligned perpendicular to each other. The gain of the instrument is varied so that the ranges and resolutions of the measurements can be adjusted depending on the measured field. The resolution for a dynamic range of ± 40 nT is 4.9 pT and for a dynamic range of ± 400 nT is 48.8 pT. MAG observations in this thesis will not exceed the latter dynamic range. The FGM has a maximum sampling rate of 32 vectors/s, however in this thesis the data are presented as 1 s averages. At the 1 Hz level the instrumental noise is less than 5 pT/$\sqrt{Hz}$.

The MAG data in this thesis is presented in Kronographic-Radial-Theta-Phi (KRTP) coordinates (i.e. spherical polar coordinates), which are spacecraft-centred for the magnetic field and planet-centred for the position of the spacecraft. An illustration of the coordinate system can be seen in Figure 4.9a. The $\mathbf{e}_r$ vector (x-axis) points radially outward from the planet to the spacecraft. $\mathbf{e}_\phi$ (z-axis) is in the azimuthal direction, positive in the direction of Saturn's rotation. $\mathbf{e}_\theta$ completes the right-hand set ($\mathbf{e}_\phi \times \mathbf{e}_r$) and is in a colatitudinal direction, positive southwards.

Maps of the spacecraft orbit and location will also be occasionally shown and are presented in the Kronocentric Solar Magnetospheric (KSM) coordinate system, which is Saturn-centred. An illustration of this system is shown in Figure 4.9b. The x-axis (X_{KSM}) is directed away from the planet towards the Sun along $\mathbf{e}_x$. The y-axis (Y_{KSM}) is directed along $\mathbf{e}_y = \mathbf{M} \times \mathbf{e}_x$ and is divided by the unit vector

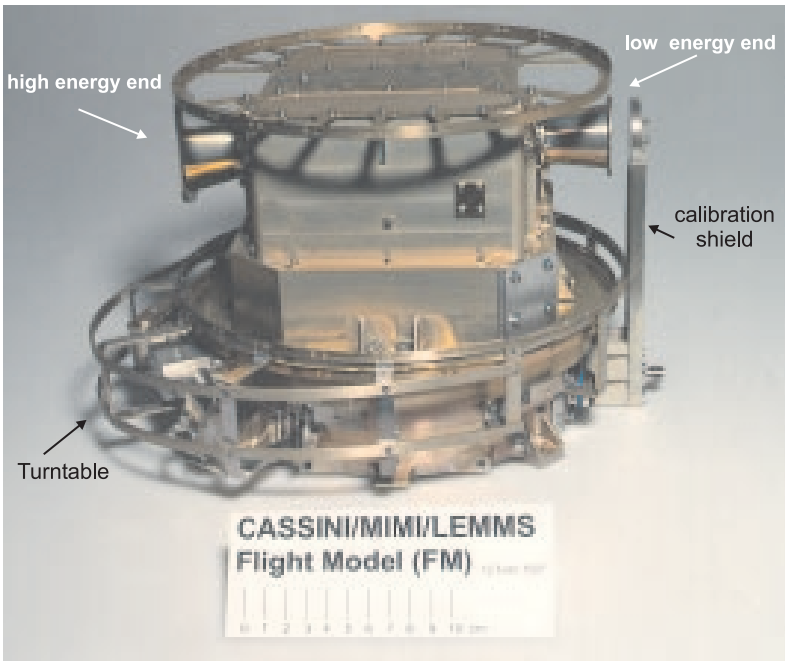

Figure 4.10: A photograph of the LEMMS flight unit. Taken from *Krimigis et al.* (2004).

normal and is in the positive duskward direction. **M** is the unit vector magnetic dipole moment of the planet. **M** lies in the X-Z plane. $\mathbf{e}_z$ is equal to $\mathbf{e}_x \times \mathbf{e}_y$.

For more information about the instrument and the available data, the reader is directed to the instrument paper (*Dougherty et al.* 2004) and the online Planetary Data System user guide (*Wei* 2012).

4.3 Low energy magnetospheric measurement system (MIMI-LEMMS)

The low energy magnetospheric measurement system (LEMMS) is designed to observe energetic electrons and ions (*Krimigis et al.* 2004). The instrument (Figure 4.10) is made of a double-ended sensor (a low energy and a high energy end). The whole instrument is mounted on a rotating platform. However the platform failed in 2005, and so now the position is fixed.

A magnetic field inside the instrument separates ions and electrons, which strike different detectors. The low energy end of the sensor observes electrons with energies of 20 keV−0.9 MeV, and ions with energies of 30 keV/q−18 MeV/q. The electrons are also processed through a pulse height analyser that produces a 64-channel energy spectrum (these are the data presented in the spectrograms of this thesis). The ion energy ranges (for protons and helium) for each channel used in this thesis are shown

Table 4.1: LEMMS low-energy-end ion and electron energy channel descriptions. Adapted from *Krimigis et al.* (2004).

	p		He			e^-	
LEMMS channels	E_{min} [MeV/q]	E_{max} [MeV/q]	E_{min} [MeV/q]	E_{max} [MeV/q]	LEMMS channels	E_{min} [MeV/q]	E_{max} [MeV/q]
A0	0.027	0.035	0.008	0.010	C0	0.020	0.030
A1	0.035	0.056	0.01	0.016	C1	0.030	0.045
A2	0.056	0.106	0.01575	0.029	C2	0.045	0.060
A3	0.106	0.255	0.02925	0.068	C3	0.060	0.100
A4	0.255	0.506	0.0675	0.130	C4	0.100	0.200
A5	0.506	0.805	0.13	0.205	C5	0.170	0.300
A6	0.805	1.6	0.205	0.4	C6	0.300	0.528
A7	1.6	3.5	0.4	0.875	C7	0.528	0.900
A8	3.5	4	0.875	4.0			

in Table 4.1.

4.4 Charge energy mass spectrometer (MIMI-CHEMS)

The charge energy mass spectrometer (CHEMS) is similar to IMS in that it uses electrostatic analysers and carbon foils followed by TOF to identify the composition of ions (*Krimigis et al.* 2004). The ions are deflected by an ESA, and then pass through a carbon foil where secondary electrons are produced. The secondary electrons are then deflected by electric fields and hit one of three MCPs to record the start time, for the TOF analysis. The TOF system determines the speed of the ions via start and stop times of the particle whilst it travels a distance of 10 cm inside the instrument. The ion then strikes one of three silicon solid state detectors (SSDs). The secondary electrons produced from the SSD are then deflected onto one of three MCPs, which then provide the stop time. The three TOF sensors cover an angular acceptance of 53° by 4° each. The energy per charge range of the instrument is 3−220 keV/q.

The detector can determine the mass-per-charge, mass, charge and energy of the ions. This is an important distinction from IMS-TOF, which only gives mass-per-charge. This means that CHEMS can for example distinguish between He^{++} and H_2^+, whilst IMS is unable to do so. CHEMS data is only presented in the final chapter (as counts/s), where we focus on the He^{++} counts in the cusp.

4.5 Radio Plasma Wave Science (RPWS)

The Radio Plasma Wave Science (RPWS) investigation consists of three electric antennae to make electric field observations, a Langmuir probe, and three magnetic antennae to determine the magnetic component of electromagnetic waves (*Gurnett et al.* 2004). RPWS measures the electron density and temperature, and the electric and magnetic field so that it can observe radio signals and plasma waves. The 10 m long antennae are mounted on orthogonal sides of the spacecraft, and point in orthogonal directions. The measurements from the antennae are fed to a set of five receivers, which cover different frequency ranges at different resolutions. Data presented in Chapter 6, are from the high frequency receiver (HFR) with a frequency range of 3.5 kHz−16 MHz. Observations from the Langmuir probe are not presented in this thesis.

Chapter 5

Methods and Coordinate Systems

In this chapter a coordinate system and a method of analysis will be explained which are used in consequent chapters. Explained first is the OAS coordinate system used to present the angular distributions of the ions observed by IMS. Finally we explain the method used to calculate the distance to the reconnection site from IMS data using the *Burch et al.* (1982) model, that is used frequently in this thesis.

5.1 OAS coordinate system for IMS

The IMS does not have a 4π steradian FOV, and in order to increase its FOV, it is mounted on an actuator. It is therefore important to know where the instrument is looking (which direction it can and cannot see) so as to understand from what direction the ions are observed in reference to the spacecraft and to the direction of the planet. It is also useful to know the related magnetic field direction, the direction of planetary corotation and the position of the Sun and Saturn.

The data is presented in a coordinate system centred on the spacecraft (the observer) which is facing Saturn (i.e. Saturn is at the centre of the plots), with θ being a polar angle away from Saturn (0° points towards Saturn [$\boldsymbol{S}$], and 180° points directly away from Saturn). The coordinate system is shown in Figure 5.1 (bottom two panels), with the corresponding 'map' plot shown in the top panel. θ is represented in the plots radially away from the centre, with 90° representing the inner circle, and 180° representing the outer circle (and is a point in space behind the spacecraft). ϕ is an azimuthal angle measured around $\boldsymbol{S}$. $\phi = 0°$ ($\boldsymbol{O}$) points in the direction of $\boldsymbol{S}\times(\Omega\times\boldsymbol{S})=\boldsymbol{O}$, where Ω is the spin axis of the planet. $\boldsymbol{A}$ completes the right−handed set.

Therefore to detect ions flowing in the plasma corotation direction, the instrument must point at θ =90° and ϕ =270° (labelled as a diamond in the top panel of Figure 5.1). This means that at the subsolar point, the direction parallel to north is on the inner circle (i.e. θ =90°) at ϕ =0°. To better explain this, if the reader can imagine they are sitting on the spacecraft facing the planet, everything in front of them is within the inner circle (with the inner circle representing the 'sides' of the observer where ϕ >90° and ϕ >270° is everything 'above', and 90°< ϕ <270° is everything below the observer). Everything behind the observer is between the inner and outer circles.

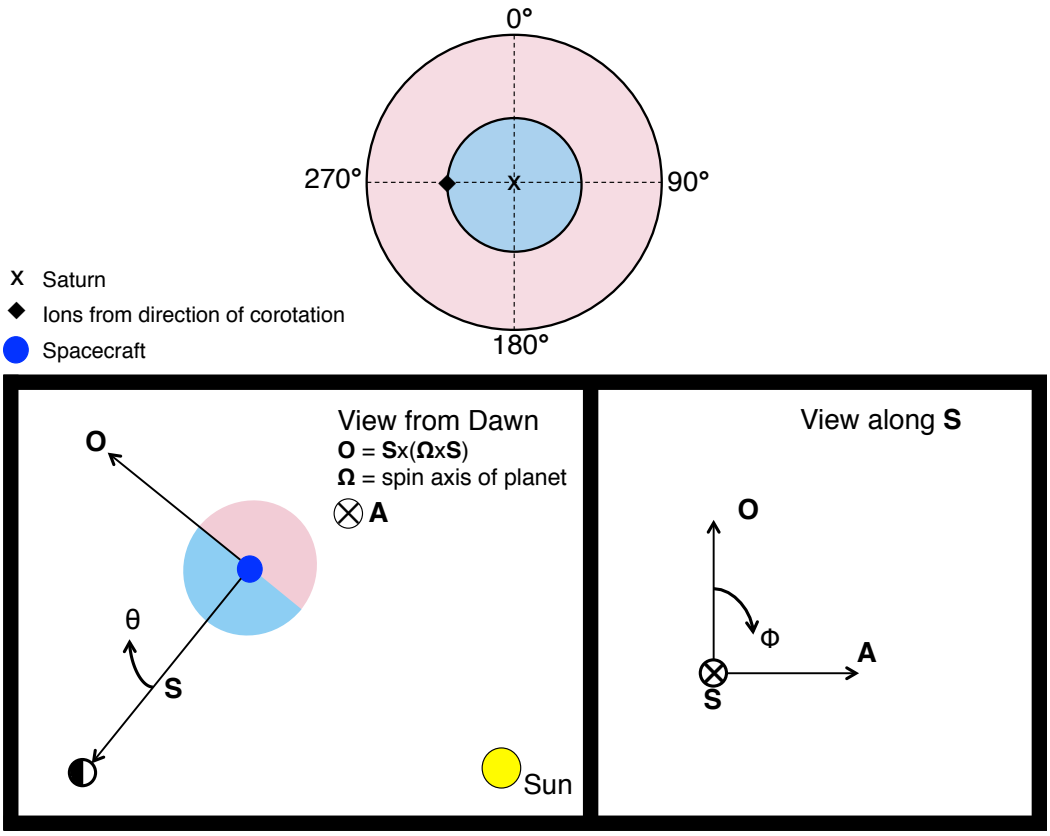

Figure 5.1: The OAS system explained. In the bottom plots the white circle represents the planet (in the bottom left the black shading is to signify the night side). The bottom left panel shows the coordinate system in the $\boldsymbol{O}-\boldsymbol{S}$ plane. $\boldsymbol{S}$ points towards the planet, and the view along $\boldsymbol{S}$ can be seen in the bottom right panel. The top panel shows the map which uses the OAS coordinate system presented in future plots, with Saturn in the centre. The pink and blue shading highlight θ, which increases radially outwards from the plot centre marked 'x' in the bottom panels. Blue is 0° to <90° and pink is >90° to 180°. This corresponds to the same highlighting in the bottom left panel. The degrees on the outer circle (top panel) correspond to ϕ, shown in the bottom right panel. In the bottom right panel, θ=0° <90° is directed into the page, and θ=>90°−180° is directed out of the page.

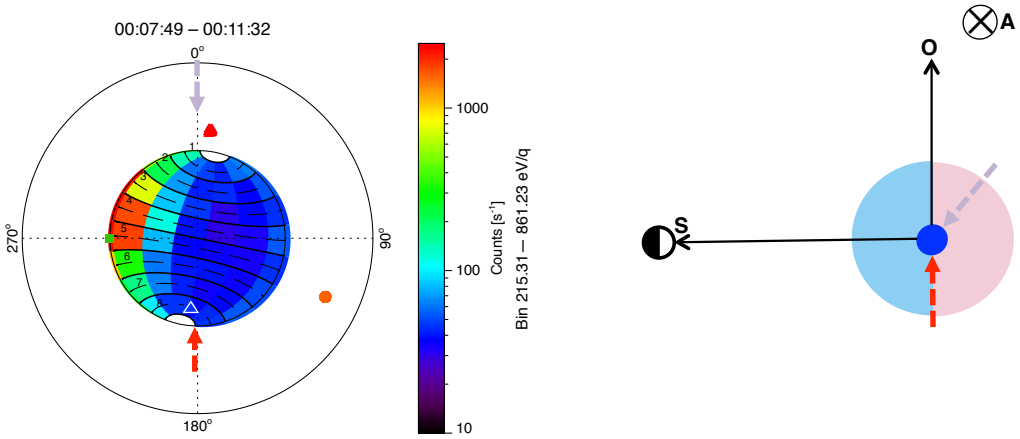

Figure 5.2: On the left: an example of IMS data shown in the OAS coordinate frame, from the 25th October 2007. Shown for reference is the Sun (orange dot) direction, magnetic field-aligned (red) and anti-field-aligned (blue) direction, as well as the look direction required to observe corotation (green). On the right: the coordinate system shown in the $\boldsymbol{O}-\boldsymbol{S}$ frame. The purple and red arrows on the right represent plasma flows (with no $\boldsymbol{A}$ component), and their corresponding location on the data plot on the left is also shown (as the tip of the arrow).

Figure 5.2 shows an example of data from the IMS plotted in OAS coordinates, from the 25th October 2007. The spacecraft is ∼10 R_S from the planet, in the equatorial plane and at ∼09:30 local time (LT). Labelled on the plot is the direction of the Sun (orange dot) and the field-aligned (red triangle) and anti-field-aligned (blue triangle) directions with respect to the magnetic field calculated from MAG. The edges of each anode (labelled 1−8, the location of the numbers show the starting point of actuation) are also shown, with the dashed line representing the centre of the anode, as it actuates. The IMS observations are shown in counts per second. The arrows in the right panel show plasma flows that correspond to the locations on the plot on the left side.

In this particular example high counts of ions are observed when the instrument actuates to look in the corotation direction, and therefore a direction going into the page on the right panel of Figure 5.2. It should be made clear that what is described as the corotation direction in these plots, is in fact the look direction required to observe corotating ions. The instrument points into the direction of corotation to detect these ions (i.e. the instrument itself points in the direction opposite to corotation in order to observe ions that are corotating). The actual direction of corotation is at a ϕ and θ angle of 90° (however ions detected in this look direction would mean the ions are flowing in an anti-corotational direction).

Plots such as these which will be shown in the following chapters occur when the spacecraft is at high latitudes, similar to that shown in Figure 5.1. The location of the spacecraft will be specified in the accompanying text, so that the reader can better understand the results.

5.2 Calculating the field-aligned reconnection distance

As is explained in previous chapters, the distance to the reconnection site from the cusp observations can be calculated from ion energy-pitch angle dispersions, using the *Burch et al.* (1982) (from now on called 'BUR82') model equation (see Eq 2.2). To achieve this for Cassini observations, the IMS data are compiled for each actuator sweep and the pitch-angle coverage is calculated for each anode, to create a pitch angle energy distribution. The data are binned into nineteen pitch angle bins. The ion dispersion in the data is determined by selection of the lowest energy bin, called the 'low energy cutoff', by using a signal-to-noise ratio of four. The noise is estimated per actuation sweep and per anode for all energy bins (in an anode) by calculating the mean of the counts from the three energy bins with the lowest counts. The uncertainty of the data is calculated using Poisson counting statistics and the accumulation time (i.e. the square root of the count rate divided by the accumulation time) for each underlying actuator sweep, anode and energy bin, and then propagated through to get an uncertainty on each pitch angle.

The magnetic induction along the field line is calculated for increments along

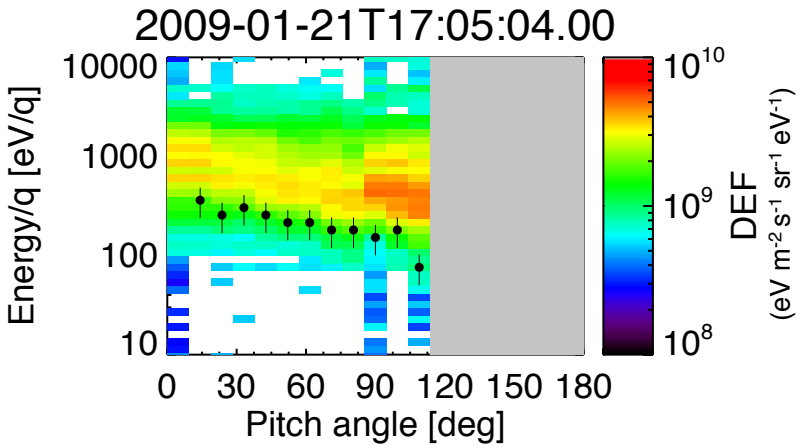

Figure 5.3: An example of a energy-pitch angle distribution, with the low energy ion cutoff for each bin highlighted (dots). This example is shown before a model fit is made. Grey bins signify no data are available due to the lack of pitch angle coverage by the instrument. This is an example from the 21st January 2009 at 17:05:04 UT.

the field line with a separation ds (taken to be 0.001 R_S), from the position of the spacecraft. This is done by tracing field lines using the *Khurana et al.* (2006) magnetospheric field line model from the position of the spacecraft to the two footpoints of the field line at the planet's surface (characterised as 60268 km from the planets centre).

The BUR82 model is then fitted to the data iteratively using a least squares curve fitting method. A least square minimisation method involves fitting a model function $\hat{y}(t_i)$ to a set of m data points $x_i(t_i)$, with error estimates of σ_i. A measure of the 'goodness-of-fit' of the model to the data is calculated using the chi-squared criterion:

$$\chi^2 = \sum_{i=1}^{m} \left[\frac{x(t_i) - \hat{y}(t_i)}{\sigma_i} \right]^2 \tag{5.1}$$

The model is fitted iteratively, in order to minimise χ^2, and to find the best-fit solution. The aim after each iteration is to find a perturbation to the parameters that the model is built upon that reduce the value of χ^2.

The Levenberg-Marquardt (L-M) method for least squares curve-fitting is used. This is done using the MPFIT code for IDL written by *Markwardt* (2009), which is an improved IDL version of the MINPACK-1 routine (*Moré* 1977; *Moré and Wright* 1993). The routine that applies MPFIT to the data was written by *C. S. Arridge* at MSSL−UCL (*Jasinski et al.* 2014).

The L-M method combines the use of two minimisation techniques: the gradient descent method and the Gauss-Newton (G-N) method. To find the local minimum of χ^2 the gradient descent method involves adjusting the model parameters such that the solution steps along the negative of the gradient of χ^2 to descend towards the minimum in χ^2. Near this minimum, χ^2 has a quadratic form, since if a Taylor-expansion of χ^2 is made, the linear term is small compared to the quadratic term. Close to the minimum the gradient descent method becomes inefficient and the L-M method then switches to the G-N method. The G-N method uses the second-order term of the expansion to converge χ^2 to the local minimum. This means that near the minimised value of χ^2, the G-N method converges to the optimal solution much faster than the gradient descent method (*Marquardt* 1963).

The L-M method varies between the two methods depending on whether the

least squares function is being successfully minimised. The L-M method applies a parameter λ, that at the start of the process is large, and changes after each iteration. When λ is large the gradient descent method is used. As the L-M method approaches the optimal solution, λ is reduced and the G-N method is approached. If after an iteration χ^2 is increased, λ increases, causing the gradient descent method to be used again.

Boundaries are applied for the parameters of the L-M method. Lower and upper limits of 10 R_S and 80 R_S respectively, are used for the field-aligned distance to the reconnection site. A lower boundary for the transit time of 1800 seconds is used.

Chapter 6

Evidence of Bursty reconnection at Saturn's Dayside Magnetopause

In this first research chapter I present the first published detailed analysis of the magnetospheric cusp at Saturn (on the 21st of January 2009), which was reported in *Jasinski et al.* (2014). A similar observation from the 3rd of August 2008 is also presented. The trajectory of both intervals will be shown first, followed by the various observations that were made in the cusp. The observations from the 21st of January 2009 and 3rd of August 2008 will from now on be called 'JAN09' and 'AUG08'.

6.1 Spacecraft Trajectory

Figure 6.1 shows the trajectories of the spacecraft during the two cusp observations. The trajectories are shown in the KSM coordinate system in the following projections: (a) X-Z (i.e. the view from dawn); (b) X-Y (i.e. the view from 'above' looking down approximately onto the north pole) and (c) Y-Z (i.e the view from the Sun). The section of the trajectories highlighted in blue and red show the part of the trajectory where the cusp for AUG08 and JAN09 is observed, respectively. In the background of the X-Z projection is a magnetic field model (grey) (*Khurana et al.* 2006), and the location of the magnetopause (dotted) during quiet solar wind conditions calculated using the *Kanani et al.* (2010) model. The field line model has been generated for the latter date, which is closer in time to equinox at Saturn (August 2009). This results in the magnetic dipole tilt of the planet being larger for the AUG08 event as it is further away in time from equinox. Therefore if the

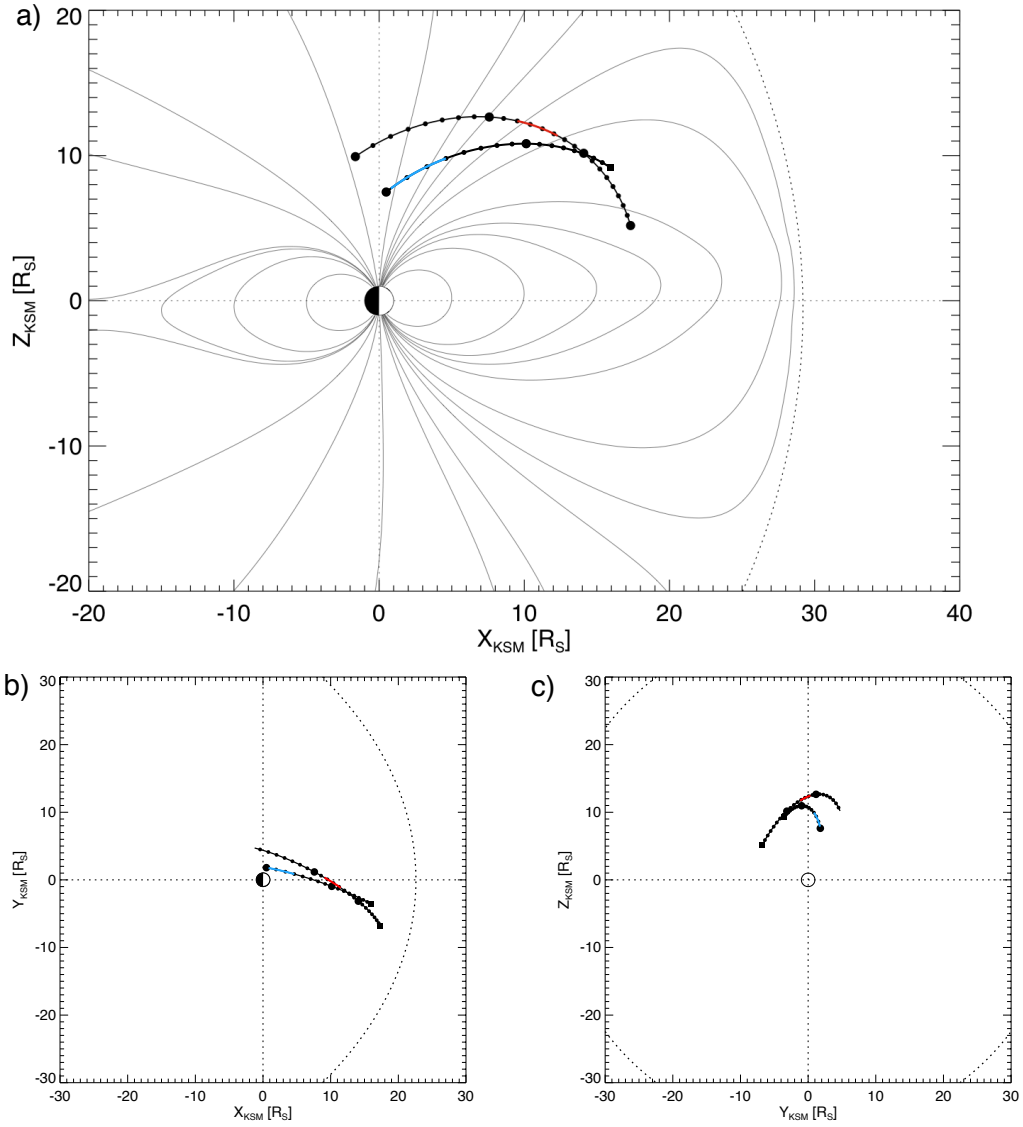

Figure 6.1: Trajectories of Cassini during the two cusp observations with each trajectory highlighted in blue and red for where the cusp is observed on the 3rd of August 2008 and 21st of January 2009, respectively. The whole trajectories are shown for the time periods of 2−3rd August and 20−22 January, both starting on the dayside and ending in or near the nightside. Panel (a) shows the X-Z projection of the orbits in the Kronocentric-Solar-Magnetospheric (KSM) coordinate system. The Sun is to the right and the view is from dawn. The large dots represent the start of a day's observations. The smaller dots are separated by three-hour intervals. Shown in grey is the Khurana magnetospheric field line model (*Khurana et al.* 2006), with the dotted line representing the average position of the magnetopause model. Panel (b): looking down onto the equatorial plane from above the north pole (X-Y plane of KSM, with the equatorial plane inclined towards the observer on the dayside), with the Sun to the right; (c) as seen from the Sun.

magnetic field line model had been produced for the AUG08 event (instead of the JAN09 interval), then the region where the northern cusp is expected (in the model) would be tilted further away from the Sun in comparison to the model generated for the JAN09 event.

Cassini is travelling in a poleward trajectory for both observations, from the equator towards higher latitudes where the cusp is expected to be seen. The spacecraft is also travelling planetward and duskward, crossing noon local time (LT). The JAN09 observation occurs at larger radial distances from the planet (16.5−15.5 R_S), lower kronocentric latitudes (42.3°−50.4°) and covers a smaller range of LTs (11:37−12:06), in comparison to the AUG08 observation: radial distances of 11.1−8.2 R_S, latitudes of 58.7°−72.7° and LTs of 12:32−14:55.

6.2 Observations from the 21st of January 2009 – 'JAN09'

An overview of the in situ observations during the day of the cusp crossing, as well as the day before are presented in Figure 6.2, showing CAPS (ELS and IMS) and MAG data. The spacecraft is at large radial distances from the planet (∼19 R_S) and at low latitudes (∼13°) at the start of the figure. Until 11:00 Universal Time (UT) on the 21st of January, the spacecraft observes high energy tenuous electrons (panel a), typical of the outer and high latitude magnetosphere. At ∼17 UT (20th January) there is an increase in flux as well as the energy of the electrons. At this time the magnetic field observation becomes disturbed, with sharp changes in the field strength, and a rotation in the B_ϕ and B_θ components. Bipolar signatures in the magnetic components may be due to a flux transfer event observation, however this would need to be investigated further. This could also be a large field aligned current similar to the observations reported by *Bunce et al.* (2008b). During the magnetospheric observations, shallow magnetic depressions coincide with increases of electron flux due to a diamagnetic effect. Before entering the cusp at 11:00 UT (21st January) there is a small decrease in energy of the observed electrons. The ion observations show no significant increases in counts above the background level until just prior and during the cusp observations. During the cusp observations (11:00-19:00 UT) it can be seen that there is a deviation from the increasing magnetic field strength (due to the planetward trajectory of the spacecraft). Instead of increasing,

the magnetic field is steady throughout the cusp and then sharply increases at the end (instead of increasing gradually); evidence that the cusp plasma is creating a diamagnetic depression due to its high density.

Figures 6.3 and 6.4 show the remote and in situ observations obtained during the cusp crossing presented in *Jasinski et al.* (2014). Figure 6.3 shows three (i−iii) polar projections of Saturn's northern aurora, observed by UVIS. These observations were taken towards the end of the cusp observations, and just after 1801, 1848 and 2012 UT (arrows [labelled 'i-iii'] pointing on the in-situ data in Figure 6.4 compare the timing of the in situ and remote observations).

The UVIS observations show bifurcations (marked with white arrows in Figure 1i−iii) which have been suggested to occur due to the opening of closed magne-

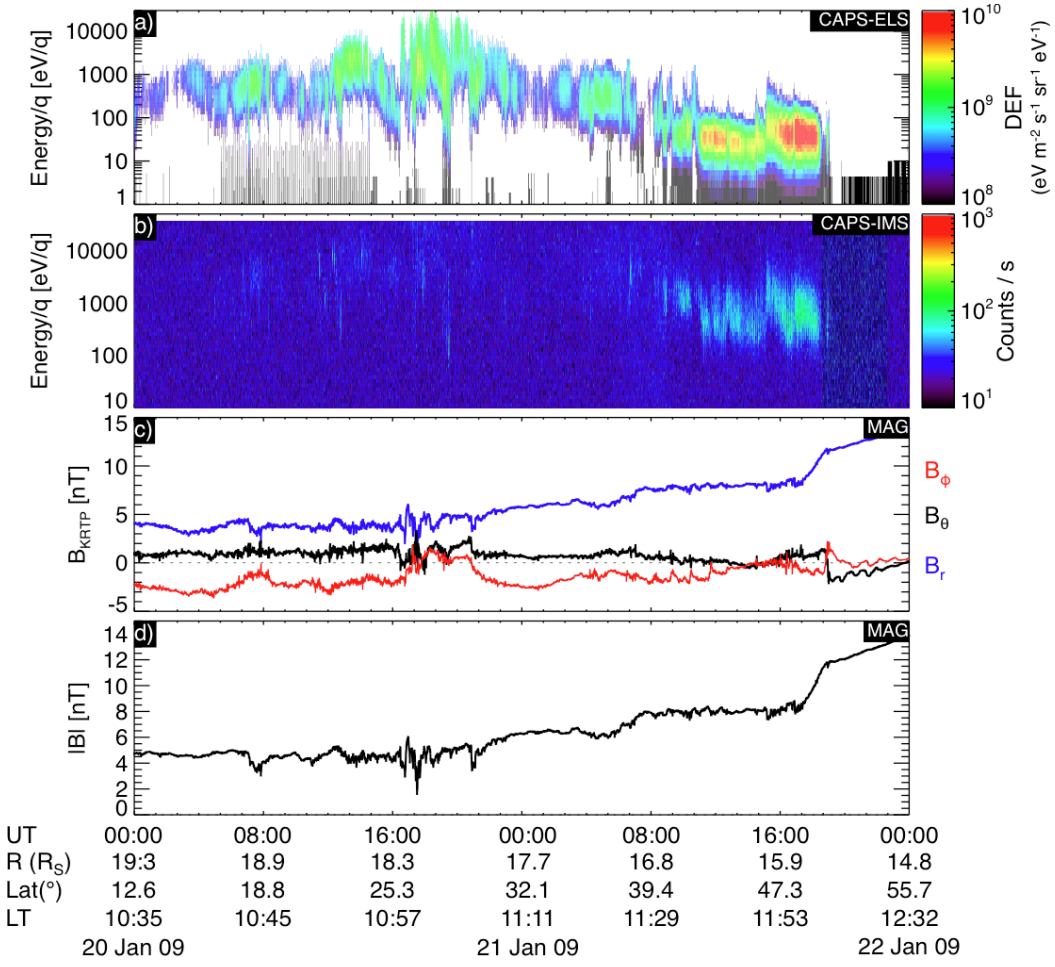

Figure 6.2: In situ observations from the 20th and the 21st of January 2009. Panel (a): omnidirectional electron flux from CAPS-ELS, with the photoelectron and background flux has been removed, (b) ions from CAPS-IMS presented in counts/accumulation, (c) the three KRTP components of the magnetic field, and (d) magnetic field magnitude from MAG.

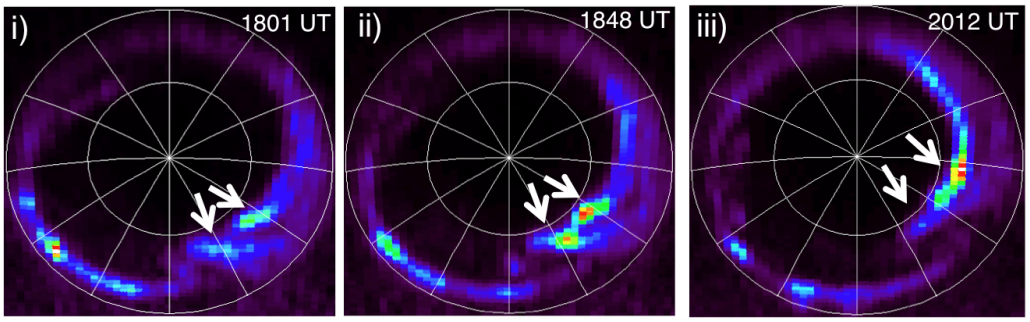

Figure 6.3: Three polar projections of Saturn's northern aurora, obtained with the FUV channel of UVIS, taken at 1801, 1848 and 2012 UT. The grid shows latitudes at intervals of 10 degrees and meridians of 30 degrees. Noon is to the bottom and dawn to the left. The times at which the images are taken in comparison to the in-situ observations are indicated by black arrows (i-iii) in Figure 6.4.

tospheric field lines at the magnetopause (*Radioti et al.* 2013). Previous studies (*Radioti et al.* 2011) have shown that during the presence of bifurcations, the main auroral emission expands with time to lower latitudes, which is indicative of the opening of flux. The expansion of the main emission is equal to the area occupied by the bifurcations, suggesting that the bifurcations represent the amount of newly opened flux and thus are signatures of magnetopause reconnection. The emissions are also rotating towards dusk, implying that either the location of the reconnection site is moving or that there is a significant azimuthal motion of the plasma in the magnetosphere due to a sub-corotating open field line. *Radioti et al.* (2013) suggested that the consecutive brightenings of the auroral bifurcations during these observations are due to multiple reconnection occurring along the same magnetic flux tube. These observations provide evidence that during these observations, reconnection was occurring at Saturn's dayside magnetopause.

The cusp observation is shown in Figure 6.4. From 0700 to 0800 UT Cassini was in Saturn's magnetosphere. In panel a), ELS data show high energy, tenuous electrons as well as in panel (b) very low ion fluxes, observations which are typical of the high latitude magnetosphere as explained earlier. In panel (c), LEMMS (energetic electron) data show increases in flux of high energy electrons when the spacecraft is in the magnetosphere.

From just before 0900 until 1100 UT, CAPS observed intermittent magnetospheric high energy tenuous plasma, and more dense cool plasma. This could be evidence of a boundary layer between the cusp and the magnetosphere (on the

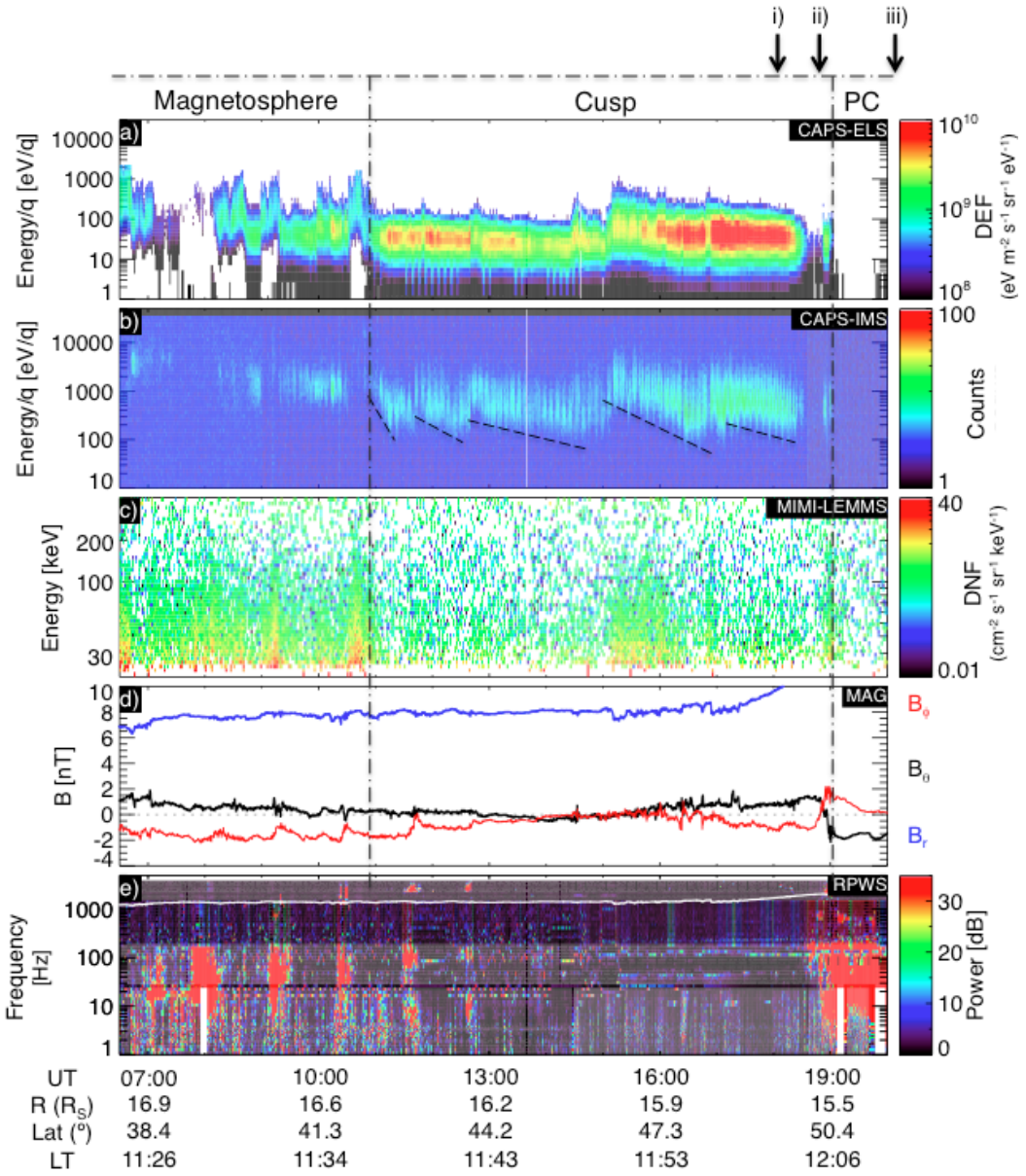

Figure 6.4: Observations from the 21st of January 2009. From top to bottom, panel (a) omnidirectional electron flux from CAPS-ELS, with the photoelectron and background flux removed, (b) ions from CAPS-IMS presented in counts/accumulation, (c) high-energy electron flux from LEMMS, (d) the three KRTP components of the magnetic field, and (e) RPWS electric field spectrogram. The stepped ion structure is underlined in panel b. The polar cap is labelled as 'PC'. The three arrows in labelled (i-iii) indicate when the auroral observations (Figure 6.3) took place.

open-closed field line boundary). At the same time, panel (d) shows that MAG observed rotations in the B_ϕ component of the magnetic field, which are indicative of field-aligned currents (FACs) (e.g., *Bunce et al.* 2008b). During this event the FACs derived from B_ϕ are found to be consistent with previous observations, and whistler mode emission was observed (panel e) by RPWS. The FACs are analysed

below in Section 6.2.1. When ELS observed lower energy electrons, IMS observed significant increases in ion fluxes.

From 1100 UT ELS observed steadier fluxes of cold dense electrons, similar to magnetosheath plasma. From this time onwards IMS observed ions which had a 'stepped' energy-latitude dispersion structure (underlined in Figure 6.4). The observed stepped ion structure is the same as the structure described in Figure 2.6c, where the velocity of the convecting field line is larger than that of the spacecraft velocity. This results in the spacecraft exiting and entering differing regions of plasma that were injected at different times and locations. This step structure in the ions, as well as the changes in the electron flux, suggests that Cassini was traversing different reconnected magnetic flux tubes in the cusp attributed to 'bursts' or 'pulses' of reconnection occurring at different areas along the magnetopause (*Lockwood and Smith* 1994; *Lockwood et al.* 2001). Therefore from 1100 until ∼1900 UT, Cassini observed the cusp, the start and end of which are marked by vertical dashed lines.

At ∼1500 UT, Cassini observed a large change in the electron flux. The observed electrons had a slightly higher energy (an increase of ∼100eV), and the most significant change in the ion dispersions is observed at this time. This is also when a local magnetic field strength decrease of ∼1 nT (∼13%) is observed by MAG. This is repeated at the beginning of the following ion dispersion. These local depressions as well as the overall depression of the magnetic field explained in Figure 6.2, show that there is a diamagnetic effect due to the large increases in plasma density and pressure whilst in the cusp, similar to the terrestrial cusp observations. The magnetic depressions are not discussed in more detail in this chapter. Magnetic depressions in the cusp are the main focus of Chapter 8.

At ∼1900 UT Cassini entered the polar cap (PC), a region with open field lines, where electron and ion fluxes were at or below the noise level. It is from this time onwards that auroral hiss is observed in RPWS. Auroral hiss is a whistler-mode emission which is observed in the Earth's polar cap region (e.g. *Gurnett* 1966). *Gurnett et al.* (2010) and *Jinks et al.* (2014) have both used auroral hiss to identify the open-closed field line boundary, and the observation of auroral hiss at the end of this event is an indication that these are open field lines and the lack of observable plasma also shows that the spacecraft entered the polar cap.

Figure 6.5 shows a comparison of the average energy distribution of the elec-

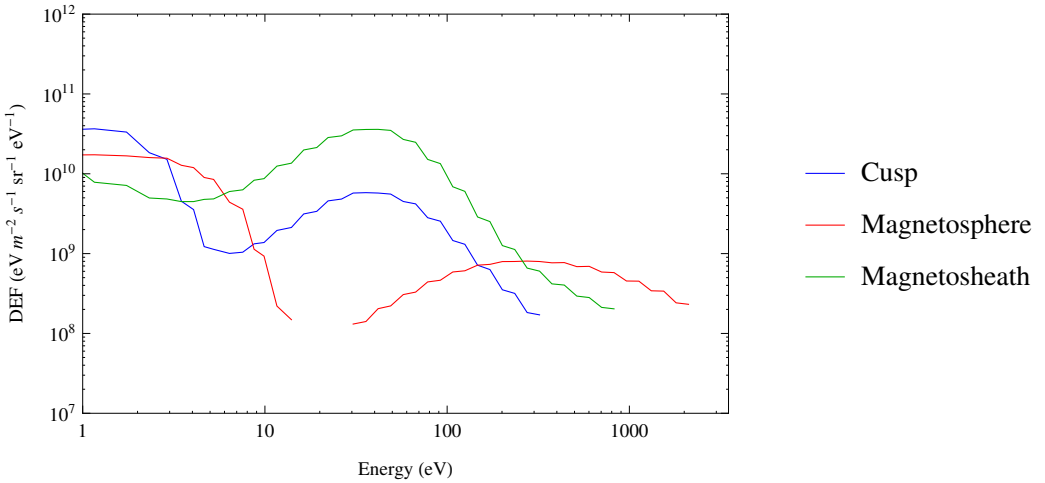

Figure 6.5: Average electron energy distributions of the cusp at 1110-1820 UT (blue), magnetosphere 0200-0700 UT (red) and magnetosheath (green) taken from the most recent interval on the 12th November 2008 1400-1900UT.

trons from 1100-1900 UT to those of the magnetosphere and the most recent magnetosheath observation. The magnetosheath observation took place at 1400-1900 UT on November 12th 2008. The electrons up to 10 eV are due to spacecraft photoelectron detections. When the flux falls to background levels it is not plotted. From 10 eV the cusp electrons are more similar in energy distribution to the magnetosheath (although a bit lower in flux) than the magnetosphere, showing that the plasma is therefore more likely of SW origin and not magnetospheric. The analysis of the field aligned currents will now be discussed.

6.2.1 Field-aligned Currents

Ampere's law states that the magnetic field $\boldsymbol{B}$ around any closed loop Γ with a surface $\boldsymbol{s}$ is equal to the current I through the loop:

$$\oint_{\Gamma} \mathbf{B} \cdot d\mathbf{s} = \mu_0 I_{through\Gamma} \tag{6.1}$$

Ampere's Law can be used to determine the magnetic field near a wire. Due to symmetry, the magnetic field magnitude is the same everywhere on a concentric circle around the wire, which can be seen in Figure 6.6a. For a wire such as this the left hand side of the above equation is just the magnetic field multiplied by the circumference of the circle, and so $I\mu_0 = \boldsymbol{B} \cdot 2\pi r$. This concept is the same for analysing the FACs in the magnetosphere.

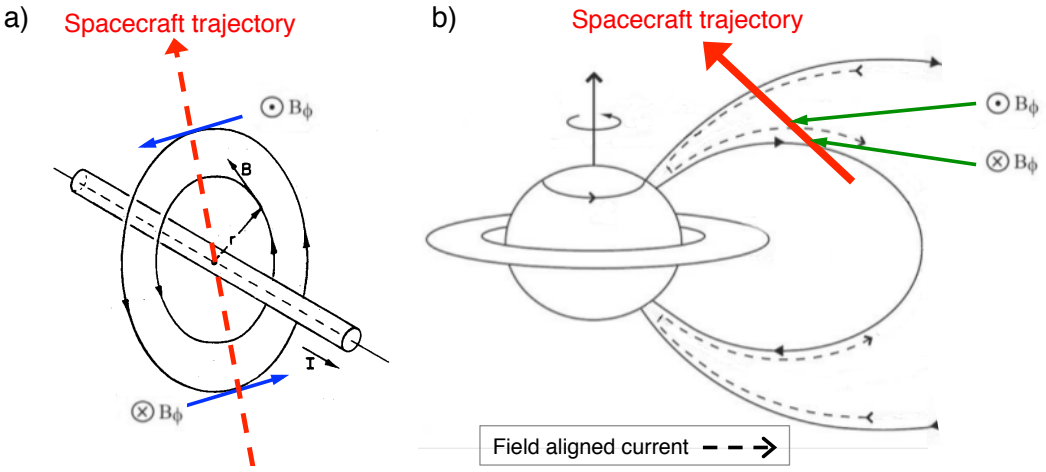

Figure 6.6: Illustration of field aligned current observation in the B_ϕ component of the magnetic field. The spacecraft trajectory is shown with respect to: a) the magnetic field outside (in 3D) a current 'I' (an illustration of Ampere's Law), and the observation of the B_ϕ component similar to panel b. Panel b), the FAC in the magnetosphere (as viewed from dawn, Sun to the right), the green arrows show where the enhancement (increase in either the direction into or out of the page) is seen in the B_ϕ component of the magnetic field (in KRTP). Both panels are adapted from *Feynman* (1964), and *Talboys et al.* (2009), respectively.

If the spacecraft passes through the current in a poleward trajectory, then it will observe a local increase in the magnetic field B_ϕ direction, shown as blue arrows in panel a. These increases are represented as the points labelled by the green arrows in panel b. By applying Ampere's Law in the same way to a circular loop which is centred on the magnetic axis of the magnetosphere (assuming axisymmetry) with a cylindrical radius ρ (e.g. *Bunce et al.* 2008b; *Badman et al.* 2012a); the equatorward flowing height-integrated ionospheric Perdersen current per azimuth which closes the FACs at the footpoints of the magnetospheric field lines is:

$$I_P = \mp \frac{\rho B_\phi}{\mu_0} \tag{6.2}$$

where the $-/+$ sign is for northern/southern hemisphere. The FAC can be estimated from the change in I_P because any increases or decreases in the Pedersen current must be balanced by an inflow or outflow of current along the field lines into the ionosphere. Therefore if the spacecraft is travelling poleward, and an increase in I_P is observed by an amount ΔI_P, then the same amount of current must have flowed out of the ionosphere in the region through which the increase was observed. A decrease in I_P whilst moving poleward requires a downward current (into the

ionosphere). These currents are necessary to produce the changes in B_ϕ observed by MAG.

In Figure 6.7b, the calculated ionospheric current I_P corresponding to the B_ϕ component can be seen in black. The red line shows the values used for the calculation of ΔI_P (at the boundaries marked by dashed vertical lines). From the difference of these values the field aligned current ΔI_P is calculated and can be seen in panel c. Each pair of FACs has been labelled in chronological order from 1 to 5, with a suffix of 'U' or 'D', for the upward or downward component of the FAC, respectively.

Panels d−f display the the particle data sets (CAPS and MIMI-LEMMS) and the RPWS observations for comparison with the calculated FACs. It can be seen that for some of the FAC observations there are increases in the high-energetic particle flux (panel d), as well as in the bursts of electrons with higher energies in panel e (spectra similar to what is observed in the magnetosphere). The downward FACs are also observed when whistler-like emission is observed in RPWS, seen in panel f by the large increases in power up to 35 dB in the ∼10-100 Hz frequency range. Whistler-mode emission in RPWS has previously been reported to be observed during FACs (*Bunce et al.* 2008a; *Talboys et al.* 2011; *Badman et al.* 2012a,b). A more detailed investigation of each set of FACs and their corresponding particle observations will now be conducted.

In Figure 6.8, observations of the FACs are presented as well as RPWS and electron data along with the pitch-angle observations of the corresponding electrons, in order to determine whether the FACs correspond to increases in electron flux in the appropriate directions. For an upward current region, downward-travelling electrons would be expected. This would mean an observation of electrons with ∼180° pitch angles in the northern hemisphere and ∼0° pitch angles in the southern hemisphere. For a downward current region, the opposite would be expected (electrons with ∼0° pitch-angles in the northern hemisphere). Figure 6.8c-f presents the observations of the 0° (field-aligned) pitch angle coverage of anodes 2 and 3 of ELS; whilst Figure 6.8g-j) show the 180° (anti field-aligned) pitch angle coverage of anodes 6 and 7 of ELS.

For the first downward current (1D), ELS has a sufficient field of view (FOV) to observe field-aligned electrons, however no intensifications of electrons are observed in the data. For the second downward (2D) current, ELS has a sufficient FOV,

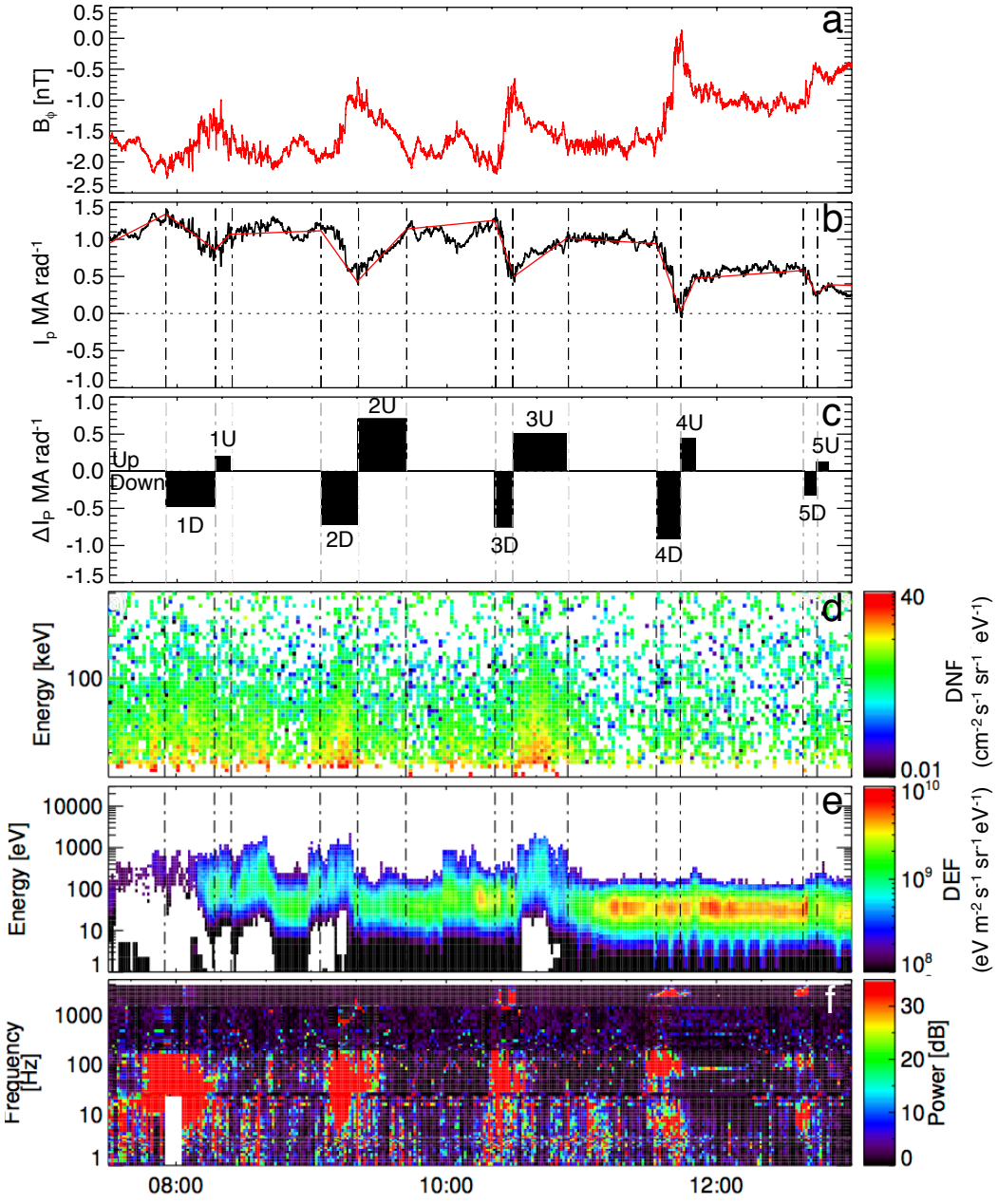

Figure 6.7: From the top to bottom: (a) the B_ϕ component of the magnetic field, (b) the calculated ionospheric current from Eq. 6.2, (c): the field aligned current magnitude, shown as 'upward from the planet' and 'downward into the planet' directed currents, with each current labelled, (d) high-energy electrons from MIMI-LEMMS, (e) low-energy electron observations by CAPS-ELS, (f) electric field spectrogram from RPWS.

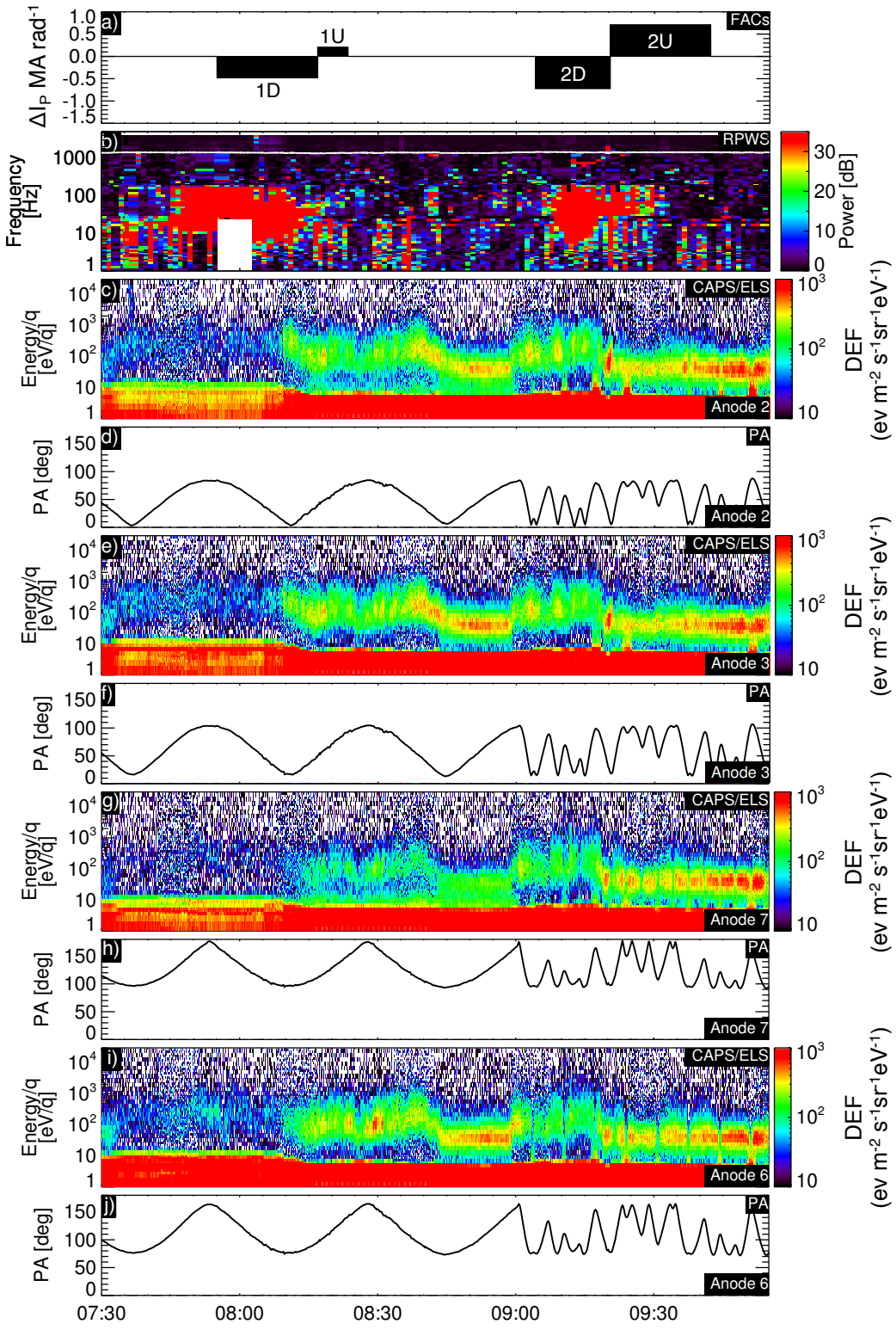

Figure 6.8: A comparison of FACs with the plasma data. From top to bottom: (a) FACs: 1D, 1U, 2D, 2U, respectively, (b) RPWS electric field spectrogram, (c) ELS anode 2 observations, (d) pitch angle (PA) coverage of anode 2, (e) ELS anode 3 observations, (f) PA coverage of anode 3, (g) ELS anode 7 observations, (h) PA coverage of anode 7, (i) ELS anode 6 observations, and (j) PA coverage of anode 6. Panels c-f focus on the field-aligned (0°) pitch angle electrons and therefore the downward region of the currents (i.e upward-travelling electrons from the planet in the northern hemisphere), whilst panels g-j focus on the anti-field aligned pitch angles (downward electrons, upward current).

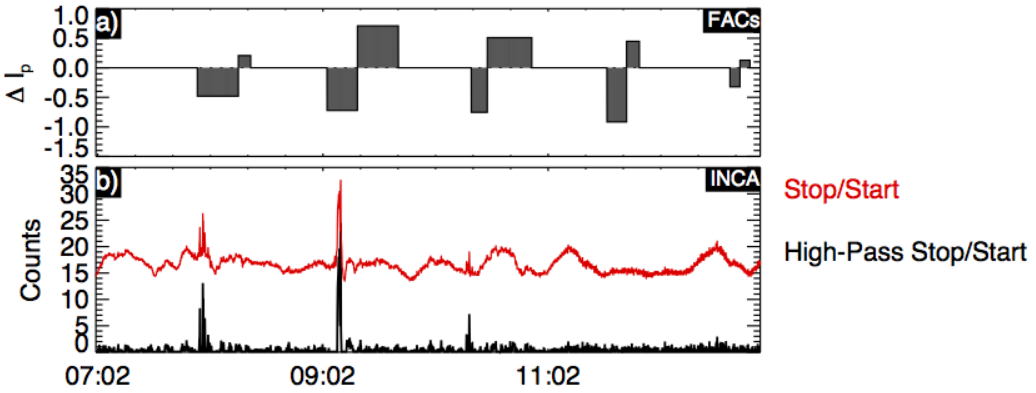

Figure 6.9: Panel: (a) Field-aligned currents obtained from B_ϕ, (b) electron counts obtained from INCA. INCA has a sufficient field of view to observe the first three downward currents. *Panel (b) was provided by Don G. Mitchell.*

and between 0900 and 0930 ELS observes increases in the flux of the electrons. In Figure 6.8b, ELS has a sufficient FOV to observe upward FACs, however ELS only observes weak increases in electron fluxes in the first upward current region (1U).

The rest of the FACs are presented in the same format and can be found in Appendix A, however their results are summarised in the text below and in Table 6.1.

For the the 3U and 3D FACs, ELS has a sufficient FOV to observe the particles, however ELS only observes increases in electron fluxes on the upward FAC but not for the downward FAC. For the 4D and 4U FAC and where possible (4U) there are no increases in electrons observed. The 5D and 5U FAC are observed whilst in the cusp, but no electrons associated with FAC are seen.

Available MIMI-INCA (ion and neutral camera) data are presented in Figure 6.9. INCA observes energetic neutral atoms as well as providing angular and energy distributions of in situ ions. INCA cannot measure electrons in calibrated physical units. However due to cross calibrations with LEMMS during times when Cassini is rolling about the Z-axis in spacecraft coordinates, INCA observes the same energetic electron beams that LEMMS observes (a quarter of a turn earlier or later depending on the direction of the roll, due to the positioning of the instruments; see Figure 4.2). Electrons can only be detected if they are field-aligned (i.e. electron beams) when the instrument's collimator is directed towards the incoming beam's direction. Ions or neutrals have a significantly higher probability of producing secondary electrons, and therefore would be recorded in the 'start' MCP and also (via the secondary electrons) the 'stop' MCP. Energetic electron beams have a very low

probability of producing secondary electrons (∼0.1%) in the instrument. Therefore signals measured in the stop MCP, with a missing signal in the start MCP are due to the detection of energetic electrons.

During this interval the voltage on the collimator plates was at 200 V, which results in an exclusion of particles between 0 and ∼10 keV/q (*Mitchell et al.* 2009), resulting in an estimation that the detected electrons are above 10 keV/q. Figure 6.9 shows that there were more counts observed in the stop MCP than the start during the first three field aligned currents. During this interval INCA has a sufficient FOV for detecting the first three downward sets of FACs; it is therefore reasonable to assume that INCA observed energetic electrons which were field aligned during the first three FACs.

In summary, the FOV is not always sufficient to observe the field-aligned currents, and even when it is, there are inconsistencies between the FAC and the electron observations. INCA observes an increase in electron flux for the first three downward currents when it has a sufficient FOV. The ELS has a sufficient FOV for the first four out of five pairs of currents, and only observes one current in each pair. The LEMMS electron channels observe increased electron flux during the second and third upward FACs. The intermittent observations of the field aligned current particles are interpreted as occasional (full) traversals of the current. When the electrons are not observed, the spacecraft is interpreted as not fully crossing the FAC, but instead observing the magnetic field rotation in B_ϕ only. The lack of FAC particle observations in the final pair of currents supports the interpretation that the spacecraft is no longer on the open-closed field line boundary which these FACs are associated with, but instead on open field lines in the cusp.

6.2.2 Ion Composition and Angular Distributions

When analysing the ion composition in the cusp and the adjacent magnetosphere, two ratios for comparison can be used: a mass-per-charge of 2 amu/q to ionised hydrogen ratio ([m/q=2]/H^+), and ionised water group to hydrogen ion ratio (W^+/H^+). The water group ions include: O^+, OH^+, H_2O^+, H_3O^+, and O_2^+. The water group originate principally from Saturn's icy moon Enceladus (as well as the other icy moons), and therefore we expect higher percentages of these ions in the magnetosphere in comparison to plasma entering the cusp from a magnetosheath origin. Both He^{++} and H_2^+ have a mass-per-charge of 2, however we would expect

Table 6.1: ELS and INCA observations during the downward (D) and upward (U) currents, and their FOVs during this time.

Current	ELS Correct FOV	ELS Observes?	INCA Correct FOV	INCA Observes?
1D	Yes	No	Yes	Yes
1U	Yes	Yes	No	-
2D	Yes	Yes	Yes	Yes
2U	Yes	No	No	-
3D	Yes	No	Yes	Yes
3U	Yes	Yes	No	-
4D	Yes	Yes	No	-
4U	Yes	No	No	-
5D	Yes	No	No	-
5U	No	-	No	-

the ions to be H_2^+ in the magnetosphere with approximate percentages composition relative to H^+ of $\sim$10−20% or more, peaking at a distance of Titan's orbit ($20R_S$) (*Thomsen et al.* 2010) which is predicted to be the source of these ions (e.g. *Cui et al.* 2008). Cold H_2^+ and W^+ have higher concentrations at the equator, contained there due to centrifugal sources, therefore reducing the abundances at higher latitudes. However in comparison, even lower abundance values for m/q=2 ions, would suggest that they are He^{++} of a solar wind origin ($\sim$4%, e.g. *Ogilvie et al.* 1989).

During the JAN09 cusp observation, the spacecraft was rolling between $\sim$11:00 and 14:00 UT, providing CAPS with an almost 4π steradian FOV. During this time, IMS completed six time-of-flight (TOF) measurements. The ions of the magnetospheric water group (W^+) species were not observed above the background levels, with only one TOF accumulation (13:11:28−13:37:03 UT) observing low counts, showing that the W^+ population is below the detectability threshold for CAPS during this time. CAPS observes slightly higher W^+ counts in the final two dispersions, at a W^+/H^+ ratio of 1.4±0.1% and 0.7±0.2% (for 15:19-16:10 and 17:01−18:31, respectively). This is extremely low in comparison to the ratios observed in the magnetospheric population at 12:00−21:50 (the day before), of 8.5±0.3%. The presence of a higher abundance of W^+ ions in the latter dispersions indicates that the spacecraft is traversing different field lines that have been reconnected at a temporally and spatially different location.

Comparing the m/q=2 to H^+ ratio between the cusp and the magnetosphere, also shows a large difference between the two regions. In the magnetosphere the

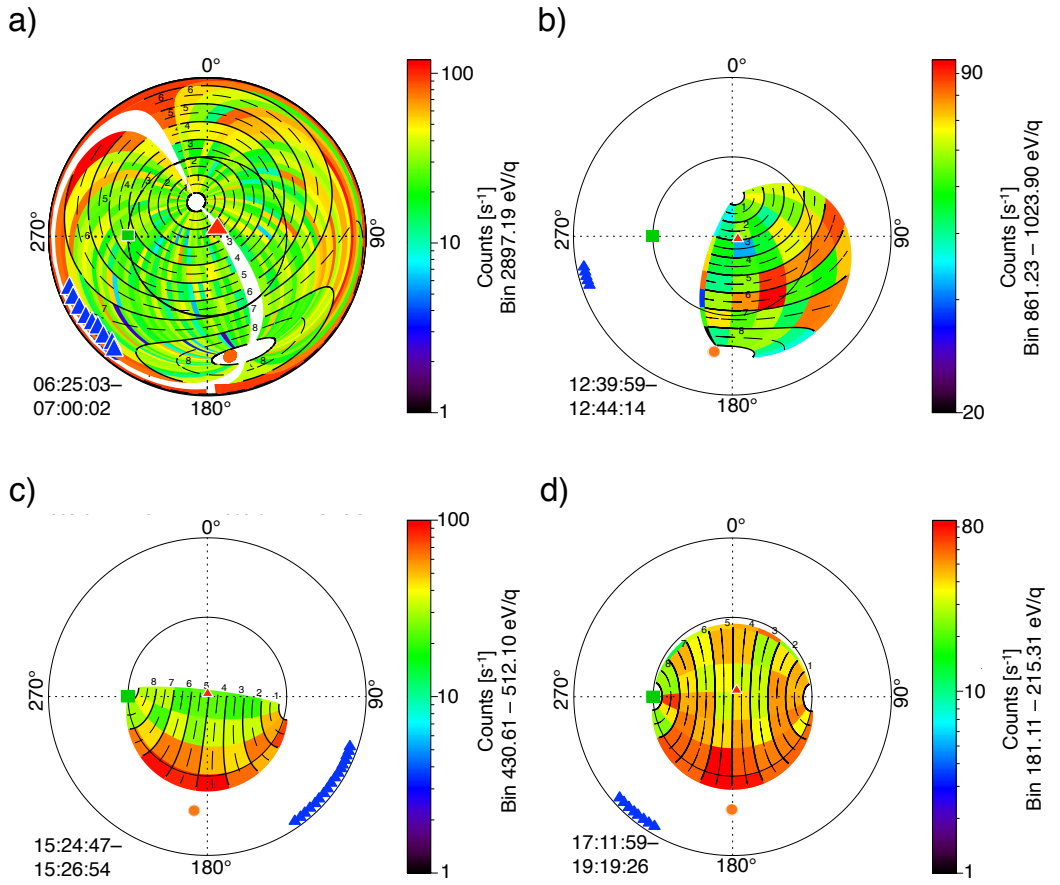

Figure 6.10: Angular distributions of ions at an average energy near the peak count rate at four different times: a) 0625-0700, b) 1240-1244, c) 1525-1527, and d) 1712-1719 UT on 21 January 2009. The centre of the plots correspond to the look direction directly toward Saturn, while the entire outer circle corresponds to the look direction away from Saturn. The dashed circle midway between the centre and the outer edge corresponds to the look direction 90° away from Saturn, with the northward-viewing direction at an azimuth (labels around the outer circle) of 0°. The look direction to see incoming corotation lies on the inner circle at an azimuth of 270°, as indicated by the green square. Flows from 'north' (or above) of the spacecraft would be seen in the upper half of the plots. The sun is represented by the orange dot, and the magnetic field directions are represented by the red and blue triangles.

percentage composition is 25.8±0.2%, which is consistent with a magnetospheric origin where the m/q=2 species is H_2^+. In the cusp the ratio is smaller, 2.62±0.02%, consistent with solar wind values with the m/q=2 species being He^{++} (*Thomsen et al.* 2010).

In addition, angular distribution plots are shown (see Figure 6.10) of the ions at selected energies and times. The angular distributions (in panel a) of the ions in the magnetosphere (06:25-07:00 UT) show they are coming primarily along the field line (blue triangle, in a direction from 'behind' the spacecraft, from the anti-parallel

field direction) from the direction of the sub-solar point. However, the ions in the three cusp panels (b), (c) and (d) are not field-aligned. The ions in the cusp are arriving from the direction of the equatorial plane between 12:45-17:15 UT, with the ions strongly convecting from the direction of the equatorial plane at 15:25-17:15 UT, which is consistent with reconnection occurring at low latitudes, followed by subsequent poleward convection through the cusp. In none of the distributions in Figure 6.10 is there evidence for a peak near the corotation direction, which is in or near the field of view for all except the 12:40-12:44 interval.

6.2.3 Summary

The identification of the region from ∼1100 to almost 1900 as the cusp is supported by three strong pieces of evidence from CAPS observations: 1) As described in greater detail above in Section 6.2.2, composition measurements indicate that the ions are of solar wind origin, with no appreciable water group ions; 2) the electron energy spectra are much more characteristic of typical magnetosheath measurements than of magnetospheric electron spectra; and 3) the ions during this period display energy-latitude and energy-pitch angle dispersions (discussed below) which are typical characteristics of a newly opened field line convecting poleward. Therefore the evidence confirms this is an observation of Saturn's cusp.

6.3 Observations from the 3rd of August 2008 – 'AUG08'

The data obtained from the AUG08 cusp crossing are presented in Figure 6.11. There are two data gaps (in all the presented instruments) occurring at 12:10−12:50 and 16:22−18:03 UT. At the beginning of the AUG08 event, energetic electrons in CAPS-ELS (panel a) and MIMI-LEMMS (panel c) are present until 14:45 UT. The energy distribution of these electrons are similar to those observed in the magnetosphere during the JAN09 event, and so the plasma is interpreted to be on closed magnetospheric field lines. Before entering the cusp (at 14:47) the spacecraft passes through a region where the energy of the electrons is gradually decreasing, and the flux of the ions increases. This is interpreted to be a high latitude extension of the low-latitude boundary layer, which would be a mixed plasma of magnetospheric and solar wind origin.

From 14:47 until 23:30 UT, Cassini passes through the cusp. IMS observes high

fluxes of ions (panel b), which have multiple energy-latitude dispersions. The data from the MIMI-LEMMS instrument (panel c) show high fluxes of energetic ions up until the cusp crossing, with a significant decrease in the first ion dispersion observed, followed by background levels of counts in the rest of the cusp interval. The high fluxes up to the ∼25 eV level in the LEMMS data are due to light contamination of the instrument.

There are four dispersions present in the data; the first is clearly observed at 14:47−16:22 UT. The second and third dispersions are very close together, and are difficult to separate. However the large increase in flux at ∼18:35 UT is designated to be the centre of the second dispersion at 18:15−18:50, with third dispersion occurring at 18:50−20:40. The argument that these are two separate dispersions is supported by the flux measured by ELS as well as in the IMS measurements. The electron flux, as well as the energy, increases at the start of the third dispersion in comparison to the end of the second dispersion. At the same time there is also a step-up in the energy of ions. Both of these observations suggest that these are two separate dispersions. If this was one dispersion, the electron flux would steadily decrease (similarly to the first dispersion) and the ions would also not increase in energy. Instead there is a clear passing of the spacecraft through two separate flux tubes filled with cusp plasma, with two different reconnection histories.

All the dispersions are in the same sense, implying that the reconnection was taking place equatorward of the cusp and is also occurring in a 'bursty' or pulsed manner (*Lockwood et al.* 2001; *Jasinski et al.* 2014) due to the 'stepped' nature of the ion dispersions.

The magnetic field (panels d and e) is strongly radial, and is increasing significantly due to the planetward trajectory of the spacecraft. No diamagnetic depressions are seen during the cusp interval. No rotations are observed on the open−closed field line boundary before the cusp. However, there is a small rotation in the B_ϕ component at ∼15:00 and ∼20:30 UT coincident with the start of the cusp observations as well as the start of the final ion energy-latitude dispersion. For the rotation at 15:00 UT, this could be due to the crossing of the open-closed field line boundary marked by a FAC, whilst for the latter this could be due to the IMF having an increased B_y component, and so the newly reconnected field line has a significant azimuthal component.

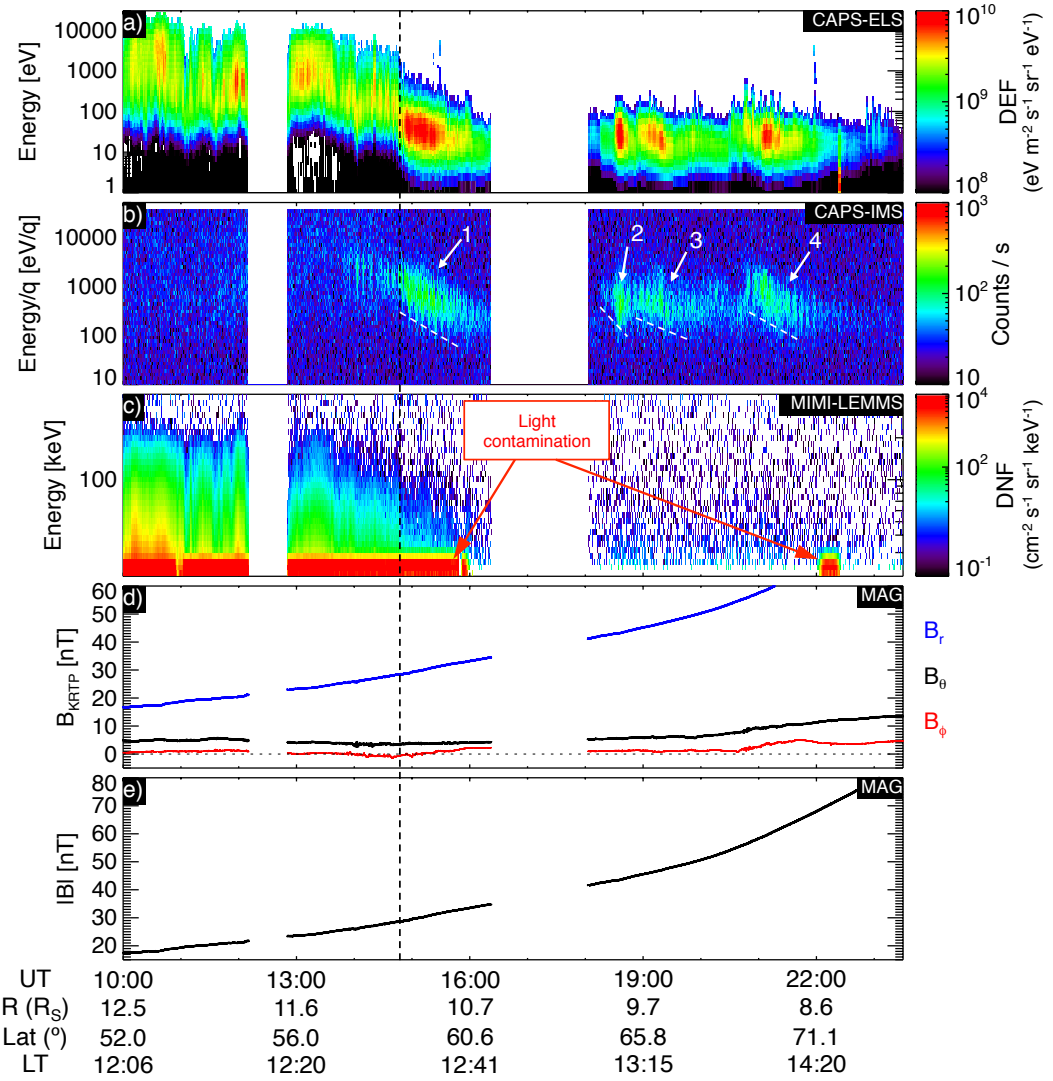

Figure 6.11: Observations from the 3rd of August 2008, with the cusp observed at 14:45–23:45 UT. From top to bottom: a) electrons from CAPS-ELS, b) ions (all anodes summed) from CAPS-IMS, c) high-energy electrons from MIMI-LEMMS (the high fluxes in up to the ∼25eV energy level are due to light contamination of the instrument), d) the three components of the magnetic field in KRTP coordinates from MAG and e) the magnitude of the magnetic field also observed by MAG.

6.3.1 Ion Composition and Angular Distributions

For AUG08 the spacecraft does not roll at all during the cusp observations as for the JAN09 observation described above. There is a small spacecraft attitude adjustment at ∼16:00 UT and two between ∼21:30 and ∼23:30 UT. However this does not provide a complete 4π steradian FOV. The spacecraft does have a look direction into the corotational direction whilst in the boundary layer just prior to the cusp at ∼14:00 UT, as can be seen in Figure 6.12a.

The ion spectrogram in Figure 6.11b is of Anode 5 of IMS. In this figure, the ion counts are at the noise level whilst in the magnetosphere prior to 14:00 UT, with only occasional observations of counts above this level. An example of a period where there is an increase above this level is shown in the OAS plot in Figure 6.12a. During this observation, anode 5 (and all the other anodes) observe background levels of counts. Anode 7 observes a slight increase in flux when it is directed to look into the direction of incoming corotational ions.

The composition of the adjacent magnetospheric plasma is estimated at 05:26−07:34 UT, the closest time with large counts above the noise level. During this time period, CAPS-IMS completes four TOF measurements; the W^+/H^+ percentage was calculated to be 32.6±1.2% and the $[m/q=2]/H^+$ was calculated to be 28.2±0.1%, the latter assumed to be H_2^+ as previously explained.

In comparison, the water group and the [m/q=2] ions observed in the cusp are much lower, as expected, with the latter ions assumed to be He^{++}, representative of a solar wind abundance. For the four cusp dispersions observed at 14:47−16:06 UT, 18:00−19:30 UT (the second and third dispersions have been binned together due

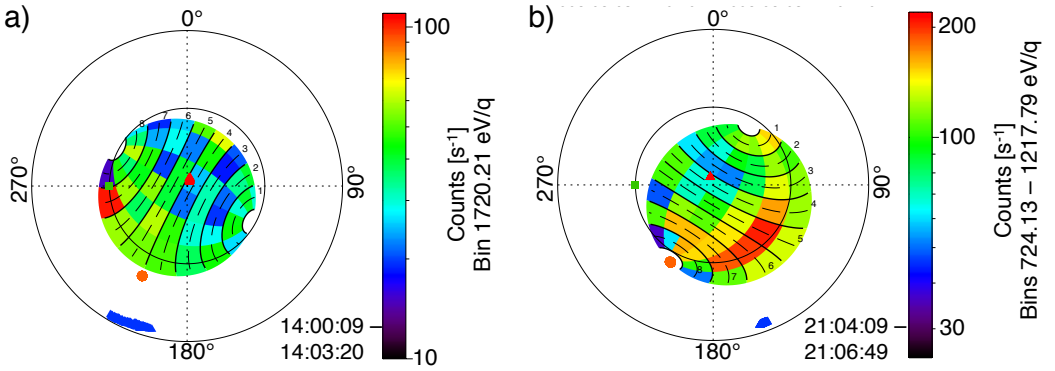

Figure 6.12: Angular distributions of the ions just prior to the cusp observation on the 3rd of August 2008 (left), and during the cusp observation (right). The format is the same as seen in Figure 6.10b−d.

to overlapping accumulation times) and 20:47−22:04 UT, the values for He^{++}/H^{+} were 4.2±0.03%, 2.4±0.03% and 2.2±0.03%, respectively. For the water group ions the counts were below the background level for the second dispersion, and had values of 0.97±0.04% and 0.67±0.07% for the first and last dispersions respectively.

An example of the look direction whilst in the magnetosphere (prior to the cusp) was already presented (Figure 6.12a). An example of the FOV of CAPS-IMS during the cusp observations can be seen in Figure 6.12b. In this example the FOV does not directly observe the corotational direction; however the counts in the direction nearest to it are at the noise level, with the majority of the (observable) flux of ions observed from a direction 'below' the spacecraft (mostly equatorward), convecting in a poleward direction. This is similar to the JAN09 event.

6.4 Calculating the field-aligned distance to the reconnection site

An example of the appearance of the ion energy-pitch angle dispersion in the energy-time spectrogram during the AUG08 event can be seen in the top panel of Figure 6.13 (IMS observations from anode 5). The bottom panel shows the corresponding pitch angle observed by anode 5 as the instrument actuates. It can be seen that as anode 5 observes lower pitch angles, the energy of the ions increases. This causes an 'M' shaped signature in the ion data in the northern hemisphere. This is the same as the first terrestrial observations reported in *Burch et al.* (1982); however they observed a 'V' signature due to the pitch angle changing from 0° to 180° (also in the northern hemisphere). The observations (in Figure 6.13) at Saturn are inverted due to the oppositely orientated magnetic poles at Saturn which results in the 'V' signature to be upside down for these observations. The upside down 'V' becomes an upside down 'W' signature because the pitch angle look direction during these observations is from 0° to an alternating amplitude of 70° and 120°. Therefore, the instrument observes ions with pitch angles of 0° twice for every time 120° is observed. This results in an 'M' shaped signature. Observations in the southern hemisphere at Saturn would show a 'W' signature with the same pitch angle coverage. The energy-latitude dispersion can also be seen in Figure 6.13, with the peak (at 0° pitch angles) and minimum (at 120° pitch angles in this observation) energies decreasing with time and latitude.

From these energy pitch-angle dispersions and also using the BUR82 method described in Chapter 5.2, the distance to the reconnection site is determined for both cusp observations. Examples of the dispersions observed after a full actuation of the instrument can be seen for both days in Figure 6.14. The low-energy ion cutoffs (dots) are marked with corresponding error bars propagated using the energy resolution of the instrument. From this cutoff the model has been fitted, with the result printed on the plot in units of Saturn radii (R_S).

During the observation of an energy-latitude dispersion, all of the plasma is assumed to be injected on the same magnetic field line at a similar location at the magnetopause. Therefore the energy-pitch angle dispersions (for each actuator sweep) would result in similar field aligned distance for the location of the reconnection during a single energy-latitude dispersion. Therefore, the JAN09 data were divided into five intervals due to the presence of the five clear energy-latitude dispersions (underlined in Figure 6.4). As can be seen in Figure 6.13, the ion counts

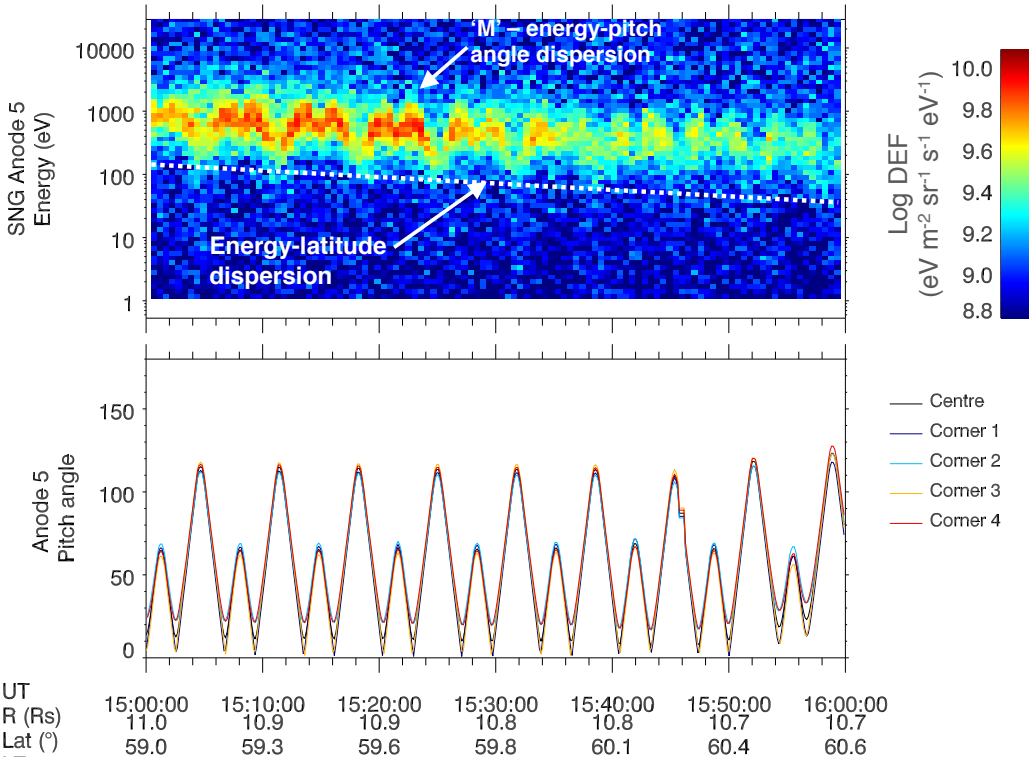

Figure 6.13: Energy-time spectrogram displaying the energy-pitch angle dispersion in the data during the AUG08 event. Top panel: CAPS-IMS ion observations from anode 5; bottom panel: the corresponding pitch angle observed by anode 5 as the instrument actuates. The baffle through which the ions enter to be detected by the instrument's anodes represents a rectangular surface. Therefore the pitch-angle of each corner of the anode's 'view' as well as the pitch-angle of the centre is shown in the bottom panel.

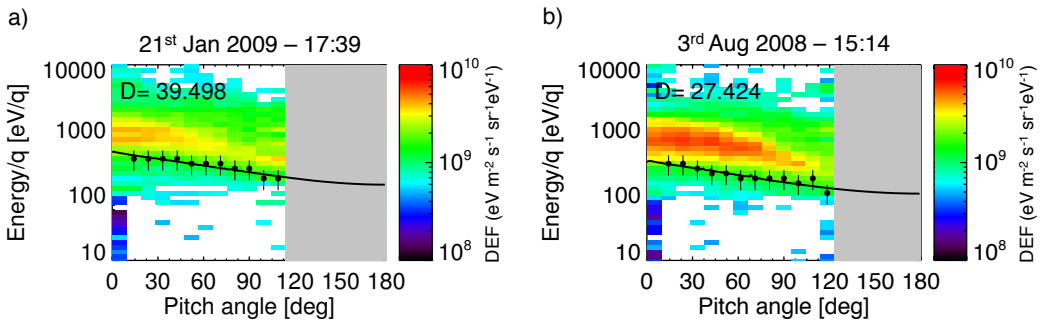

Figure 6.14: Examples of an ion pitch angle dispersion observed by IMS for the (a) JAN09 and (b) AUG08 events. Also shown is the modelled curve created using the BUR82 method, which estimates the distance (D) to the reconnection site in R_S.

decrease with spacecraft time from the start of the energy-latitude dispersion, and so the observed pitch-angle dispersions become less clear. For AUG08 the data were binned into four intervals, however due to the lack of clear energy-pitch angle dispersion or an unsuccessful fitting of the BUR82 model (or a combination of the the two) there are no results for the last two bins, and only two model fits for the second bin. Table 6.2 shows the results of the binned field-aligned reconnection distances. The errors on the average $\Delta\bar{x}$ were calculated using the following error propagation equation:

$$\Delta\bar{x} = \sqrt{\frac{1}{n^2}\sum_{i=1}^{n}\Delta x_i^2} \tag{6.3}$$

where Δx_i are the individual errors on results which are then binned (n is the number of results in a bin). The standard deviation shows how much variation there is from the mean (i.e the scatter), for bins with more than two results. A full table of all the individual results is shown in Appendix A.

6.5 Summary, Discussion and Conclusions

For the JAN09 event, the overall plasma observations show that Cassini observed high energy tenuous plasma in the magnetosphere. As the spacecraft travelled to higher latitudes, it passed through field-aligned currents. The magnetic signature of the current was observed in the B_ϕ component of the magnetic field, as rotations whilst travelling poleward and planetward. Whistler like emission was observed in the RPWS instrument; emission previously shown to occur with FACs. The particle data show enhancements in electron flux (in the appropriate directions)

Table 6.2: The field-aligned distances from Cassini to the site of reconnection calculated from ion pitch angle-energy dispersions for the JAN09 and AUG08 observations. The second and third dispersions for AUG08 have been binned together. The mean distances are shown with their propagated standard errors, as well as the standard deviation from the mean.

21st Jan 2009		
Time (UT)	Mean Distance (R_S)	Standard Deviation (R_S)
11:00-11:50	27 ± 5	8
11:50-12:45	39 ± 7	7
12:45-15:00	49 ± 6	6
15:00-17:00	51 ± 2	5
17:00-18:00	46 ± 4	10

3rd Aug 2008		
Time (UT)	Mean Distance (R_S)	Standard Deviation (R_S)
14:47 – 16:06	32 ± 7	3
18:39 – 18:49	26 ± 8	–
18:50 – 19:30	–	–
20:47 – 22:04	–	–

intermittently for the four FACs in ELS, every time for the first three in INCA (when the FOV of the instruments is conducive for these observations) and no enhancements in the final FAC. These currents are interpreted to lie on the open-closed field line boundary. The study investigating the location of the open-closed boundary reported by *Jinks et al.* (2014) found it to lie between an ionospheric colatitude of 10° (from plasma data) and 12° (from RPWS data) during the orbit that the AUG08 observation takes place. Using a dipole approximation, the value for the invariant colatitude at the point from when the spacecraft enters the cusp was found to be ∼9°. The authors do not investigate the JAN09 event's orbit, however the invariant colatitude of the FACs were found to be ∼11°; this is lower than the average of 13.3° that *Jinks et al.* (2014) found in the northern hemisphere, but similar to the AUG08 event.

The observations of the two FACs in the equatorward part of the cusp are interpreted to represent layers that moved towards and away from the spacecraft without completely passing over it. This means that the spacecraft observed the FAC magnetic signature without fully traversing it (and therefore did not observe the corresponding particles). For the AUG08 event, the spacecraft also passed through the magnetosphere directly into the cusp, with no FACs observed on the

open-closed field line boundary.

Evidence that reconnection was occurring from auroral observations has already been reported for the JAN09 observations. *Radioti et al.* (2013) suggested that the consecutive brightenings of the auroral bifurcations are due to multiple reconnection along the same magnetic flux tube. From the available IMS data it is not possible to infer whether this is happening during these observations; however the conclusion is that both the in situ data and the UVIS observations confirm dayside reconnection is occurring on this day.

Whilst in the cusp (for both days of observation), IMS observed ion energy-latitude dispersions: consistent with the effect of magnetopause reconnection and poleward convection of open field lines. There also could be a possible azimuthal component to the dispersion due to the subcorotating field lines, however this is not investigated in this report. The ion compositions from time-of-flight observations by IMS show that the water group ion abundance are extremely low, with background levels of counts observed for the majority of the time. In comparison to the magnetosphere (as a percentage of the H^+ counts) the water group ion fluxes are found to be up to six times lower than in the magnetosphere for JAN09, and up to fifty times less for AUG08.

The m/q=2 ions in the cusp are suggested to be He^{++} and not H_2^+, as they are found to be significantly lower in abundance compared to the magnetosphere, with similar values to those found in the solar wind. The m/q=2 ions in the magnetosphere are assumed to be H_2^+. The angular distributions of the ions in the cusp show that they are observed when the look direction of the instrument includes the direction below the spacecraft (equatorward, and perpendicular to the planetward direction), which is consistent with poleward convection of a newly opened magnetospheric field line.

The changes in the plasma regime whilst in the cusp, as well as 'step-like' energy-latitude dispersions in the ion observations suggest that reconnection is pulsed at the magnetopause, and not steady (*Lockwood and Smith* 1994). Examples of cusp ion steps at the terrestrial cusp are presented in Figure 6.15 (*Lockwood et al.* 2001; *Farrugia et al.* 1998). The JAN09 and AUG08 observations are much more similar to the observations in panel a. The steps in the observations from panel a) are abrupt due to the large variations (falling to almost zero) in the reconnection

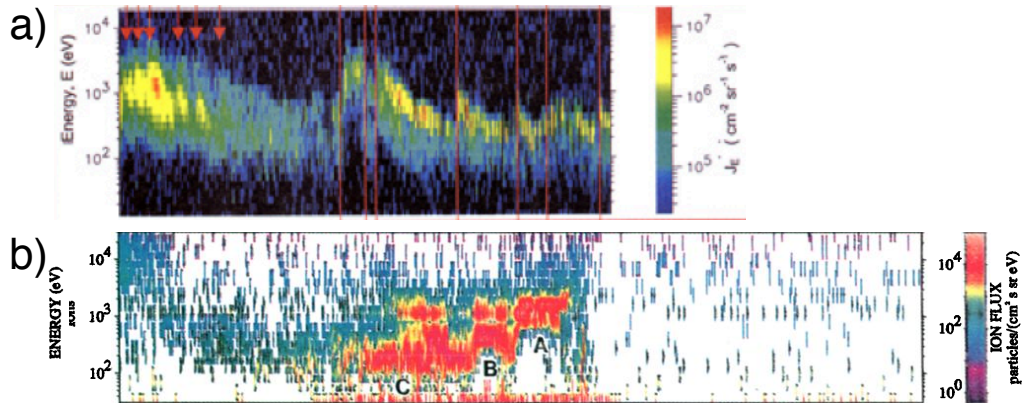

Figure 6.15: Adapted examples of terrestrial stepped ion energy latitude dispersions from: a) *Lockwood et al.* (2001) and b) *Farrugia et al.* (1998).

rate. The observations presented in panel b) show steps which have 'ramps' between them, making them less abrupt. This is due to the reconnection rate not varying significantly between the ion enhancements. The dispersions are also less clear in the latter observation due to the spacecraft having a larger longitudinal component to its trajectory. This comparison suggests the reconnection was pulsed at Saturn during the cusp observations, with reconnection slowing in between the 'bursts'.

Also observed are ion energy pitch-angle dispersions, which have been used to calculate the varying field-aligned distance to the reconnection site. The reconnection distance values for both days examined in this chapter share similar values. The distances are consistent with reconnection sites occurring near the subsolar region and slightly towards the north for the earlier JAN09 bins and for the AUG08 event, which is in agreement with the findings of *Desroche et al.* (2013) (reconnection sites poleward of the subsolar region). In contrast, for the later JAN09 bins the locations of the reconnection site are consistent with a position southward of the subsolar point. The calculations for the different bins for the JAN09 show that the reconnection location during the cusp observation moves southward from a northern position on the magnetopasue, passing near the subsolar point and ending in a southern position. The results indicate that while reconnection is occurring along the magnetopause, it is probably not occurring in a steady manner.

The trajectory for AUG08 explores a greater region of local time in comparison to JAN09, and so the observations show that the cusp is spread in local time. Therefore the energy-time dispersions for AUG08 are more likely to contain an element

of azimuthal dispersion as the open field line sub-corotates with the planet, as well as the usual poleward dispersion associated with analogous events at Earth. The Earth's cusp can also be spread in local time when there is a strong B_y component of the IMF however, without accurate solar wind data at Saturn, this cannot be further investigated. For the JAN09 event, where a subsolar reconnection site is predicted, it is much more likely that an azimuthal convection at Saturn, due to the sub-corotation of the field line, is the cause. If the IMF has a large B_y component, then reconnection will most likely be suppressed (*Masters et al.* 2012), at the subsolar point. Reconnection will most likely occur when there are large local shear angles (so a small B_y component), decreasing the likelihood that the azimuthal motion is due to the IMF B_y. However as the magnetosheath magnetic field is draped along the magnetopause, reconnection could occur away from the subsolar point where the IMF field has a B_y component, and therefore azimuthal motion of the cusp could be occuring similarly to Earth observations. *Badman et al.* (2013) have previously reported reconnection occurring with the IMF having a B_y component.

Multiple ion energy-latitude dispersions are likely due to temporal variations, as studied previously at Earth. As changes in the electron flux and energy at the edges of the dispersions are observed, as well as a change in the plasma composition, this is interpreted to not be a spatial feature (i.e. the 'wobbling' of the cusp over the spacecraft). If this was the case, one would expect a similar observation to that which is shown in Figure 2.7, where there is a normal followed by a reverse-sense dispersion. Instead, a step-up in the ion energy-latitude dispersions is observed, as well as increases in the energy flux, showing that the spacecraft is passing through cusp plasma with different reconnection histories.

In conclusion, Cassini did cross the Kronian cusp, and this is the first such analysis presented at Saturn. The characteristics of the cusp at Saturn are very similar to the terrestrial cusp, with the presence of two types of dispersions: energy-latitude and energy-pitch angle. The observations on the different days are very similar. The plasma observations are not continuous, with many changes in the energy and flux which are matched with the ion energy-latitude dispersions, showing that these observations occurred during very active reconnection events. Both days' observations begin in the magnetosphere and transition into the cusp followed by the polar cap. At Earth the cusp has been observed more intermittently between layers

of the magnetosphere or separately within the polar cap. These two observations at Saturn show that the cusp might be a more defined layer directly between the magnetosphere and polar cap, which is not unreasonable due to generally lower reconnection rate values at Saturn. The duration of the cusp crossing was large in comparison to Earth (hours as opposed to tens of minutes at Earth; e.g., *Pitout et al.* 2009)]. The spacecraft velocity during the JAN09 and AUG08 events was ∼6 km s^{-1} and ∼9 km s^{-1} with observation durations of approximately 8 and 7 hours, respectively. The velocity of the Cluster (C1) spacecraft in the example shown in Figure 2.4, is ∼4.5 km s^{-1} with an observation duration of 0.5 hours. Therefore the duration of the observation (to a first approximation) is due to the cusp being significantly larger at Saturn, rather than a difference in spacecraft velocity. This study also confirms that, although it has been previously reported that magnetic reconnection at Saturn is suppressed (*Masters et al.* 2012), there are instances when reconnection does occur, and its effects can be observed in the manifestation of solar wind plasma entering into the magnetosphere via the cusp.

Chapter 7

Survey of differing Cusp Observations at Saturn

This chapter presents a survey of the different types of cusp observations made by Cassini between 2007 and 2013. Nine events are discussed and presented in four different groups: southern summer, isolated cusp, tenuous plasma, and northern summer. The data from one example case study is discussed in detail from each group, with the full data from the other cusps displayed in Appendix B. Also presented are propagated upstream solar wind conditions in Section 7.6. The trajectory and location of the cusps are presented in Section 7.7.

7.1 Southern 'Summer' 2007 Cusp

This section discusses three observations made in early 2007 and are the only instances where the cusp is traversed in the southern hemisphere. Two of the events involve observing the cusp twice with a temporal separation of approximately Saturn's rotational period of ∼10.7 hours. These occurred on the 16th of January (from now on known as 'JAN07'), and the 1st−2nd of February ('FEB07'). These observations will be published in a paper (*Arridge et al.,* in prep.) which is currently in preparation (at the time of writing of this thesis). Any work not done by myself from this paper will be explicitly specified (and can be found as part of the brief discussion in Section 7.1.2 [found on page 157], and the reconnection distances calculated for JAN07 and FEB07 can be found in Table 7.1 [on page 169]). Otherwise the work has been my own.

In this thesis, the individual cusps from each of these days will be labelled with

suffixes of 'a' and 'b' in order to distinguish between the two when necessary. The final observation occurred on the 8th of March ('MAR07') and was of a solitary cusp. The trajectory for all the events occurs with the spacecraft travelling equatorward, duskward (crossing near-noon) and anti-planetward.

7.1.1 Overview of an example case study – FEB07

The two days of data presented in Figure 7.1 are probably one of the most interesting sets of observations made by Cassini in the high-latitude magnetosphere, due to the variety of different boundary crossings that occur, with the spacecraft travelling all the way from the polar cap into the solar wind within $\sim$17R_S. The different boundaries are separated by dashed lines, and the different regions are labelled at the top.

Figure 7.1 starts at 12:00 on the 1st of February, and ends at 24:00 UT on the 2nd of February. At the start of the event background levels of electrons and ions are observed in ELS, IMS and LEMMS, which is interpreted to be the spacecraft traversing field lines connected to the polar cap, where no plasma above the detectability threshold of the instruments is observed. At $\sim$15:30 UT the spacecraft enters the cusp (FEB07−a), where plasma with low energies and a high density is present (LEMMS still only observes noise in panel c). An ion energy−latitude dispersion is observed; it is orientated in the opposite direction to the examples shown in the previous chapter, due to the spacecraft travelling equatorward and not poleward, and therefore causing the low energy ions to be observed first. The compositional analysis of the ions reveals that the W^+ species are one or two counts above the background level during this time, and therefore the signal-to-noise ratio is low. As discussed in the previous chapter, due to the low ratio (to H^+) of the m/q=2 ions, this species is interpreted to be He^{++}, and its abundance as a percentage of H^+ is found to be 1.9$\pm$0.04%.

The magnetic field magnitude is observed to decrease (panel e) upon entering the cusp reaching a maximum drop of $\sim$4 nT at 17:50 UT (marked by a blue arrow labelled 'depression'). The drop in magnitude is greater than the overall gradual decrease of the field strength due to the anti-planetward trajectory of the spacecraft. This diamagnetic depression is a characteristic observation at the terrestrial cusp. Upon leaving the cusp and entering the magnetosphere at 18:52 UT, the magnetic field strength does not increase sharply, but instead more gradually, with

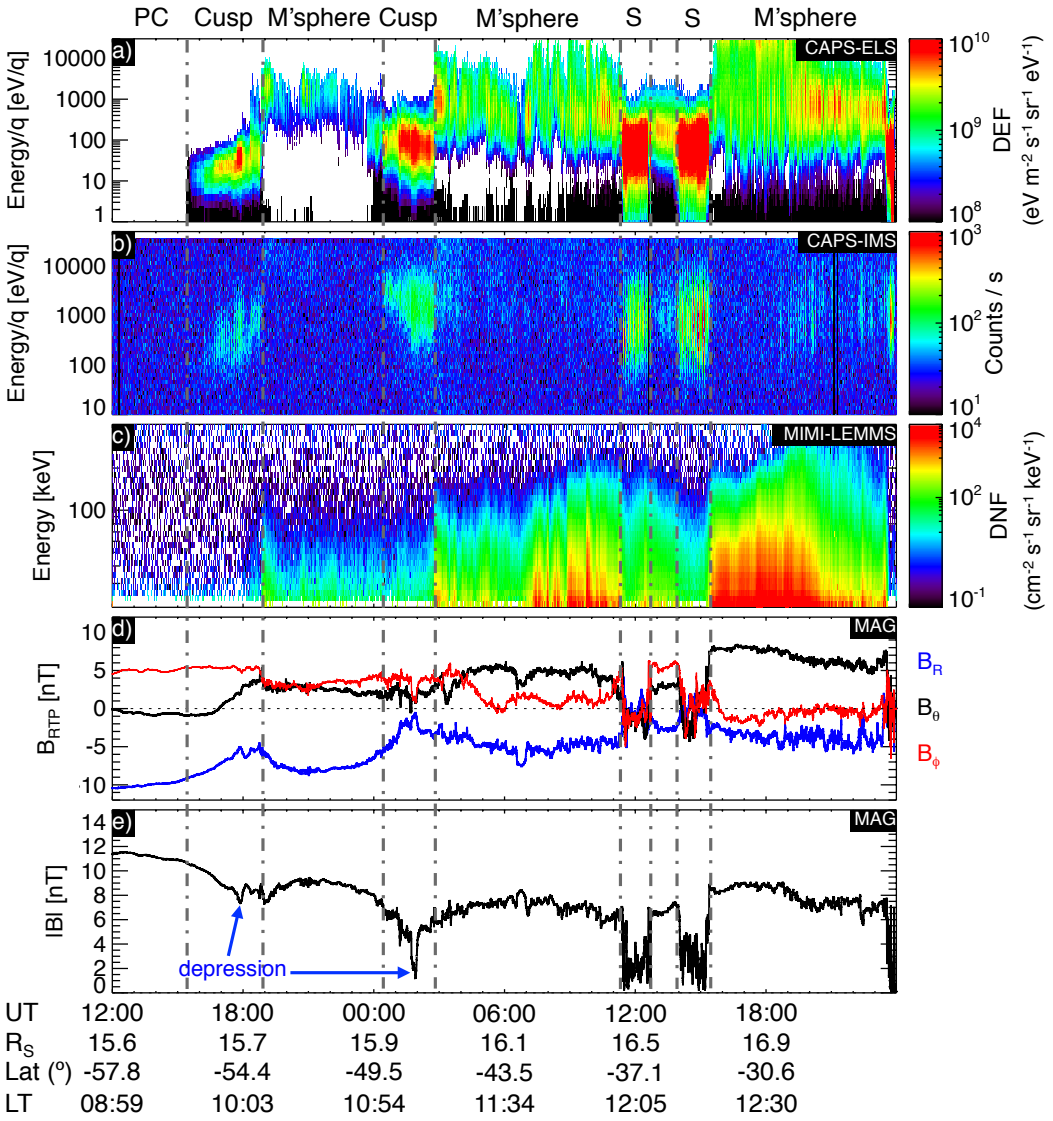

Figure 7.1: Cassini data presented for the 1st and 2nd of February 2007 observations. The figure starts at 12:00 UT on the 1st and ends at 24:00 UT on the 2nd. The data are shown in the following order: a) CAPS-ELS electron spectrogram (all anodes averaged), b) CAPS-IMS ion spectrogram from anode 5, c) MIMI-LEMMS high energy electron spectrogram, d) the three components of the magnetic field in KRTP coordinates from MAG and e) the magnetic field magnitude from MAG. The polar cap is labelled as 'PC', the magnetosphere as 'M'sphere' and the magnetosheath as 'S'. The bow shock is crossed approximately 15 minutes before the end of the plot, however a dashed line has not been drawn as it would be bordering the edge of the figure.

the complete depression not centred on the centre of the cusp interval. A narrow boundary layer is observed just before entering the magnetosphere where we see a small increase in flux of energetic electrons in LEMMS from 18:20 UT, as well as a gradual increase in energy of the observed electrons in ELS (just prior to the second grey dashed vertical line).

Cassini is in the magnetosphere where observations of higher energy electrons are observed in LEMMS and ELS. In the magnetosphere the large ratio (to H^+) of the m/q=2 ions leads to its interpretation as H_2^+ (it was interpreted to be He^{++} in the cusp), and has a percentage (of H^+) of 9.0±0.3%. Before entering the cusp a second time, the spacecraft crosses another boundary layer where lower energy electrons (compared to the magnetosphere, but higher than the cusp) are observed for twenty minutes (this can be seen just before the third grey dashed vertical line). At ∼00:25 UT (now the 2nd of February), the spacecraft enters the cusp once again (FEB07−b). The ions display a 'reverse sense' energy-latitude dispersion. The ion composition shows a larger ratio (than the first cusp) for He^{++} (m/q=2) to H^+, which is 4.7±0.02%. Lower fluxes of high energy electrons are still observed in LEMMS (c), implying there is some mixing of plasma from the magnetosphere in the cusp. Another diamagnetic depression is observed with a decrease from ∼8 to 1 nT observed, which is much stronger than that observed at FEB07−a.

The spacecraft re-enters the magnetosphere at 02:46 UT where no boundary layer is observed such as the one for FEB07-a. The spacecraft remains in the magnetosphere until 11:26 UT where it crosses the magnetopause and enters the magnetosheath (labelled 'S' in Figure 7.1), where there is a significant drop in the magnetic field strength as well as a rotation. A further five magnetopause crossings occur at 12:36 (inward), 12:40 (outward), 12:42 (inward), ∼14:00 (outward) and 15:23 UT (inward), with the magnetosheath and magnetosphere observed in between the boundary crossings. A comparison of the cusp and magnetosheath plasma in this figure shows the similarity in the density and energy between the two regions, which is unsurprising as the the latter is the source for the former (assuming that the cusp plasma was injected from a similar region in the magnetosheath, i.e. near the subsolar point).

Analysis of the first magnetopause crossing is presented in Figure 7.2. During this magnetopause crossing the plasma β is calculated on either side of the magne-

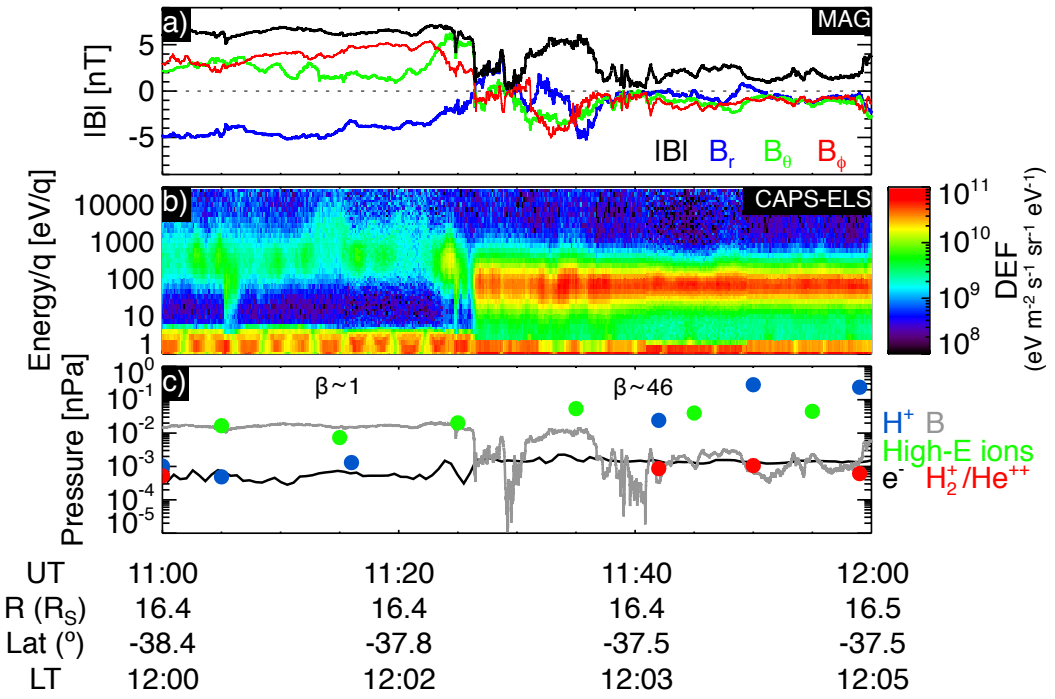

Figure 7.2: The first magnetopause crossing during the FEB07 event is presented in the following order: a) the components and magnitude of the magnetic field, b) electron spectrogram from anode 5 of ELS and c) the magnetic pressure and the components of the plasma pressure used to calculate the plasma beta (β) on either side of the magnetopause current layer.

topause current layer. The magnetopause current layer is observed between 11:26:16 and 11:26:29 UT. To calculate the total plasma pressure, the pressure moments from ELS and IMS (*Lewis et al.* 2010; *Thomsen et al.* 2010) are taken for the low energy particles as well as particle pressures from the MIMI instrument for the high-energy particle population (the pressure calculation for the MIMI bin centred at 11:24 is not used as it overlaps the magnetopause). The IMS produces pressure moments for three groups of species: H^+, H_2^+/He^{++}, and W^+. Averages of 1, 5, 10 and 15 minutes are taken from the MAG, ELS, MIMI and IMS data respectively. There were no reliable water group moments available for this analysis, and the only available H_2^+/He^{++} pressure moment before the magnetopause crossing is at 12:00 UT, which is used here (but its not within the 15 minutes average). This would lead to a slight underestimation of the plasma β value. From the results, the magnetosphere has a plasma-β value of $\sim$1, which is below the average ($\sim$2) found in the survey reported by (*Masters et al.* 2012). The value found in the magnetosheath is significantly higher at $\beta\sim$46, and is found in the upper limit of the median values found at Saturn's magnetosheath (*Masters et al.* 2012). The magnetic shear across the

boundary was found to be ∼150°, which would most likely result in reconnection to be suppressed locally (with the observed values of plasma β). Of course these values are not directly associated with the cusp observations. The location where reconnection took place to inject the plasma would have been present along the magnetopause with slightly different local conditions in comparison. However if the magnetosheath β value was similar at the reconnection site for the cusp plasma entry to the magnetopause crossing analysed here (which is not an unfair assumption due to the increase in Alfvénic Mach number during this event [see Section 7.6]), then the magnetic shear must have been near anti-parallel when the plasma was injected into the cusp.

Cassini remains in the magnetosphere until 23:32 UT. Between ∼ 20:00 until 23:00 UT, bursts of high energy electron flux are seen with a period of approximately one hour. These bursts are similar to those reported by (*Mitchell et al.* 2009; *Badman et al.* 2012a; *Roussos et al.* 2015). The magnetosheath is observed once again until 23:54 UT, where the spacecraft crosses the bow shock and enters the solar wind.

This is a very interesting day that shows that the magnetosphere is being very severely compressed, with the solar wind observed at 17 R_S and a magnetosphere-to-solar wind crossing of only 25 minutes. Observations an hour later at the next bow shock crossing show electrons accelerated to relativistic speeds (*Masters et al.* 2013).

7.1.2 Summary of other observations – JAN07 & MAR07

Both the JAN07 and MAR07 events occur in the southern hemisphere, and both follow the same order of observations; the spacecraft starts in the polar cap, and travelling equatorward crosses through the cusp and into the magnetosphere. However, similar to the FEB07 observations, the JAN07 event observes the cusp twice, this time with a separation of ∼7 hours.

In the first cusp observation (JAN07-a, shown in Appendix B), the water group ion counts are only slightly above the background, and just like in the previous examples the plasma composition is largely dominated by He^{++}([m/q=2]/H^+ of 1.78±0.03%). There is a brief transition from the cusp to the magnetosphere via a boundary layer of electrons with slightly higher energies. A small magnetic field depression is observed, with the minima centred on the boundary layer, and contin-

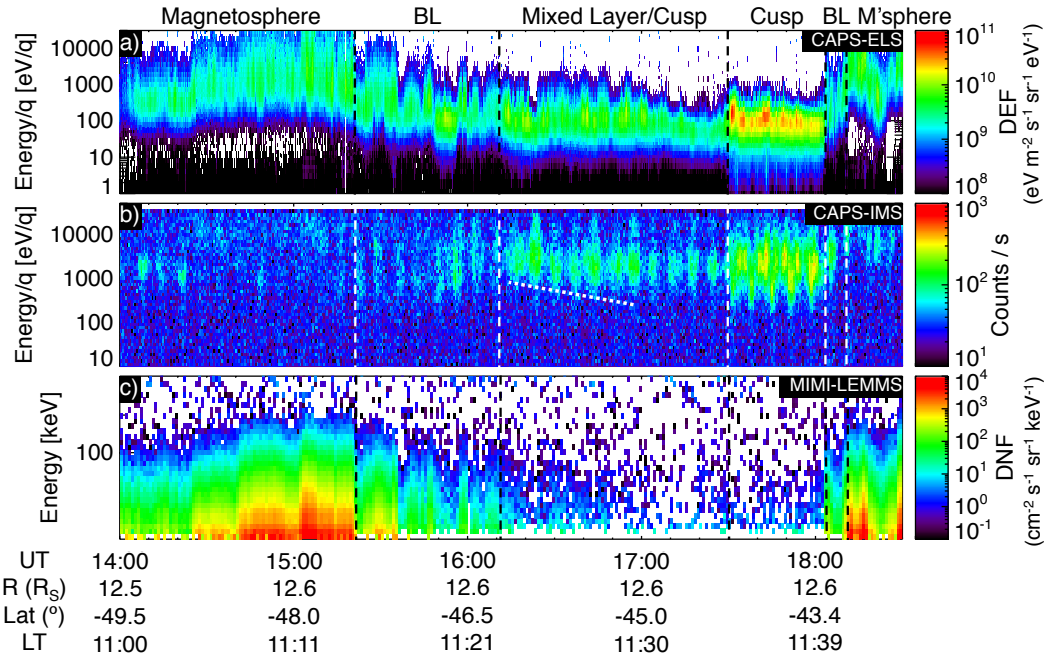

Figure 7.3: A higher time resolution figure focusing on the cusp boundary layer observed for the JAN07-b event. Particle observations are presented in panel a) electrons from CAPS-ELS data, (b) ions from IMS data and (c) energetic electrons from MIMI-LEMMS data.

uing into the magnetosphere for a short period of time. This is very similar to the FEB07-a diamagnetic depression observation, but shallower.

Whilst in the magnetosphere the water group has an abundance (as a percentage of H^+) of 3.5±0.24 and the [m/q=2] ions are interpreted to be H_2^+ due to the high percentages of H^+ of 10.3±0.1. Before entering the cusp a second time, the spacecraft observes the longest in duration boundary layer of all the observations, spanning ∼1 hour, see Figure 7.3 (labelled 'BL' in the figure). The boundary layer can be seen as a gradual decrease in energy of electrons in both the ELS and LEMMS instruments, as well as an increase in flux of ions when entering the cusp. The spacecraft then enters the cusp (labelled 'Mixed Layer/Cusp' in the figure) at ∼16:10 UT. This region has a lower percentage of [m/q=2] ions (as % of H^+) than the magnetosphere, but higher than the cusp, 6.8±0.1%. This is interpreted to be a mixed layer of both solar wind He^{++} and magnetospheric H_2^+ (hence the label as a mixed layer/cusp). This is supported by the angular distributions of the ions (Figure 7.4), which show the ions to be observed from a direction of both the subsolar point and corotation. The W^+ ions are also similar in percentage (of H^+) to the magnetosphere with 3.9±0.2%. There is also an energy-latitude dispersion observed in the 'mixed layer-cusp' (underlined in the Figure 7.3b), as well as a magnetic field

depression (shown in Figure B.1).

The entry into this mixed layer is marked by the increase in the electron and ion densities. The plasma is slightly higher in energy than the next region labelled 'cusp', and higher density than the magnetosphere, however no high energy electrons are observed above the background level in LEMMS. The lack of energetic electrons as well as the large increase in ion density (and composition) also supports this to be the cusp and not a boundary layer or the magnetosphere. Large counts of W^+ ions suggest that during these observations plasma of both solar wind and magnetospheric origin (which were energised at the reconnection site and injected through the cusp) are observed.

Whilst in the 'cusp' (labelled in Figure 7.3) there is a very large increase in flux of ions and low energy electrons. There is a strong diamagnetic depression (shown in Figure B.1 of the appendices), with a global decrease in the magnetic field as well as two very intense acute depressions. Upon re-entering the magnetosphere, the spacecraft passes through another boundary layer for ~5 minutes, where a gradual increase is observed in the energy of the electrons in ELS and increased fluxes in LEMMS.

Therefore the JAN07-b cusp is characterised by two different plasma regions. This is similar to the different regions observed in the JAN09 and AUG08 events (discussed in the previous chapter), where multiple dispersions were seen, except here the differences in plasma density and energy are more pronounced. Instead of stepped ion-energy latitude dispersion there is a 'step up' in the density of the

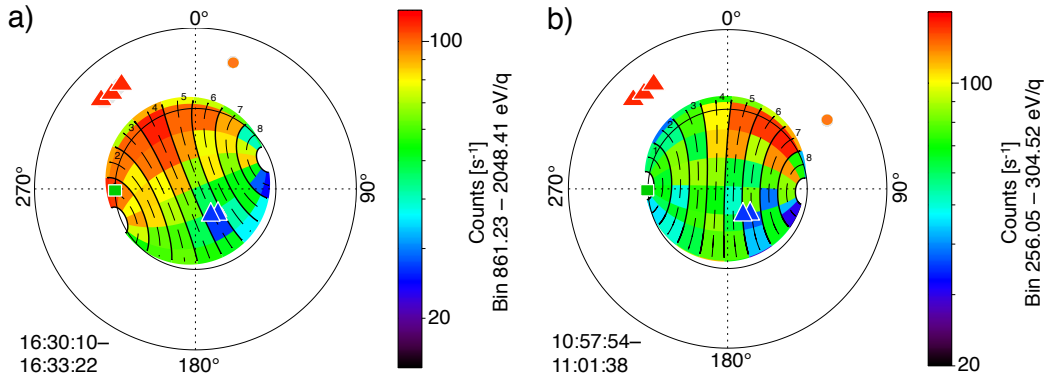

Figure 7.4: The angular distributions of the ions during the mixed layer of the JAN07-b event at 16:30 UT, and the JAN07-a cusp at 11:00 UT. The spacecraft is in the southern hemisphere, just before noon (~11:00) LT.

ions (a step-up in the maximum energy of the ions is also observed). This would imply that (like the previous examples) the spacecraft is crossing field lines which have a different reconnection history. Unlike the previous examples where the effect is partly due to the difference in the field line convection and spacecraft velocities, the step in this example is more likely due to a different location of magnetopause reconnection with different local conditions as supported by the large change in plasma parameters.

The observation of the cusp twice with large time separations has been interpreted to be due to the oscillation of the cusp (*Arridge et al.,* in prep.). The auroral oval has been shown to oscillate with a period near Saturn's rotational period (*Nichols et al.* 2008, 2010), and is produced from particles precipitating from field aligned currents due to the rotational shear between open and outer closed field lines (*Bunce et al.* 2008b). Therefore if the oval oscillates then one would expect the ionospheric location of the cusp (which is just poleward of the open-closed field line boundary) to also be observed to oscillate if the trajectory of the spacecraft is suitable (the analysis for this result was done by C. S. Arridge for the paper in preparation). It has also been shown that the southern polar cap boundary is controlled by the southern planetary period oscillation phase (*Jinks et al.* 2014) but not for the northern polar cap. However *Bunce et al.* (2014) have shown that the northern auroral oval also oscillates, and therefore this would imply that the northern cusp may also oscillate. This may not be observed in the JAN09 and AUG08 observations because the trajectory of the spacecraft was not conducive to such an event occurring. However, this has not been quantitatively examined in this thesis.

If the 'cusp oscillation' interpretation is correct then this would explain the 'reverse-sense' dispersion observed in JAN07-b and FEB07-b to actually be a normal-sense dispersion observed in reverse as the cusp oscillates back over the spacecraft (and not a signature of lobe reconnection). This scenario will now be explained.

The ion energy-latitude dispersion in the JAN07-b event (Figure 7.3) is in the opposite direction of the JAN07-a cusp. Normally this would be understood to be a change in the location of the reconnection site from a subsolar position to a lobe location. However with an oscillating cusp (and an auroral oval), this is no longer a definite conclusion.By looking at the direction arrival of the ions, the meaning of the

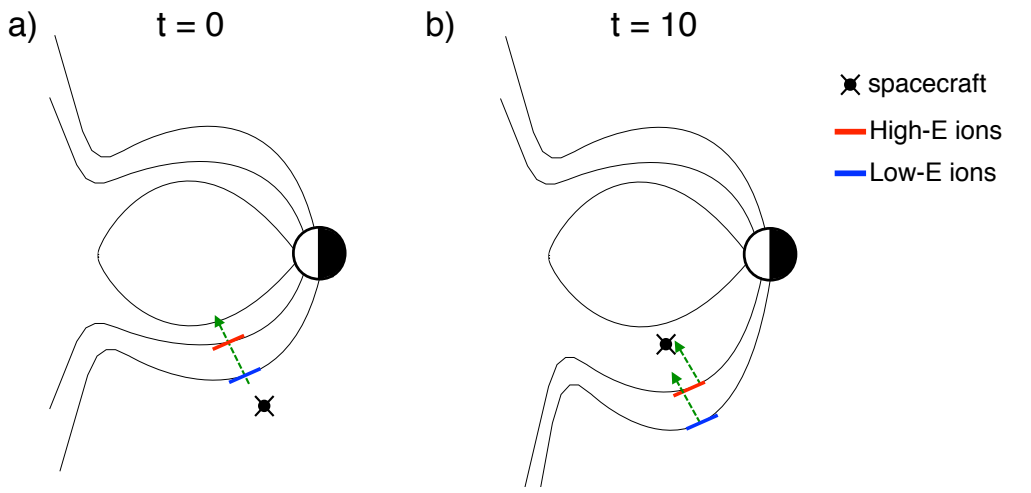

Figure 7.5: An illustration of the observation of a reverse ion-energy latitude dispersion whilst the cusp is oscillating ('E' is energy).

energy-latitude dispersions can be determined. For both dispersions in JAN07 (a and b) the ions are observed from a subsolar direction (see Figure 7.4, (a) shows an example of the observed ion direction for JAN07-b, whilst (b) shows it for JAN07-a). For the FEB07-a observation the ions are also observed from this direction. However for the FEB07-b interval the instrument is not fully actuating (actuation is less than $\sim 1°\text{min}^{-1}$), and so no meaningful conclusions as to whether there are more counts observed in a particular direction can be made. The spacecraft is travelling equatorward so for the first cusp crossing (JAN07-a) the spacecraft (with a velocity filter arising from subsolar reconnection) observes the low energy ions first, followed by the energetic ions, as seen in Figure 7.5a (green arrow is the spacecraft trajectory). The spacecraft then enters the magnetosphere. Ten hours later, the cusp then oscillates back over the spacecraft which is shown in panel b (green arrows now show the motion of the cusp over the spacecraft). This time (with respect to the spacecraft) the spacecraft enters the cusp from the same position it left, so the higher energy ions are observed first. This results in a dispersion observed in the opposite direction, even though reconnection is not occurring in the lobes.

The MAR07 event is very similar to the first forays into the southern cusp of the previous two examples (JAN07-a and FEB07-a) and is shown in Figure B.2. Before entering the cusp, CAPS observes very tenuous bursts of plasma with low energies, which could be the plasma mantle. However there is no significant increase in electron flux in the anti-planetward direction to support this hypothesis (CAPS

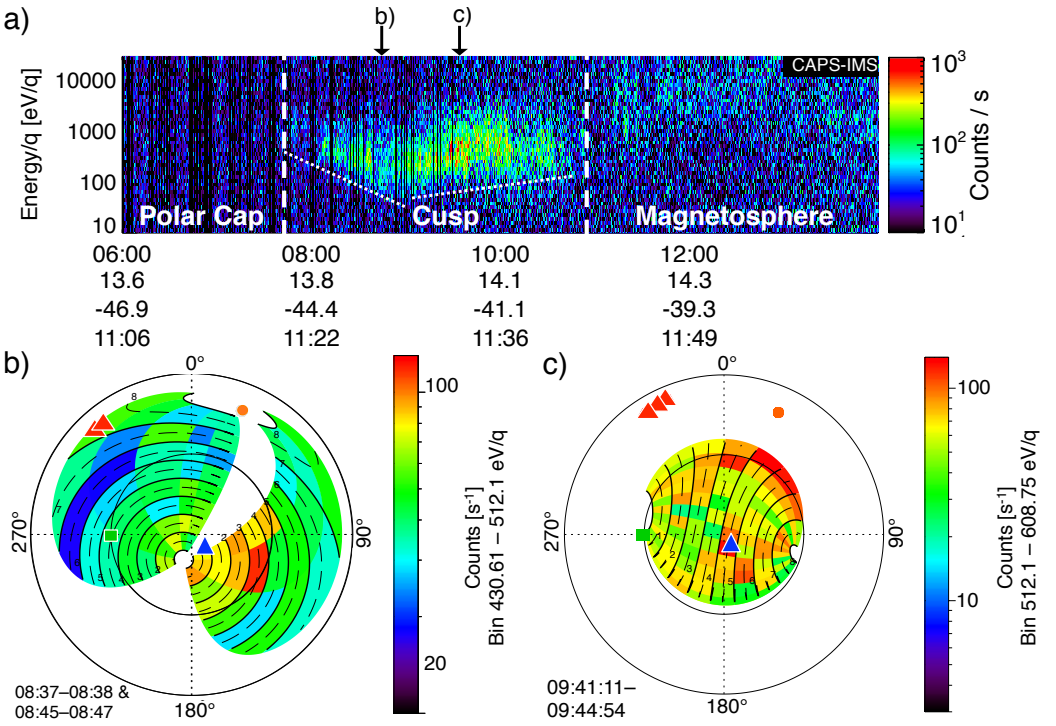

Figure 7.6: A high-time resolution spectrogram of the ion observations from IMS displaying the two different energy-latitude dispersions (underlined) from the MAR07 event (panel a). Panels b and c, show the angular distributions of the ions at a point in each dispersion (the times relative to the spectrogram are shown with arrows).

covered pitch angles of 80−180°).

Once in the cusp, there are two energy-latitude dispersions. The first is a 'reverse sense' dispersion, underlined in Figure 7.6a. The ions observed are arriving from a higher latitude, in the anti field-aligned direction, where one would expect lobe reconnection to be occurring, shown in panel b (the labels 'b' and 'c' show what time the corresponding angular distribution plots in panels a and b correspond to in the spectrogram in panel a). The second dispersion is a 'normal sense' dispersion, with the ions arriving from an equatorward direction. This is also supported by the angular distributions of the ions. Therefore unlike the previous two examples (JAN07 and FEB07) the change in dispersion orientation is due to reconnection occurring in two opposite locations (lobe and subsolar positions). Of course, without multiple spacecraft, it is not possible to determine whether reconnection in these two locations was occurring at the same time or not.

In both dispersions in the MAR07 data, there is an azimuthal component in the ion arrival direction, which would most likely be due to a large B_y component of the IMF, dragging the field line in the opposite direction to corotation. The two

dispersions are also accompanied by a slight energisation of electrons between the two populations. When leaving the cusp into the magnetosphere, the spacecraft once again observes a narrow boundary layer of plasma with decreasing density and an increasing energy (shown in Figure B.2).

In all of these cusp events, there is a boundary layer observed before crossing into the magnetosphere from the cusp. This is observed as a mixing of the magnetospheric and magnetosheath particles as well as an observed gradual increase (or decrease if entering the cusp from the magnetosphere) of the electron energy in ELS, and increases in flux of energetic electrons in LEMMS.

7.2 Isolated Cusp

Presented in this section is an interesting observation of a cusp not directly adjacent to the magnetosphere, but isolated from it by a brief traversal of the polar cap. The event occurred on the 25th of May 2008 (from now on called 'MAY08'), and was observed in the northern hemisphere, with the spacecraft travelling polewards, and planetward. The MAY08 event occurs with the spacecraft (unlike in the previous cusps) in the polar cap, with no plasma observed within the detectability threshold of the instrumentation. There is no direct transition of the spacecraft from the magnetosphere through to the cusp. Instead the spacecraft exits the polar cap, passes through a brief boundary layer, characterised by very tenuous plasma, and then proceeds through to cross the cusp.

7.2.1 Overview of the MAY08 observation

The data is presented in Figure 7.7. The spacecraft is already in the polar cap at 00:00 UT where plasma detection was at the background level of the instrumentation. A very tenuous electron population is seen until 01:30 UT, with energies slightly higher than those in the cusp, representing a boundary layer before entering the cusp. At 01:30 until 02:30 UT the spacecraft observes dense cold electrons in the cusp, and very high fluxes of ions in the energy-latitude dispersion.

For the first half an hour after exiting the cusp, the spacecraft observes very low fluxes above the background, and then for the following half hour, a higher energy population of electrons are observed in ELS and LEMMS (the high fluxes below $\sim$25 keV just after 05:00 and 08:30 UT are light contamination in the LEMMS instrument). This is interpreted to be the same or a similar boundary layer that was

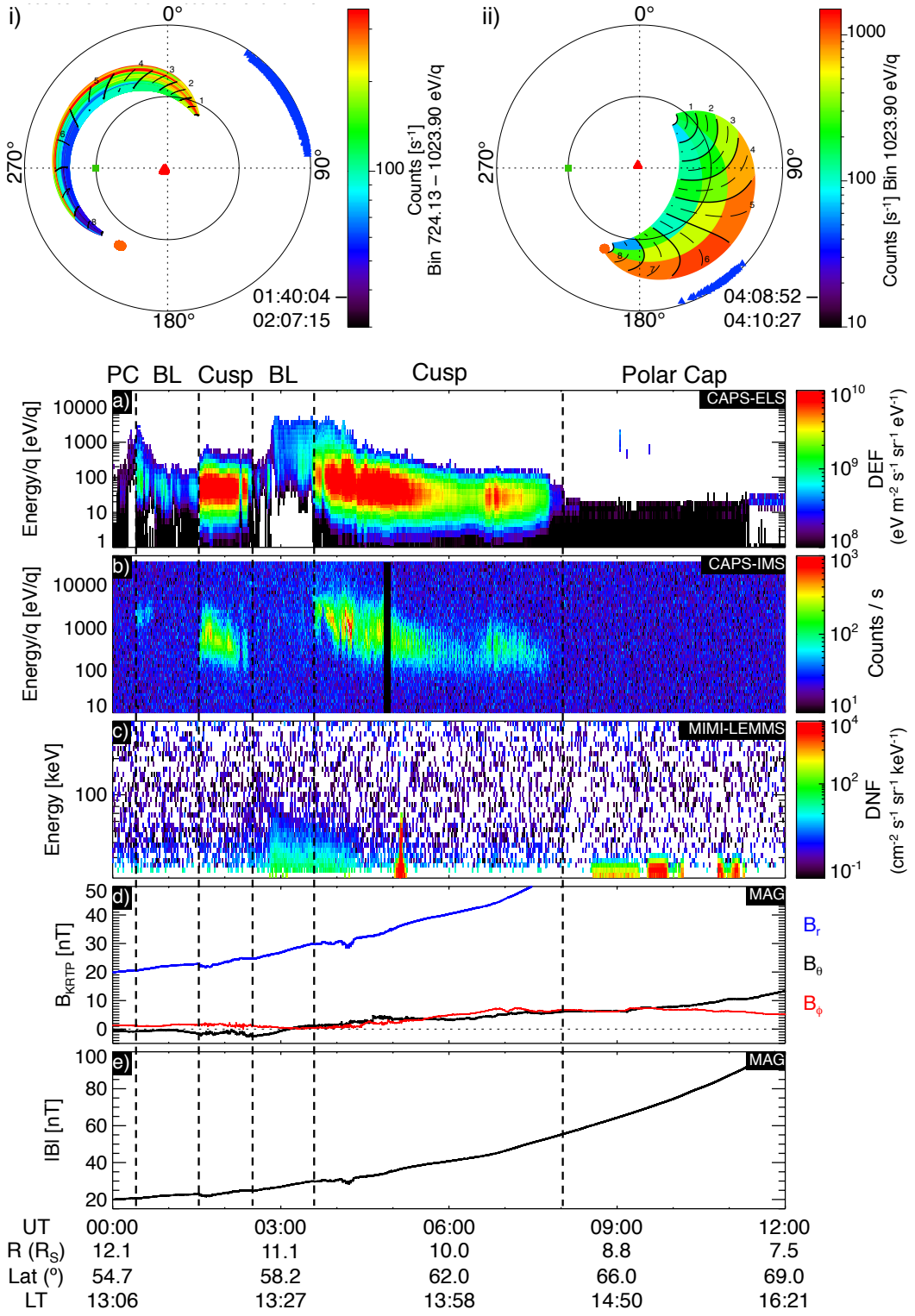

Figure 7.7: Observations from the 25th of May 2008, with the cusp observed at 01:30−02:30 and 03:30−07:45 UT. From top to bottom: i and ii) show the ion angular distributions during the first two ion dispersions, a) electrons from CAPS-ELS, b) ions from CAPS-IMS, c) high-energy electrons from MIMI-LEMMS, d) the three components of the magnetic field in KRTP coordinates from MAG and e) the magnitude of the magnetic field also observed by MAG.

observed by the spacecraft before entering the cusp (at 01:30 UT). Upon re-entering the cusp at 03:30 UT, the higher energy electrons are observed for almost an hour in the cusp. There are a few bursts of increased flux in the plasma, with the largest being associated with a small magnetic depression at ∼04:10 UT. There is a clear energy-latitude dispersion, with a gradual decrease in flux. At 06:40 UT, there is another dispersion with an increase in ion energy observed, before the cusp is exited at ∼09:00UT and the spacecraft re-enters the polar cap.

For the first dispersion (at 01:30-02:30 UT), the ion angular distributions can be seen in Figure 7.7i). It can be seen in the plot that the look direction does not vary significantly for half an hour (in this example) and that for most of the first dispersion the instrument was not actuating, resulting in (including the spacecraft not rolling) the FOV not moving greatly. At 00:00−02:00 UT the actuator was not fully actuating and was moving at $\sim 0.02^{\circ}$ s^{-1}. At 02:00−04:00 the actuator is fixed in position, and full actuation resumes at 04:00 UT. At 04:00 UT there is an increase in the electron and ion flux. Panel ii) presents the angular distributions of the ions during the second cusp dispersion, showing that there are increases in ion flux from the direction 'below' the spacecraft. Whereas previous examples showed the ions to be observed from a more equatorward direction, this example shows that they also have a slightly anti-planetward arrival direction at the spacecraft, suggesting that the ions were injected at a location northward of the subsolar point, possibly at higher latitudes.

The isolated nature of the cusp could hence be explained by an onset of reconnection after the spacecraft crossed the open-closed field line boundary. Once the spacecraft had entered open field lines where no plasma was observed, reconnection had taken place. The reconnected field lines then subsequently convected over the spacecraft, at which time injected plasma was observed by the spacecraft.

7.3 Tenous Cusp Observations

7.3.1 Overview of both observations

The two observations in question have been grouped together, due to the similarity in the ELS and IMS data, and the relevant observations having short timescales. The days of the observations were 24th of September 2008 ('SEP08') and 23rd of November 2008 ('NOV08').

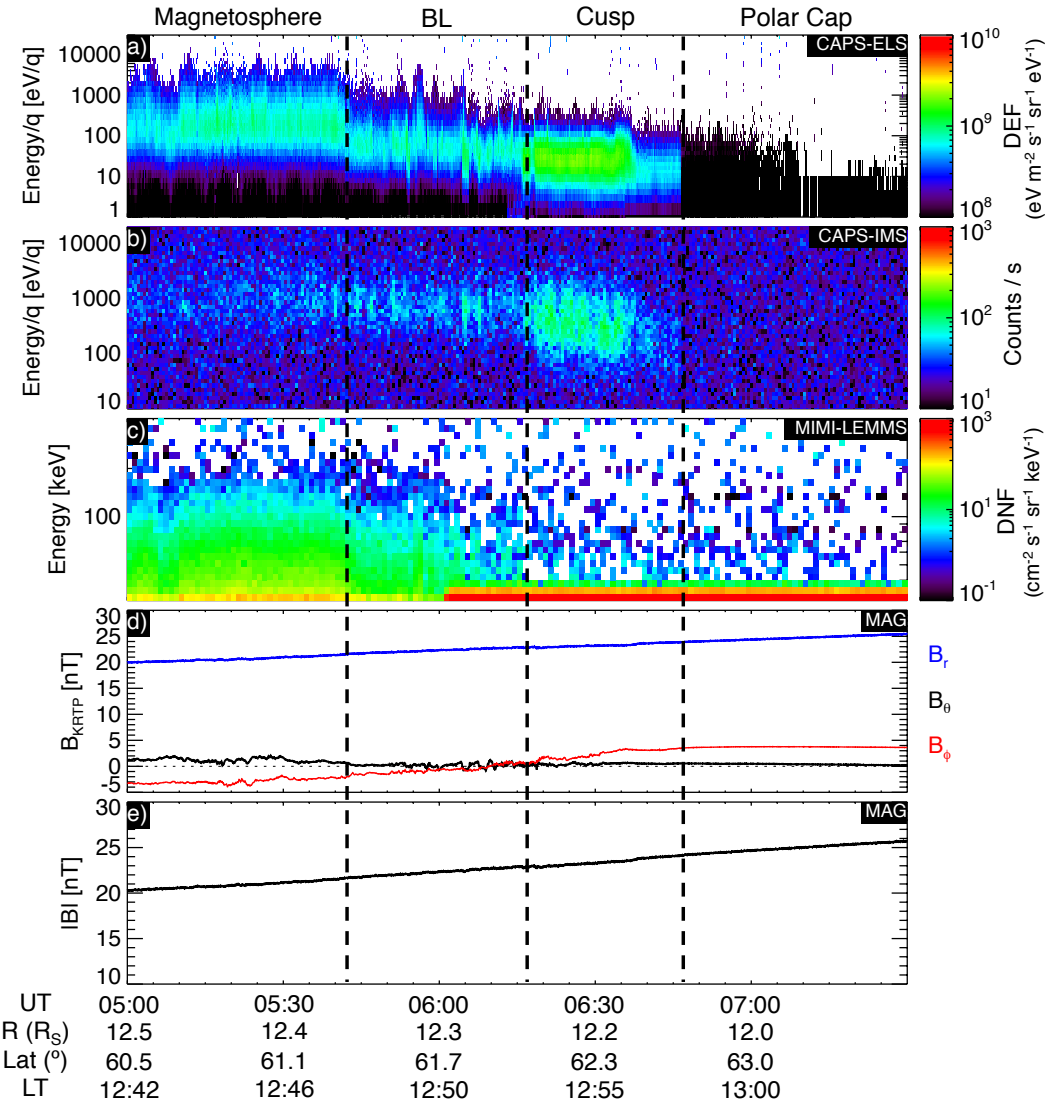

Figure 7.8: Observations from the 23rd of November 2008, with the cusp observed at 06:15−06:45 UT. From top to bottom: a) electrons from CAPS-ELS, b) ions from CAPS-IMS, c) high-energy electrons from MIMI-LEMMS, d) the three components of the magnetic field in KRTP coordinates from MAG and e) the magnitude of the magnetic field also observed by MAG.

The data for the NOV08 observations are presented in Figure 7.8. Before the cusp observation, the spacecraft (similar to previous cusp intervals) crossed a boundary layer, where the energy of the electrons gradually decreased (observed by ELS and LEMMS panels a and c). The determination of the composition of these ions is difficult due to the TOF accumulation overlapping the boundary layer and the cusp. However in the magnetosphere (03:54−05:36 UT) the water group percentage (of H^+) was 5.3±0.4%, which decreased to 1.3±0.2% in the overlapping bin (05:36−06:27 UT). There were no W^+ counts above the background level in the cusp.

The start of the 'pristine' cusp observations was at 06:15 UT (06:50 for the SEP08 event presented in Appendix B). High energy electrons are not observed in MIMI-LEMMS (panel c) during the NOV08 cusp crossing, however during the SEP08 observation they are. This could be due to the field line having only just been reconnected and the high energy magnetospheric electrons have not had enough time to leave the newly opened field line.

In both days the cusp observations do not last longer than approximately 30 minutes. Indeed the September observation has a data gap, and the actual data are collected for no more than 10 minutes. However, the electrons are already lower in energy before the data gap occurs, implying that Cassini may already be in the cusp during the time of the data gap. Assuming the spacecraft is in the cusp during the data gap, the cusp interval would be approximately 20 minutes in duration.

The NOV08 observations show a weak "normal-sense" ion dispersion, with high energies observed at lower latitudes, indicating reconnection occurring at the dayside sub solar magnetopause (Figure 7.8). The SEP08 observation does not show any significant dispersion.

The magnetic field orientation for both observations is the same; very strongly in the radial direction. The NOV08 observation (Figure 7.8) has a rotation in the B_ϕ component at the start of the cusp crossing, and the B_θ is largely negligible. The SEP08 observation on the other hand, has a largely negligible B_ϕ component, with a slightly stronger B_θ component.

7.4 Northern 2013 'Summer' Cusp

The CAPS instrument was switched off permanently in 2012, due to a short circuit. Therefore there are no low energy particle observations for the high latitude orbits in 2013, and so another source of data must be a base for the search for the cusp during this period. MAG is used to locate magnetic field depressions which have been observed frequently at the terrestrial cusp as well as in some previous Saturn cusp examples. A study of the MAG data reveals three events with magnetic depressions in the cusp which will be described in this section. The cusp crossings took place on the 14th of June 2013 ('JUN13'), 24th of July 2013 ('JUL13') and the 17th of August 2013 ('AUG13'). All three northern observations occur with the spacecraft travelling equatorward in the pre-noon region, and are in the mid-to-high altitude range (14−18 R_S).

An overview of the JUN13 cusp will be presented, followed by a description of the other events and a discussion. The observations of the JUL13 and AUG13 events can be found in Appendix B.

The cusp was identified using a combination of the MAG and LEMMS instruments. First of all, a magnetic decrease greater than any gradual change of the magnetic field strength (due to the spacecraft trajectory) identified the diamagnetic depression. The spacecraft orbits will be discussed later, but the trajectories favoured pre-noon northern observations, which occurred within ∼20 R_S at high latitudes. Southern observations occurred with large radial distance resulting in an exit of the magnetosphere, and entry into the magnetosheath and solar wind before high (southern) latitudes were reached.

Once a depression was located the energetic electron observations from LEMMS were used to determine whether there was a decrease in (or a complete lack of) flux, similar to previous cusp examples. A magnetic depression with no energetic particles would provide evidence that there is a plausible plasma population below the LEMMS detectability threshold present (that would have been observed by CAPS had it still been activated).

Depressions are not observed in the AUG08, SEP08 and NOV08 observations. This is largely reasoned to be due to their low radial distances (∼8−12 R_S) from the planet, making the field more difficult to depress, as well as very low density plasma present in the SEP08 and NOV08 cusps (discussed in the next chapter in

more detail). However the orbits during 2013 had large radial distances (>14 R_S) when the cusp would be most likely to be observed, making it more likely that a detectable field depression would occur, if the cusp is traversed.

7.4.1 Overview of an example case study – JUN13

The data from the JUN13 observation is presented in Figure 7.9, where the high energy electron (panel a) and magnetic field (panels b and c) data are shown. Before entering the cusp, the spacecraft observes high-energy electron counts at the noise level, with a burst of electrons occurring just before the cusp at 18:50 UT, which coincides with a small rotation in the B_ϕ component of the magnetic field. The magnetic field depression starts at 19:40 UT (with a field strength of ∼11.5 nT) which is marked as the start of the cusp. At 21:00 UT, the depression reaches a minimum field strength of ∼8.5 nT. At 21:40, there is local drop in the magnetic field (∼1 nT), and a burst of high energy electrons, which is interpreted as a brief entry into the boundary layer between the cusp and the magnetosphere, before re-entering the cusp.

The cusp is exited at 22:10 UT, where the spacecraft enters a boundary layer of increased flux of energetic electrons. At 22:35 UT there is a clear crossing into the magnetosphere where LEMMS observes the highest fluxes of energetic electrons in this event, which is also marked by a rotation in B_ϕ which could be the observation of a field aligned current on the open-closed field line boundary. The B_ϕ rotation is also clearly seen upon entering the boundary layer at ∼22:10 UT.

7.4.2 Summary of other observations

The JUN13 and JUL13 observations are similar in the fact that the magnetic field depressions are also centred on the cusp position deduced from the LEMMS data. The JUL13 event has no increase in flux of electrons observed in LEMMS when exiting or entering the cusp. The cusp is defined by the magnetic field depression and observation of He^{++} ions by CHEMS (shown in Figure C.4 and discussed in the next chapter). There are short bursts (∼30 minutes) of increased flux an hour and two hours before the start of the cusp, however this aspect is similar to the MAY08 observation because it appears to be isolated within the polar cap. It is not put in the same group as the MAY08 event, because it has a clear magnetic field depression, and there is not an increase in flux of energetic electrons during

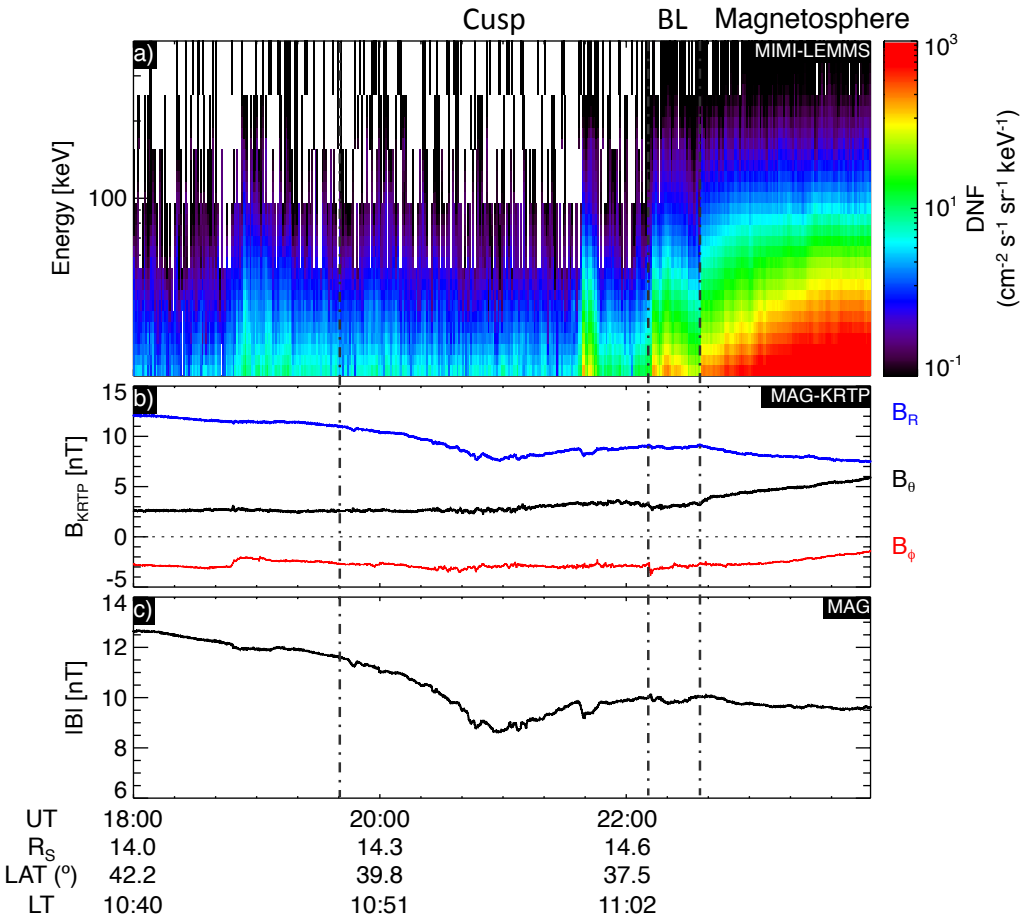

Figure 7.9: Observations from the 14th of June 2013, with the cusp observed at 19:40−22:35 UT. From top to bottom: a) high-energy electrons from MIMI-LEMMS, b) the three components of the magnetic field in KRTP coordinates from MAG and c) the magnitude of the magnetic field also observed by MAG.

the observation.

The AUG13 cusp observation is in a sense the opposite of the JUL13 observation because it is bounded on both sides to the magnetosphere. There is a boundary layer observed for ∼4 hours before and ∼2.5 hours after the cusp interval, with slightly lower fluxes of energetic electrons than the magnetosphere.

Whereas the magnetic field depression in the JUN13 observation is gradual, the JUL13 and AUG13 observations both have large erratic changes in their depressions, which would probably be due to density changes in the low energy plasma. During the first half of the JUN13 depression, there are background levels of electrons observed in LEMMS which, if the observation is similar to the 2007 cusp observations, would imply that the depression is not centred on the cusp, but on the boundary layer adjacent to the cusp. This boundary also has a rotation in the B_ϕ compo-

nent of the magnetic field, marking the open-closed boundary with the magnetic signature of a FAC (e.g. *Bunce et al.* 2008b; *Jasinski et al.* 2014).

7.5 Composition and Distance to the Reconnection Site

The composition of the cusp plasma as well as any regions adjacent have been mentioned throughout the chapter, however a summary of the results for the events presented in this chapter can be found in Table 7.1 (for the cusps with available IMS data).

The magnetosphere adjacent to the cusp has a variety of W^+/H^+ percentages ranging from 3.5±0.2% (JAN07) to 32.6±1.2% (AUG08). These percentages are much lower in the cusp with the lowest being 0.29±0.02% and the highest 1.3±0.2% (MAY08 and NOV08 respectively). The [m/q=2]/H^+ in the magnetosphere adjacent to the cusp has percentages from 8.3±0.27% to 28.2±0.1% (MAR07 and AUG08, respectively), suggesting these ions to be H_2^+. The ions would be expected to be H_2^+ in the magnetosphere with approximate percentages of ∼10−20% (as a percentage of H^+) or more, whilst lower percentages for the [m/q=2] ions are expected to be associated with He^{++} (*Thomsen et al.* 2010).

In the cusp these [m/q=2]/H^+ values are lower, ranging between 1.5±0.05 and 4.76±0.03 (MAR07 and AUG08 respectively), which suggest that this component of the plasma is He^{++} and of a solar wind origin. The region that is identified as a 'boundary layer' (FEB07−b) that has been interpreted as having mixed cusp and magnetospheric plasma with a value 7.42±0.04 % ([m/q=2]/H^+), which is higher than any of the cusp observations but lower than any of the magnetospheric observations, thus providing further evidence for our interpretation.

From the available ion energy-pitch angle dispersions the distance to the reconnection site using the BUR82 method was also calculated. Similar to previous cusp events, if the dispersion was not clear, the signal to noise ratio was low or the model was unable to be successfully fitted, a calculation could be made. However for the successful fits, the results were all binned together within the same energy-latitude dispersions, with error propagated using Equation 6.3. The binned results can be seen in Table 7.1. The individual results for separate dispersions can be found in Appendix B. All the individual distances for FEB07 and JAN07 (found in the appendix) were calculated by *C. S. Arridge* (for the paper *Arridge et al.,* in

Table 7.1: Data for events discussed in this chapter, presenting the composition of the ions in the magnetosphere adjacent to the cusp, and in the cusp itself, for water group ions (W^+) and ions with a mass-per-charge of 2amu/q (m/q=2), as a percentage ratio by number of ionised hydrogen (H^+). Also presented (on the right hand side) are the estimated distances to the reconnection site from energy-pitch angle dispersions. The binned values for FEB07 (and JAN07-a) for the distances to the reconnection site are taken from *Arridge et al.*(in prep.).

			Composition		Reconnection Distance	
Date	Description	Time (UT)	W^+/H^+ (%)	[m/q=2]/H^+ (%)	Mean (R_S)	σ (R_S)
JAN07	Cusp - 1st Dispersion - 'a'	10:05 – 11:21	—	1.78 ± 0.03	50 ± 20	16
	Magnetosphere	13:04 – 15:37	3.5 ± 0.2	10.3± 0.1	—	—
	Cusp / Mixed Layer -'b'	17:24	—		16 ± 3	—
	Cusp -'b'	16:03 – 17:20	—	7.42 ± 0.04	26 ± 3	9
FEB07	Cusp - 1st Dispersion	16:50 – 18:32	—	1.93 ± 0.04	50 ± 20	15
	Magnetosphere	18:58 – 23:39	—	9.0 ± 0.3	—	—
	Cusp - 2nd Dispersion	01:26 – 02:43	0.42 ± 0.04	4.76 ± 0.03	37 ± 9	5
MAR07	Cusp - 1st Dispersion	07:45 – 09:02	0.93 ± 0.18	2.2 ± 0.56	16 ± 1	2
	Cusp - 2nd Dispersion	09:02 – 10:02	—	1.5 ± 0.05	15.6 ± 0.4	0.1
	Magnetosphere	11:06 – 14:01	4.7 ±1.2	8.3 ± 0.27	—	—
MAY08	Cusp - 1st Dispersion	01:26 – 02:30	—	4.3 ±0.03	—	—
	Cusp - 2nd Dispersion	03:34 – 05:42	0.29 ± 0.02	3.6 ± 0.02	16 ± 3	4
	Cusp - 3rd Dispersion	05:43 – 07:50	0.42 ± 0.40	2.1± 0.1	—	—
SEP08	Magnetosphere	02:43 – 04:00	9.6 ± 5.6	16.9 ± 0.3	—	—
	Cusp	05:42 – 07:24	0.6 ± 0.5	2.1 ± 0.03	21 ± 5	—
NOV08	Magnetosphere	03:54 – 05:36	5.3 ± 0.4	15.7 ± 0.1	—	—
	Cusp - Bin 1	05:36 – 06:27	1.3 ± 0.2	3.1 ± 0.1	—	—
	Cusp - Bin 2	06:27 – 06:53	—	3.4 ± 0.1	—	—

prep.). The binned values are different here for the JAN07 event, as *Arridge et al.,* do not treat the 'mixed cusp layer' in JAN07-b separate from the second dispersion labelled 'cusp'.

The calculated field-aligned distances were then traced along field-lines using the *Khurana et al.* (2006) magnetospheric field-line model (alongside propagated solar wind dynamic pressures which are discussed in the following section) and the location of the reconnection site was estimated. The results can be seen in Figure 7.10, where the locations are shown as if viewed from the Sun in the Y-Z plane (in the KSM co-ordinate system). The estimated sites (for reconnection) occur over a large range of locations, including low and high latitudes. The large calculated field aligned distances ($\sim$50 R_S) for the JAN07-a and FEB07 events (as well as the latter calculations for JAN09) are more feasible with an expanded magnetosphere. For the JAN07-a and FEB07 events, if lower projections for the solar wind dynamic pressure were to be used (than the solar wind model predicts), then these locations would move equatorward. The distribution of the reconnection locations is largely centred slightly poleward (towards the north) of the subsolar point, with only the JAN09 event located very far south of the subsolar point.

7.6 Solar Wind Propagations

Unlike at the terrestrial magnetosphere, where there are spacecraft upstream of the Kronian magnetosphere observing the conditions in the solar wind (SW), it is a lot more difficult to correlate SW changes to processes in the magnetosphere with a single spacecraft such as Cassini. Therefore solar wind propagation models are used to try and estimate the conditions upstream of Saturn's magnetosphere. For the first part of this section, an in depth analysis of the solar wind conditions for the JAN09 event is shown, which was partly presented in *Jasinski et al.* (2014). In the following part, mSWiM (*Zieger and Hansen* 2008) model propagations are shown for all the cusp events.

7.6.1 Estimations for the JAN09 cusp

In Figure 7.11, Saturn Kilometric Radiation (SKR) observations are presented as well as model estimations (from two models: ENLIL and mSWiM) of the solar wind conditions upstream of Saturn's magnetosphere, from the 14th of January until the 9th of February (40th day of the year [DOY]) 2009. SKR can be used as a proxy

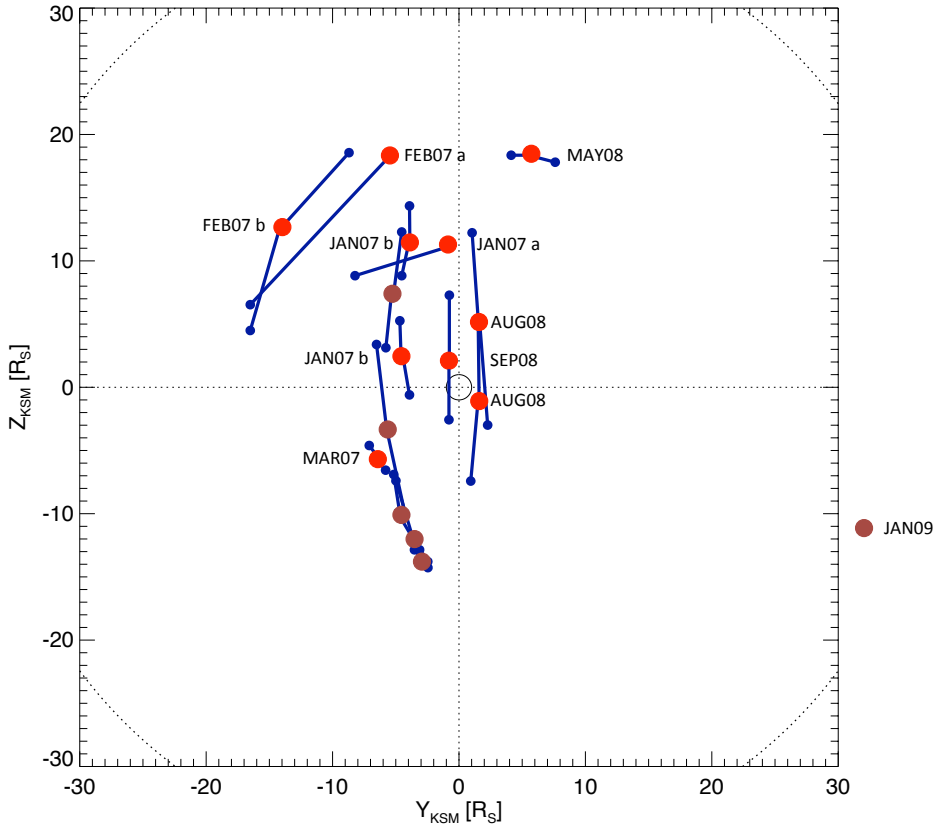

Figure 7.10: A projection of the estimated locations of reconnection from the calculated field-aligned distances (using the energy-pitch angle dispersions and the BUR82 model) are shown in red, and associated errors in blue. The plot is in the Y-Z KSM plane (as viewed from the Sun) with the sunlit planet in the centre and an average model magnetopause location (dotted) also shown (calculated using the *Kanani et al.* (2010) model and the compressed standoff distance value (22 R_S) from the bimodal distribution found by *Achilleos et al.* (2008)).

for upstream conditions. The increase of SKR intensity and subsequent extension towards low frequencies has been often shown to arise from interplanetary shocks (*Desch and Rucker* 1983, 1985; *Badman et al.* 2008), but also more recently from internal processes as well (*Lamy et al.* 2013). SKR is observed by the Radio Plasma Wave Science (RPWS) instrument (*Gurnett et al.* 2004), as is shown in the top panel.

Model heliospheric solar wind conditions at Saturn modelled by ENLIL are shown in the middle panels of Figure 7.11. ENLIL is a 3D magnetohydrodynamic model of the heliosphere that is time-dependent. ENLIL uses and finds the solutions to equations regarding plasma, magnetic field, momentum and energy transport using a Flux-Corrected-Transport algorithm, with initial and boundary conditions set from ground-based solar magnetogram observations (*Odstrcil* 2003). The inner

boundary of ENLIL is dependant on the coronal model to which it is connected, either the Magnetohydrodynamic Algorithm outside a Sphere (MAS) or the Wang-Sheeley-Arge (WSA) model. The ENLIL-MAS model was used for these observations. The MAS model extends from 1 Solar radius ($R_\odot$) to 30 $R_\odot$. Magnetograms are used for the input at its inner boundary to determine the magnetic field radial component. The density and temperature of the plasma are calculated from conservation of momentum flux and thermal pressure balance. The model is run with an initial start up phase of sixty simulated days before the input of the magnetogram, to allow the inner boundary condition to influence the solution at Saturn. The following 27.27 days in the model introduce the magnetogram inputs which then propagate outwards to Saturn's orbit.

In the two bottom panels of Figure 7.11 the mSWiM model is presented. mSWiM is an MHD model of predicted solar wind conditions at various bodies of interest, propagated from spacecraft observations at 1AU, from either Earth, Stereo A or Stereo B spacecraft (*Zieger and Hansen* 2008). The most accurately predicted solar wind property of the model is the solar wind velocity, followed by the magnitude of the IMF and density. Ideally one would also like to use the normal component of the IMF (B_{Normal} − component closest to a planetary Z axis) to test whether reconnection is controlled by the orientation of the IMF as for the Earth. However, B_{Normal} is very inaccurate having shown insignificant correlation between model and observations. The propagations are most accurate for observations where the selected spacecraft near Earth orbit (at 1 AU) and Saturn were aligned within 75 days of opposition. It has been shown that the uncertainty in predicted arrival time near apparent opposition is ±15 hours. Propagations outside these alignments (75 days) are not as accurate but are, however, still statistically significant (*Zieger and Hansen* 2008). The JAN09 event occurred within 31 days of apparent opposition.

From ENLIL, the following parameters are presented in Figure 7.11: subsolar magnetopause distance, ram pressure, magnetic field strength and velocity. The velocity (v_{SW}), number density and field strength (B) predicted at Saturn by the models are used to calculate the dynamic pressure (P_{RAM}) of the solar wind using the equation:

$$P_{RAM} = \rho v^2 \tag{7.1}$$

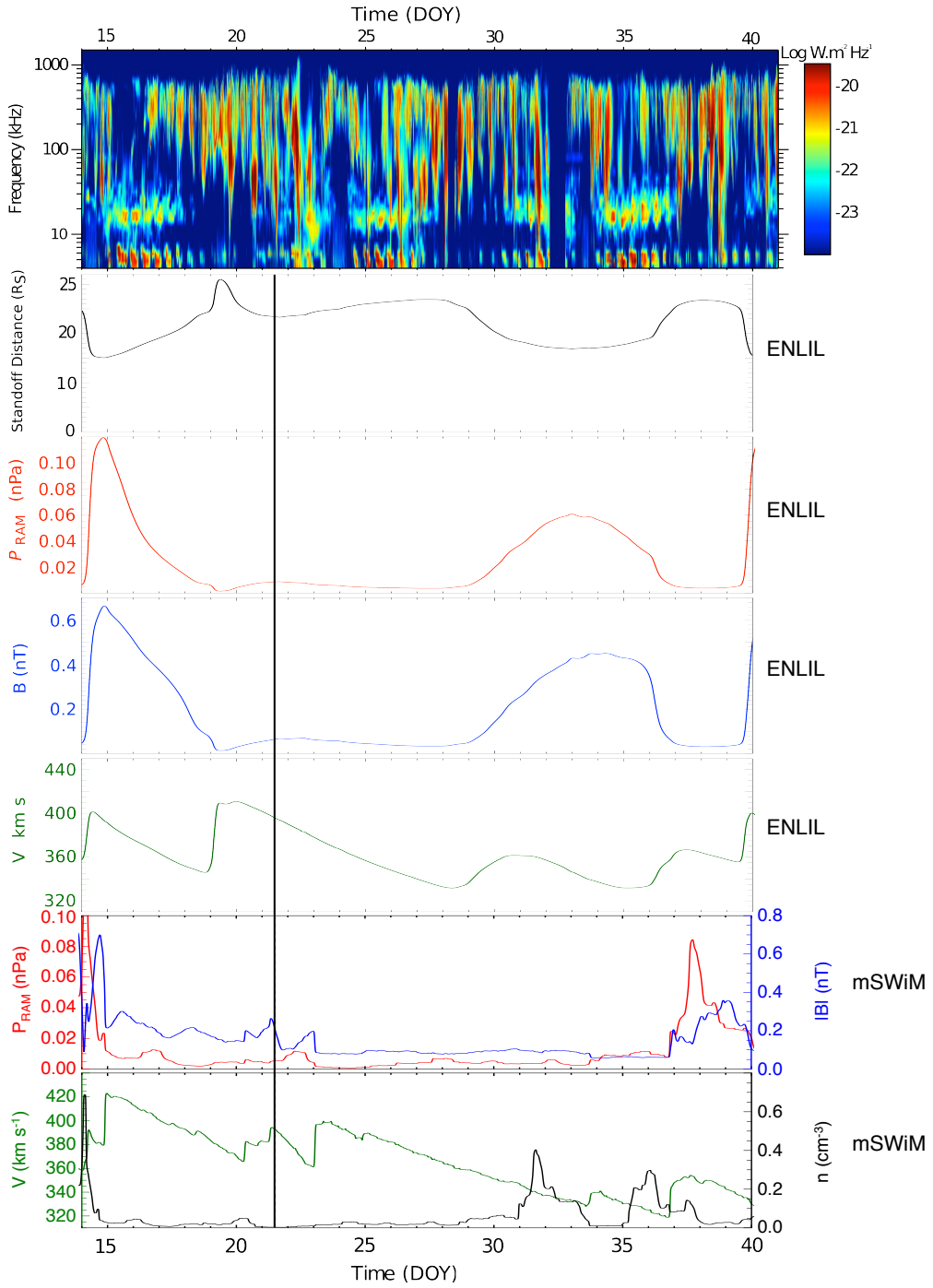

Figure 7.11: Upstream conditions for 14 Jan - 9 Feb 2009. Saturn Kilometric Radiation (SKR) as observed by RPWS (presented as a flux density at 1AU). The data have been processed as explained by *Lamy et al.* (2008) [*this panel was provided by L. Lamy*]. Below the panel of SKR observations, presented are ENLIL solar wind conditions model results: standoff distance of the magnetopause (estimated using dynamic pressure from ENLIL), ram pressure, the magnetic field strength, velocity, and mSWiM propagated solar wind conditions: velocity, number density, magnetic field magnitude and dynamic pressure (with an uncertainty of 15 hours).

The mass density (ρ) is calculated assuming the ions are protons (not including a 4% alpha particle population introduces an uncertainty of only ∼8% on the density). The magnetopause stand-off distance (R_0) is correlated approximately to the dynamic pressure by $R_0 \sim P_{RAM}^{-1/5}$ (*Hansen et al.* 2005; *Arridge et al.* 2006; *Kanani et al.* 2010). Therefore the behaviour of P_{RAM} represents whether the magnetosphere is being compressed. For the ENLIL data the standoff distance is approximated by using the equation:

$$R_{standoff} = \sqrt[5]{\frac{B_0^2}{2\mu_0 P_{RAM}}} \tag{7.2}$$

where μ_0 is the permeability of free space and B_0 is the equatorial magnetic field strength of the planet taken to be 21000 nT. This is a good first approximation of the standoff distance for Saturn's magnetopause. The *Kanani et al.* (2010) model calculates a standoff distance using $R_{standoff} = 10.3P_{RAM}^{-0.2}$ (where P_{RAM} here is in nPa). A comparison of the results for an arbitrary dynamic pressure of 0.05 nPa, gives a standoff distance of ∼20 R_S using Equation 7.2, and ∼19 R_S using the *Kanani et al.* (2010) model, showing that our calculations are a suitable approximation to determine $R_{standoff}$ as well as understanding whether the magnetosphere is being compressed by the solar wind during these observations.

mSWiM observations are presented for the same time period, and present velocity, number density, ram pressure and magnetic field strength. The day of the cusp observations is marked by a dashed line on DOY 21.

Comparing mSWiM to ENLIL, it can be seen that the two different models have very similar results. In both models, there are major peaks in the velocity, magnetic field strength and ram pressure on ∼15 DOY. The second most distinctive increase in solar wind parameters occurs on DOY∼34 (P_{RAM} and |B|) in ENLIL, however this is not seen in mSWiM for |B|, and is delayed for P_{RAM} until DOY∼37-38. Furthermore the peaks on DOY ∼40 in ENLIL occur two to three days earlier in mSWiM. These can be explained by the temporal errors within the models. For ENLIL, the arrival time uncertainty of the model at 5.4 AU can be at least 4 days and may be larger at 9 AU (*Jian et al.* 2011), in comparison to an mSWiM uncertainty of ∼15 hours.

The comparison of RPWS observations with both ENLIL and mSWiM simu-

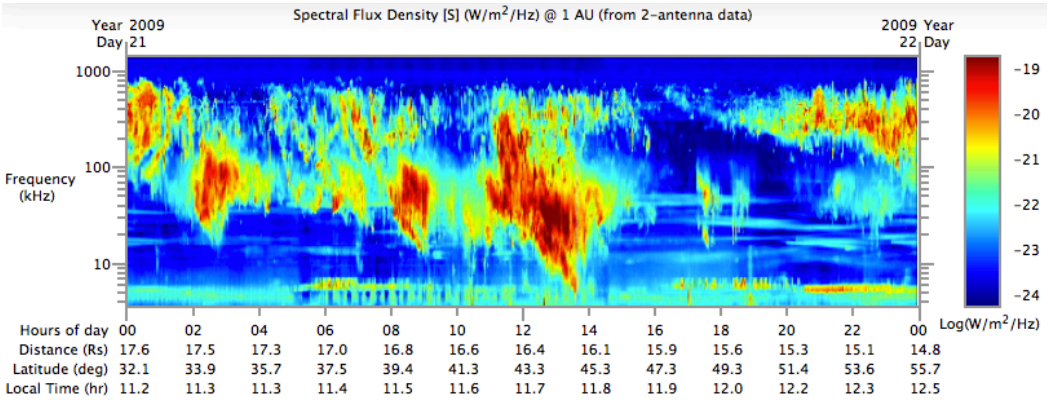

Figure 7.12: Saturn kilometric radiation as observed by RPWS on the day of the cusp observation. On the x-axis is the universal time shown in hours. The data is presented as a flux density at 1AU (Log W m^{-2} Hz^{-1})

lations over an extended period of time shows intensified SKR emission (observed by RPWS) when (i) close to the predicted arrival (from ENLIL and mSWim) of solar wind velocity fronts, around the time of our cusp observations on DOY 19-20 (modest increase of dynamic pressure), and other time periods on DOY 29-30 and 39-40 (larger increases of pressure) and (ii) at times seemingly unrelated to changes in solar wind parameters. The first of these events (DOY 19-20) matches the interval investigated above within the uncertainty of ENLIL propagation. This supports the possibility that the magnetosphere was in a compressed state during the interval examined here, which would provide more favourable conditions for dayside reconnection (e.g., *Jackman et al.* 2004; *Masters et al.* 2012; *Badman et al.* 2013).

In Figure 7.12 high resolution dynamic spectra of RPWS-HFR data between 3.5 and 1500 kHz, of the SKR observations (*Lamy et al.* 2008) are presented. The figure shows the whole day on the 21st of January 2009, with time in hours at the bottom. During the time we have identified as a cusp crossing ($\sim$11$-$19 hours UT), there were intense SKR emissions extending to low frequencies (as low as 3.5 kHz) observed. Both the models and the observations of the SKR suggest that the magnetosphere is being compressed making the conditions favourable for the occurrence of dayside reconnection.

7.6.2 Survey of upstream conditions using mSWiM

The following events occur within 75 days of apparent conjunction: JAN07 (54 days from apparent conjunction), FEB07 (38 days), MAR07 (3 days), MAY08 (38 days) and the JAN09 (31 days), JUN13 (17 days), JUL13 (53 days) and AUG13 (69 days).

The following days occurred outside 75 days of apparent conjunction: AUG08 (108 days), SEP08 (150 days) and NOV08 (90 days).

The velocity (v_{SW}), number density and field strength (B) predicted at Saturn by mSWiM were used to calculate the solar wind Alfvénic Mach number (M_A) using the equation:

$$M_A = \frac{v_{sw}\sqrt{\mu_0 \rho}}{B} \tag{7.3}$$

P_{RAM} indicates whether the magnetosphere is being compressed, whilst a high M_A (dependant on low magnetic field strengths, high densities and high velocities) in the solar wind would produce a high-β magnetosheath, making it more likely for reconnection to be suppressed and to only occur when the magnetic field lines are near completely anti-parallel (*Slavin et al.* 1984; *Masters et al.* 2012). The results are presented in Figure 7.13, with P_{RAM} and M_A presented in black and red respectively, for ten days on either side of each event (except for JAN07 and FEB07 which are presented together in panel a). The number of days from apparent opposition can be found in brackets for each observation. Separate presentations of the velocity, number density and field strength of the solar wind can be found in Appendix B.

For almost half of the cusp observations [JAN07 and FEB07 (Figure 7.13a), SEP08 (e) and NOV08 (f) and JUL13 (i)] there is a significant increase in the ram pressure, especially for SEP08 which has the largest peak of ∼0.15nPa. These would correspond to large compressions of the magnetosphere, which have been shown to provide more favourable conditions for dayside reconnection (e.g., *Jackman et al.* 2004). However it also important to note that two of these days also have the largest amount of days from apparent opposition (all >75 days).

Three of the other six days (MAR07, MAY08, JAN09) do not occur during peaks but they do occur during modest increases in ram pressure. MAY08 is at the start of a large pressure increase, with a modest increase having already occurred. However the increases for MAR07 and JAN09, are extremely modest and less significant. The other three days occur during periods of very low predicted ram pressures.

High (Alfvénic Mach numbers (which would produce a high β magnetosheath)

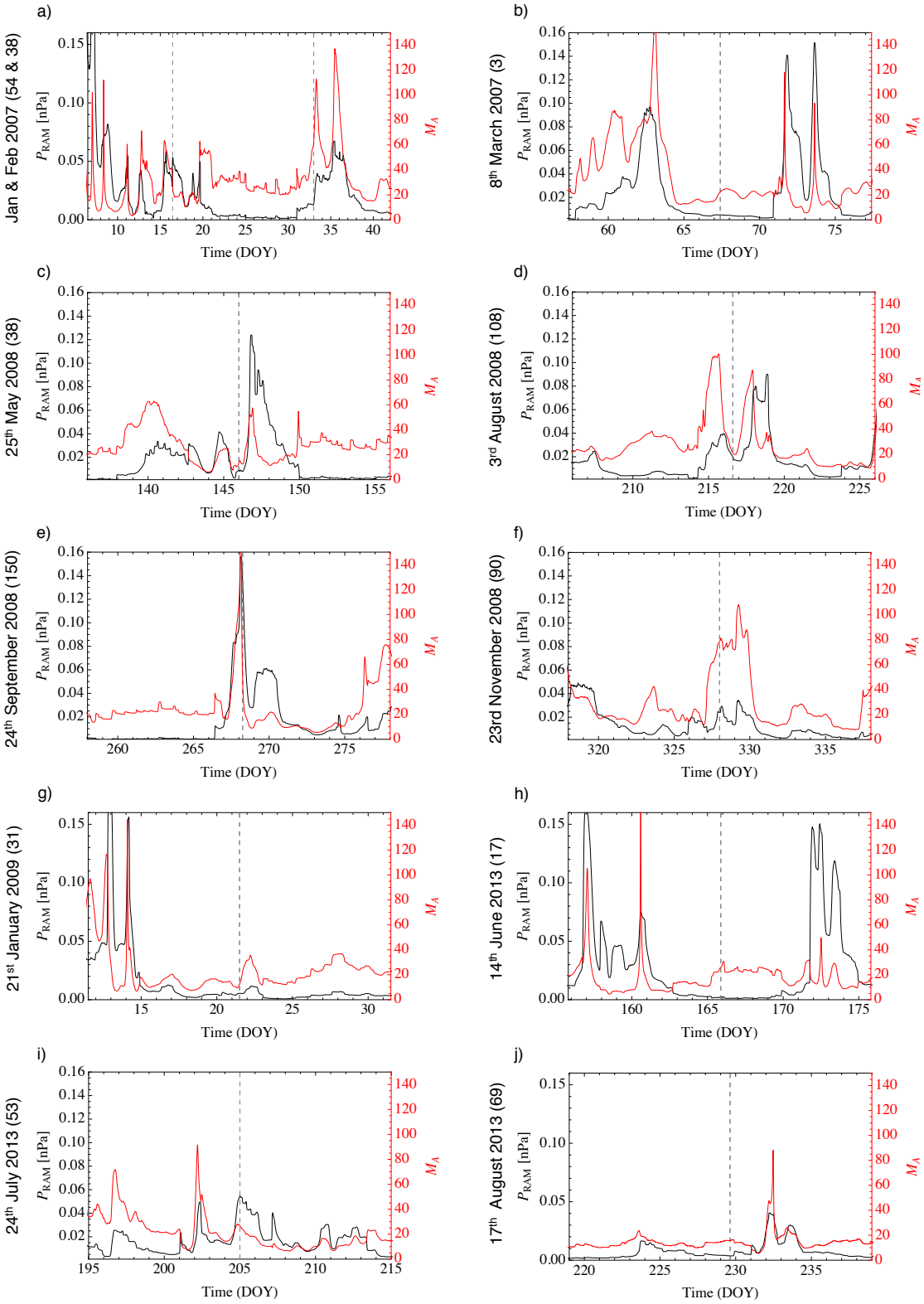

Figure 7.13: mSWiM propagations of the upstream solar wind conditions at Saturn for 10 days before and after the cusp observations (with an uncertainty of 15 hours). The ram pressure (P_{RAM}) and the Alfvénic Mach number (M_A) are presented in black and red, respectively. The number of days since apparent conjunction is shown in brackets next to each observation. The dashed line represents the start of the cusp observation. The day of year is labelled as 'DOY'.

would most likely lead to a suppression of reconnection such that it only occurs for anti-parallel field lines. Therefore it is interesting to see that for JAN07, FEB07, SEP08 and NOV08, M_A is at a peak or very large (>40), meaning the reconnection that occurred to produce the entry of solar wind plasma through the cusp must have occurred at a location on the magnetopause where the magnetic shear was very large. The lowest M_A of ∼10 was observed for JAN09. For the other five observations M_A was modest, averaging ∼20 and did not occur during significant peaks or troughs.

7.7 Location of the Cusp observations

During the years of 2007 and 2008, the Cassini spacecraft performed a series of highly inclined orbits (peak absolute latitudes of >50°) where the trajectory provided the opportunity to obtain cusp observations presented in this thesis. Cassini began to exit an equatorial orbit (with apokrones on the nightside) on the 22nd of July 2006, and reached latitudes of ∼50° for the first time on the the 27th of October 2006. However the latitude of the orbits peaked in the dusk (dawn) sector in the northern (southern) hemisphere, whereas cusp observations require an orbit near noon local time (LT).

The details of the times (UT) and locations of the cusp observations are shown in Table 7.2. In 2007 the orbit of the spacecraft had adjusted to be able to observe the southern cusp, with the latitude peaking in the noon sector in the south. High-latitude northern observations were still occurring in the dusk and night sectors of the magnetosphere, which were not suitable for cusp detection. There are three

Cusp Date	Time (UT)	Distance (R_S)	Latitude (°)	Local Time
JAN07	09:56 – 18:04	12.6	-54.5 – -43.4	10:10 – 11:39
FEB07	15:40 – 26:46	15.6 – 16.0	-56.0 – -46.8	09:39 – 11:14
MAR07	08:03 – 10:50	13.8 – 14.2	-43 – -40.8	11:22 – 11:42
MAY08	01:33 – 07:47	11.6 – 9.3	56.4 – 64.4	13:16 – 14:26
SEP08	06:15 – 07:12	10.6 – 10.3	60.6 – 62.2	12:32 – 12:41
NOV08	06:16 – 06:47	12.2 – 12.2	62.0 – 62.7	12:53 – 12:57
AUG08	14:47 – 22:59	11.1 – 8.2	58.7 – 72.7	12:32 – 14:55
JAN09	11:00 – 19:00	16.5 – 15.5	42.3 – 50.4	11:37 – 12:06
JUN13	19:40 – 22:10	14.3 – 14.6	39.8 – 37.5	10:51 – 11:02
JUL13	00:00 – 05:30	15.4 – 15.3	51.37 – 55.03	10:28 – 11:20
AUG13	14:00 – 16:05	18.5 – 18.4	38.0 – 33.0	10:13 – 10:22

Table 7.2: Locations and times of observations for all the cusps presented in this thesis.

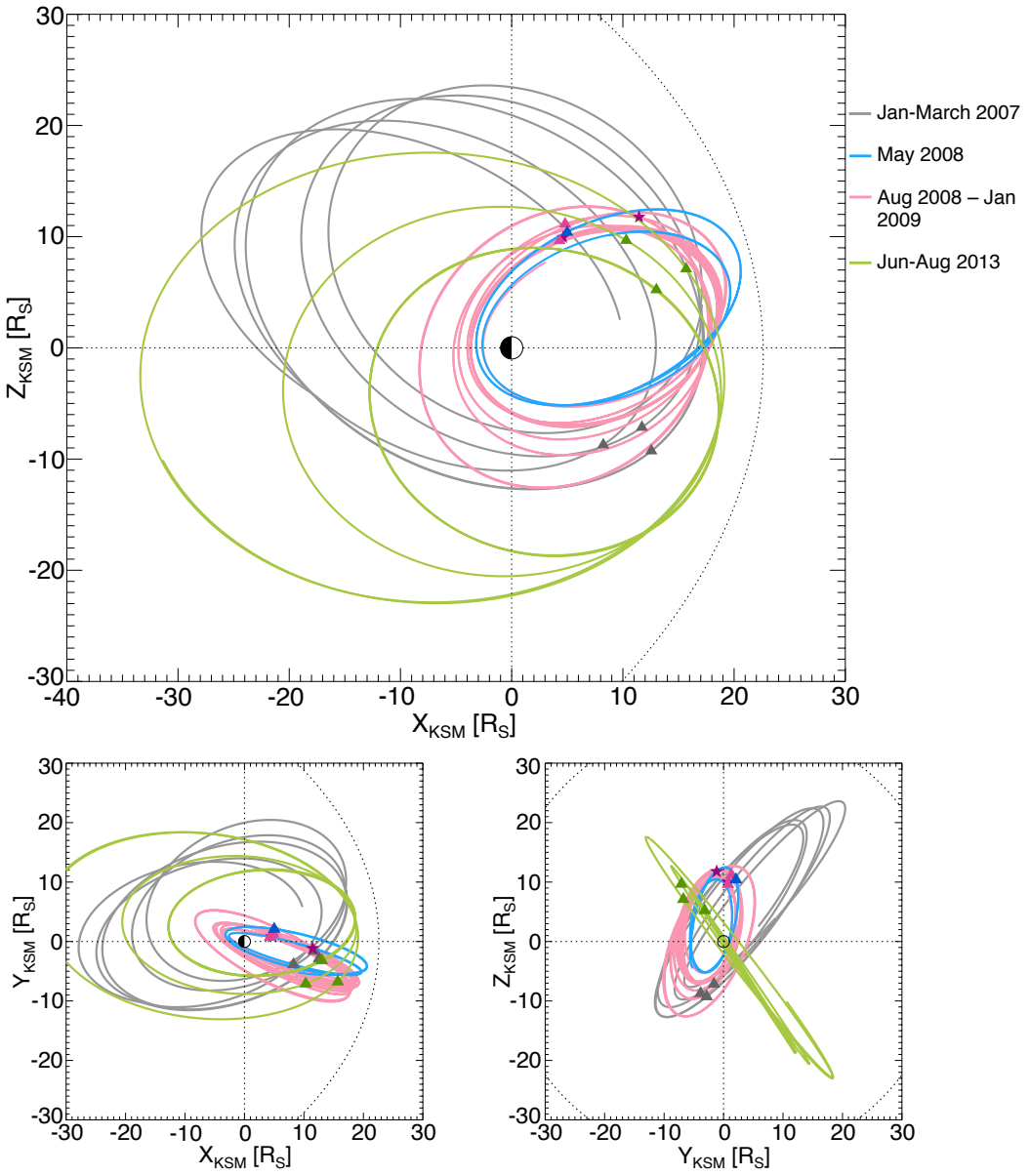

Figure 7.14: The trajectory of the spacecraft and locations of the cusp for the different orbits and observations. The orbit of the satellite is presented for four different time periods (shown in the legend) with the location of the cusp observation displayed as a triangle of the same colour as the orbit. The JAN09 and AUG 08 observations are displayed as stars to distinguish them from the SEP08 and NOV08 events, which are all located on the same set of orbits. The trajectories are presented in the Kronocentric Solar Magnetospheric (KSM) co-ordinate system, where X points towards the Sun, Y equals the normalised cross product of the magnetic dipole direction with X, and Z completes the right-hand set (and lies in the plane formed by X and the magnetic axis). The average magnetopause location (dotted) at $\sim$22R$_S$ (the lower value from the bimodal distribution found by *Achilleos et al.* (2008)) is also shown (calculated using the *Kanani et al.* (2010) model). The X-Y and Y-Z planes are shown in the bottom-left and bottom-right respectively.

southern cusp observations presented in this thesis (JAN07, FEB07, and MAR07). The orbit of the spacecraft during these events is presented in grey in Figure 7.14; the three grey triangles present the locations of the cusp observations.

From the 9th of April 2007, the inclination of Cassini's orbit was being reduced until it was completely equatorial in the summer of 2007. From the 30th of August 2007, the inclination was once again increased until the trajectory favoured northern cusp observations, with latitudes $>50^{\circ}$ first occurring on the 1st of March 2008.

The trajectory of Cassini during the MAY08 observation is presented (blue) in Figure 7.14. During this time Cassini performs a sequence of orbits with a smaller perikrone of 2.7 R_S until July (the blue inner trajectory). Then the spacecraft performed a sequence of orbits with a larger perikrone of $3.2R_S$ (outer pink trajectory) from the beginning of August onwards. It is during these (pink) series of orbits that the four further northern cusp observations are observed. The AUG 08 and JAN09 are shown as stars (the AUG08 star is next to the blue and pink triangles), and the SEP08 and NOV08 are shown as pink triangles, to distinguish the two groups in the figure.

After a series of equatorial orbits, the spacecraft once again began a series of highly inclined trajectories in 2013. The orbits where the spacecraft observed the cusp in 2013 are shown in green. This time the part of the orbits in the northern hemisphere sampled the pre-noon region. The southern hemisphere part of the trajectory did not sample the correct area of the magnetosphere for southern cusp observations during this period. The trajectories had large altitudes when they sampled the high southern latitude region, and often crossed the magnetopause and observed the magnetosheath.

From the description of the spacecraft orbits, it can be seen that for each set, the trajectories were such that only one hemisphere in one quadrant (dawn−noon) was optimal to sample the cusp. In the northern hemisphere the cusp was observed at a range of altitudes and latitudes (Table 7.2) because the northern hemisphere had a variety of trajectories to allow this. The southern hemisphere observations occurred on only one set of orbits and therefore all share a similar location.

7.8 Discussion and Conclusions

Complementing the two events presented in the previous chapter, a further nine more cusp observations in the in situ data have been presented, two of which have two separate cusp observations with a separation of 7−10 hours. Including the observations presented in Chapter 6, this brings the total of cusp crossings to thirteen. Eleven of these crossings are adjacent to a boundary layer of mixed plasma before entering the magnetosphere, which are similar to terrestrial observations (e.g. *Dunlop et al.* 2005). The outbound crossings of JAN07-b and FEB07-b (which have the magnetosphere on both sides of the observation) however do not have a boundary layer, and instead pass directly into the magnetosheath. In contrast the AUG13 observation does have a boundary layer present on either side of the event.

Bunce et al. (2008b) used the JAN07 observations to provide evidence that the main auroral oval is produced by field-aligned currents close to the open-closed field line boundary. These FACs occur due to a velocity shear between the open (or outer and subcorotating) and closed (corotating) field-lines (*Cowley and Bunce* 2003). The FACs are detected after JAN07-a until 23:00 UT, and include the JAN07-b observation (Figures 7.3 and B.1). Taking the poleward edge of the FAC to occur on an L-shell of ∼34, then the invariant latitude is found to be ∼10°, much more poleward than the average of 15.6° found in the southern hemisphere by *Jinks et al.* (2014) (the authors did not investigate this particular orbit in their dataset). If the auroral oval is oscillating then it is feasible that the cusp could be observed a second time (*Arridge et al.,* in prep.) adjacent to the open-closed boundary discussed by *Bunce et al.* (2008b). These FACs observed on the JAN07 observation are different to those observed during the JAN09, FEB 07, JUN13 and AUG13 events. These events are much more short-lived, with the rotation lasting a few minutes and usually during the boundary layer observation adjacent to the cusp (*Badman et al.* 2014, showed that the duration of the FAC observation can explained by the spacecraft velocity, however this is not explored further in this thesis.). If the boundary layer were located on the outermost closed field lines, then the structure of the auroral FACs would be in agreement with the findings of *Bunce et al.* (2008b).

The cusp is observed twice (double observation with a time separation of ∼10.7 hours) for two of the three southern cusp observations, but this phenomenon is not

seen in any of the northern observations. *Arridge et al.,(in prep.)* attribute this to the oscillation of the southern auroral oval as found for the main auroral emission by *Nichols et al.* (2008). *Bunce et al.* (2014) have shown that the northern auroral oval also oscillates. Further investigation into checking whether the spacecraft trajectory in the northern hemisphere is conducive to detecting the cusp twice (with a separation of ∼10.7 hours) should be undertaken to see whether Cassini should observe oscillations in the northern cusp during our events.

One-hour-period bursts of high energy electron flux have been found for some of the magnetospheric observations (adjacent to the cusp), most obviously observed in the FEB07 observation between 20:00 and 23:00 UT, and the JUL13 event between 21:00 and 23:00 UT the day before. *Roussos et al.* (2015) reported a statistical survey of similar bursts found in the LEMMS observations. These bursts were found to map to the dayside magnetopause, with their cause not currently understood; they have been suggested to be related to reconnection processes. If this relation is true, it would not be surprising that the bursts are located close to the open-closed field line boundary.

All of the cusp observations have been compared to the propagated upstream solar wind data from the propagation model, mSWiM. Eight (JAN07, FEB07, SEP08, NOV08, JUL13, JAN 09, MAY08) out of eleven cusp events occurred during increases in the ram pressure of the solar wind, five of which occur during significant peaks (>0.05 nPa), while the other three have coincide with modest increases in ram pressure. It is worth noting that two of these events occur 75 days after apparent opposition, and so the propagated parameters are less accurate (*Zieger and Hansen* 2008). An increase in ram pressure produces a compression of the magnetosphere which has been shown to provide more favourable conditions for reconnection to occur (*Jackman et al.* 2004). Three of these eight observations also do not have high Alfvénic Mach numbers, resulting in a lower β magnetosheath. Hence for these observations, the reconnection that must have led to the cusp events must have occurred at a location on the magnetopause where the local magnetic shear must have been extremely large, i.e. close to 180° (*Slavin et al.* 1984; *Masters et al.* 2012). Of the other four observations that do not coincide with increases in ram pressure, only one (AUG13) had an M_A of ≤20. The others did not occur during peaks or troughs in M_A. The B_{Normal} component of the IMF is not presented as it is the

least accurate of the variables produced by mSWiM, and therefore it is not possible to correlate the orientation of the predicted IMF to the observations. However for periods of high M_A, one would assume that the local shear angle at a reconnection site would have to be very high or anti-parallel.

The results show that reconnection and subsequent cusp observations can occur during a variety of solar wind conditions. However the presence of so few cusp examples during overlapping spacecraft orbits (specifically the latter half of 2008) imply that the necessary solar wind conditions required for reconnection to occur are not as common at Saturn as at Earth, supporting the conclusion of *Masters et al.* (2012), that reconnection at Saturn is most often surpressed. This finding also supports the open flux investigation reported by *Badman et al.* (2013). From a large set of auroral images, the authors found that although Saturn has a similar relative amount of open flux (2-11%) as Earth, the usual percentage of flux that was closed in between observations is much lower (∼13%, whilst at Earth ∼40-70%). Assuming that, over adequately large timescales, the amount of flux opened is equal to the amount closed, opening of flux occurs during fewer events or at a lower rate than at Earth.

The variety of the characteristics of the plasma observations suggest different processes ongoing during the different cusp observations. The most striking is the first observation of lobe reconnection occurring during MAR07 (Figure 7.6). A "reverse-sense" ion energy latitude dispersion is observed. This is then followed by a "normal-sense" dispersion. This is the only example we present which has reconnection occurring at two different locations during the same cusp interval.

The SEP08 and NOV08 events both present very tenuous plasma observations. The low ion counts make it difficult to discern an energy-latitude dispersion. There is a possible dispersion in the NOV08 event, however it is inconclusive. Due to the weak ion counts, it is also not possible to deduce from what direction the ions are observed. These two observations are very similar to each other but not to the other events. The reason these observations are so short in duration could be due to reconnection having only just occurred at the magnetopause, and so the spacecraft enters the polar cap quite soon after the start of the cusp. This is supported by the observation of high-energy electrons in the MIMI-LEMMS instrument characteristic of the magnetosphere (panel c) during SEP08, with the interpretation that if the

field line had just been newly reconnected, not all of the magnetospheric energetic electrons would have left the field line and would still be observed.

Multiple ion energy-latitude dispersions are observed during the MAY08 observation. The observation of magnetospheric plasma (high energy electrons in panels Figure 7.7a,c) between the first and second dispersions implies that this may be a temporal observation of the cusp motion over the spacecraft, and not two separate cusps. A similar observation was found at Earth (e.g. *Zong et al.* 2008; *Escoubet et al.* 2013), where a double cusp was observed, and was shown to be the motion of the cusp due to a change in the IMF orientation. Without multiple spacecraft to test whether the cusp has moved, this hypothesis cannot be verified.

The continuous observation of the cusp during the second and third consecutive dispersions is different. The multiple dispersions are not due to a motion of the cusp because there is a change in electron energy distributions. If the cusp had moved we would expect the electron energy distribution to be the same. Moreover there is no change in the ion energies. If the cusp had moved, the ion energy would be dispersed in the opposite sense on neighbouring intervals. However there is a step-up in the energy which shows that 'pulsed' reconnection is also occurring on this day. This is a similar observation to the JAN09 and AUG08 events presented in Chapter 6. The locations of the MAY08 and AUG08 events are very similar, and the energy-pitch angle analysis reveals a similar field-aligned distance to the reconnection site. This finding indicates the possibility that the same area of the magnetopause is being reconnected for these two events. The MAY08 and JUL13 observations also differ from all the others in that the spacecraft is already on open field lines mapping to the polar cap (observation of background levels of electrons and ions in the instruments). In the other cusp observations however, there is a definite transition from magnetospheric plasma (on closed) field lines, to the cusp plasma on open field lines. This comparison shows that the spacecraft is already traversing open field lines at the start of the observations for MAY08 and JUL13. These findings in their entirety suggests that there is severe motion of the cusp and magnetospheric field lines over the spacecraft.

The ion compositions in the cusp and the adjacent magnetosphere show that the [m/q=2]/H^+ ratio is much higher in the magnetosphere (8.3±0.27−28.2±0.1) and is in agreement with other studies that suggest this region contains H_2^+ (*Thomsen*

et al. 2010). In the cusp this ratio is much lower (average of 2.8±0.2) which is similar to solar wind observations and therefore the m/q=2 ion is more likely to be He^{++}. The average He^{++} to H^+ abundance ratio in the solar wind is ∼3% and ∼5% at solar minimum and maximum respectively (*Ogilvie et al.* 1989), which is the same as the values found in the cusp. These authors reported very occasional abundance ratios of He^{++}/H^+ of ∼10%, however these occurrences are very rare. The water group to proton (W^+/H^+) ratio, is also much higher in the magnetosphere in comparison to the cusp, as expected (the moon Enceladus is the main source of water group ions).

The field-aligned distance to the reconnection site was calculated for each dispersion (Table 7.1), and has produced a varied set of results. The results presented in this chapter had a range of values of 16±1 to 50±20 R_S in comparison to the previous chapter of 27±5 to 51±2 R_S (for the JAN09 and AUG08 events). The calculated field-aligned distances to the reconnection site were then used to estimate the location of the reconnection site along the magnetopause (shown in Figure 7.10). This showed that reconnection occurred at various areas along the magnetopause, with most of the cusp days producing locations polewards (towards the north) of the subsolar regions, towards higher latitudes. This is in agreement with *Desroche et al.* (2013) who modelled the regions more likely to be reconnected along the magnetopause (as well as independent MHD simulations of the IMF effect on Saturn's magnetosphere by *Fukazawa et al.* 2007) and showed that such regions would be generally poleward of the subsolar point. An example of the locations viable for reconnection based on diamagnetic suppression (modelled by *Desroche et al.* 2013) is shown in Figure 7.15. As mentioned above, most of the calculated reconnection sites are in agreement with *Desroche et al.* (2013), but most of the JAN09, as well as the MAR07 reconnection locations lie outside the predicted areas found by *Desroche et al.* (2013) (i.e. southward of the subsolar point). However, the simulations by *Desroche et al.* (2013) are for southern summer conditions (whilst three of our events are during northern winter) as well as for certain local IMF orientations (indicated in Figure 7.15), and without a detailed knowledge of the upstream IMF, it is difficult to make any more detailed comparison between their predictions and our calculated reconnection locations for MAR07 and JAN09. The results generally show that the cusp maps to reconnection occurring over a wide range of locations along the magnetopause, despite the lower reconnection efficiency at Saturn in comparison to

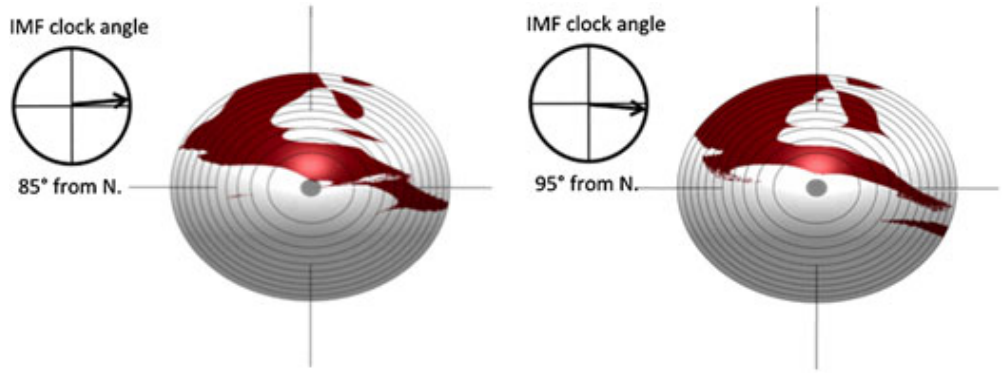

Figure 7.15: Areas viable for reconnection to occur along Saturn's magnetopause based on suppression by the diamagnetic drift reported by *Desroche et al.* (2013), for two IMF orientations. The area where reconnection can occur is shown in red and is centred north of the subsolar point.

that at the Earth.

Strong diamagnetic depressions in the cusp have been widely studied and are often observed at Earth (e.g. *Zhou et al.* 2001; *Trattner et al.* 2012) and at Mercury (*Winslow et al.* 2012). Diamagnetic depressions at Earth have been correlated with highly energetic particles in the cusp (e.g. *Chen et al.* 1997, 1998; *Nykyri et al.* 2011a,b). Such depressions are observed during eight of the eleven events that have been studied in the Saturnian system in this thesis. Some of the observed depressions would not be treated as a depression in certain studies which impose a criterion of at least a 20% decrease in magnetic field strength (*Niehof et al.* 2010). The strength of the depression has been suggested to be correlated to the reconnection rate (*Slavin et al.* 2014), and this could mean that lower reconnection rates (which are expected at Saturn) could thus result in less significant magnetic field depressions. To try and elucidate the physics of the diamagnetic depressions in Saturn's cusp and shed further light on magnetopause reconnection at Saturn, the penultimate chapter of this thesis focuses on the diamagnetic depressions.

Chapter 8

Diamagnetic Depressions in the Cusp

In this chapter the magnetic field observations in the cusps are investigated more closely. The field aligned currents determined from the B_ϕ component of the magnetic field were analysed in the magnetosphere in Chapter 6. However this chapter takes a different route and focuses on the cusp observations, specifically the decreases in the magnetic field magnitude. The analysis involves comparing the magnetic field observations from MAG to that of a magnetic field model. The depth of the depressions are calculated as well as the consequent magnetic pressure decreases. These results are compared to particle pressures observed by the plasma instruments. The association of energetic He^{++} solar wind ions with the diamagnetic depressions at Earth is well established (e.g. *Chen et al.* 1997, 1998), and therefore these particles at Saturn are also examined, as well as other high energy particles that could be causing the depressions.

The previous chapters have introduced all the cusp observations present in the Cassini data, and most of these events had (to varying degrees) a magnetic field depression. An interesting characteristic of the magnetic field depression (which was briefly mentioned in previous chapters) is the observation of the depression sometimes not being centred on the cusp itself, but on the equatorward boundary. The cause of this effect is also examined.

All the cusp observations which occurred in the summer hemisphere presented a depression. The winter observations only present depressions in two out of the five events, and these are also the least obvious decreases in magnitude. This interesting seasonal effect will be discussed at the end of this chapter. The analysis of the magnetic fields is introduced first, starting with the magnetic field model.

8.1 The Magnetic Field Model

The data were compared to a magnetic field model in order to calculate the magnetic pressure change during the depression. The location within the magnetosphere is used as an input to calculate the model magnetic field at the specified location. The position of the spacecraft is used to define the location in the magnetosphere. At this location the model then calculates the strength of an axisymmetric, internal magnetic field (therefore B_ϕ is not in this model) with superimposed model ring current fields. The axisymmetric internal magnetic field is calculated as a spherical harmonic expansion and uses the coefficients from *Burton et al.* (2010) (g_1^0, g_2^0 and g_3^0 are the Gauss coefficients [dipole, quadrupole and octupole] taken to be 21191 nT, 1586 nT, and 2374 nT).

The model also generates magnetic fields induced by the ring current. The ring current parameters are taken from *Bunce et al.* (2007). These parameters are dependent on the subsolar positions of the magnetopause, which are predicted using velocity and density propagations by mSWiM to calculate the standoff distance. The field vectors associated with the ring current sheet are calculated from the model described by *Connerney et al.* (1981, 1983), using the analytical approximations presented in *Giampieri and Dougherty* (2004). The cylindrical radial and axial components of the model field are then transformed to radial and theta components (B_R and B_θ) in KRTP. These values are then added to the axisymmetric field vectors from the internal model. The original ring current model written by *Giampieri and Dougherty* (2004) in Matlab was translated into IDL and added to the axisymmetric model calculations to complete the routine put together by *C. S. Arridge* (2008). The output of this routine is used here.

After calculating the model magnetic field at the position of the spacecraft, the following method is used to calculate the magnetic pressure deficit associated with the decrease in the observed magnetic field data from MAG. The calculated magnetic pressure deficits will be compared to the observed plasma pressure to investigate any anti-correlation. This method has been used previously to compare the magnetic and plasma pressures at Mercury's equatorial magnetosphere (*Korth et al.* 2011), as well as the cusp at Mercury (*Winslow et al.* 2012), both of which used data from the MESSENGER spacecraft.

By comparing the MAG data to the magnetic field model, the depression was

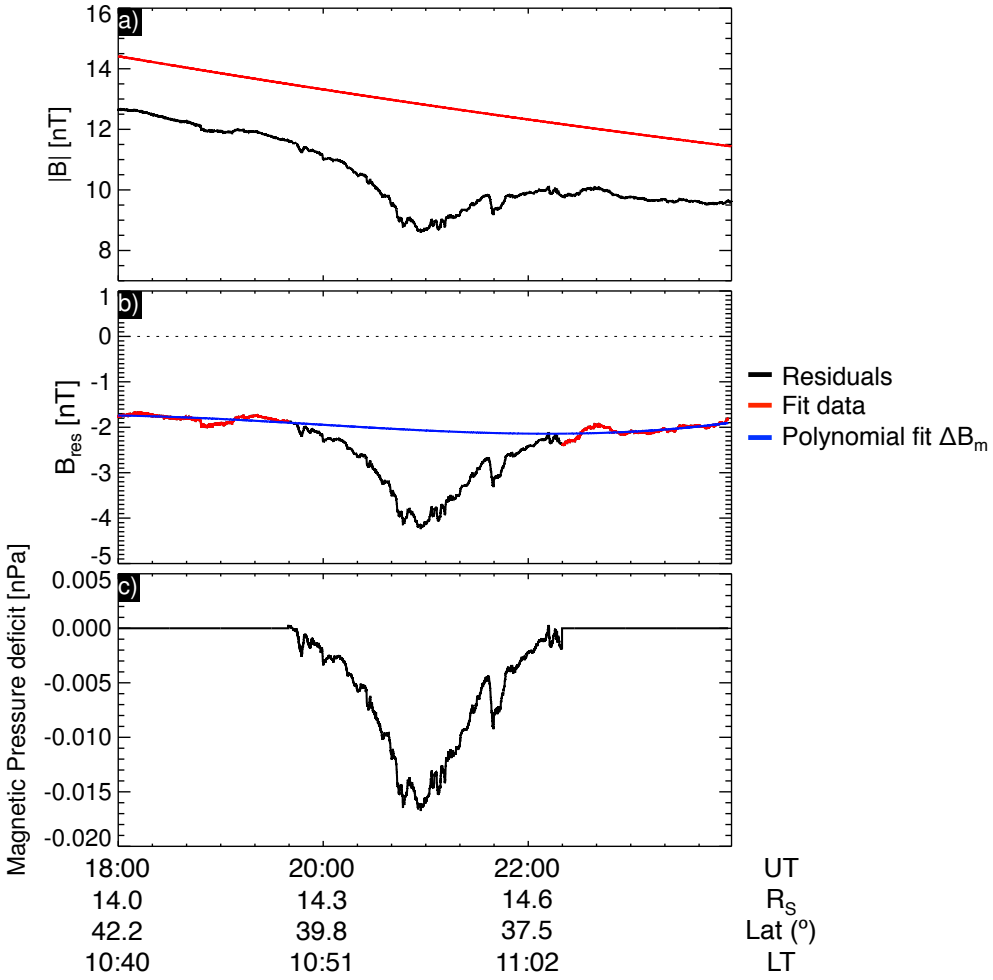

Figure 8.1: An example of the magnetic model, MAG data and the pressure calculated for the JUN13 cusp. Panel a) the model (red) and 1 second average MAG data, b) the residuals of the magnetic depression (black) the fitted residual before and after the depression (blue) and the polynomial fit (red), and c) the calculated magnetic pressure deficit.

selected by eye from where the MAG data (observed magnitude) first departed from the general trend of the model. This can be seen in an example (for the JUN13 event) in Figure 8.1a. The observed magnetic field (i.e. 1 second averaged MAG data in black) at 19:40 UT is no longer decreasing at the same rate as the field model (shown in red), which is taken to be the start of the depression. The observed field is at a minimum at ∼21:00 UT, which marks the centre of the depression. At 22:20 UT, the observed field resumes its general decrease in magnitude similar to the field model.

The model magnetic field was subtracted from the observations, to obtain the total residual field $B_{res} = |B|_{obs} - |B|_{model}$. The result of this subtraction (B_{res}) can be seen in panel b) of Figure 8.1 in red and black, where the black residual

field highlights the depression and the red shows the constant residual field. The depression was removed from the residual data, so that the background unperturbed residual magnetic field could be calculated during the depression. This was achieved by applying a third degree polynomial fit to the steady part of the residual field (i.e. before and after the depression) shown in red. The resulting polynomial fit can be seen in blue (in Figure 8.1b) and represents the residual field in the absence of a diamagnetic depression.

The calculated polynomial fit was then added to the model, so that the unperturbed magnetic field could be estimated. B_{res} was then subtracted from the unperturbed field and the result was used to calculate the magnetic pressure using the magnetic pressure Equation 1.39. This pressure thus represents the magnetic pressure deficit that occurs due to the depression. This calculation can be written in the following equation:

$$\Delta p_B = \frac{(|B_{model} + \Delta B_m|)^2 - |B|^2}{2\mu_0} \tag{8.1}$$

where ΔB_m is the polynomial fit, and Δp_B is the magnetic pressure deficit arising from the observed depression (as mentioned previously, this method is explained in *Korth et al.* (2011), and has been used for Mercury cusp analysis (*Winslow et al.* 2012)). The resulting pressure deficit resulting from the magnetic depression can be seen in panel c of Figure 8.1.

This pressure deficit is used to predict the plasma pressure increase that is required to balance the total plasma pressure considering this is a diamagnetic effect, from $P_{Plasma} = P_{Total} - P_{Mag}$. This calculated pressure will be compared to the observed particle pressures.

This method was completed for all the depressions. The model subtraction and magnetic pressure deficit calculation process can be seen for each depression in the appendix in Chapter C. However, a summary of the magnetic pressure deficits of all the cusp observations (in comparison) can be seen in Figure 8.2. The panels are arranged chronologically. The time is centred on the centre of the depressions characterised as 00:00, so that the duration of the observations can be seen and compared. The pressures are scaled so that the depth of the depressions can also be compared. The dashed lines indicate the entry and exit of the cusp intervals as

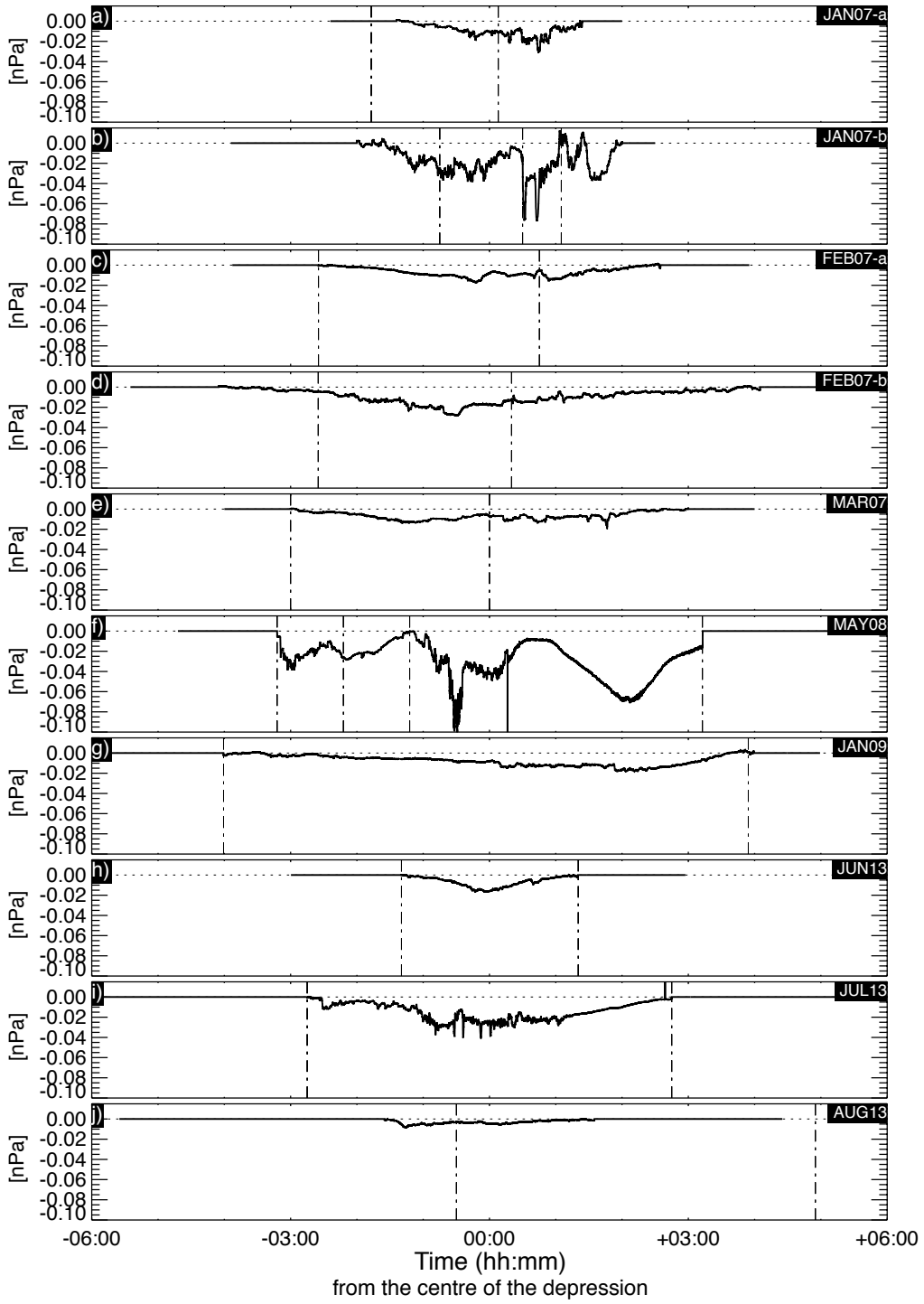

Figure 8.2: The magnetic pressure deficits of all the cusp observations listed chronologically with the JAN07 and FEB07 separated into their two separate cusps *a* and *b*. The x-axis is zero on the centre time of the depressions, and time is displayed in the hh:mm format, with six hours on either side of the centre. The dashed lines represent the entry and exit of cusp plasma interval as characterised by CAPS observations described in previous chapters.

categorised by CAPS observations in the previous chapters. For panel (b), the first dashed line represents the start of the 'mixed/cusp' (labelled as such in the previous chapter, in Figure 7.3) plasma region, followed by the cusp plasma during the JAN07-b event. Panel (f) shows the two entries and exits of the cusp observations for the MAY08 event.

It should be immediately noted that the last major depression during the MAY08 (panel f) observation at ∼+02:00 is most likely an artefact of the magnetic field model subtraction due to such large magnetic field strengths as well as overlaps between model and data. However the first two decreases in pressure are observed in the magnetic field data as depressions (specifically the depressions at approximately -03:00 and -00:30). The MAY08 observation has the most dramatic and the strongest magnetic pressure decrease. This is due to the field strengths being significantly higher, with total field magnitudes of ∼30 to 40 nT. In comparison the field strengths in the other depressions occur between ∼8 and 15 nT. The JAN07-b depression has the second strongest magnetic pressure decrease, due to the field being depressed to a magnitude of ∼2 nT (∼85% decrease), values similar to the magnetosheath. The regions on either side of the cusp (for JAN07-b) can clearly be seen to also depress the magnetic field. The entrance into the depression starting in the magnetosphere followed by the mixed plasma forms a shallow depression and the "cusp-proper" creates a very sharp decrease as described previously. Another two depressions are observed upon exiting the cusp, in the magnetosphere again.

The JAN09 depression is interpreted to occur during the whole cusp observation and not for just the small ∼2 nT field decreases at ∼00:00 and +02:00. The model field was observed to increase steadily throughout the cusp, whilst the observed field did not, creating a large increase in field strength upon exiting the cusp, thereby defining the exit out of the depression.

Magnetic depression observations in 2007 (panels a-e) and the final observation (j) can be seen to not be at the centre of the cusp interval (as indicated by the dashed lines), and continues into the magnetosphere. For the JAN07-b event, the depression occurs on either side of the cusp (i.e. in the magnetosphere).

Example depressions observed at Mercury and Earth are presented in Figure 8.3 for comparison, from the MESSENGER and Cluster missions (*Winslow et al.* 2012; *Shi et al.* 2009a). An example magnetic pressure deficit from MESSENGER data

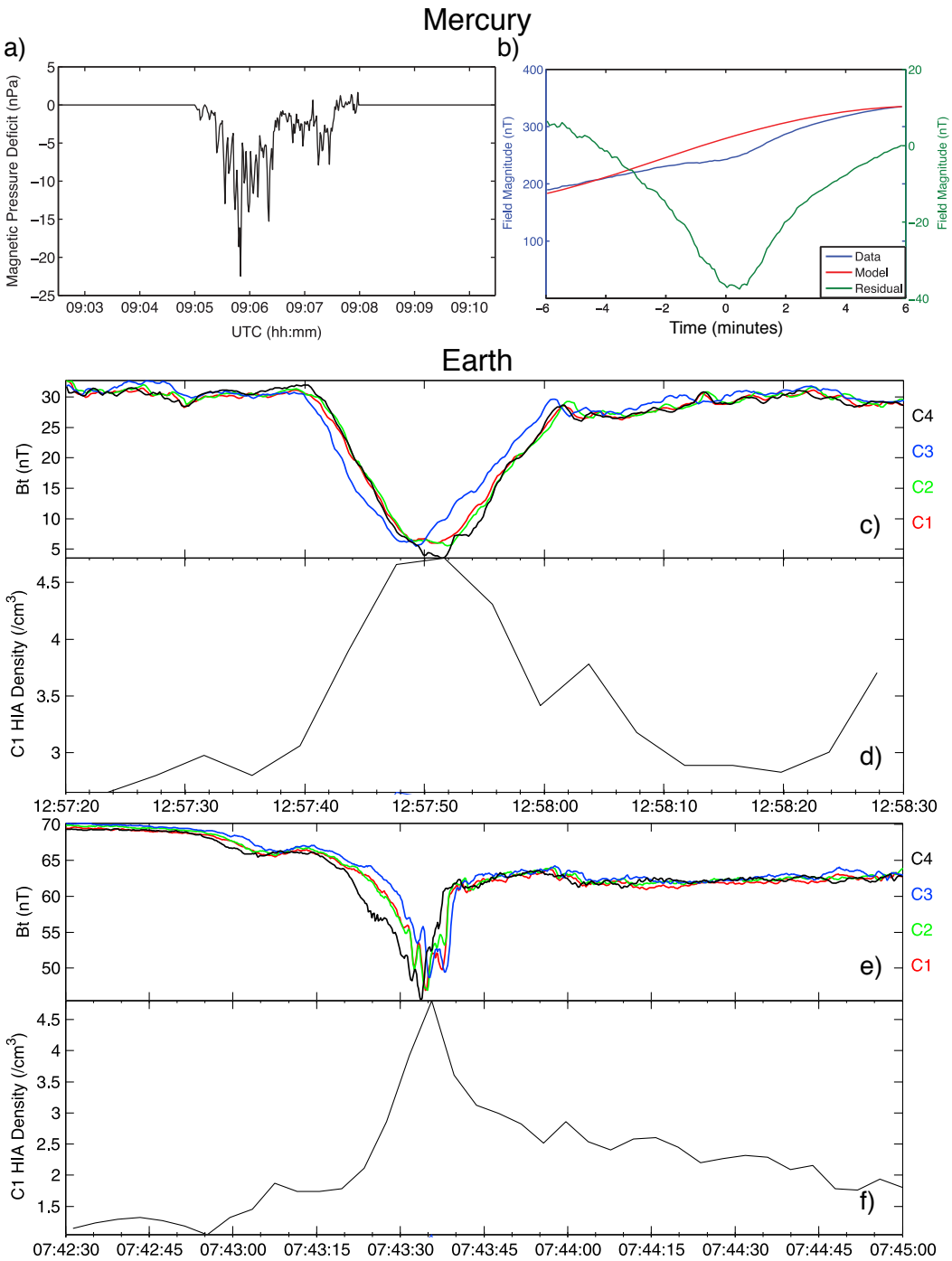

Figure 8.3: Magnetic depression examples from Mercury and Earth observations (adapted from *Winslow et al.* 2012; *Shi et al.* 2009a). Panel a is an example of the magnetic pressure deficit calculation from a MESSENGER cusp crossing, whilst panel b is a superposed epoch analysis of many cusp observations with the observed field (blue), model (red) (both indicated by the scale on the left) and residual magnetic field (green). Panels c−d show two examples of Earth depression observations obtained by the Cluster spacecraft (C1−C4) and their corresponding hot ion densities (from C1), shown below.

(panel a) shows much larger depths (over 20 nPa) compared to the largest observed at Saturn (0.1 nPa). The observations are also more turbulent and short-lived (minutes compared to hours). The superposed epoch analysis from the MESSENGER data of 169 cusp crossings (out of 279 orbits) is presented in panel b; these data show that the magnetic depths are significantly larger. The depressions observed at Saturn are of the order of a few nT (the largest being ∼10 nT for JAN07-b), whilst at Mercury ∼40 nT is typical. The terrestrial cusp magnetic field does not fluctuate as much as at Mercury (panels c and e), however the depressions have similar depths (tens of nT). The hot ion densities in the terrestrial cusp are also presented for the corresponding depressions (panels d and f). It can be seen that the densities are anti-correlated with the magnetic field strength changes.

Voyager 2 crossed through Neptune's cusp during its flyby (*Szabo et al.* 1991; *Lepping et al.* 1992). However due to the dramatic offset between the planet's rotational and magnetic axes (∼47°, *Ness et al.* 1989), the cusp was pointed towards the Sun, and so the spacecraft crossed from the magnetopause directly into the cusp. The data can be seen in Figure 8.4. The region inbetween the two dashed lines is identified to be the cusp by *Szabo et al.* (1991). Two decreases in the magnetic field at ∼18:30 and ∼19:30 UT can be seen. However it is not clear whether these are depressions as they are similar to the changes in the magnetic field seen in the magnetosheath. The ion density is also observed to decrease upon entering the cusp from the magnetosheath, but it is not possible to determine whether any density changes are correlated to the magnetic field.

The Saturn magnetic pressure depressions (associated with the cusp intervals) will now be compared to plasma pressure observations from various in situ instruments onboard Cassini.

8.2 Comparison of plasma and magnetic pressures

8.2.1 Overview for MAR07

The magnetic field analysis and pressure deficit calculation as well as the particle pressure components for the MAR07 depression are presented in Figure 8.5. Panels a to c are in the same format as Figure 8.1 and show the MAG data and magnetic field model (shown in panel a), the residual magnetic field and the polynomial fit (in panel b) and the calculated magnetic pressure deficit (c). Panels (d) to (g) show

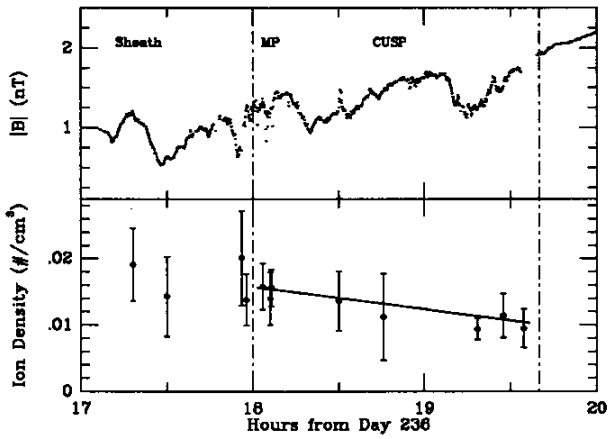

Figure 8.4: Magnetic and ion observations from Voyager 2 in Neptune's cusp (*Szabo et al.* 1991). The region between the two dashed lines is identified as the cusp. 'MP' stands for the magnetopause.

calculated CAPS moments including (d) ELS pressure, (e) ELS density, (f) IMS proton pressure and (g) IMS m/q=2 pressure. Panel (h) shows the calculated high energy particle pressure from CHEMS. The CHEMS He^{++} and W^{+} observations are also shown in panels (i) and (j), as time-energy spectrograms. The vertical dashed lines show where the cusp is during these observations (the first half of the depression). The pressures are not scaled, so that each component can be seen fully. The magnetic pressure deficit (c) reaches a general trough of -0.012 nPa (a short-lived drop is observed just before the end of the depression to reach -0.02 nPa).

Much of the electron pressure is at the noise level, except for the latter half of the cusp and the second half of the depression. The electron pressure contributes the least to the total plasma pressure due to the very small electron mass, however the depression changes in the cusp are directly anti-correlated to the electron density. This shows that the depression is a diamagnetic effect as there are more particles gyrating to produce an opposing magnetic field which creates the depression.

The energetic particle pressure (from CHEMS) is the most dominant component of the plasma pressure. The peaks are anticorrelated with the magnetic pressure deficit troughs. The CHEMS pressure is higher at these times ($\sim$0.025 and $\sim$0.045 nPa) than the magnitude of the magnetic pressure deficits ($\sim$0.012 nPa).

During the latter half of the depression (adjacent to the cusp, in the labelled 'magnetosphere') there is an increase in flux of both energetic He^{++} and W^{+} ions

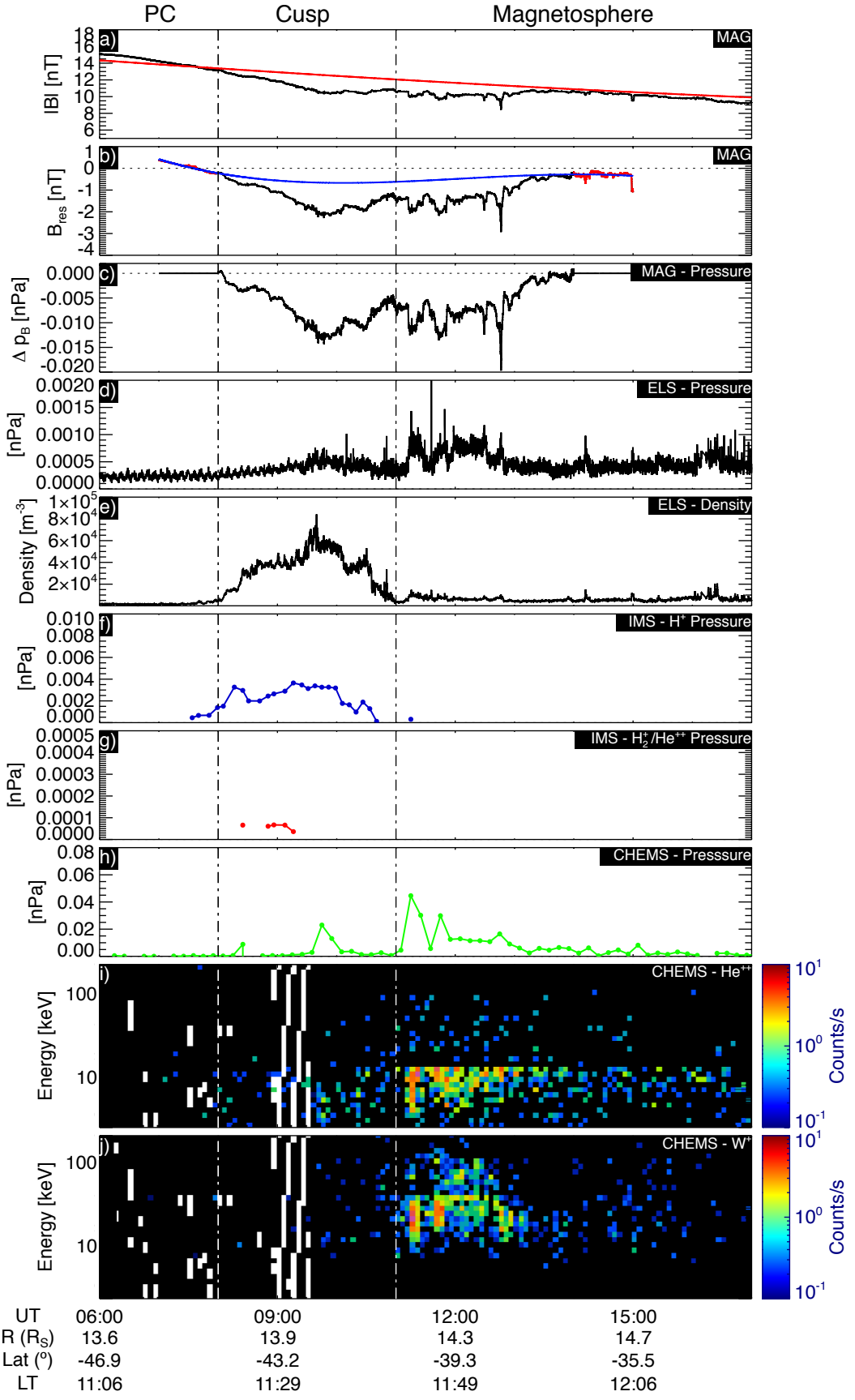

Figure 8.5: All the pressure observations, including the magnetic pressure analysis (top three panels) for the MAR07 event. Time-energy spectrograms for He^{++} and W^{+} observed by CHEMS are also shown (panels i and j). The pressure axes are not uniformly scaled. Figures in the same format for the other depressions can be found in Appendix C.

(panels i and j). Assuming that the alpha particles are of a solar wind origin and the water group ions are of a magnetospheric origin, increased counts of both (with high energies) at the same time would suggest this to be a heated, mixed plasma.

At Earth, the cusp magnetic depressions are usually centred on the high density magnetosheath plasma. In the MAR07 example, the depression is observed to continue into the magnetosphere where there is evidently a high-pressure, mixed plasma layer next to the cusp, characterised by the (energetic) high CHEMS pressures and increased counts of He^{++} and W^{+}. This is a different region to the 'boundary layer' that was observed in previous chapters. The boundary layer was observed as a gradual increase of energy (and decrease in flux) of electrons observed in ELS. An example of this can be seen in Figure 8.6, labelled 'BL'. The transition can be seen between the low-energy magnetosheath-like plasma in the cusp and the higher-energy tenuous plasma in the magnetosphere. However once the spacecraft is in the higher energy region (labelled "depressed m'sphere layer"), the magnetic field depression continues until the particle flux (of high energy electrons and the transient He^{++} and W^{+} in CHEMS) and subsequently the plasma pressure decreases.

The CAPS-IMS plasma moment data were acquired from the NASA online Planetary Data System (PDS). Unfortunately the data are not provided with any uncertainty values so error bars could not be shown on any of this data.

The uncertainty on the MIMI pressure is dependent on the count rate during the interval. The data has a time resolution of 10 minutes, and so the uncertainty will be the square root of the total counts during this time interval. For a resolution of 10 minutes the uncertainty will be 4%-13% (for a count rate of 1 c/s - 0.1 c/s) (*Sergis et al.* 2009). An additional error of less than 30% is present due to CHEMS under-resolving the pitch angle distribution which is lower than the scatter in the data due to the dynamics of the system (*Sergis, priv. comm.*). This is a general understanding of the MIMI pressure calculations but is not run for each pressure moment.

Arridge et al. (2009) estimate the errors for the density and temperature for the CAPS-ELS data, and for values found in the cusp show that the error is of the order of 10% or less (for both the density and temperature). These errors have not been run for each data point (hence why there are no error bars on the plots). The technique run by *Arridge et al.* (2009) is an analysis of the noise properties of

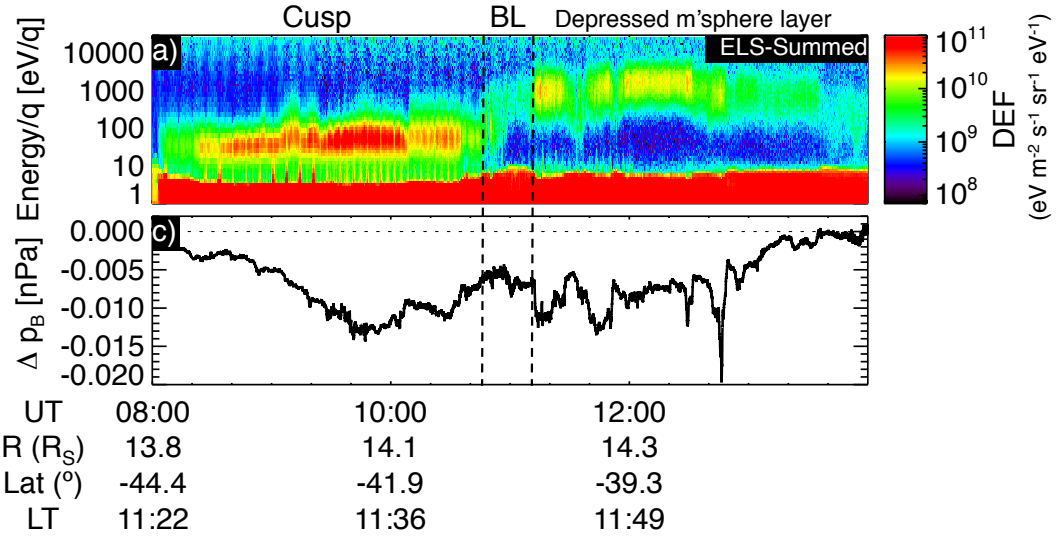

Figure 8.6: ELS observations of the different layers adjacent to the cusp, with the magnetic pressure deficit (b) for the MAR07 cusp. The boundary layer 'BL' has been discussed in the previous chapters. The high pressure magnetospheric layer which continues the depression of the magnetic field outside the cusp.

CAPS-ELS and their effect on the plasma moments, and as such does not provide an estimate of uncertainty for every plasma moment.

8.2.2 Summary of JAN07 and FEB07

The JAN07 and FEB07 (Figures 8.7 and 8.8, respectively) magnetic field analyses as well as the plasma pressure observations are presented in the same format as for the MAR07 overview shown in Figure 8.5. First, JAN07 will be described.

The JAN07-a depression peaks in the magnetosphere (∼12:30 UT), and the cusp's presence only adds to make the decrease appear more gradual. This morphology of the magnetic depression is the same as the MAR07 event, where the depression is also observed in the magnetosphere. The electron pressure is very low in the cusp due to the low energies, with an increase in the magnetosphere (higher energies), where it is anti-correlated to the magnetic pressure decrease. The depression begins when there is large increase in the electron density (when the spacecraft is partway through the cusp). Similar behaviour has been reported at Earth, where a magnetic decrease coincides with an increase in density within the cusp, causing the depression to not always be throughout the whole cusp crossing (*Niehof et al.* 2008). The IMS H^+ pressure steadily increases and maximises during the minimum depression, and accounts for approximately half of the magnetic pressure decrease. The high energy ion pressure in CHEMS contributes the other half of the pressure

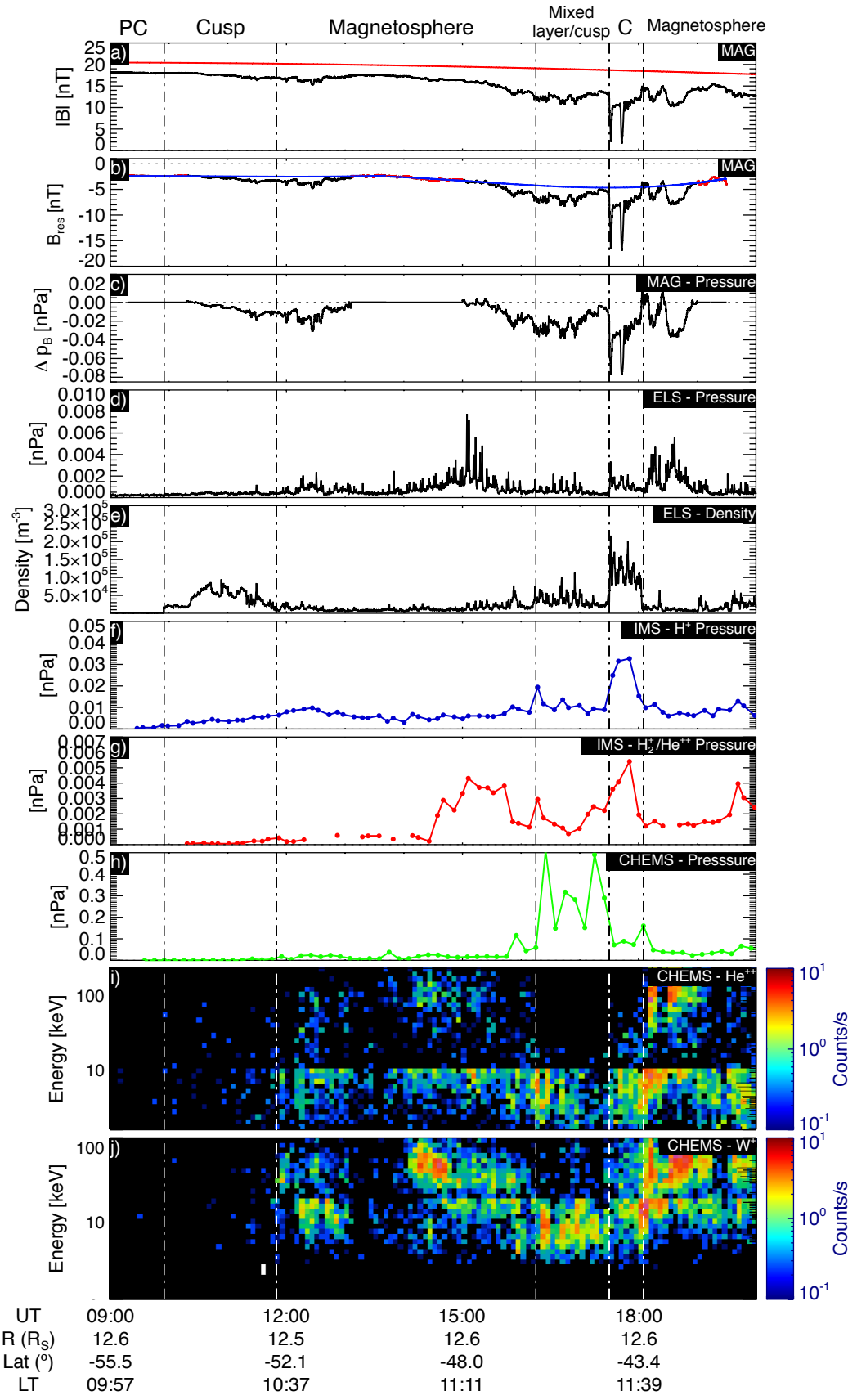

Figure 8.7: All the pressure observations, including the magnetic pressure analysis (top three panels) for the JAN07 event. This figure is in the same format as Figure 8.5.

equivalent to the depression, also peaking in the magnetosphere.

The start of the second depression in the JAN07 event occurs (at ∼15:30UT) with a large increase in the m/q=2 ion pressure (IMS), but it is still lower than the other pressure components. However this seems to be the cause for the start of the depression. The mixed plasma cusp region (the start of which is marked by the third dashed line in Figure 8.7) occurs during extremely large increases of pressure observed by CHEMS (increase from 0.1 nPa to 0.5 nPa) with a large increase in flux observed of energetic W^+ ions by CHEMS. However this pressure enhancement is significantly larger than the magnitude of the magnetic pressure decrease (0.02 nPa). During the JAN07-b depressions, the CHEMS pressure does not follow an anticorrelated trend to the magnetic pressure deficit. The first depression (between the third and fourth dashed lines) is shallow but has a large CHEMS pressure increase, whilst the following deep depression sees a decrease in the CHEMS pressure.

During the latter part of the cusp (between the fourth and fifth dashed lines at ∼17:45 UT), increases in He^{++} and H^+ pressures are observed (∼0.006 nPa and ∼0.04 nPa, respectively) as well as a significant increase in the electron density and pressure. The ion data is at too low a time-resolution to be able to determine whether there is an increase in pressure during the two strongest depressions in the magnetic field. The final two small depressions in the magnetosphere occur during increases in flux of energetic He^{++} and W^+ (CHEMS) as well as an observed increase in the ELS pressure.

Figure 8.8 presents pressure observations for the FEB07 events. The minimum magnetic pressure depression inside the FEB07-a cusp (at ∼17:50 UT) occurs during significant increases of all the components of the plasma pressure (except for electrons), including a burst of pressure observed in CHEMS. Similar to the MAR07 event, the depression is seen with a large increase in electron density. The depression continues into the magnetosphere, and it is during this interval that an increase in flux can be seen in the energetic He^{++} and W^+ (panel i and j) as well as an increased electron pressure. The presence of both solar wind (He^{++}) and magnetospheric (W^+) ions would (just like previous examples) suggest this to be plasma that has been mixed and heated.

The second depression is observed (between the third and fourth dashed lines) during a burst of energetic He^{++} at the 1 keV energy level, as well as increased

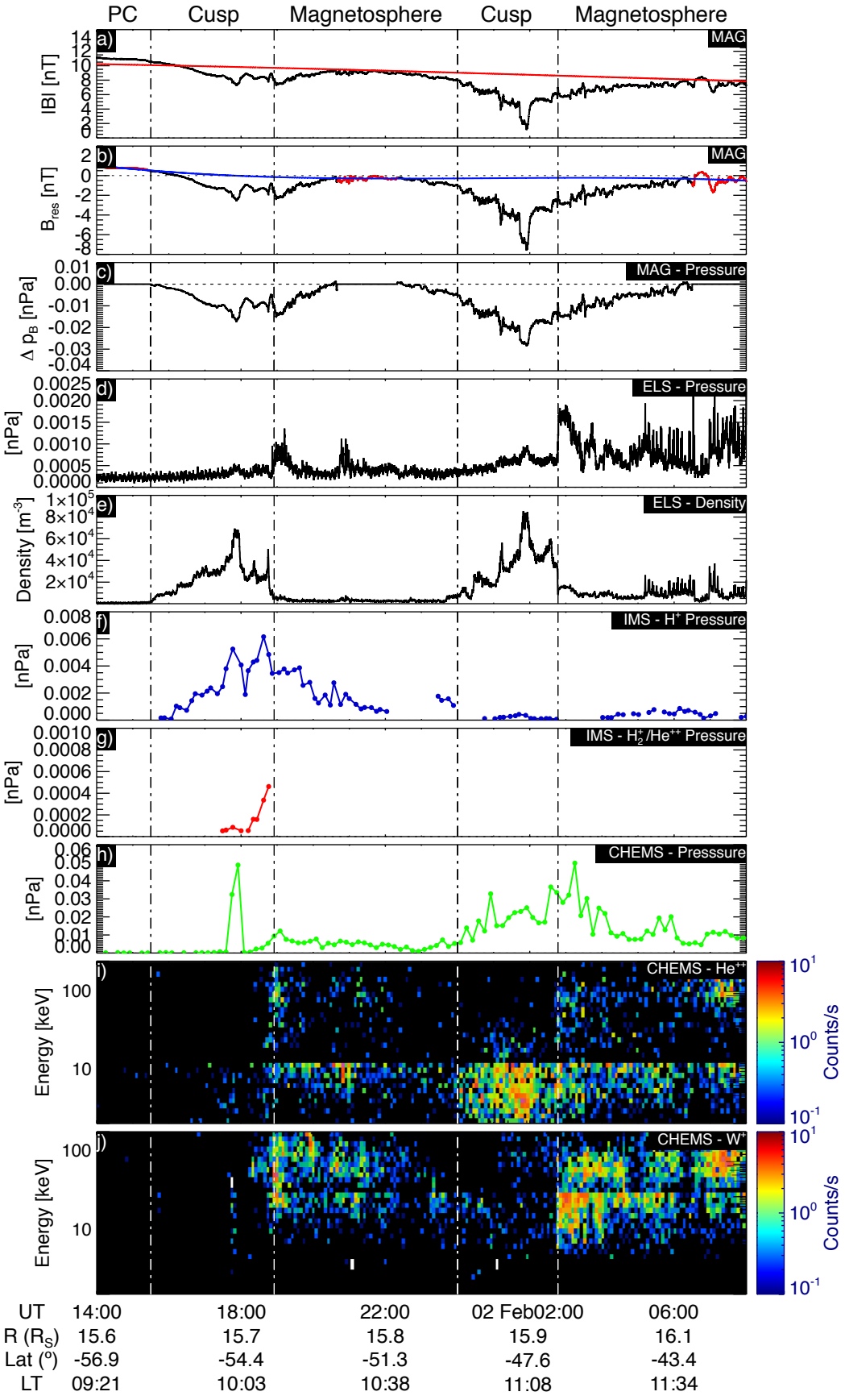

Figure 8.8: All the observations pressure observations, including the magnetic pressure analysis (top three panels) for the FEB07 event. This figure is in the same format as Figure 8.5.

electron and energetic ion pressures. A burst of W^+ is observed upon exiting the cusp at the end of the depression, including high electron pressures. The magnetic pressure deficit in the first cusp is $\sim$ 0.015 nPa whilst the pressures increase by $\sim$0.05 and 0.005 nPa (CHEMS and IMS). In the second cusp the pressure changes are more similar at $\sim$0.03 nPa. In the first cusp encounter, there is a discrepancy between the observed plasma and magnetic pressure changes, with the plasma pressure significantly larger. Upon exiting the second cusp, the magnetic depression does not end, but continues to decrease in magnitude gradually during a coincident decrease in CHEMS pressure. During this period, even though the plasma pressure is decreasing, it remains larger than the magnitude of the magnetic pressure deficit.

8.2.3 Summary of other observations

The rest of the observations have been summarised in one plot shown in Figure 8.9. In this figure, the pressure axes are not scaled so an individual comparison of the magnetic to plasma pressure can be made. The observations are grouped and plotted on different timescales (see the caption for more details). Plasma pressure observations are presented on a logarithmic scale due to the vastly different values for the different components of the plasma (with the corresponding magnetic pressure observations in the panel above), however the CHEMS pressure, which is the most dominant) is shown on the same scale as the magnetic pressure deficit, so that it can be compared to both the magnetic pressure and the other plasma pressure components. Particle pressures are shown from IMS (H^+ and [m/q=2], i.e. H_2^+ or He^{++}) as well as the total pressure observed by CHEMS. These observations are all presented separately in separate figures in Appendix C (in the same format as Figures 8.5, 8.7 and 8.8).

For the MAY08 observation the magnetic depression is well correlated with the electron pressure and density, however the plasma pressure increase of all the components at -00:30 does not account for the total magnetic pressure change, which is the largest observed at $\sim$0.1 nPa. Even though there are large peaks in all of the low energy plasma pressure components, the plasma pressure change is much lower than that in the magnetic pressure, in contrast to previous examples. There is also a large increase in flux observed in the energetic He^{++} ions during this central depression trough (see Figure C1.2).

H^+ (IMS) pressure during the JAN09 event is the most anti-correlated to the

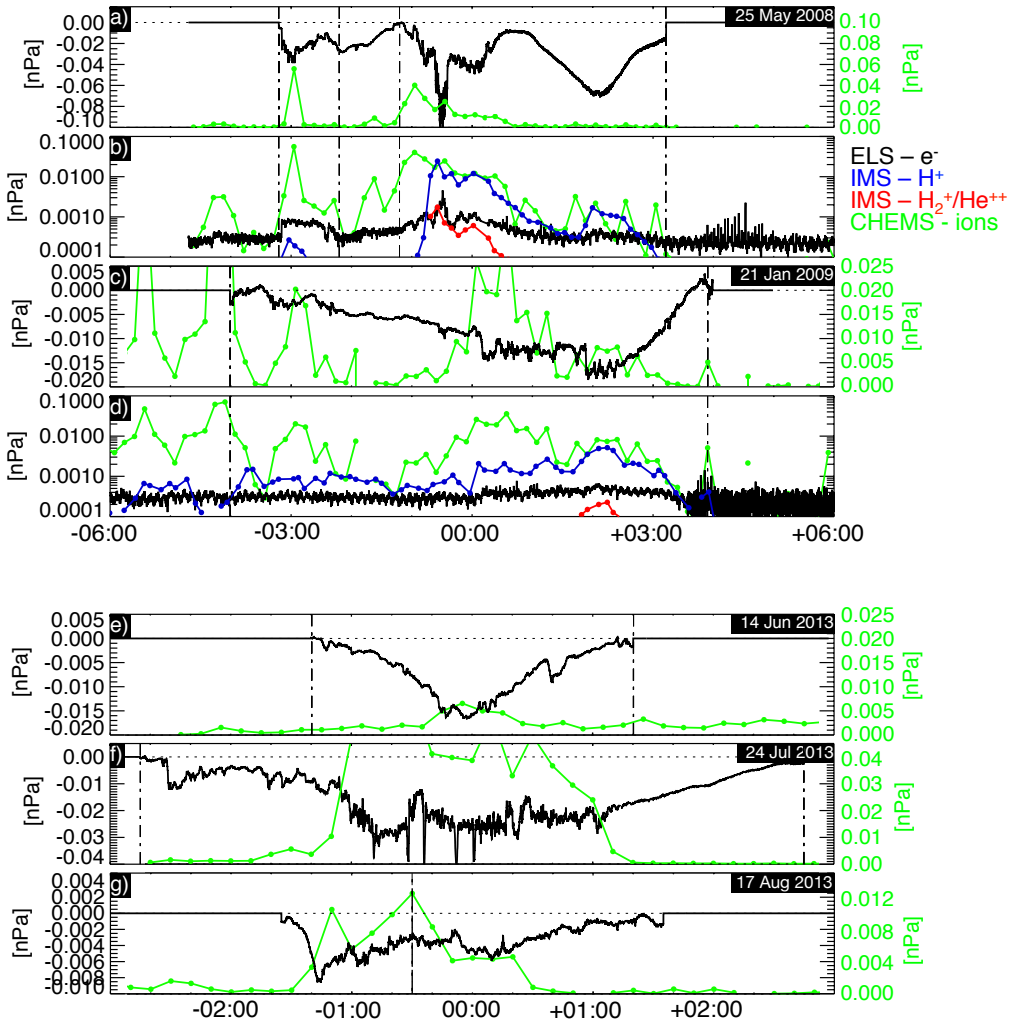

Figure 8.9: Magnetic pressure decreases and observed plasma pressures, with the former above the latter. The magnetic pressures are not on the same scale, and neither are the observed plasma pressures. The most dominant plasma pressure component (from CHEMS) is shown twice (to scale with the magnetic pressure, and to compare to plasma pressures). The MAY08 and JAN09 observations are presented on different timescales from the 2013 observations.

magnetic depression, with a gradual increase with a peak in both pressures, similar to the electron density. There do seem to be increases in the CHEMS pressure which correlate to the two sharp drops in magnetic field at 00:00 and +02:00 in Figure 8.9c), where the pressure of the magnetic depression is higher than the CHEMS pressure. The final decrease in the depression occurs (at ∼+02:00 in Figure 8.9) with modest increases in both H^+ and CHEMS pressure, which this time match (approximately) the magnetic pressure changes (∼0.015 nPa).

The final observed magnetic depressions occurring in 2013 are all very well correlated with increases in CHEMS pressures. For JUN13 the observed plasma

pressure however is less than half the value of the magnetic pressure decrease (∼-0.015nPa). There is also a small increase in energetic He^{++} flux (see Figure C.3). For the JUL13 and AUG13 events the CHEMS pressures overcompensate for the magnetic pressure decrease by ∼0.06 nPa and up to ∼0.006 nPa respectively. There is also a very large increase in the energetic He^{++} flux (the highest fluxes observed in the cusp) for the JUL13 event, as well as some increase in energetic water group ion flux (see Figure C.4). This indicates that this plasma is composed of mixed solar wind and magnetosphere particles. The AUG13 depression is mainly centred on the high water group fluxes in the magnetosphere, with the depression decreasing in the cusp (similar to the southern observations).

8.2.4 Discussion of the observations

From comparing the magnetic field and plasma measurements it has been shown that the particle and magnetic pressure changes do not compensate each other for most of the events. The method presented here calculates the magnetic pressure, with the polynomial used as a 'baseline' for the subtraction from the model. From the figures showing the method (Figures 8.1, 8.5, 8.7, and 8.8), the model field magnitude is stronger than that measured by MAG. The model field can vary for different solar wind dynamic pressures and therefore magnetopause standoff distances, and without upstream monitors this value can only be estimated. The polynomial addition removes any possibility of a larger background field that is caused by an unobservable global depression. This results in the calculated magnetic pressure deficit being a conservative lower estimate.

However, even with slightly more liberal calculations, the results would still not account for some of the large discrepancies with the plasma pressure observations. For most of the depressions the CHEMS (usually the most dominant plasma pressure) pressures are two or three times larger than the magnetic pressure deficit, and for two examples they are lower. Also for some observations the CHEMS pressure peaks do not match the troughs of the magnetic deficits, the most obvious being during the JAN07-b depression. All the depressions in the cusp are observed during an increase (and a complete anti-correlation) in the low energy electron density (where ELS is available), which is usually matched by a corresponding ELS pressure peak (but not necessarily a complete anti-correlation between magnetic and plasma pressure changes). This aspect is similar to the observations at the terrestrial cusp

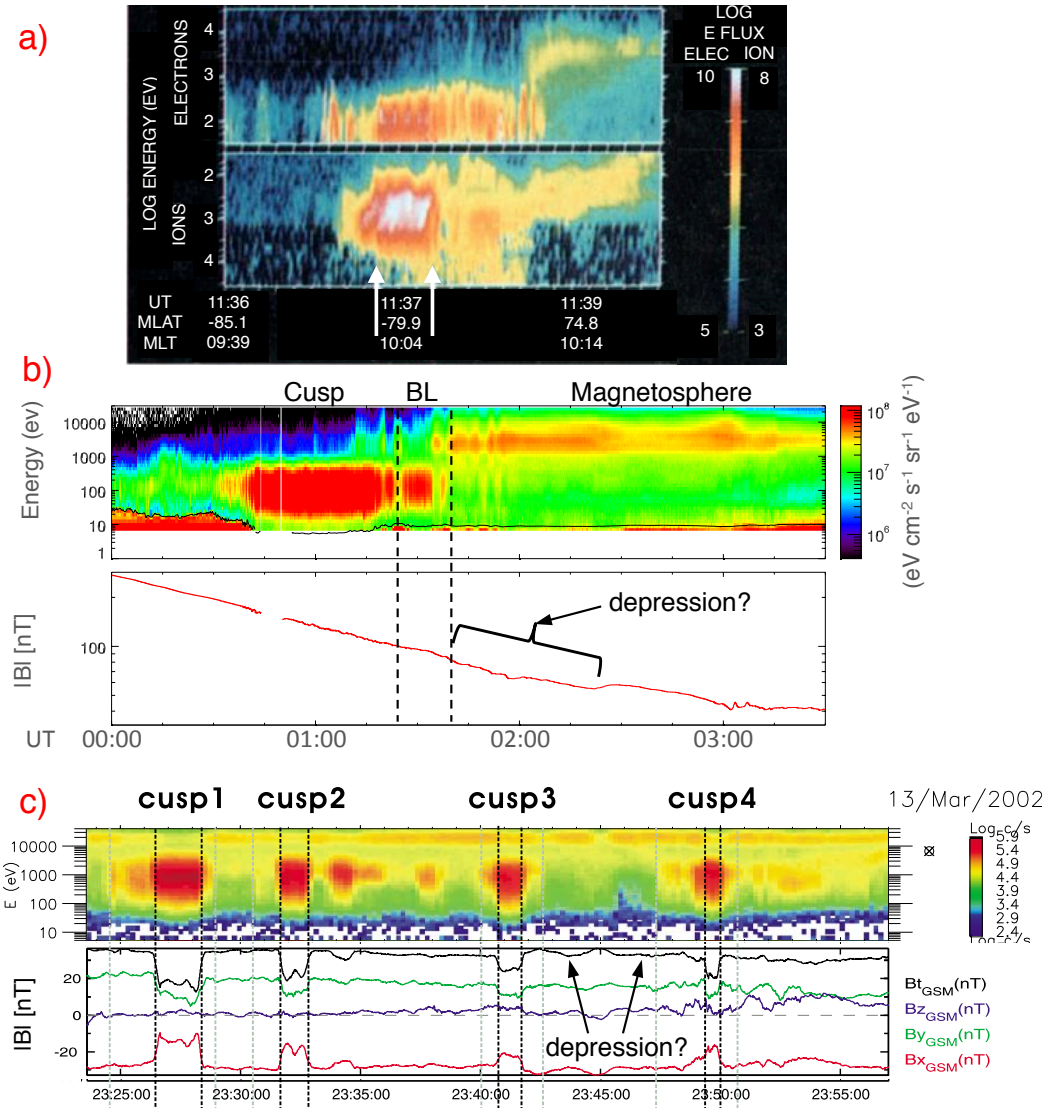

Figure 8.10: Earth observations of the cusp and magnetic field depressions. Panel a) is adapted from *Newell and Meng* (1988), and shows a DMSP-F7 cusp observation (two white arrows point to it) and the cleft region (later in time) with more energetic plasma. Panel b) shows Cluster (C2) electron data, where the spacecraft passes through the cusp and then (what is identified by *Bogdanova et al.* 2008) the boundary layer 'BL', similar to the Saturn observations, and the magnetosphere. The magnetic data also shows a possible depression in the magnetosphere. Panel (c) is adapted from *Shi et al.* (2009b), electron and magnetic data show the cusp and associated magnetic field depressions. Depressions are also observed in the adjacent magnetosphere.

(*Niehof et al.* 2008). However *Niehof et al.* (2008) found that the 'cusp diamagnetic cavities' (CDCs) also occurred during increases in the energetic He^{++} counts.

This finding introduces two different characteristic observations at Saturn, where although the energetic He^{++} is observed in the depression, it is not always observed during the large low-energy electron density increases in the cusp, but instead in the adjacent magnetosphere. This was illustrated in Figures 8.5 and 8.6, where a higher-energy plasma population is observed in the magnetosphere, where the depression continues. This higher-energy electron population with slightly higher densities nearer the cusp is similar to terrestrial observations which were called the 'cleft' in the 1980s, and once thought to be part of the cusp. An example of the terrestrial data (electrons with ions underneath) can be seen in Figure 8.10a (*Newell and Meng* 1988). The cusp region can be seen in the middle of the plot shown by the two white lines, followed by a boundary layer and then the cleft (the high energy electrons and ions).

A similar observation can be seen from the Cluster data (C2 spacecraft) in Figure 8.10b. This event was discussed (and the electron data presented) by *Bogdanova et al.* (2008). The authors locate the boundary layer in many cusp crossings (which they identify to be a high-latitude extension of the low-latitude boundary layer), before entering the magnetosphere. The authors do not present the corresponding magnetometer data (shown here), which shows a possible depression in the adjacent magnetosphere. For terrestrial magnetic cavity studies this would not be classed as a depression as it does not have a magnitude decrease of at least 20% (e.g. *Niehof et al.* 2008, 2010). This is very similar to the MAR07 observations, except that in the MAR07 interval the depression occurs in both the cusp and the adjacent magnetosphere.

Other similar observations made by Cluster (C1) are presented in Figure 8.10c. Ion and magnetic data show multiple cusp observations with their corresponding magnetic depressions. However, in the adjacent region, where high energy plasma is observed, a smaller depression is also observed (examples marked by the labelled arrow in Figure 8.10c). These high energy regions are labelled the 'high-latitude-trapping region' by the authors (*Shi et al.* 2009b), and correspond to the last closed field lines of the magnetosphere.

The Saturn examples are slightly different, with the depressions not usually

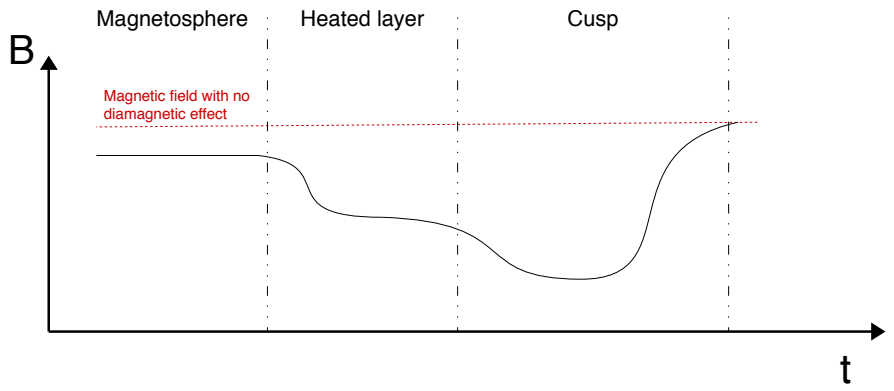

Figure 8.11: (a) An illustration of the magnetic field observations.The red line shows the magnetic field which is free of plasma, and no diamagnetic effect is observed.

centred on the cusp as defined from the plasma observations. In the cusp the depression is usually anti-correlated with the low-energy plasma density and pressure. The particles producing a diamagnetic effect in the dense magnetosheath plasma depress the field in the cusp. As the spacecraft crosses out of the cusp the larger plasma pressure continues to depress the magnetic field in the adjacent magnetospheric layer. This plasma pressure then decreases and the magnetic depression is no longer observed. But instead of causing two depressions like the previous Earth example, the depression is largely continuous. This is schematically illustrated in Figure 8.11.

Within this high pressure plasma region in the magnetosphere, there are observations of increases in the flux of doubly ionised helium and water group ions, usually more so than in the cusp (except for the FEB07-b event). The composition of this plasma, as well as increases in the CHEMS pressure (and high energy proton counts observed in LEMMS), would suggest a mixed plasma of solar wind and magnetospheric origin.

If the assumption is taken that the alpha particles are observed due to an injection from the magnetosheath at the same time as (or shortly before) the reconnection event (that is attributed to the cusp plasma being present), then we assume that the presence of He^{++} suggests that the alpha particles also lie on open field lines. Therefore, by taking an equatorward trajectory for the spacecraft (for the southern cusp observations), Cassini will have passed through the polar cap and then into the cusp filled with low-energy plasma, followed by further open field lines with the higher energy particles. This means that what we have assumed earlier is

the magnetosphere (and labelled as such in the plots) is actually an equatorward region of the cusp. This would therefore fit a simple velocity filter paradigm, where (for an equatorward trajectory) the low energy plasma is observed, followed by the energetic alpha particles (in CHEMS). This will make the depression lie solely in the cusp (now that we have redefined this layer temporarily for this explanation). Although this interpretation appears sensible there are problems.

Firstly, the ion energy latitude dispersion observed in the IMS data would be expected to continue into this region, as well as an observation of a gradual electron dispersion linking the two regions. The electron observations from ELS during JAN07-a (Figure B.1) is the only event that displays a possible gradual change that appears to be an electron energy-latitude dispersion. The other observations show the two regions to be more distinct from each other. Of course if the field line convection speed is much greater than the spacecraft speed then a 'step-up' in energy would be seen in the electrons, as seen in Figure 2.6. In all the southern hemisphere the spacecraft is travelling equatorward, so in the opposite direction of the field line ($V_S \ll V_C$). If this plasma is injected at the same time, there should not be a time separation (such as the one observed) between the observation of low-energy electrons and high-energy alpha particles. A 50 eV electron characteristic of the magnetosheath would have an approximate field aligned velocity of ∼4000 km/s whilst a 10 keV/q He^{++} ion velocity would be ∼1000 km/s. This would mean that the electrons should be observed closer to the open-closed field line boundary, but instead the opposite is true.

However, if the field line was open, then the magnetospheric plasma would most likely have left the field line into the magnetosheath. A 1 keV equatorial magnetospheric electron at L∼25 (for the MAR07 example) would remain on a field line for ∼3 minutes (assuming a near field-aligned equatorial pitch angle). During this event the spacecraft has an equatorward velocity of ∼1.8 km s^{-1}. The observation of the depression in the magnetosphere lasts approximately for two hours (with He^{++} present). Since the magnetospheric plasma will only remain on an open field line for a few minutes, this field line cannot be newly opened as the spacecraft remains in this region for a significantly larger timescale.

Furthermore, there is a boundary layer observed between the two regions that has been interpreted to be the high-latitude extension of the low-latitude boundary

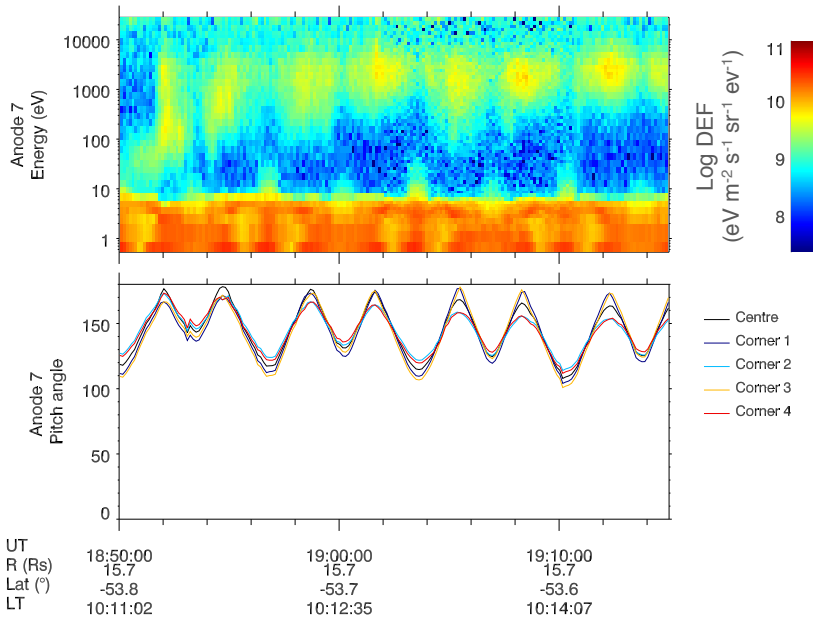

Figure 8.12: Anti-field aligned electron observation by ELS in the depressed magnetic field adjacent to the FEB07-a cusp. The top panels shows ELS Anode 7 observations, and below is the corresponding pitch angle look direction of the instrument.

layer. An example of this can be seen in Figure 8.6 labelled 'BL'. This layer separates the two regions, and would not be expected to occur if this was one cusp observation (divided into two different energy layers).

Secondly, the observation of a significant increase in the water group ions upon entering the high-pressure plasma region where the depression continues provides evidence that these are closed field lines with magnetospheric plasma present. 'Significant' here being defined by the fact that there are no W^+ ions observed above the detectability threshold of the instrument in the cusp, and they are in the high-pressure plasma region, with very high counts. This provides evidence that the labelling of this region 'magnetosphere' remains correct.

A possible explanation would be that this region is part of the auroral field aligned currents formed due to the velocity shear between open and closed field lines, which has heated the plasma. During these events full pitch angle coverage is not available. However, the pitch angle distributions of the electrons observed in ELS during this layer show that there are large increases in flux at the 180° pitch angle (upward from planet in the southern hemisphere) during all the observations in the transition layer (the only exception being the FEB07-b event where ELS is fixed). An example can be seen in Figure 8.12 (the other examples can be found

in the appendix). The top panel shows the observations from Anode 7 of ELS, and the bottom panel shows the pitch angle look direction. Upward (from the planet) electrons would not be associated with the aurora, as downward electrons are required to produce the emission.

8.3 Seasonal and Solar Wind Effect

At Earth it has been shown that magnetic field depressions are larger in the summer cusp (e.g. *Zhou et al.* 2001). The magnetic field depressions in the cusp (reported in this thesis) mainly occur in the summer hemisphere, with only two of the five cusp observations displaying depressions in the magnetic field in the winter hemisphere.

This effect is due to the summer cusp being tilted towards the incoming solar wind (shown in Figure 8.13), where the magnetosheath flow is slower and the density is higher. This results in a plasma with a higher density entering the summer cusp and subsequently depressing the magnetic field more than for the case of the winter cusp. Therefore, if the magnetosheath flow is slower, and density is larger nearer the subsolar point, it would be expected that cusp magnetic field depressions should be stronger at lower latitudes relative to the planet-Sun line (*Zhou et al.* 2001). In order to test this at Saturn, the magnetic field depressions have been arranged in order of increasing latitude from the planet-Sun line in Table 8.1, to see if there is a correlation. From the results, the depth of the depressions are not observed to decrease with increasing latitude, so this argument is apparently not valid for Saturn.

Figure 8.14 shows the magnetic depression relationship with the dynamic pressure and velocity of the solar wind. The Pearson correlation coefficient (r) which gives a measure of how well parameters are correlated has also been calculated. The Pearson coefficient is equal to 1 for a perfect positive correlation, -1 for a perfect anti-correlation, and 0 when no correlation is present. A strong positive correlation was found for the solar wind dynamic pressure, and a moderate positive correlation for the velocity.

These plots indicate that the depression is generally greater for larger solar wind ram pressures and velocities. A compressed magnetosphere and high solar wind velocities have been found to produce larger reconnection voltages at the magnetopause (*Jackman et al.* 2004). This has also been reported (*Zhou et al.* 2001) at

Table 8.1: The locations and depths of magnetic field depression (ΔB) arranged by latitude (relative to the ecliptic plane) magnitude.

Latitude (°)	|ΔB| (nT)	Distance (R_S)	Cusp
19	2.3	18	AUG13
19	2.2	14.3	JUN13
-28	2.6	13.8	MAR07
-29	12.3	12.6	JAN07-a
32	8.8	15.4	JUL13
-33	8.7	16	FEB07-b
-39	1.8	12.5	JAN07-b
-40	3.2	15.7	FEB07-a
45	2.9	16.5	JAN09
63	3.8	11.6	MAY08
65	–	11.1	AUG08
66	–	10.6	SEP08
66	–	12.2	NOV08

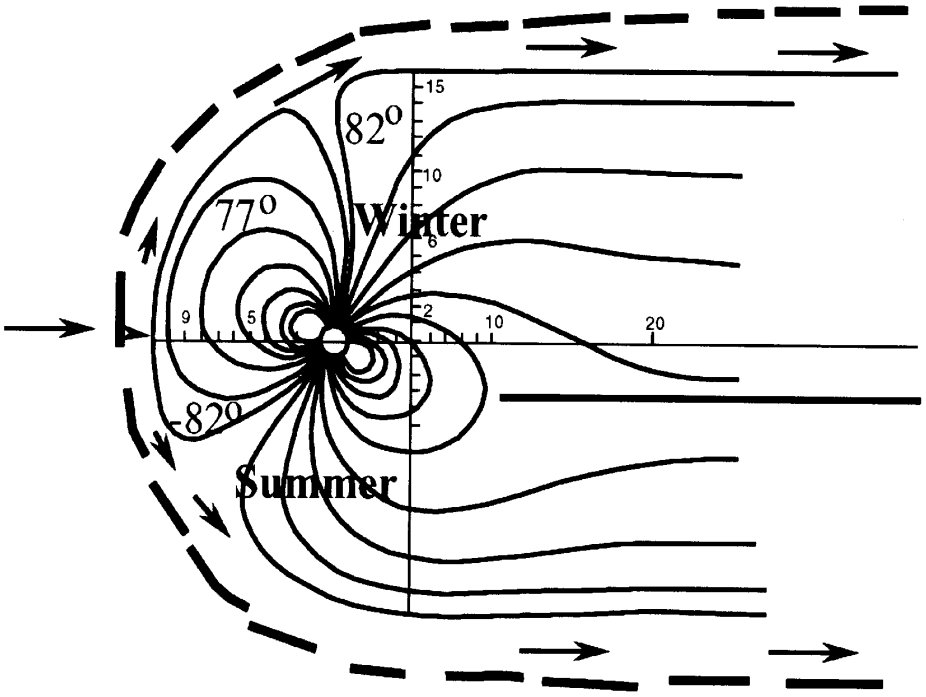

Figure 8.13: A depiction of the tilted terrestrial magnetosphere with the summer and northern hemispheres labelled. This shows that the cusp in the summer hemisphere is at lower latitudes relative to the ecliptic, where the magnetosheath flow is slower and denser in comparison to the winter hemisphere. This produces larger depressions at Earth in the summer hemisphere (*Wing et al.* 2005).

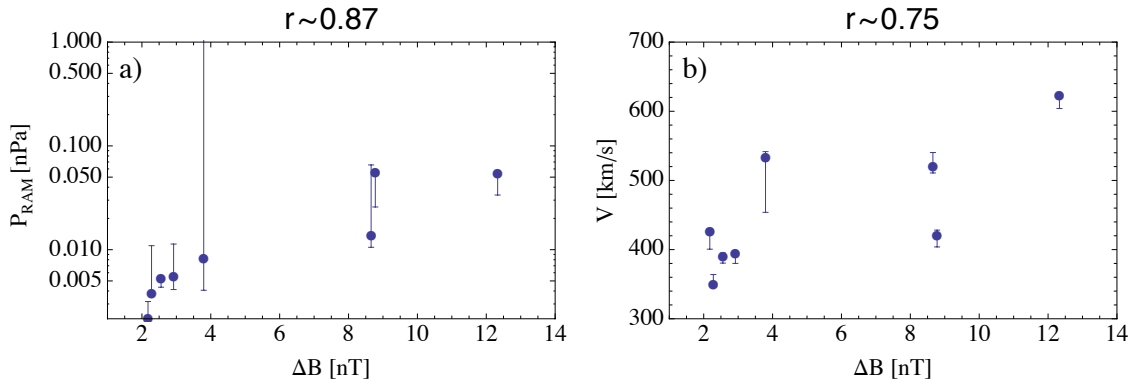

Figure 8.14: The correlations between solar wind parameters (P_{RAM} and velocity) and the depth of the magnetic field depression (ΔB). The Pearson correlation coefficient (r) is shown for both sets of data, with P_{RAM} and V having strong and moderate (respectively) positive correlations with ΔB.

the terrestrial magnetosphere (where diamagnetic depression depth increased with solar wind dynamic pressure).

No correlations could be found with the Alfvenic Mach number (M_A) of the solar wind and the depressions with so few data points. As mentioned previously one would expect larger depressions in the cusp with higher upstream M_A values, as this would be associated with a stronger shock, a more dense magnetosheath and therefore larger pressures in the cusp to depress the field.

The relevance of the He^{++} ions to the magnetic depression is analysed and presented in Figure 8.15. The minimum of the magnetic field during the depression (B_{min}), the event-averaged magnetic field strength (<B>) and the difference in strength of the magnetic field between maximum and minimum are shown. This shows that with the present data, no strong correlation can be found between the number of helium counts and the depth of the depression, nor the minimum magnetic field nor the magnetic field strength in general. High He^{++} counts are observed for both low and high magnetic field depths. In comparison, at Earth (e.g. *Chen et al.* 1998) found strong correlations between the depth of the magnetic field depression and the alpha particle counts.

8.4 Discussion

The magnetic depressions at Saturn have been presented and characterised in this chapter. A model of an axisymmetric internal magnetic field with a ring current field has been subtracted from the data. From this magnetic field subtraction,

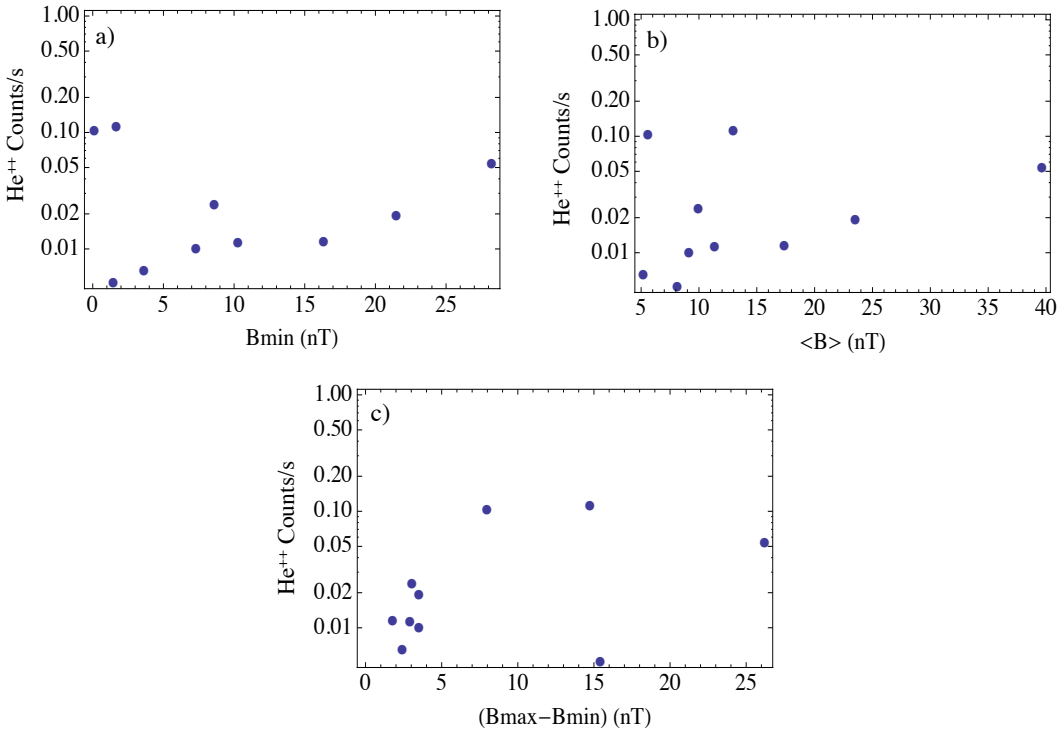

Figure 8.15: He^{++} counts are presented in relation to different variables of the observed magnetic field depression, a) the minimum magnetic field (B_{min}) found in the depression, b) the event averaged magnetic field strength in the depressions and c) the difference between the magnetic field strength at the maximum observed (usually at the start of the depression) and the minimum observed.

the magnetic pressure decrease in the depression was calculated and compared to observed plasma pressures, densities and fluxes of the various plasma components. The calculated magnetic pressure deficit was explained to be a lower limit because of the method used.

It has been shown that the magnetic depressions (mostly in the southern hemisphere) are not always centred on the cusp, but on the boundary with magnetospheric particles. The density of the plasma, which is of magnetosheath origin, is anti-correlated to the magnetic field depression in the cusp. The high plasma pressure in the magnetosphere adjacent to the cusp acts to continue the depression of the magnetic field (into the magnetosphere). The presence of mixed plasma of solar wind and magnetospheric origin during the latter half of the depressions introduces a problem of exactly defining this layer. The layer could either be reconnected (open) field lines, with energised solar alpha particles, or the auroral current region which is observed to occur on the open-closed field line boundary. Due to the duration of the

observation of this layer, this region is most likely to be on closed magnetospheric field lines, leaving the observation of solar wind particles an open question.

The plasma pressures in the cusp were sometimes found to overcompensate for the magnetic pressure decrease found in the depression. The combination of low depression depths found in the cusp at low magnetic field strengths (10-20 nT), and the absence of depressions in higher magnetic field strengths (30-40 nT) (unless there are very high electron densities), reveals the magnetic field to be much more difficult to depress at Saturn in comparison to observations at Earth and Mercury, and that depressions only occur at larger radial distance (>10 R_S).

Highly energetic He^{++} ions were observed during some portion of the magnetic depression in seven out of ten of the events. No significant correlation with the data available was found between the number of alpha particles observed and the depression of the magnetic field. This shows that although the helium ions are present, they are not necessarily the component of the plasma driving the depression in the observation at Saturn in comparison to Earth.

The depressions are expected to be stronger in the summer hemisphere due to increased magnetosheath densities and lower velocities whilst entering the cusp at lower latitudes to the ecliptic (from Earth observations). A comparison of the latitudes of the depressions revealed no trend and therefore this expectation is inconclusive. Although most of the observations of the magnetic depressions at Saturn occur in the summer hemisphere, with only 10 data points it is not possible to confirm this hypothesis with the limited observations from the Cassini spacecraft. The only conclusion that could be drawn from this analysis is that the cusps with no magnetic depression present occurred at the highest latitudes and lowest radial distances.

Chapter 9

Final Remarks

The role of reconnection and its effects on the dynamics of Saturn's magnetosphere is a highly discussed subject. The existence and relative importance of a Dungey Cycle driving Saturn's magnetosphere has been debated, with both extremes suggested (no or very little reconnection with magnetosheath plasma entry due to the magnetic field minimum at high latitudes; or a strong Dungey Cycle superimposed onto the Vasyliunas Cycle). The work of *Masters et al.* (2012) has shown that the conditions (during Cassini magnetopause crossings) for reconnection at Saturn are mostly suppressed to occur only at anti-parallel magnetic shears.

This thesis has continued this discussion with the presentation and analysis of the magnetospheric cusp at Saturn; a region in the magnetosphere where shocked solar wind plasma has direct entry due to previously closed field lies having undergone reconnection with the interplanetary magnetic field. In Chapter 1 the basic concepts of plasma physics were introduced as well as magnetospheric structure and dynamics. Chapter 2 presented the history of cusp observations at Earth and its characteristic observational signatures. Chapters 3 and 4 introduced Saturn's magnetosphere (and previous work on reconnection at Saturn) and the Cassini spacecraft with its instrumentation. Chapter 5 explained the method of calculating the distances to the site of reconnection from observations.

The first analysis of cusp observations at Saturn was presented in Chapter 6. The identification of the cusp was completed using low-energy plasma observations from the CAPS instrument. Other instrumentation was then used to complement this data set. The data and analysis of the two cusp crossings were presented to confirm this was the cusp at Saturn. The presence of energy-latitude dispersions

as well as energy-pitch angle dispersions in the ion data were similar to terrestrial cusp observations. The plasma data provided evidence that the cusp plasma was injected at different sites at the magnetopause, with some of the locations similar to those produced by modelling in the literature. Magnetic reconnection was shown to occur in a 'bursty' or a 'pulsed' manner. Signatures of field-aligned currents in the B_ϕ component of the magnetic field were investigated, and the associated particle signatures were observed mostly in the magnetosphere and equatorward region of the cusp.

Other cusp events were analysed and presented in Chapter 7. These were mostly identified from low-energy plasma observations (as in the previous chapter) however three cusp intervals were identified with magnetic field data and high-energy plasma observations (as the low-energy plasma data were not available). From this total of 11 cusp intervals, three cusp events were observed in the southern magnetosphere whilst eight were observed in the north.

The cusps were found at a range of latitudes from 37.5° to 72.7° in the north and -40.8° to -50.6° in the south, as well as a range of local times (09:39 - 14:55) and radial distances from the planet (8.2 - 18.5 R_S). The composition in the cusp is found to have a He^{++} to H^+ abundance ratio of 1.5% - 4.8% which is similar to solar wind observations of between ∼3% and 5% (*Ogilvie et al.* 1989). The solar wind conditions were found to vary between the different observations. The solar wind dynamic pressure as well as the Alfvénic Mach number varied between the available cusp observations, showing that reconnection can occur for a range of solar wind conditions at Saturn.

Two of the cusps were observed twice with a separation of 7 to 10 hours, bringing the number of individual cusp crossings to thirteen. Field-aligned currents were observed on the open-closed field line boundary for three events. Evidence of both lobe and subsolar reconnection occurring at the same time was observed during a single cusp observation. Whether this is a temporal or spatial effect is unconfirmed due to the lack of multiple spacecraft present. The distance to the reconnection site was calculated (from the available ion data), using energy-pitch angle dispersions. Using these distances the location along the magnetopause of the reconnection site was estimated. The resulting locations were largely found to occur near or north of the subsolar point, in agreement with the findings of *Desroche et al.*

(2013). However the reconnection site for two cusp events was found to also occur south of the subsolar point, showing that reconnection can occur in these regions as well.

Ten of the thirteen cusp observations also contained depressions of the local magnetic field strength; this result was presented in Chapter 8. The magnetic field pressure decrease was calculated via a technique involving magnetic field model subtraction. These calculations were then compared to the observed plasma pressures during the depressions. The overcompensation of the plasma pressure in comparison to the magnetic pressure decrease, as well as the low magnetic field depths show that the field at Saturn is more 'difficult to depress' than at Earth. The depressions were also not always centred on the cusp. Instead the presence of a high-plasma-pressure layer adjacent to the cusp has been found to also depress the magnetic field into the magnetosphere. The most likely explanation is that this is a closed magnetic field region with magnetospheric plasma, however the reason for the observation of solar wind energetic He^{++} ions in this region remains undetermined.

9.1 Open Questions and Further Work

The observations in this thesis were all selected due to similarities with the Earth's cusp. However the role of reconnection is different at Saturn, and so the data need to be surveyed for other possible observations of reconnection in the high latitudes that are different to what is expected at Earth. There are cusp-like intervals that are irregular or unusual (located in the high latitudes). Are these plasma observations indicative of the cusp? Why do they differ from the events presented in this thesis? These events need to be further investigated and characterised. How much of an effect does azimuthal motion of open magnetospheric field lines have on the cusp plasma observations? This aspect should be further investigated via theoretical modelling.

A search for flux transfer events (a product of magnetic reconnection) at Saturn has been conducted with the Cassini data (*Lai et al.* 2012). However, this work was limited to the equatorial region. Are there FTE observations in the high-latitude magnetosphere at Saturn? Are there other FTE-like signatures that should be investigated? A survey should be completed at higher latitudes for FTEs or FTE-like signatures, to explore whether they occur at other locations.

The final proximal orbits that have been planned for the end of the Cassini mission in 2016 and 2017 should be investigated for observations of the low altitude cusp. The trajectory of the spacecraft will have a perikrone on the dayside at approximately noon local time. These data will allow for the characterisation of the cusp at low altitudes, thus complementing the work in this thesis at 'medium' to high altitudes. The CAPS instrument would be extremely useful in this analysis if it were to be switched back on. However, if it is not, then the analysis will have to be done with other particle instruments (such as the LEMMS and CHEMS instruments) similar to what has been achieved with the 2013 observations presented in this thesis.

The Cassini-Huygens Mission has been one of the most ambitious and successful adventures into the outer Solar System, and this thesis ends with a breathtaking image (below) of Saturn's illuminated rings.

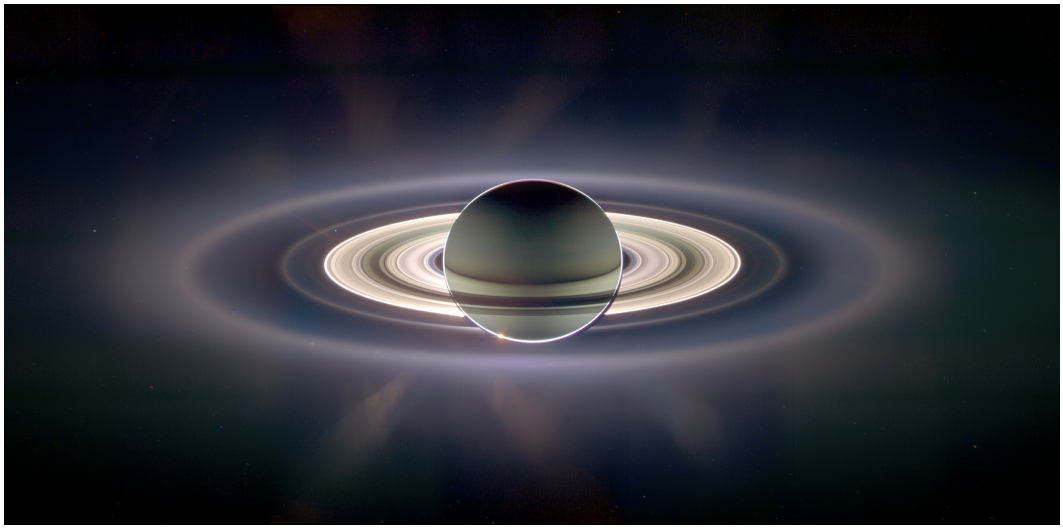

Figure 9.1: An exaggerated colour image taken whilst Cassini was in Saturn's shadow, and therefore the rings have been illuminated by the Sun. The E-ring can be seen as the most outermost ring visible (Credit: Cassini Imaging Team/SSI/JPL/ESA/NASA/APOD)

Appendix A

Evidence of Bursty Reconnection - Additional figures and tables

In this appendix, additional figures for the field-aligned current analysis and tables for the energy-pitch angle analysis are presented.

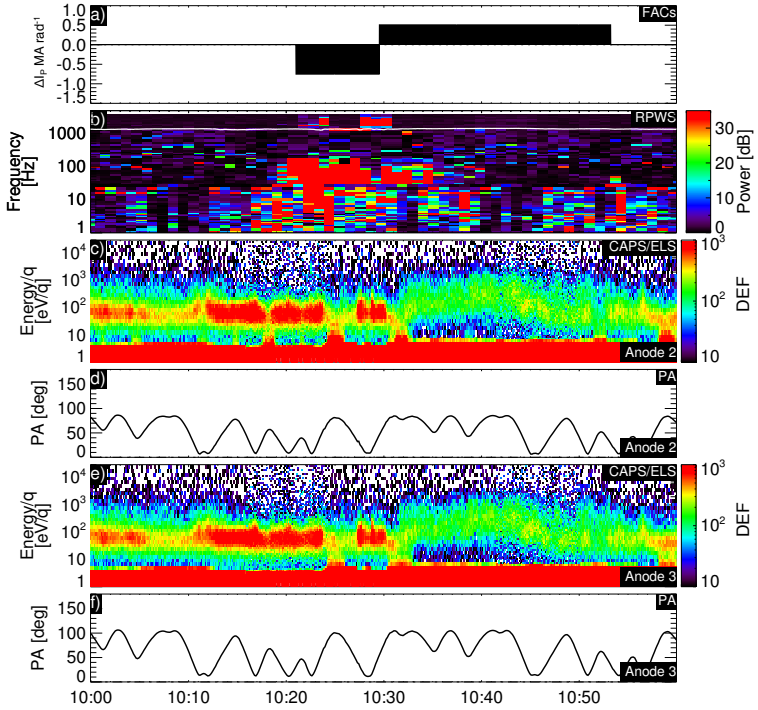

(a) Field aligned electrons from Anodes 2 and 3 (ELS).

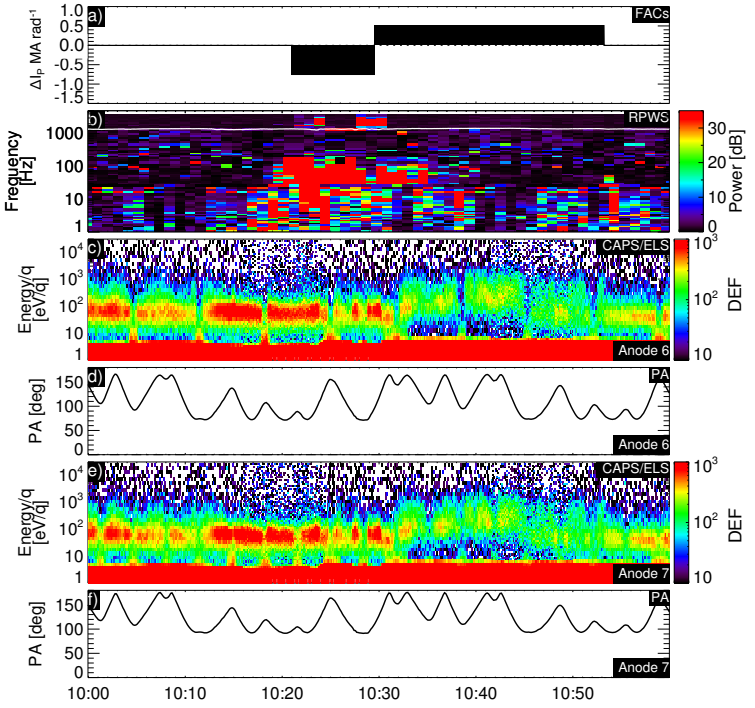

(b) Anti-field aligned electrons from Anodes 7 and 6 (ELS).

Figure A.1: FAC analysis for the JAN09 cusp interval. In both subfigures from top to bottom: (a) FACs: 3D, 3U, respectively; (b) RPWS electric field spectrogram, (c) ELS single anode observations, (d) pitch angle (PA) coverage of corresponding anode above, (e) ELS single anode observations, and (f) pitch angle (PA) coverage of the corresponding anode above. The units of the data in the panels are: (a) MA rad^{-1}, (c,e) Log DEF (eV m^{-2} s^{-1} sr^{-1} eV^{-1}). Part a (top) focuses on the field-aligned 0° PA electrons and therefore the downward region of the currents (i.e electrons upward from the planet), whilst the part b (bottom) focuses on anti-field aligned pitch angles (downward electrons, upward current).

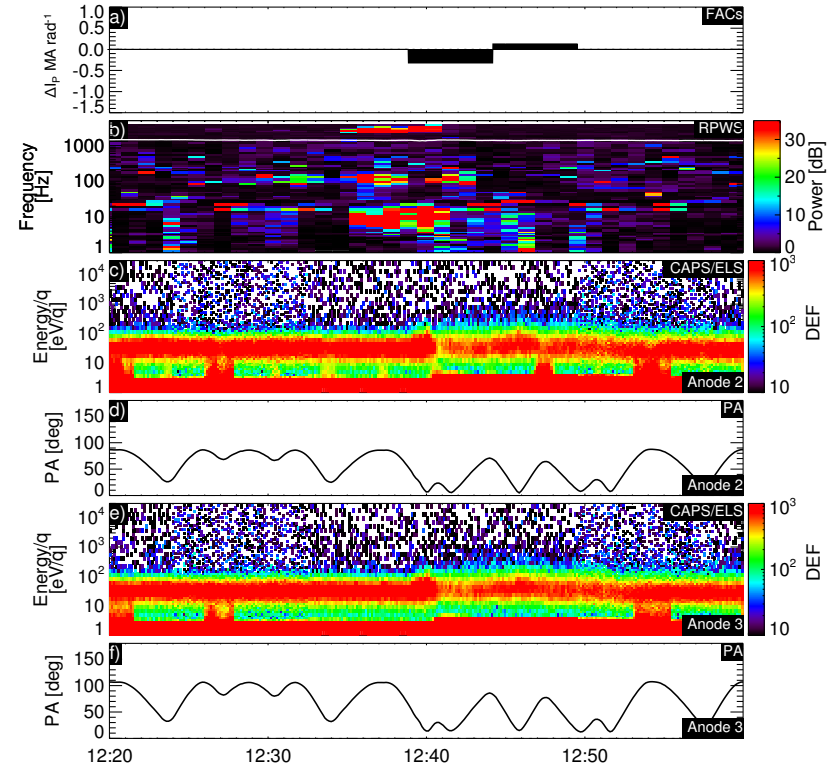

(a) Field aligned electrons from Anodes 2 and 3 (ELS).

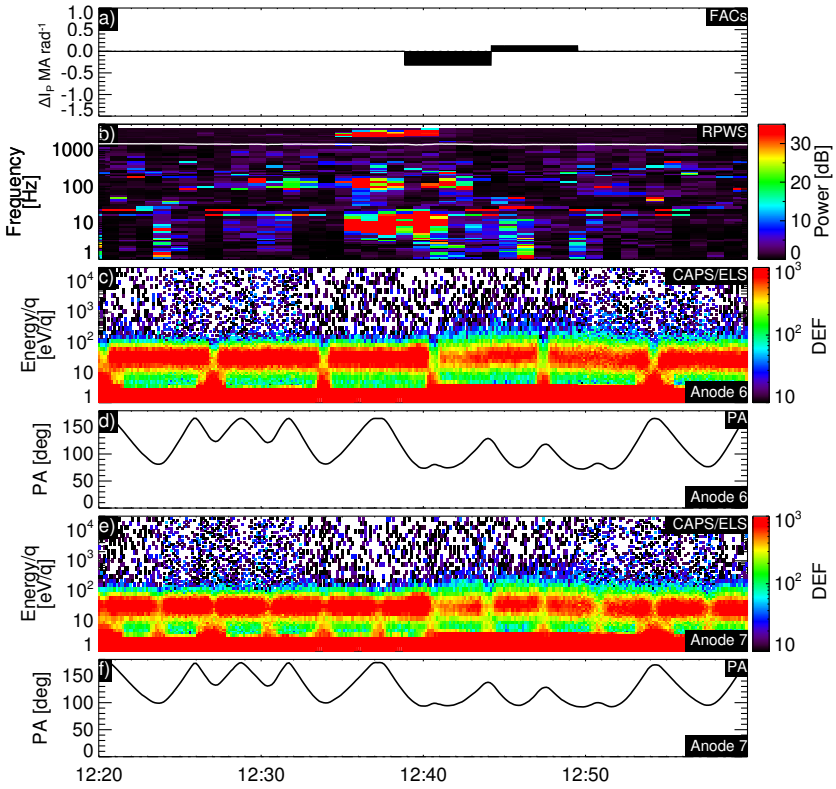

(b) Anti-field aligned electrons from Anodes 7 and 6 (ELS).

Figure A.2: FAC analysis for the JAN09 cusp interval. Panels: (a) FACs: 4D, 4U. The figures are in the same format as Figure A.1.

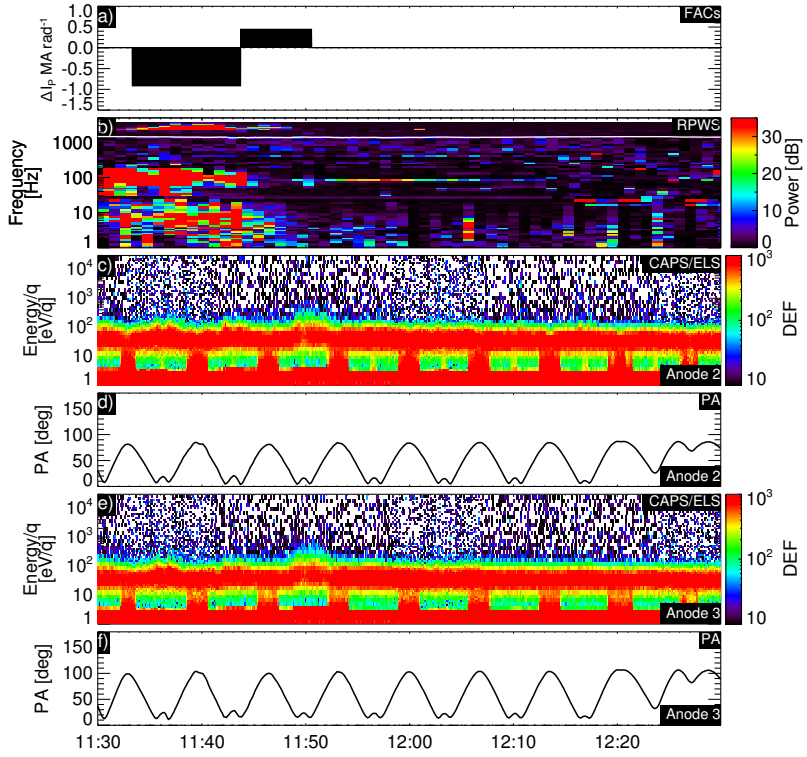

(a) Field aligned electrons from Anodes 2 and 3 (ELS).

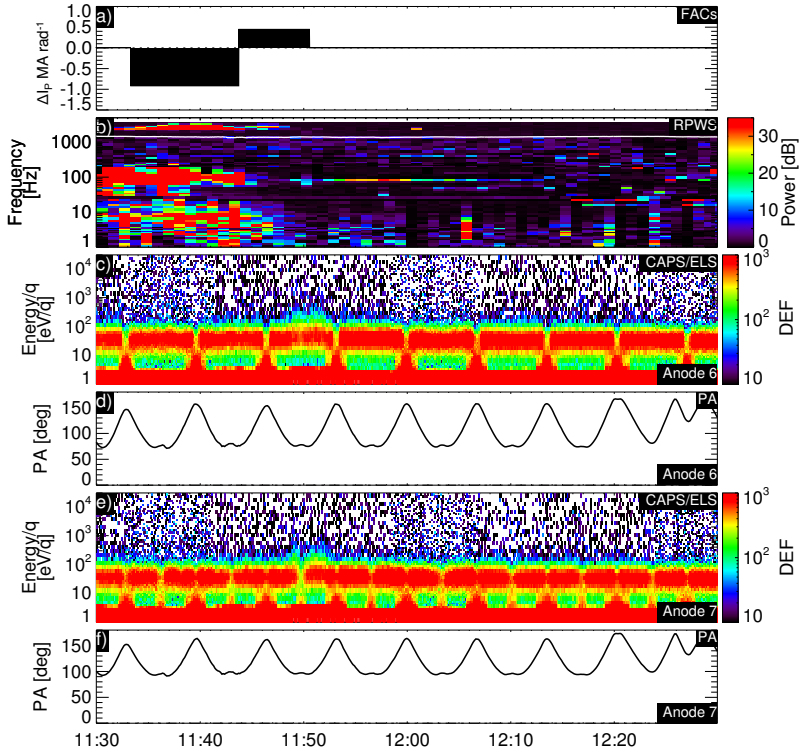

(b) Anti-field aligned electrons from Anodes 7 and 6 (ELS).

Figure A.3: FAC analysis for the JAN09 cusp interval. Panels: (a) FACs: 5D, 5U. The figures are in the same format as Figure A.1.

Table A.1: The field-aligned distances from Cassini to the site of reconnection calculated from ion pitch angle-energy dispersions for JAN09. These are calculated for individual pitch-angle dispersions. The averages and standard deviation for each energy-latitude dispersion can be found in Table 6.2.

Dispersion #	Time (UT)	Distance (R_S)	Dispersion #	Time (UT)	Distance (R_S)
1	11:02:24	18.2 ± 7.9	2	12:03	30.5 ± 8.6
	11:09	24.5± 8.9		12:17	42.6 ± 18.7
	11:15	49.1± 12.9		12:30	44.8 ± 26.3
	11:22	26.0± 4.8		12:37	42.8 ± 18.0
	11:29	39.1± 22.7		12:44	30.5 ± 8.5
	11:36	15.0± 4.3			
	11:49	28.0 ± 6.8			
3	12:57	49.7 ± 13.5	4	15:16	47.9 ± 29.5
	13:10	41.9 ± 13.9		15:30	55.5 ± 14.8
	13:24	47.8 ± 27.1		15:44	56.5 ± 46.5
	13:31	54.8 ± 15.4		16:04	44.0 ± 26.8
	13:37	56.1 ± 17.1		16:17	56.8 ± 39.1
	13:41	55 ± 13.1		16:51	49.1 ± 29.8
	13:55	51 ± 24	5	17:18	46.9 ± 24.3
	14:02	40 ± 24.6		17:25	38.2 ± 21.7
	14:09	50 ± 25.5		17:39	39.5 ± 23.2
	14:35	57 ± 11.9		18:06	61.1 ± 39.5
	14:56	40.8 ± 34.5			

Table A.2: The field-aligned distances from Cassini to the site of reconnection calculated from ion pitch angle-energy dispersions for AUG08. These are calculated for individual pitch-angle dispersions. The averages and standard deviation for each energy-latitude dispersion can be found in Table 6.2.

Dispersion #	Time (UT)	Distance (R_S)
1	15:01	31.7 ± 15.1
	15:07	35.8 ± 16.3
	15:14	27.4 ± 11.4
	15:21	32.9 ± 9.8
2	18:41	28.7 ± 12.8
	18:50	24.0 ± 10.0
3&4	–	–

Appendix B

Survey of Cusp Observations - Additional figures and tables

In this appendix, additional figures are presented, which are discussed in Chapter 7. Observations from the cusp events are presented first, followed by extra solar wind analysis and additional variables from mSWiM.

The cusp observations are presented in the following order: JAN07, MAR07, SEP08, JUL13, and AUG13 (Figures B.1-B.5).

Displayed below (Figures B.6−B.8) are the velocity, number density, magnetic field strength and the calculated ram pressure from the mSWim model for all the cusp observations. This complements the data presented in Chapter 7.6.

Table B.1: The field-aligned distances from Cassini to the site of reconnection calculated for MAR07 and MAY08. These are calculated for individual pitch-angle dispersions.

MAR07			MAY08		
Dispersion #	Time (UT)	Distance (R_S)	Dispersion #	Time (UT)	Distance (R_S)
1	08:06	14 ± 4	2	03:32	12 ± 1
	08:13	16± 4		03:59	18 ± 7
	08:20	18± 1		04:27	19 ± 7
	08:27	16± 1	NOV08		
	08:34	15± 1	Dispersion	Time	Distance
	09:07	15± 1	1	06:58	26 ± 9
	09:21	16 ± 1		06:51	16 ± 4
	09:55	15.7 ± 0.4		06:58	26 ± 9

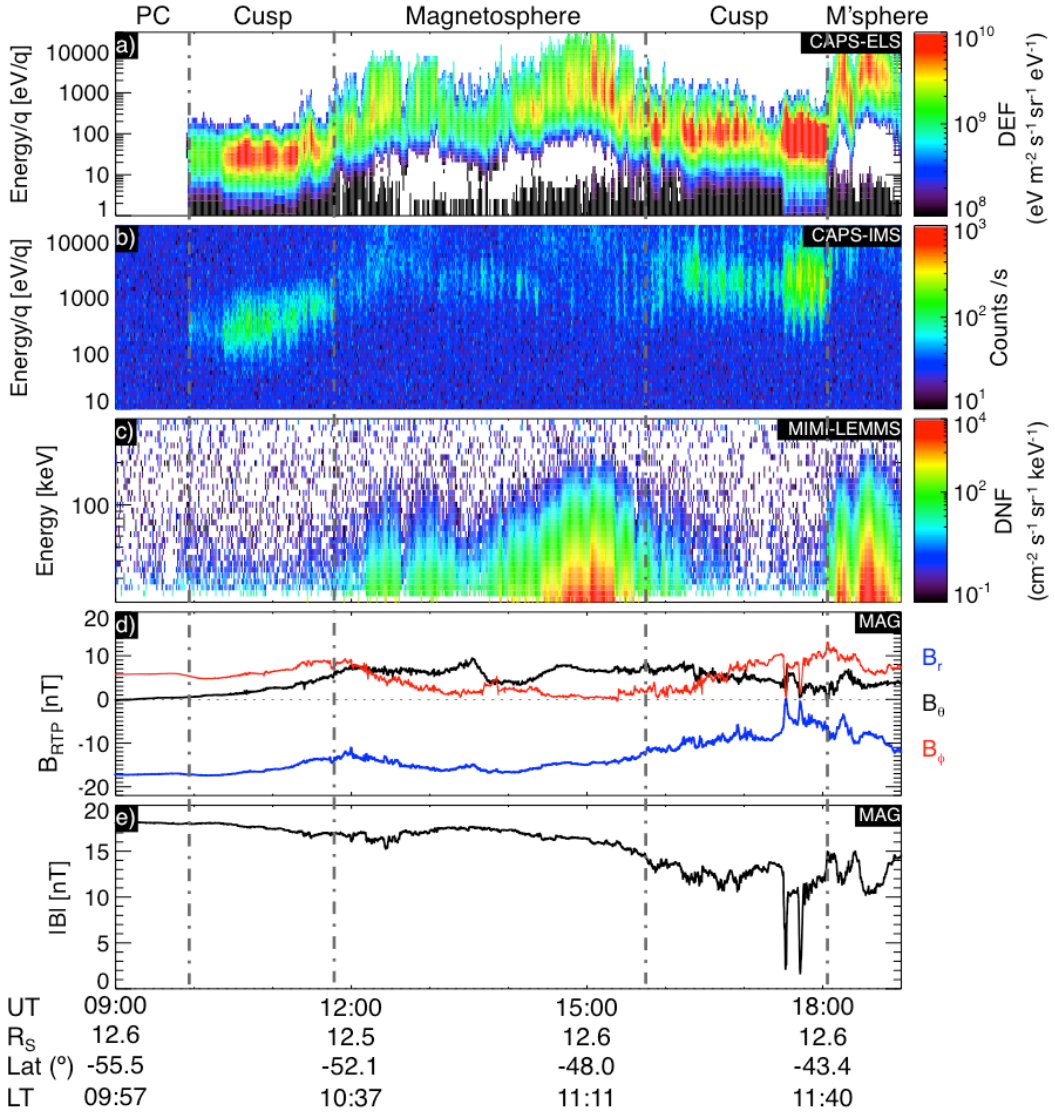

Figure B.1: Observations from JAN07, with the cusp observed. The data are presented in the following order (from the top going down): a) electrons from CAPS-ELS, b) ions from CAPS-IMS, c) high-energy electrons from MIMI-LEMMS, d) the three components of the magnetic field in KRTP coordinates from MAG and e) the magnitude of the magnetic field also observed by MAG.

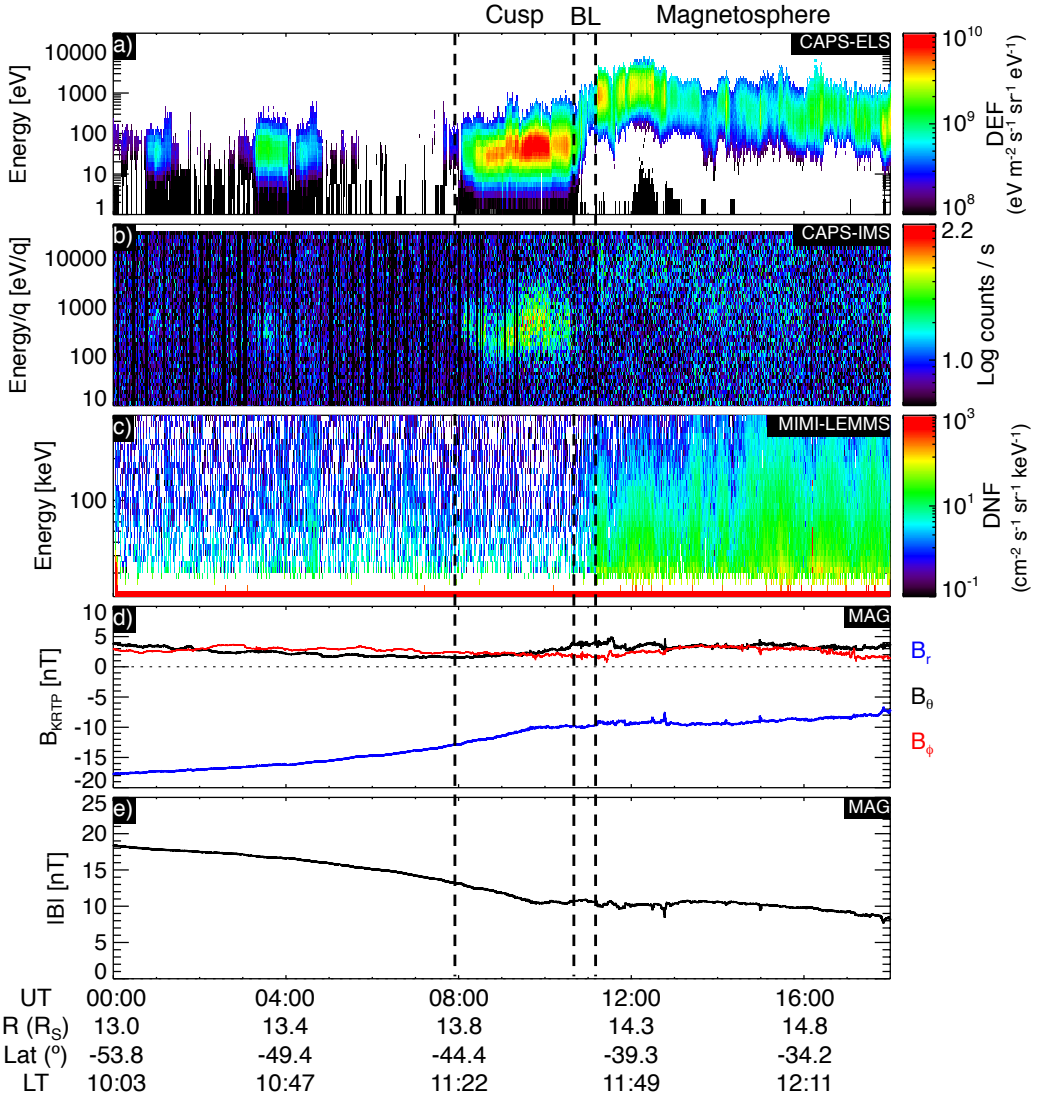

Figure B.2: Cusp observations from MAR07 with the cusp observed at 08:03−10:50 UT. The data are presented in the same format as Figure B.1.

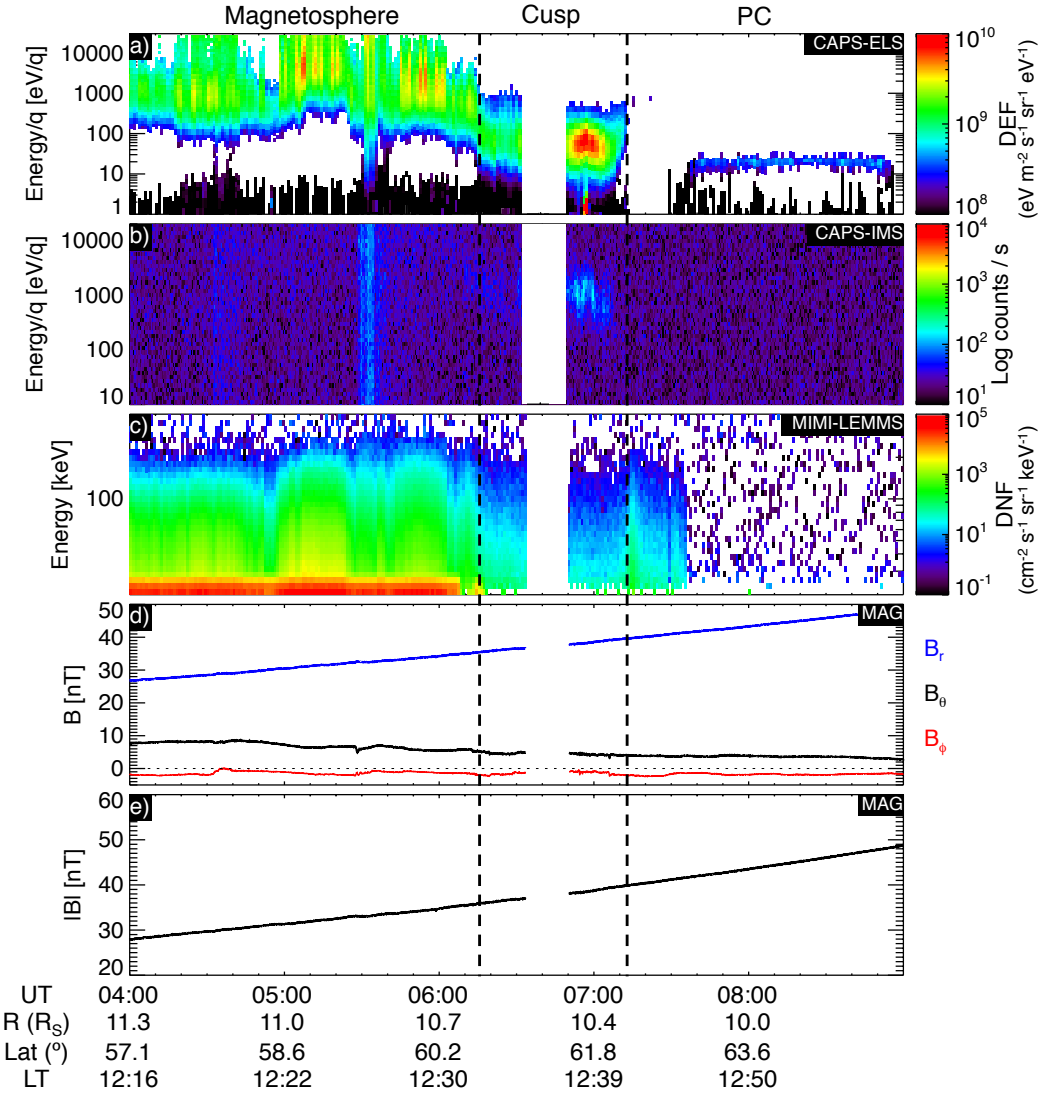

Figure B.3: Cusp observations from SEP08, with the cusp observed at 06:50−07:20 UT. The data are presented in the same format as Figure B.1

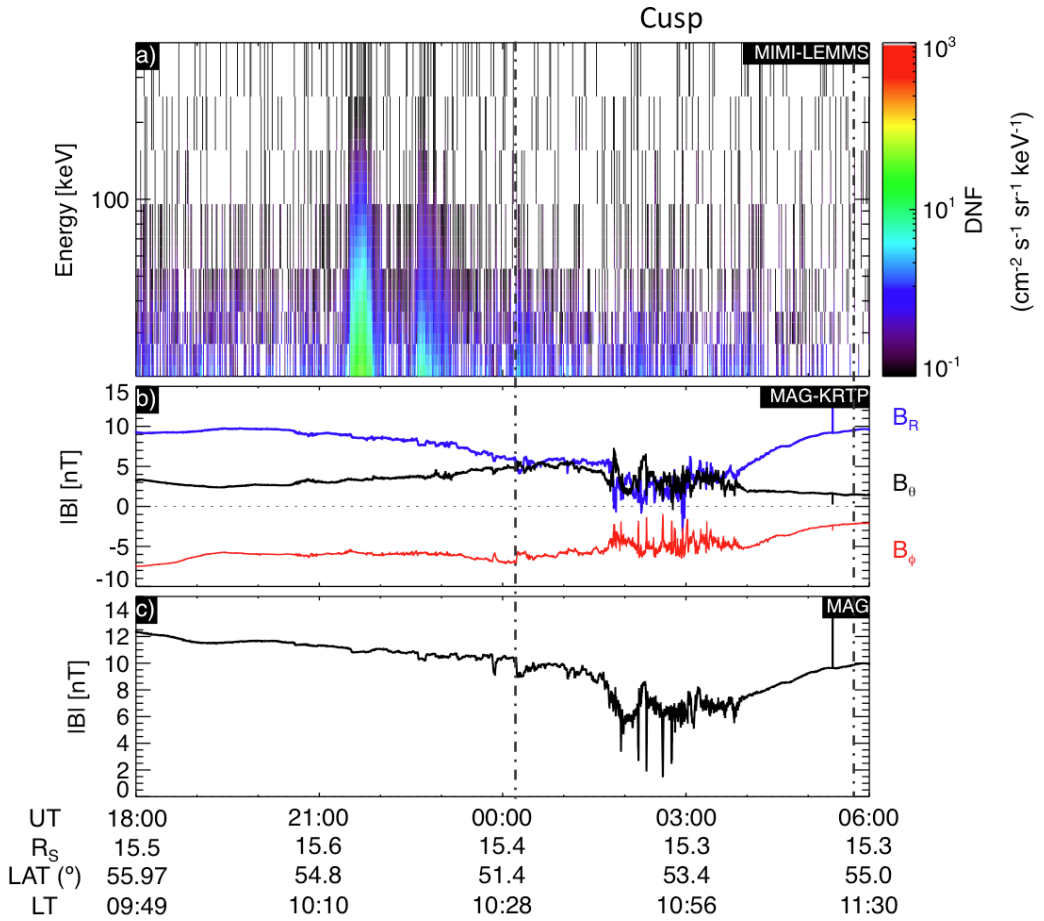

Figure B.4: Cusp observations from JUL13. The data are presented in the following order: a) high-energy electrons from MIMI-LEMMS, b) the three components of the magnetic field in KRTP coordinates from MAG and c) the magnitude of the magnetic field also observed by MAG.

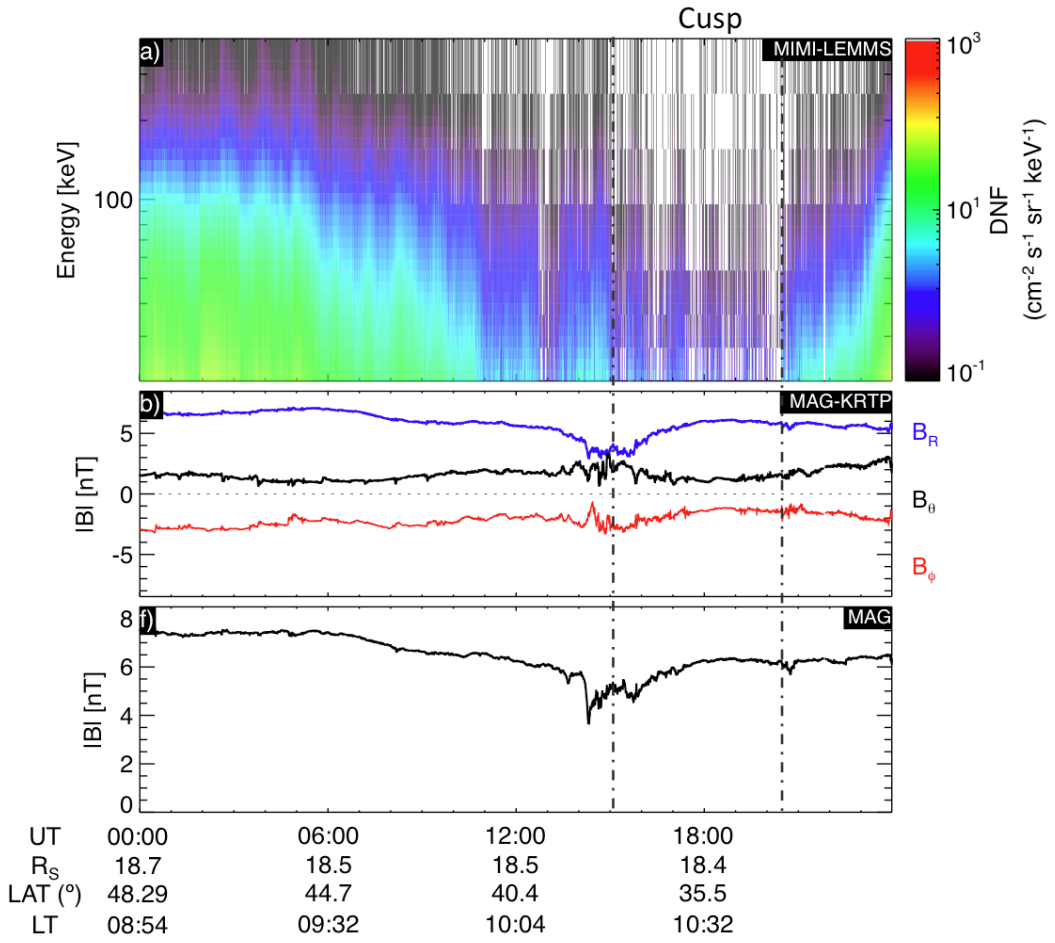

Figure B.5: Cusp observations from AUG13. The data are presented in the same format as Figure B.4.

Table B.2: The field-aligned distances from Cassini to the site of reconnection calculated for JAN07 and FEB07. These are calculated for individual pitch-angle dispersions and were taken from *Arridge et al.*(in prep.).

JAN07		
Dispersion #	Time (UT)	Distance (R_S)
1	10:24	70 ± 60
	10:57	50 ± 30
	11:04	50 ± 40
	11:25	40 ± 20
	11:32	80 ± 60
	11:38	40 ± 20
2	17:24	16 ± 3
3	17:38	40 ± 10
	17:44	24 ± 6
	17:51	21 ± 5
	17:58	30 ± 8
	18:05	18 ± 5

FEB07		
Dispersion #	Time (UT)	Distance (R_S)
1	18:02	60 ± 60
	18:16	50 ± 30
	18:23	30 ± 20
2	00:04	30 ± 20
	01:08	33 ± 9
	03:00	40 ± 40

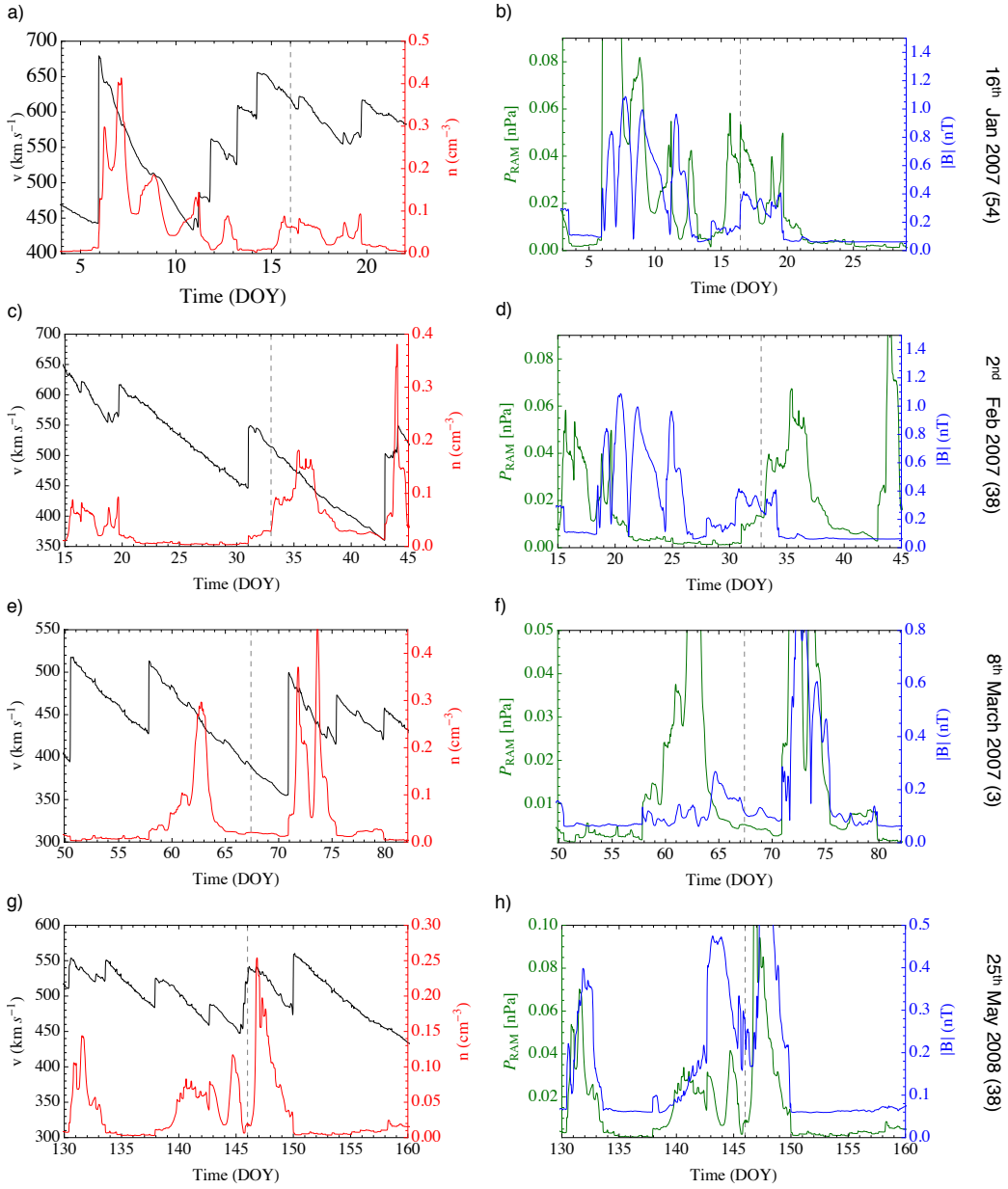

Figure B.6: The velocity (black), number density (red), ram pressure (green) and the magnetic field strength (blue) of the IMF as propagated by mSWiM, presented for the JAN07, FEB07, MAR07 and MAY08 observations.

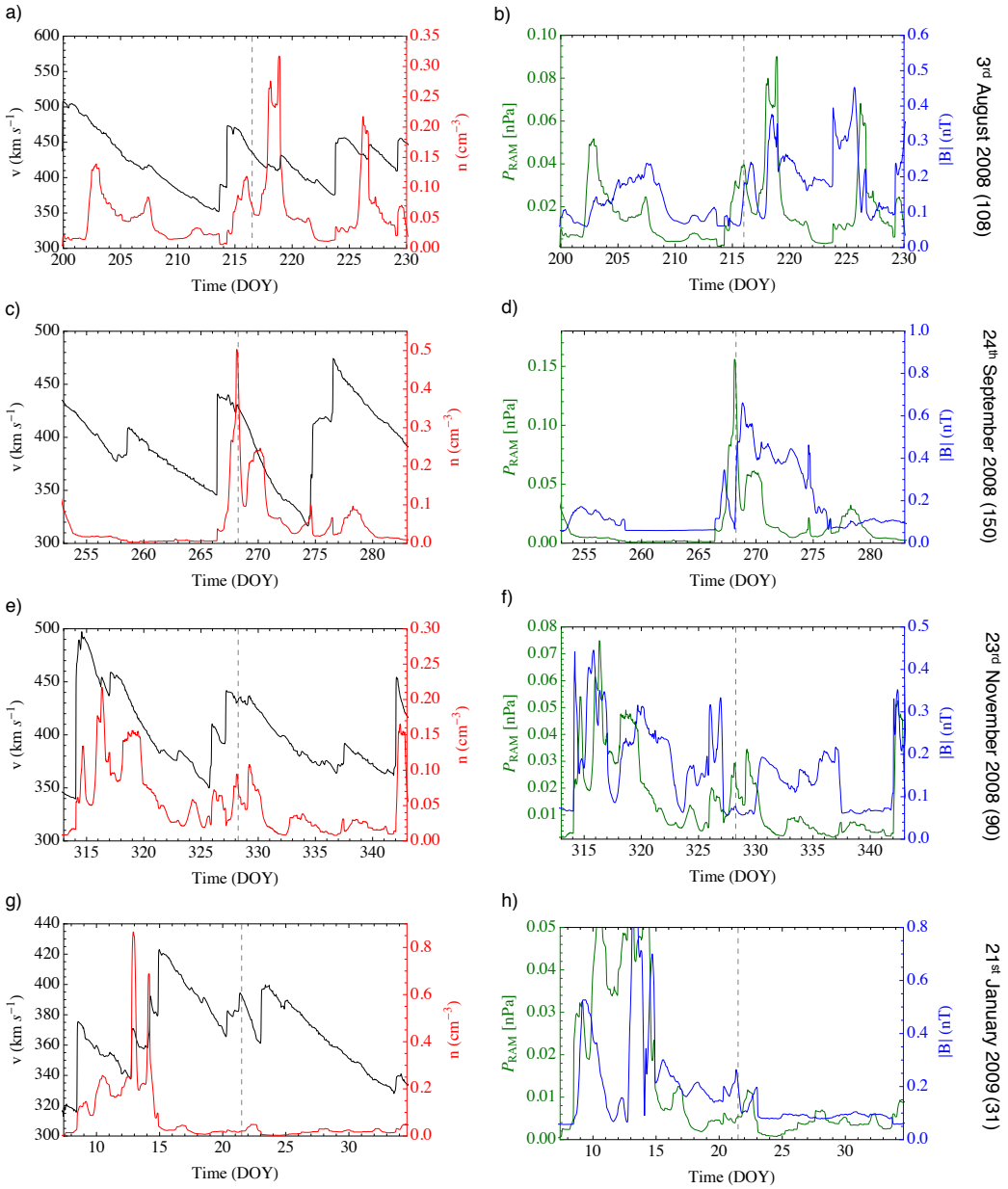

Figure B.7: mSWiM results for the AUG08, SEP08, NOV08, and JAN09 observations presented in the same format as Figure B.6.

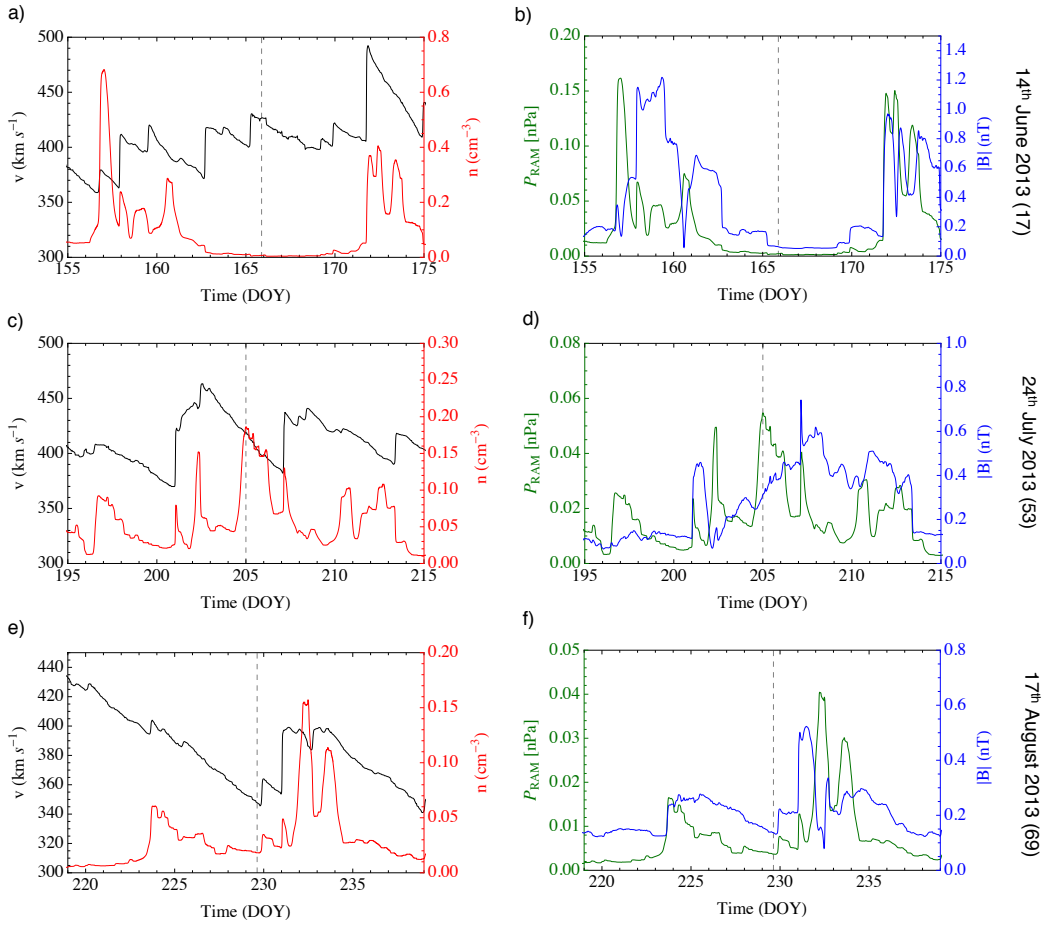

Figure B.8: mSWiM results for the JUN13, JUL13, and AUG13 observations presented in the same format as Figure B.6.

Appendix C

Magnetic Depressions - Additional figures

This section provides additional figures in the same format as Figure 8.8 (FEB07) for the other magnetic depression observations. The magnetic pressure analysis is shown as well as the plasma pressure components in separate panels and energy-time spectrograms of He^{++} and W^{+} from CHEMS.

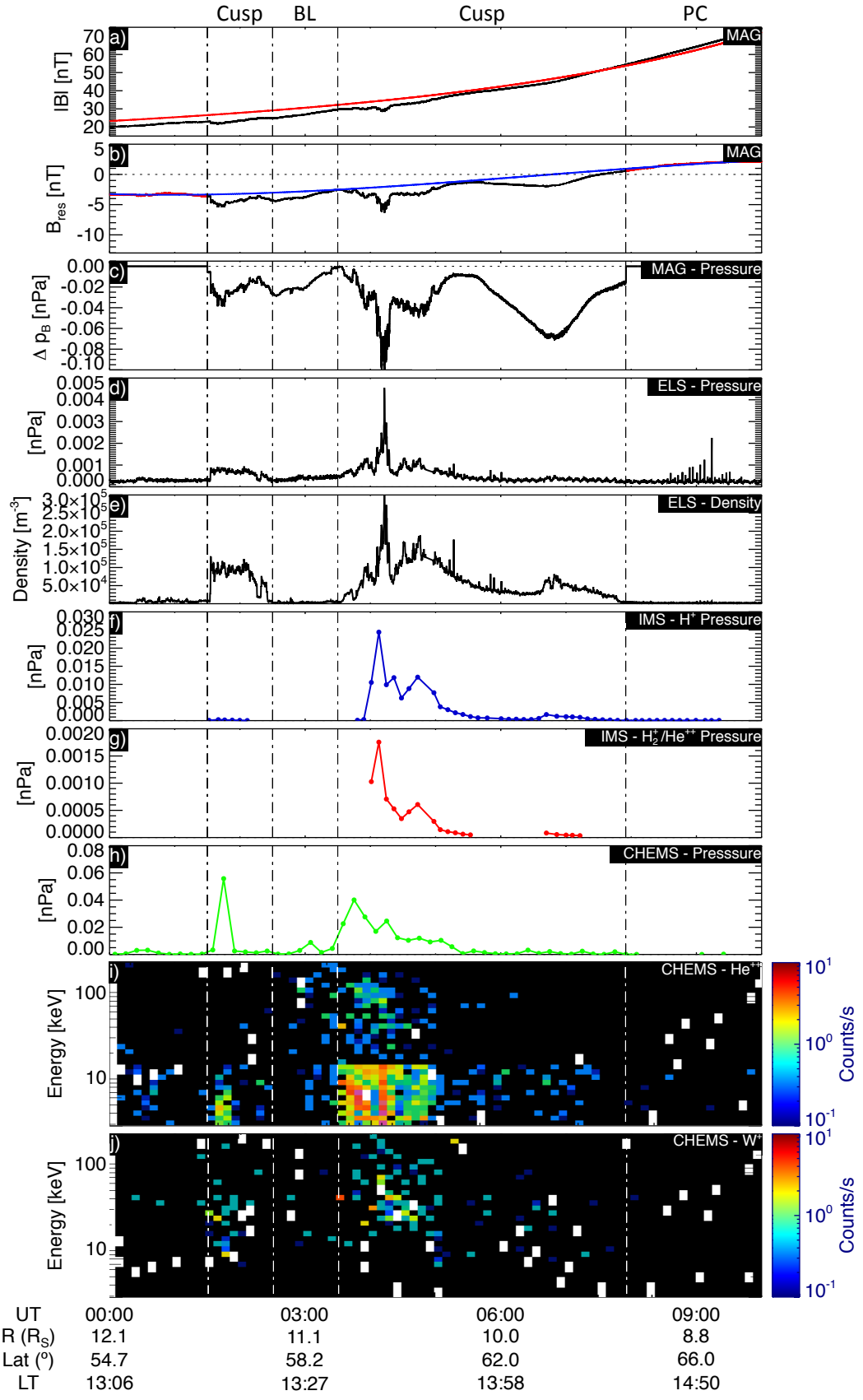

Figure C.1: Magnetic and particle pressure presented for MAY08 in the same format as found in Figure 8.8.

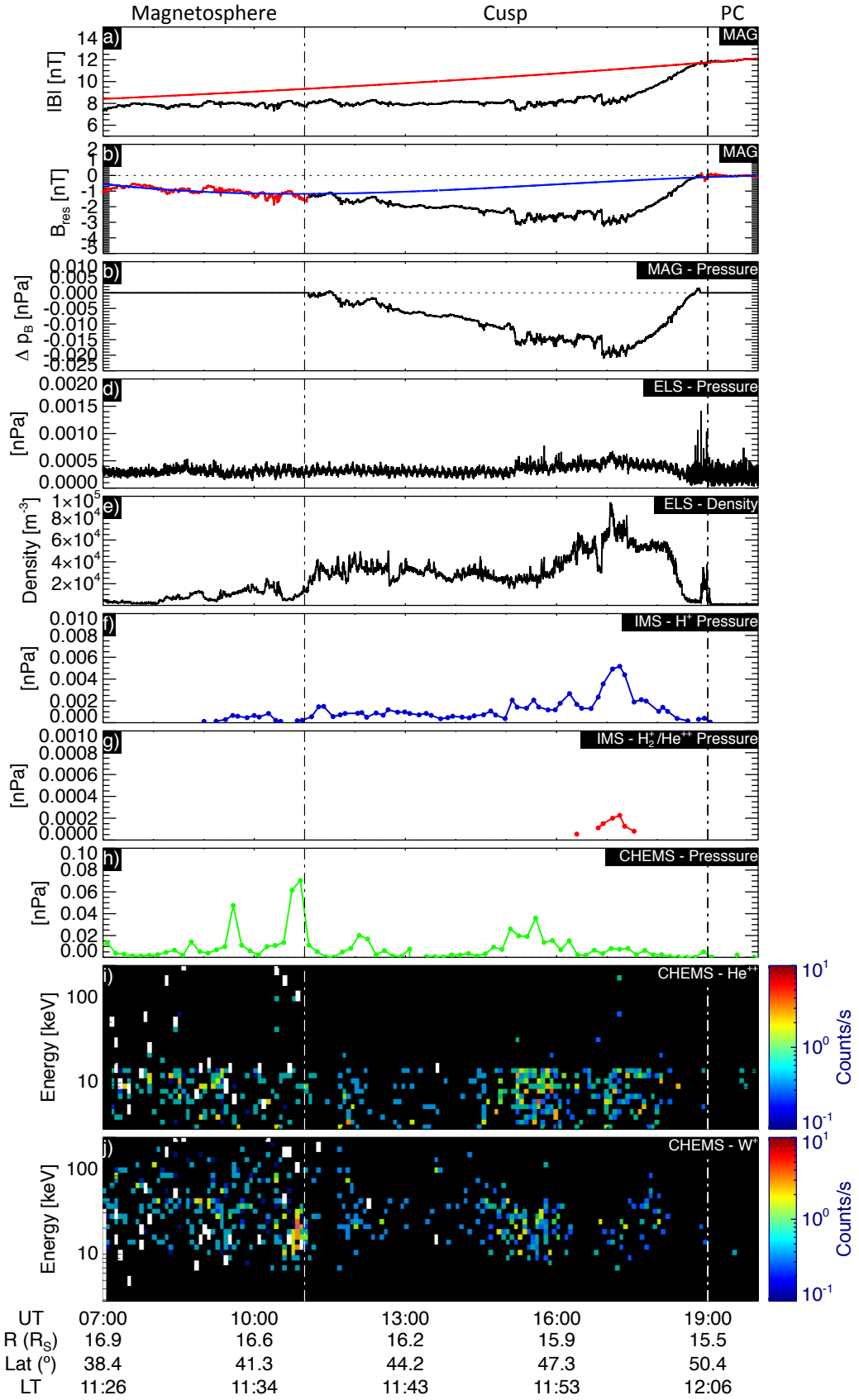

Figure C.2: Magnetic and particle pressure presented for JAN09 in the same format found in Figure 8.8.

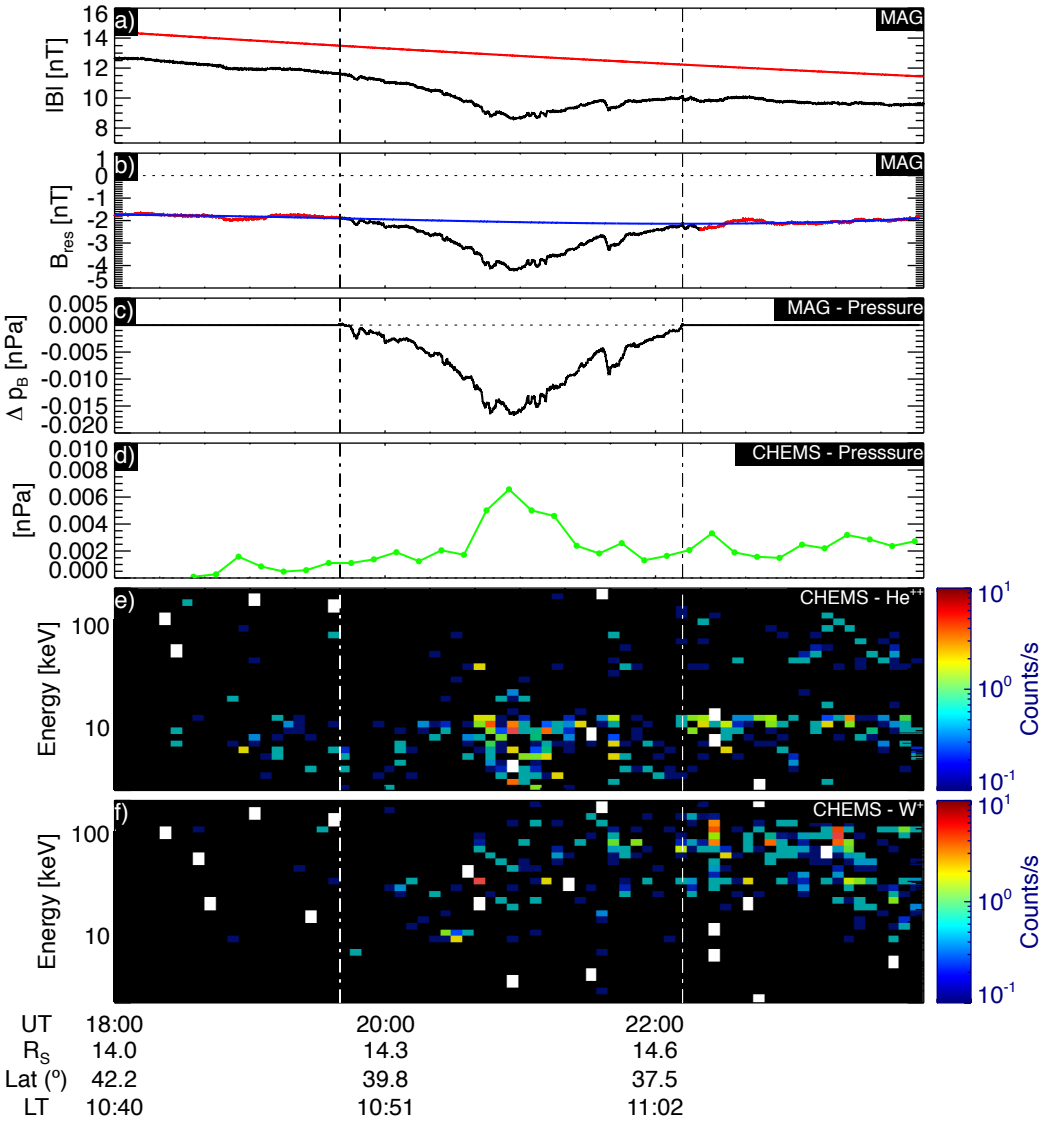

Figure C.3: Magnetic and particle pressure presented for JUN13: a) magnetic field magnitude from MAG (black) and the magnetic field model (red), b) residual magnetic field with data (red) that is fit with a polynomial (blue), c) the magnetic pressure deficit due to the depression, d) high energy ion pressure from CHEMS, e) and f) He^{++} and W^{+} (respectively) energy time spectrograms from CHEMS.

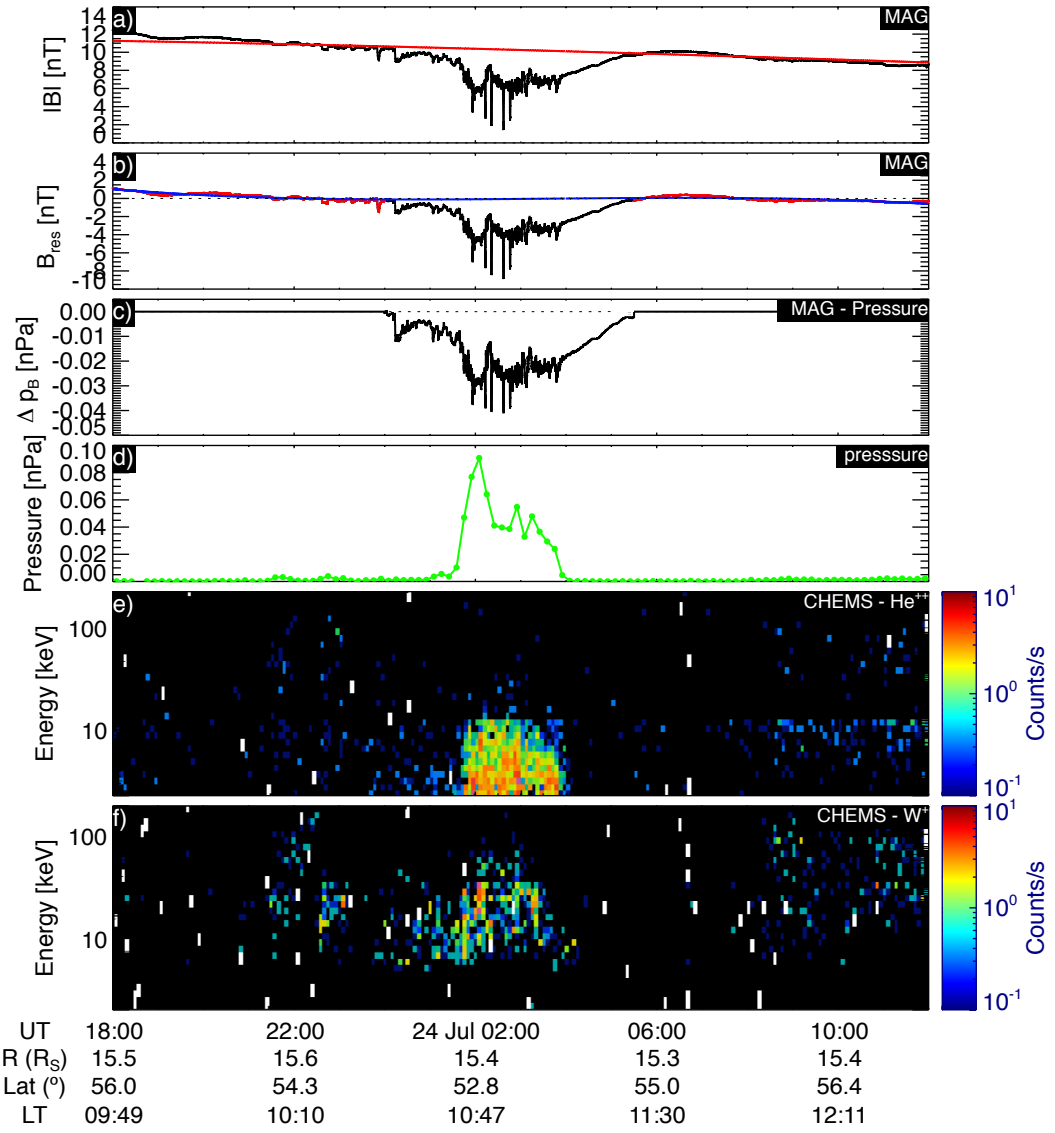

Figure C.4: Magnetic and particle pressure presented for JUL13 in the same format found in Figure C.3.

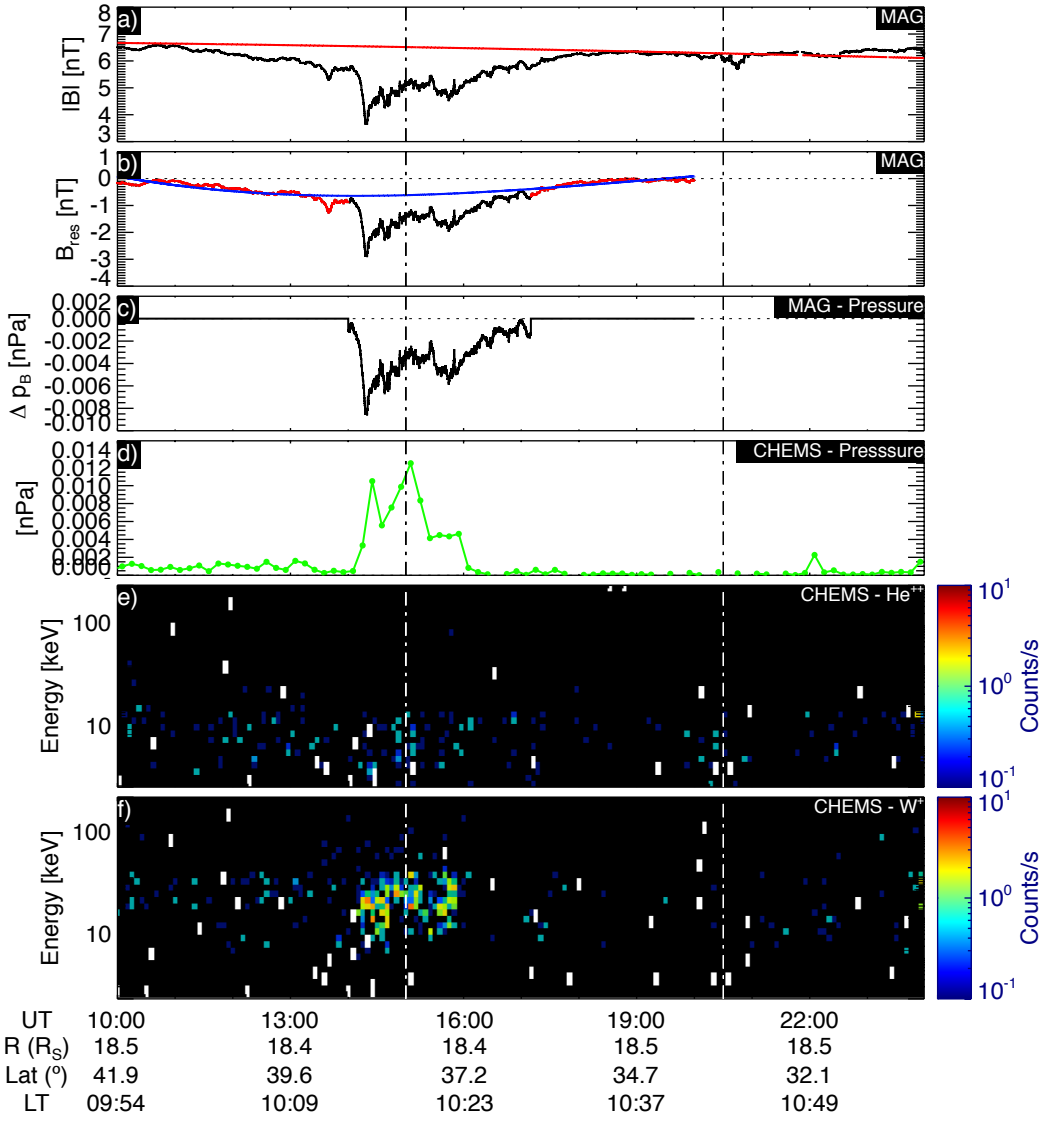

Figure C.5: Magnetic and particle pressure presented for AUG13 in the same format found in Figure C.3.

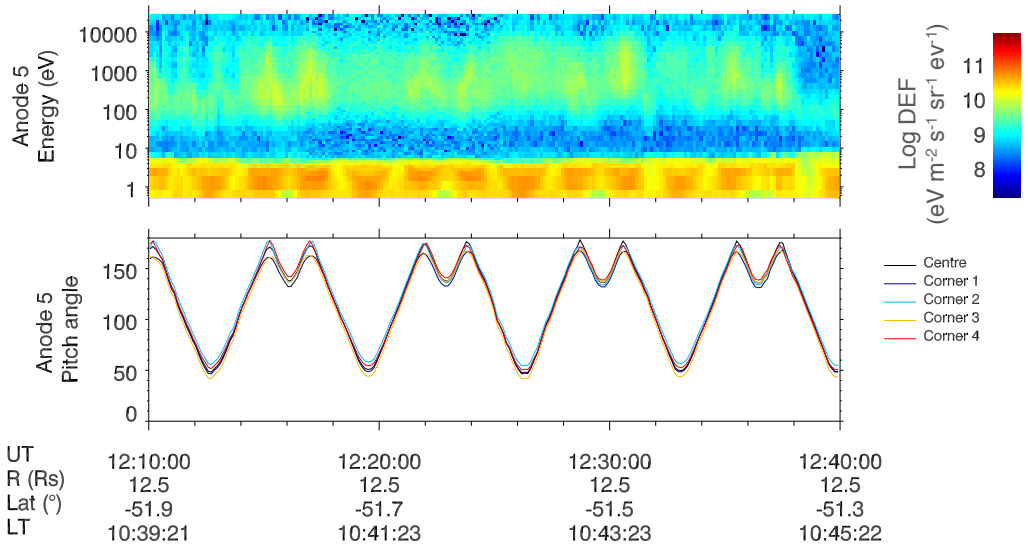

Figure C.6: Anti-field-aligned electron observation by ELS in the depressed magnetic field adjacent to the JAN07-a cusp. The top panels shows ELS Anode 5 observations, and below it is the corresponding pitch angle look direction of the instrument.

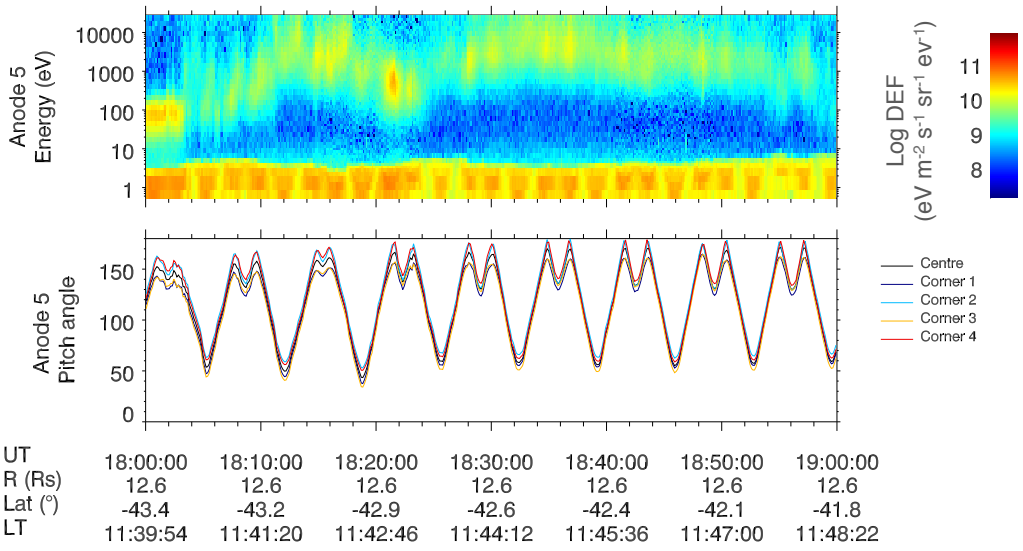

Figure C.7: Anti-field-aligned electron observation by ELS in the depressed magnetic field adjacent to the JAN07-b cusp, in the same format as Figure C.6.

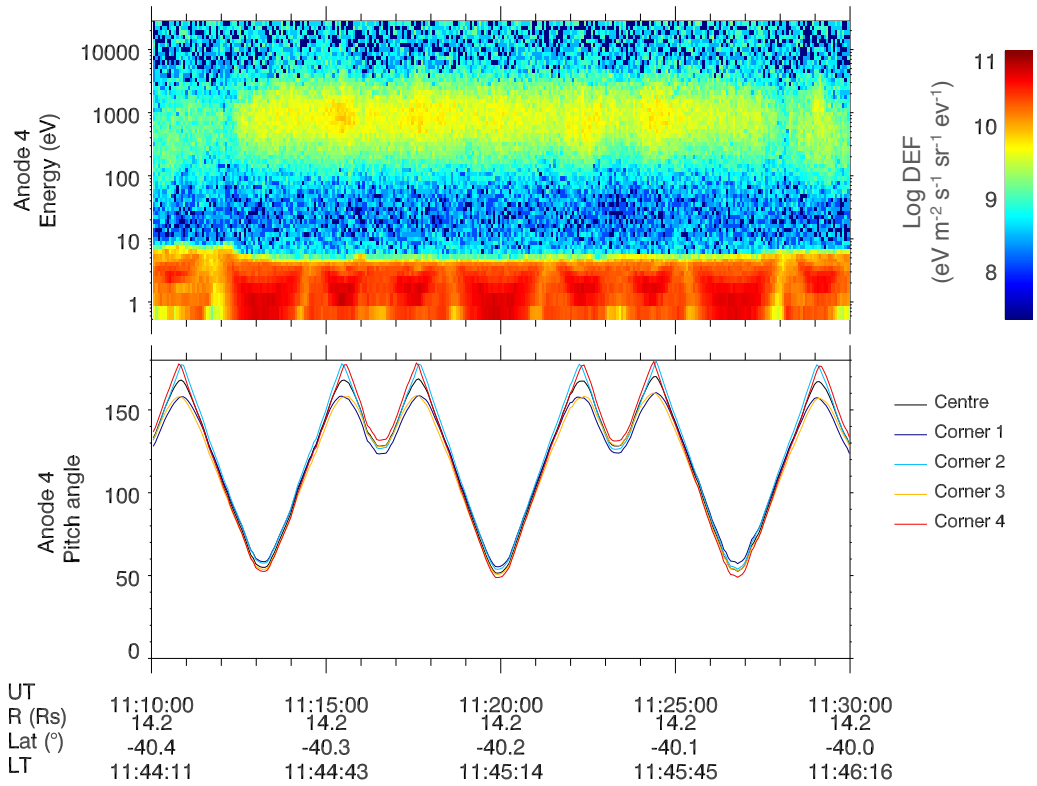

Figure C.8: Anti-field-aligned electron observation by ELS in the depressed magnetic field adjacent to the MAR07 cusp, in the same format as Figure C.6.

Bibliography

Achilleos, N., C. S. Arridge, C. Bertucci, C. M. Jackman, M. K. Dougherty, K. K. Khurana, and C. T. Russell (2008), Large-scale dynamics of saturn's magnetopause: Observations by cassini, *J. of Geophys. Res.*, *113*(A11), doi: 10.1029/2008JA013265.

Achilleos, N., P. Guio, and C. S. Arridge (2010), A model of force balance in Saturn's magnetodisc, *MNRAS*, *401*, 2349–2371, doi:10.1111/j.1365-2966.2009.15865.x.

Acuna, M. H., and N. F. Ness (1980), The magnetic field of Saturn - Pioneer 11 observations, *Science*, *207*, 444–446, doi:10.1126/science.207.4429.444.

Acuna, M. H., N. F. Ness, and J. E. P. Connerney (1980), The magnetic field of Saturn - Further studies of the Pioneer 11 observations, *J. Geophys. Res.*, *85*, 5675–5678, doi:10.1029/JA085iA11p05675.

Alfvén, H. (1942), Existence of Electromagnetic-Hydrodynamic Waves, *Nature*, *150*, 405–406, doi:10.1038/150405d0.

Andre, M., L. Matson, H. Koskien, and R. Erlandson (1988), Local transverse ion energization in and near the polar cusp, *Geophys. Res. Lett.*, *15*, 107–110, doi: 10.1029/GL015i001p00107.

Arridge, C., N. Andr, H. McAndrews, E. Bunce, M. Burger, K. Hansen, H.-W. Hsu, R. Johnson, G. Jones, S. Kempf, K. Khurana, N. Krupp, W. Kurth, J. Leisner, C. Paranicas, E. Roussos, C. Russell, P. Schippers, E. Sittler, H. Smith, M. Thomsen, and M. Dougherty (2011), Mapping magnetospheric equatorial regions at saturn from cassini prime mission observations, *S. Sci. Rev.*, *164*(1-4), 1–83, doi:10.1007/s11214-011-9850-4.

Arridge, C. S., N. Achilleos, M. K. Dougherty, K. K. Khurana, and C. T. Russell (2006), Modeling the size and shape of Saturn's magnetopause with variable dynamic pressure, *J. Geophys. Res.*, *111*, A11227, doi:10.1029/2005JA011574.

Arridge, C. S., K. K. Khurana, C. T. Russell, D. J. Southwood, N. Achilleos, M. K. Dougherty, A. J. Coates, and H. K. Leinweber (2008), Warping of Saturn's magnetospheric and magnetotail current sheets, *J. of Geophys. Res.*, *113*, A08217, doi:10.1029/2007JA012963.

Arridge, C. S., L. K. Gilbert, G. R. Lewis, E. C. Sittler, G. H. Jones, D. O. Kataria, A. J. Coates, and D. T. Young (2009), The effect of spacecraft radiation sources on electron moments from the Cassini CAPS electron spectrometer, *Plan. and S. Sci.*, *57*(7), 854 – 869, doi:10.1016/j.pss.2009.02.011.

Axford, W. I., and C. O. Hines (1961), A unifying theory of high-latitude geophysical phenomena and geomagnetic storms, *Canadian Journal of Physics*, *39*, 1433.

Badman, S., G. Provan, E. Bunce, D. Mitchell, H. Melin, S. Cowley, A. Radioti, W. Kurth, W. Pryor, J. Nichols, S. Jinks, T. Stallard, R. Brown, K. Baines, and M. Dougherty (2014), Saturns auroral morphology and field-aligned currents during a solar wind compression, *Icarus*, doi:10.1016/j.icarus.2014.11.014.

Badman, S. V., S. W. H. Cowley, L. Lamy, B. Cecconi, and P. Zarka (2008), Relationship between solar wind corotating interaction regions and the phasing and intensity of Saturn kilometric radiation bursts, *Annales Geophysicae*, *26*, 3641–3651, doi:10.5194/angeo-26-3641-2008.

Badman, S. V., N. Achilleos, C. S. Arridge, K. H. Baines, R. H. Brown, E. J. Bunce, A. J. Coates, S. W. H. Cowley, M. K. Dougherty, M. Fujimoto, G. Hospodarsky, S. Kasahara, T. Kimura, H. Melin, D. G. Mitchell, T. Stallard, and C. Tao (2012a), Cassini observations of ion and electron beams at Saturn and their relationship to infrared auroral arcs, *J. of Geophys. Research*, *117*, A01211, doi:10.1029/2011JA017222.

Badman, S. V., N. Achilleos, C. S. Arridge, K. H. Baines, R. H. Brown, E. J. Bunce, A. J. Coates, S. W. H. Cowley, M. K. Dougherty, M. Fujimoto, G. Hospodarsky, S. Kasahara, T. Kimura, H. Melin, D. G. Mitchell, T. Stallard, and C. Tao

(2012b), Correction to "Cassini observations of ion and electron beams at Saturn and their relationship to infrared auroral arcs", *Journal of Geophys. Res.*, *117*, A04220, doi:10.1029/2012JA017617.

Badman, S. V., A. Masters, H. Hasegawa, M. Fujimoto, A. Radioti, D. Grodent, N. Sergis, M. K. Dougherty, and A. J. Coates (2013), Bursty magnetic reconnection at Saturn's magnetopause, *Geophys. Res. Lett.*, *40*, 1027–1031, doi:10.1002/grl.50199.

Badman, S. V., C. M. Jackman, J. D. Nichols, J. T. Clarke, and J.-C. Gérard (2014), Open flux in Saturn's magnetosphere, *Icarus*, *231*, 137–145, doi:10.1016/j.icarus.2013.12.004.

Bagenal, F., and S. Bartlett (2015), Magnetospheres of the outer planets comparison, Available at `http://lasp.colorado.edu/home/mop/files/2012/04/JSEM.jpg`(2015).

Baumjohann, W., and R. A. Treumann (1996), *Basic space plasma physics*.

Biermann, L. (1951), Kometenschweife und solare Korpuskularstrahlung, *Zeitschrift Für Astrophysik*, *29*, 274–286.

Bogdanova, Y. V., C. J. Owen, M. W. Dunlop, J. A. Wild, J. A. Davies, A. D. Lahiff, M. G. G. T. Taylor, A. N. Fazakerley, I. Dandouras, C. M. Carr, E. A. Lucek, and H. Rme (2008), Formation of the low-latitude boundary layer and cusp under the northward imf: Simultaneous observations by cluster and double star, *J. of Geophys. Res.*, *113*(A7), doi:10.1029/2007JA012762, a07S07.

Bunce, E. J., S. W. H. Cowley, I. I. Alexeev, C. S. Arridge, M. K. Dougherty, J. D. Nichols, and C. T. Russell (2007), Cassini observations of the variation of Saturn's ring current parameters with system size, *J. of Geophys. Res.*, *112*, A10202, doi:10.1029/2007JA012275.

Bunce, E. J., C. S. Arridge, S. W. H. Cowley, and M. K. Dougherty (2008a), Magnetic field structure of Saturn's dayside magnetosphere and its mapping to the ionosphere: Results from ring current modeling, *J. of Geophys. Res.*, *113*, A02207, doi:10.1029/2007JA012538.

Bunce, E. J., C. S. Arridge, J. T. Clarke, A. J. Coates, S. W. H. Cowley, M. K. Dougherty, J.-C. Gérard, D. Grodent, K. C. Hansen, J. D. Nichols, D. J. Southwood, and D. L. Talboys (2008b), Origin of Saturn's aurora: Simultaneous observations by Cassini and the Hubble Space Telescope, *J. Geophys. Res.*, *113*(12), A09209, doi:10.1029/2008JA013257.

Bunce, E. J., D. C. Grodent, S. L. Jinks, D. J. Andrews, S. V. Badman, A. J. Coates, S. W. H. Cowley, M. K. Dougherty, W. S. Kurth, D. G. Mitchell, and G. Provan (2014), Cassini nightside observations of the oscillatory motion of Saturn's northern auroral oval, *J. of Geophys. Res.*, *119*, 3528–3543, doi:10.1002/2013JA019527.

Burch, J. L. (1973), Rate of erosion of dayside magnetic flux based on a quantitative study of the dependence of polar cusp latitude on the interplanetary magnetic field, *Radio Science*, *8*, 955–961, doi:10.1029/RS008i011p00955.

Burch, J. L., P. H. Reiff, R. A. Heelis, W. B. Hanson, J. D. Winningham, C. Gurgiolo, J. D. Menietti, J. N. Barfield, and R. A. Hoffman (1982), Plasma injection and transport in the mid-altitude polar cusp, *Geophys. Res. Lett.*, *9*, 921–924, doi:10.1029/GL009i009p00921.

Burch, J. L., P. H. Reiff, J. D. Menietti, J. D. Winningham, R. A. Heelis, W. B. Hanson, S. D. Shawhan, E. G. Shelley, M. Sugiura, and D. R. Weimer (1985), IMF By-dependent plasma flow and Birkeland currents in the dayside magnetosphere. I - Dynamics Explorer observations, *J. Geophys. Res.*, *90*, 1577–1593, doi:10.1029/JA090iA02p01577.

Burton, M. E., B. Buratti, D. L. Matson, and J.-P. Lebreton (2001), The Cassini/Huygens Venus and earth flybys: An overview of operations and results, *J. Geophys. Res.*, *106*, 30,099–30,108, doi:10.1029/2001JA900088.

Burton, M. E., M. K. Dougherty, and C. T. Russell (2010), Saturn's internal planetary magnetic field, *Geophys. Res. Lett.*, *37*, L24105, doi:10.1029/2010GL045148.

Burton, R. K., R. L. McPherron, and C. T. Russell (1975), The terrestrial magnetosphere - A half-wave rectifier of the interplanetary electric field, *Science*, *189*, 717, doi:10.1126/science.189.4204.717.

Candidi, M., G. Mastrantonio, S. Orsini, and C.-I. Meng (1989), Evidence of the influence of the interplanetary magnetic field azimuthal component on polar cusp configuration, *J. Geophys. Res.*, *94*, 13,585–13,591, doi:10.1029/JA094iA10p13585.

Carbary, J. F., D. G. Mitchell, P. Brandt, E. C. Roelof, and S. M. Krimigis (2008), Periodic tilting of Saturn's plasma sheet, *Geophys. Res. Lett.*, *35*, L24101, doi:10.1029/2008GL036339.

Chapman, S., and V. C. A. Ferraro (1931a), a New Theory of Magnetic Storms, *Terrestrial Magnetism and Atmospheric Electricity (J. Geophys. Res.)*, *36*, 77–97, doi:10.1029/TE036i002p00077.

Chapman, S., and V. C. A. Ferraro (1931b), a New Theory of Magnetic Storms, *Terrestrial Magnetism and Atmospheric Electricity (J. Geophys. Res.)*, *36*, 171–186, doi:10.1029/TE036i003p00171.

Chapman, S., and H. Zirin (1957), Notes on the Solar Corona and the Terrestrial Ionosphere, *Smithsonian Contributions to Astrophysics*, *2*, 1.

Chen, F. F. (1974), *Introduction to plasma physics*.

Chen, J., T. A. Fritz, R. B. Sheldon, H. E. Spence, W. N. Spjeldvik, J. F. Fennell, and S. Livi (1997), A new, temporarily confined population in the polar cap during the August 27, 1996 geomagnetic field distortion period, *Geophys. Res. Lett.*, *24*, 1447–1450, doi:10.1029/97GL01369.

Chen, J., T. A. Fritz, R. B. Sheldon, H. E. Spence, W. N. Spjeldvik, J. F. Fennell, S. Livi, C. T. Russell, J. S. Pickett, and D. A. Gurnett (1998), Cusp energetic particle events: Implications for a major acceleration region of the magnetosphere, *J. Geophys. Res.*, *103*, 69–78, doi:10.1029/97JA02246.

Connerney, J. E. P., M. H. Acuna, and N. F. Ness (1981), Modeling the Jovian current sheet and inner magnetosphere, *J. Geophys. Res.*, *86*, 8370–8384, doi:10.1029/JA086iA10p08370.

Connerney, J. E. P., M. H. Acuna, and N. F. Ness (1983), Currents in Saturn's magnetosphere, *J. Geophys. Res.*, *88*, 8779–8789, doi:10.1029/JA088iA11p08779.

Cowley, S., E. Bunce, and R. Prangé (2004a), Saturn's polar ionospheric flows and their relation to the main auroral oval, *Annales Geophysicae*, *22*, 1379–1394, doi: 10.5194/angeo-22-1379-2004.

Cowley, S. W. H., and E. J. Bunce (2003), Corotation-driven magnetosphere-ionosphere coupling currents in Saturn's magnetosphere and their relation to the auroras, *Annales Geophysicae*, *21*, 1691–1707, doi:10.5194/angeo-21-1691-2003.

Cowley, S. W. H., and E. J. Bunce (2003), Corotation-driven magnetosphere-ionosphere coupling currents in saturns magnetosphere and their relation to the auroras, *Annales Geophysicae*, *21*(8), 1691–1707, doi:10.5194/angeo-21-1691-2003.

Cowley, S. W. H., J. P. Morelli, and M. Lockwood (1991), Dependence of convective flows and particle precipitation in the high-latitude dayside ionosphere on the X and Y components of the interplanetary magnetic field, *J. Geophys. Res.*, *96*, 5557–5564, doi:10.1029/90JA02063.

Cowley, S. W. H., E. J. Bunce, and J. M. O'Rourke (2004b), A simple quantitative model of plasma flows and currents in Saturn's polar ionosphere, *J. Geophys. Res.*, *109*, A05212, doi:10.1029/2003JA010375.

Cowley, S. W. H., S. V. Badman, E. J. Bunce, J. T. Clarke, J.-C. Gérard, D. Grodent, C. M. Jackman, S. E. Milan, and T. K. Yeoman (2005), Reconnection in a rotation-dominated magnetosphere and its relation to Saturn's auroral dynamics, *J. Geophys. Res.*, *110*, A02201, doi:10.1029/2004JA010796.

Coxon, J. C., S. E. Milan, L. B. N. Clausen, B. J. Anderson, and H. Korth (2014), The magnitudes of the regions 1 and 2 birkeland currents observed by ampere and their role in solar wind-magnetosphere-ionosphere coupling, *J. of Geophys. Res.*, *119*(12), 9804–9815, doi:10.1002/2014JA020138, 2014JA020138.

Crary, F. J., J. T. Clarke, M. K. Dougherty, P. G. Hanlon, K. C. Hansen, J. T. Steinberg, B. L. Barraclough, A. J. Coates, J.-C. Gérard, D. Grodent, W. S. Kurth, D. G. Mitchell, A. M. Rymer, and D. T. Young (2005), Solar wind dynamic pressure and electric field as the main factors controlling Saturn's aurorae, *Nature*, *433*, 720–722, doi:10.1038/nature03333.

Cravens, T. E. (2004), *Physics of Solar System Plasmas.*

Cui, J., R. V. Yelle, and K. Volk (2008), Distribution and escape of molecular hydrogen in Titan's thermosphere and exosphere, *J. of Geophys. Res.*, *113*, E10004, doi:10.1029/2007JE003032.

de Keyser, J., M. W. Dunlop, C. J. Owen, B. U. Ö. Sonnerup, S. E. Haaland, A. Vaivads, G. Paschmann, R. Lundin, and L. Rezeau (2005), Magnetopause and Boundary Layer, *Space Sci. Rev.*, *118*, 231–320, doi:10.1007/s11214-005-3834-1.

Desch, M. D., and H. O. Rucker (1983), The relationship between Saturn kilometric radiation and the solar wind, *J. Geophys. Res.*, *88*, 8999–9006, doi:10.1029/JA088iA11p08999.

Desch, M. D., and H. O. Rucker (1985), Saturn radio emission and the solar wind - Voyager-2 studies, *Advances in Space Research*, *5*, 333–336, doi:10.1016/0273-1177(85)90159-0.

Desroche, M., F. Bagenal, P. A. Delamere, and N. Erkaev (2013), Conditions at the magnetopause of Saturn and implications for the solar wind interaction, *J. of Geophys. Res.*, *118*, 3087–3095, doi:10.1002/jgra.50294.

Dessler, A. (1980), Mass-injection rate from io into the io plasma torus, *Icarus*, *44*(2), 291 – 295, doi:10.1016/0019-1035(80)90024-X.

Dougherty, M. K., S. Kellock, D. J. Southwood, A. Balogh, E. J. Smith, B. T. Tsurutani, B. Gerlach, K.-H. Glassmeier, F. Gleim, C. T. Russell, G. Erdos, F. M. Neubauer, and S. W. H. Cowley (2004), The Cassini Magnetic Field Investigation, *SSR*, *114*, 331–383, doi:10.1007/s11214-004-1432-2.

Dougherty, M. K., K. K. Khurana, F. M. Neubauer, C. T. Russell, J. Saur, J. S. Leisner, and M. E. Burton (2006), Identification of a Dynamic Atmosphere at Enceladus with the Cassini Magnetometer, *Science*, *311*, 1406–1409, doi:10.1126/science.1120985.

Dougherty, M. K., L. W. Esposito, and S. M. Krimigis (2009), *Saturn from Cassini-Huygens*, doi:10.1007/978-1-4020-9217-6.

Dungey, J. W. (1961), Interplanetary Magnetic Field and the Auroral Zones, *Phys. Rev. Lett.*, *6*, 47–48, doi:10.1103/PhysRevLett.6.47.

Dunlop, M. W., B. Lavraud, P. Cargill, M. G. G. T. Taylor, A. Balogh, H. Réme, P. Decreau, K.-H. Glassmeier, R. C. Elphic, J.-M. Bosqued, A. N. Fazakerley, I. Dandouras, C. P. Escoubet, H. Laakso, and A. Marchaudon (2005), Cluster Observations of the CUSP: Magnetic Structure and Dynamics, *Surveys in Geophysics*, *26*, 5–55, doi:10.1007/s10712-005-1871-7.

Eastman, T. E., S. A. Boardsen, S.-H. Chen, S. F. Fung, and R. L. Kessel (2000), Configuration of high-latitude and high-altitude boundary layers, *J. Geophys. Res.*, *105*, 23,221–23,238, doi:10.1029/1999JA900269.

Erlandson, R. E., L. J. Zanetti, T. A. Potemra, M. Andre, and L. Matson (1988), Observation of electromagnetic ion cyclotron waves and hot plasma in the polar cusp, *Geophys. Res. Lett.*, *15*, 421–424, doi:10.1029/GL015i005p00421.

Escoubet, C. P., M. F. Smith, S. F. Fung, P. C. Anderson, R. A. Hoffman, E. M. Basinska, and J. M. Bosqued (1992), Staircase ion signature in the polar cusp: A case study, *Geophys. Res. Lett.*, *19*(17), 1735–1738, doi:10.1029/92GL01806.

Escoubet, C. P., J. M. Bosqued, J. Berchem, K. J. Trattner, M. G. G. T. Taylor, F. Pitout, H. Laakso, A. Masson, M. Dunlop, H. Reme, I. Dandouras, and A. Fazakerley (2006), Temporal evolution of a staircase ion signature observed by cluster in the mid-altitude polar cusp, *Geophys. Res. Lett.*, *33*(7), doi:10.1029/2005GL025598, l07108.

Escoubet, C. P., J. Berchem, K. J. Trattner, F. Pitout, R. Richard, M. G. G. T. Taylor, J. Soucek, B. Grison, H. Laakso, A. Masson, M. Dunlop, I. Dandouras, H. Reme, A. Fazakerley, and P. Daly (2013), Double cusp encounter by Cluster: double cusp or motion of the cusp?, *Annales Geophysicae*, *31*, 713–723, doi:10.5194/angeo-31-713-2013.

Farrugia, C. J., P. E. Sandholt, W. F. Denig, and R. B. Torbert (1998), Observation of a correspondence between poleward moving auroral forms and stepped cusp ion precipitation, *J. of Geophys. Res.*, *103*(A5), 9309–9315, doi:10.1029/97JA02882.

Fear, R. C., A. N. Fazakerley, C. J. Owen, and E. A. Lucek (2005), A survey of flux transfer events observed by Cluster during strongly northward IMF, *Geophys. Res. Lett.*, *32*, L18105, doi:10.1029/2005GL023811.

Fear, R. C., S. E. Milan, A. N. Fazakerley, E. A. Lucek, S. W. H. Cowley, and I. Dandouras (2008), The azimuthal extent of three flux transfer events, *Annales Geophysicae*, *26*, 2353–2369, doi:10.5194/angeo-26-2353-2008.

Fear, R. C., S. E. Milan, A. N. Fazakerley, K.-H. Fornaçon, C. M. Carr, and I. Dandouras (2009), Simultaneous observations of flux transfer events by THEMIS, Cluster, Double Star, and SuperDARN: Acceleration of FTEs, *J. of Geophys. Res.*, *114*, A10213, doi:10.1029/2009JA014310.

Feynman, R. P. (1964), *Feynman lectures on physics. Volume 2: Mainly electromagnetism and matter*.

Fouchet, T., J. I. Moses, and B. J. Conrath (2009), *Saturn: Composition and Chemistry*, p. 83, doi:10.1007/978-1-4020-9217-6_5.

Frank, L. A. (1971), Plasma in the earth's polar magnetosphere., *J. Geophys. Res.*, *76*, 5202–5219, doi:10.1029/JA076i022p05202.

Fritz, T. A., J. Chen, and G. L. Siscoe (2003), Energetic ions, large diamagnetic cavities, and Chapman-Ferraro cusp, *J. of Geophys. Res.*, *108*, 1028, doi:10.1029/2002JA009476.

Fukazawa, K., S.-i. Ogi, T. Ogino, and R. J. Walker (2007), Magnetospheric convection at Saturn as a function of IMF BZ, *Geophys. Res. Lett.*, *34*, 1105, doi:10.1029/2006GL028373.

Gérard, J.-C., D. Grodent, J. Gustin, A. Saglam, J. T. Clarke, and J. T. Trauger (2004), Characteristics of Saturn's FUV aurora observed with the Space Telescope Imaging Spectrograph, *J. Geophys. Res.(Space Physics)*, *109*, A09207, doi:10.1029/2004JA010513.

Gérard, J.-C., E. J. Bunce, D. Grodent, S. W. H. Cowley, J. T. Clarke, and S. V. Badman (2005), Signature of Saturn's auroral cusp: Simultaneous Hubble Space Telescope FUV observations and upstream solar wind monitoring, *J. Geophys. Res.*, *110*(9), A11201, doi:10.1029/2005JA011094.

Giampieri, G., and M. Dougherty (2004), Modelling of the ring current in Saturn's magnetosphere, *Annales Geophysicae*, *22*, 653–659, doi:10.5194/angeo-22-653-2004.

Gombosi, T. I. (1999), *Physics of the Space Environment*.

Gosling, J. T., M. F. Thomsen, S. J. Bame, T. G. Onsager, and C. T. Russell (1990a), The electron edge of the low latitude boundary layer during accelerated flow events, *Geophys. Res. Lett.*, *17*, 1833–1836, doi:10.1029/GL017i011p01833.

Gosling, J. T., M. F. Thomsen, S. J. Bame, R. C. Elphic, and C. T. Russell (1990b), Plasma flow reversals at the dayside magnetopause and the origin of asymmetric polar cap convection, *J. Geophys. Res.*, *95*, 8073–8084, doi:10.1029/JA095iA06p08073.

Gosling, J. T., M. F. Thomsen, S. J. Bame, R. C. Elphic, and C. T. Russell (1991), Observations of reconnection of interplanetary and lobe magnetic field lines at the high-latitude magnetopause, *J. Geophys. Res.*, *96*, 14,097, doi:10.1029/91JA01139.

Gurnett, D. A. (1966), A satellite study of VLF hiss, *J. Geophys. Res.*, *71*, 5599–5615, doi:10.1029/JZ071i023p05599.

Gurnett, D. A., W. S. Kurth, D. L. Kirchner, G. B. Hospodarsky, T. F. Averkamp, P. Zarka, A. Lecacheux, R. Manning, A. Roux, P. Canu, N. Cornilleau-Wehrlin, P. Galopeau, A. Meyer, R. Boström, G. Gustafsson, J.-E. Wahlund, L. Åhlen, H. O. Rucker, H. P. Ladreiter, W. Macher, L. J. C. Woolliscroft, H. Alleyne, M. L. Kaiser, M. D. Desch, W. M. Farrell, C. C. Harvey, P. Louarn, P. J. Kellogg, K. Goetz, and A. Pedersen (2004), The Cassini Radio and Plasma Wave Investigation, *Space Sci. Rev.*, *114*, 395–463, doi:10.1007/s11214-004-1434-0.

Gurnett, D. A., A. M. Persoon, A. J. Kopf, W. S. Kurth, M. W. Morooka, J.-E. Wahlund, K. K. Khurana, M. K. Dougherty, D. G. Mitchell, S. M. Krimigis, and N. Krupp (2010), A plasmapause-like density boundary at high latitudes in Saturn's magnetosphere, *Geophys. Res. Lett.*, *37*, L16806, doi:10.1029/2010GL044466.

Haerendel, G., G. Paschmann, N. Sckopke, H. Rosenbauer, and P. C. Hedgecock (1978), The frontside boundary layer of the magnetosphere and the problem of reconnection, *J. of Geophys. Res.*, *83*(A7), 3195–3216, doi:10.1029/JA083iA07p03195.

Hansen, C. J., L. Esposito, A. I. F. Stewart, J. Colwell, A. Hendrix, W. Pryor, D. Shemansky, and R. West (2006), Enceladus' Water Vapor Plume, *Science*, *311*, 1422–1425, doi:10.1126/science.1121254.

Hansen, K. C., A. J. Ridley, G. B. Hospodarsky, N. Achilleos, M. K. Dougherty, T. I. Gombosi, and G. Tóth (2005), Global MHD simulations of Saturn's magnetosphere at the time of Cassini approach, *Geophys. Res. Lett.*, *32*, L20S06, doi:10.1029/2005GL022835.

Hargreaves, J. K. (1995), The solar-terrestrial environment. An introduction to geospace - the science of the terrestrial upper atmosphere, ionosphere and magnetosphere., *Camb. Atmos. Space Sci. Ser., Vol. 5*.

Heikkila, W. J. (1972), The morphology of auroral particle precipitation., in *Space Research Conference*, edited by S. A. Bowhill, L. D. Jaffe, and M. J. Rycroft, pp. 1343–1355.

Heikkila, W. J. (1985), Definition of the cusp, in *The polar cusp; Proceedings of the Advanced Research Workshop on the Morphology and Dynamics of the Polar Cusp, Lillehammer, Norway, May 7-12, 1984 (A86-24001 09-46). Dordrecht, D. Reidel Publishing Co., 1985, p. 387-395.*, edited by J. A. Holtet and A. Egeland, pp. 387–395.

Heikkila, W. J., and J. D. Winningham (1971), Penetration of magnetosheath plasma to low altitudes through the dayside magnetospheric cusps., *J. Geophys. Res.*, *76*, 883–891, doi:10.1029/JA076i004p00883.

Hill, T. W., and P. H. Reiff (1977), Evidence of magnetospheric cusp proton acceleration by magnetic merging at the dayside magnetopause, *J. Geophys. Res.*, *82*, 3623–3628, doi:10.1029/JA082i025p03623.

Huddleston, D. E., C. T. Russell, G. Le, and A. Szabo (1997), Magnetopause struc-

ture and the role of reconnection at the outer planets, *J. Geophys. Res.*, *102*, 24,289–24,004, doi:10.1029/97JA02416.

Huddleston, D. E., C. T. Russell, M. G. Kivelson, K. K. Khurana, and L. Bennett (1998), Location and shape of the Jovian magnetopause and bow shock, *J. Geophys. Res.*, *103*, 20,075–20,082, doi:10.1029/98JE00394.

Hundhausen, A. J. (1972), *Coronal Expansion and Solar Wind*.

Isbell, J., A. J. Dessler, and J. H. Waite, Jr. (1984), Magnetospheric energization by interaction between planetary spin and the solar wind, *J. Geophys. Res.*, *89*, 10,716–10,722, doi:10.1029/JA089iA12p10716.

Jackman, C. M., and C. S. Arridge (2011), Solar Cycle Effects on the Dynamics of Jupiter's and Saturn's Magnetospheres, *Sol. Phys.*, *274*, 481–502, doi:10.1007/s11207-011-9748-z.

Jackman, C. M., N. Achilleos, E. J. Bunce, S. W. H. Cowley, M. K. Dougherty, G. H. Jones, S. E. Milan, and E. J. Smith (2004), Interplanetary magnetic field at ∼9 AU during the declining phase of the solar cycle and its implications for Saturn's magnetospheric dynamics, *J. of Geophys. Res.*, *109*, A11203, doi:10.1029/2004JA010614.

Jackman, C. M., C. T. Russell, D. J. Southwood, C. S. Arridge, N. Achilleos, and M. K. Dougherty (2007), Strong rapid dipolarizations in Saturn's magnetotail: In situ evidence of reconnection, *Geophys. Res. Lett.*, *34*, L11203, doi:10.1029/2007GL029764.

Jackman, C. M., C. S. Arridge, N. Krupp, E. J. Bunce, D. G. Mitchell, H. J. McAndrews, M. K. Dougherty, C. T. Russell, N. Achilleos, G. H. Jones, and A. J. Coates (2008), A multi-instrument view of tail reconnection at Saturn, *J. of Geophys. Research (Space Physics)*, *113*, A11213, doi:10.1029/2008JA013592.

Jackman, C. M., J. A. Slavin, and S. W. H. Cowley (2011), Cassini observations of plasmoid structure and dynamics: Implications for the role of magnetic reconnection in magnetospheric circulation at Saturn, *J. of Geophys. Res.*, *116*, A10212, doi:10.1029/2011JA016682.

Jasinski, J. M., C. S. Arridge, L. Lamy, J. S. Leisner, M. F. Thomsen, D. G. Mitchell, A. J. Coates, A. Radioti, G. H. Jones, E. Roussos, N. Krupp, D. Grodent, M. K. Dougherty, and J. H. Waite (2014), Cusp observation at Saturn's high-latitude magnetosphere by the Cassini spacecraft, *Geophys. Res. Lett.*, *41*, 1382–1388, doi:10.1002/2014GL059319.

Jia, X., K. C. Hansen, T. I. Gombosi, M. G. Kivelson, G. Tth, D. L. DeZeeuw, and A. J. Ridley (2012), Magnetospheric configuration and dynamics of saturn's magnetosphere: A global mhd simulation, *J. of Geophys. Res.*, *117*(A5), doi: 10.1029/2012JA017575.

Jian, L. K., C. T. Russell, J. G. Luhmann, P. J. MacNeice, D. Odstrcil, P. Riley, J. A. Linker, R. M. Skoug, and J. T. Steinberg (2011), Comparison of Observations at ACE and Ulysses with Enlil Model Results: Stream Interaction Regions During Carrington Rotations 2016 - 2018, *Sol. Phys.*, *273*, 179–203, doi: 10.1007/s11207-011-9858-7.

Jinks, S. L., E. J. Bunce, S. W. H. Cowley, G. Provan, T. K. Yeoman, C. S. Arridge, M. K. Dougherty, D. A. Gurnett, N. Krupp, W. S. Kurth, D. G. Mitchell, M. Morooka, and J.-E. Wahlund (2014), Cassini multi-instrument assessment of Saturn's polar cap boundary, *J. of Geophys. Res.*, *119*, 8161–8177, doi:10.1002/2014JA020367.

Jones, G. H., E. Roussos, N. Krupp, C. Paranicas, J. Woch, A. Lagg, D. G. Mitchell, S. M. Krimigis, and M. K. Dougherty (2006), Enceladus' Varying Imprint on the Magnetosphere of Saturn, *Science*, *311*, 1412–1415, doi:10.1126/science.1121011.

Joy, S. P., M. G. Kivelson, R. J. Walker, K. K. Khurana, C. T. Russell, and T. Ogino (2002), Probabilistic models of the Jovian magnetopause and bow shock locations, *J. of Geophys. Res.*, *107*, 1309, doi:10.1029/2001JA009146.

Kanani, S. J., C. S. Arridge, G. H. Jones, A. N. Fazakerley, H. J. McAndrews, N. Sergis, S. M. Krimigis, M. K. Dougherty, A. J. Coates, D. T. Young, K. C. Hansen, and N. Krupp (2010), A new form of Saturn's magnetopause using a dynamic pressure balance model, based on in situ, multi-instrument Cassini measurements, *J. Geophys. Res.*, *115*, A06207, doi:10.1029/2009JA014262.

Khurana, K. K., C. S. Arridge, H. Schwarzl, and M. K. Dougherty (2006), A Model of Saturn's Magnetospheric Field Based on Latest Cassini Observations, *AGU Spring Meeting Abstracts*, p. A1.

Khurana, K. K., M. K. Dougherty, C. T. Russell, and J. S. Leisner (2007), Mass loading of Saturn's magnetosphere near Enceladus, *J. of Geophys. Res.*, *112*, A08203, doi:10.1029/2006JA012110.

Kivelson, M. G., and C. T. Russell (1995), *Introduction to Space Physics*.

Korth, H., B. J. Anderson, J. M. Raines, J. A. Slavin, T. H. Zurbuchen, C. L. Johnson, M. E. Purucker, R. M. Winslow, S. C. Solomon, and R. L. McNutt, Jr. (2011), Plasma pressure in Mercury's equatorial magnetosphere derived from MESSENGER Magnetometer observations, *Geophys. Res. Lett.*, *38*, L22201, doi: 10.1029/2011GL049451.

Krimigis, S. M., J. F. Carbary, E. P. Keath, T. P. Armstrong, L. J. Lanzerotti, and G. Gloeckler (1983), General characteristics of hot plasma and energetic particles in the Saturnian magnetosphere - Results from the Voyager spacecraft, *J. Geophys. Res.*, *88*, 8871–8892, doi:10.1029/JA088iA11p08871.

Krimigis, S. M., D. G. Mitchell, D. C. Hamilton, S. Livi, J. Dandouras, S. Jaskulek, T. P. Armstrong, J. D. Boldt, A. F. Cheng, G. Gloeckler, J. R. Hayes, K. C. Hsieh, W.-H. Ip, E. P. Keath, E. Kirsch, N. Krupp, L. J. Lanzerotti, R. Lundgren, B. H. Mauk, R. W. McEntire, E. C. Roelof, C. E. Schlemm, B. E. Tossman, B. Wilken, and D. J. Williams (2004), Magnetosphere Imaging Instrument (MIMI) on the Cassini Mission to Saturn/Titan, *Space Sci. Rev.*, *114*, 233–329, doi:10.1007/ s11214-004-1410-8.

Krimigis, S. M., D. G. Mitchell, D. C. Hamilton, N. Krupp, S. Livi, E. C. Roelof, J. Dandouras, T. P. Armstrong, B. H. Mauk, C. Paranicas, P. C. Brandt, S. Bolton, A. F. Cheng, T. Choo, G. Gloeckler, J. Hayes, K. C. Hsieh, W.-H. Ip, S. Jaskulek, E. P. Keath, E. Kirsch, M. Kusterer, A. Lagg, L. J. Lanzerotti, D. LaVallee, J. Manweiler, R. W. McEntire, W. Rasmuss, J. Saur, F. S. Turner, D. J. Williams, and J. Woch (2005), Dynamics of Saturn's Magnetosphere from MIMI During Cassini's Orbital Insertion, *Science*, *307*, 1270–1273, doi:10.1126/science.1105978.

Krimigis, S. M., N. Sergis, D. G. Mitchell, D. C. Hamilton, and N. Krupp (2007), A dynamic, rotating ring current around Saturn, *Nature*, *450*, 1050–1053, doi: 10.1038/nature06425.

Krupp, N., E. Roussos, A. Lagg, J. Woch, A. L. Müller, S. M. Krimigis, D. G. Mitchell, E. C. Roelof, C. Paranicas, J. Carbary, G. H. Jones, D. C. Hamilton, S. Livi, T. P. Armstrong, M. K. Dougherty, and N. Sergis (2009), Energetic particles in Saturn's magnetosphere during the Cassini nominal mission (July 2004-July 2008), *Planet. Space Sci.*, *57*, 1754–1768, doi:10.1016/j.pss.2009.06.010.

Lai, H. R., H. Y. Wei, C. T. Russell, C. S. Arridge, and M. K. Dougherty (2012), Reconnection at the magnetopause of Saturn: Perspective from FTE occurrence and magnetosphere size, *J. of Geophys. Res.*, *117*, A05222, doi: 10.1029/2011JA017263.

Lamy, L., P. Zarka, B. Cecconi, R. Prangé, W. S. Kurth, and D. A. Gurnett (2008), Saturn kilometric radiation: Average and statistical properties, *J. of Geophys. Res.*, *113*, A07201, doi:10.1029/2007JA012900.

Lamy, L., R. Prange, W. Pryor, J. Gustin, S. V. Badman, H. Melin, T. Stallard, D. Mitchell, and P. C. Brandt (2013), Multispectral simultaneous diagnosis of saturn's aurorae throughout a planetary rotation, *J. of Geophys. Res.*, *118*(8), 4817–4843, doi:10.1002/jgra.50404.

Lavraud, B., A. Fedorov, E. Budnik, A. Grigoriev, P. J. Cargill, M. W. Dunlop, H. Rème, I. Dandouras, and A. Balogh (2004), Cluster survey of the high-altitude cusp properties: a three-year statistical study, *Annales Geophysicae*, *22*(8), 3009–3019, doi:10.5194/angeo-22-3009-2004.

Lemaire, J. (1982), A brief panorama, *Advances in Space Research*, *2*, 3–10, doi: 10.1016/0273-1177(82)90084-9.

Lepping, R. P., L. F. Burlaga, A. J. Lazarus, V. M. Vasyliunas, A. Szabo, J. Steinberg, N. F. Ness, and S. M. Krimigis (1992), Neptune's polar cusp region: Observations and magnetic field analysis, *J. of Geophys. Res.*, *97*(A6), 8135–8144, doi:10.1029/92JA00314.

Lewis, G. R., C. S. Arridge, D. R. Linder, L. K. Gilbert, D. O. Kataria, A. J. Coates, A. Persoon, G. A. Collinson, N. André, P. Schippers, J. Wahlund, M. Morooka, G. H. Jones, A. M. Rymer, D. T. Young, D. G. Mitchell, A. Lagg, and S. A. Livi (2010), The calibration of the Cassini-Huygens CAPS Electron Spectrometer, *Planet. Space Sci.*, *58*, 427–436, doi:10.1016/j.pss.2009.11.008.

Linder, D. R., A. J. Coates, R. D. Woodliffe, C. Alsop, A. D. Johnstone, M. Grande, A. Preece, B. Narheim, and D. T. Young (1998), The Cassini CAPS Electron Spectrometer, *Washington DC American Geophysical Union Geophysical Monograph Series*, *102*, 257.

Lockwood, M., and M. F. Smith (1992), The variation of reconnection rate at the dayside magnetopause and cusp ion precipitation, *J. Geophys. Res.*, *97*, 14,841, doi:10.1029/92JA01261.

Lockwood, M., and M. F. Smith (1993), Comment on mapping the dayside ionosphere to the magnetosphere according to particle precipitation characteristics by newell and meng, *Geophys. Res. Lett.*, *20*(16), 1739–1740, doi:10.1029/93GL01967.

Lockwood, M., and M. F. Smith (1994), Low and middle altitude cusp particle signatures for general magnetopause reconnection rate variations. 1: Theory, *J. Geophys. Res.*, *99*, 8531–8553, doi:10.1029/93JA03399.

Lockwood, M., W. F. Denig, A. D. Farmer, V. N. Davda, S. W. H. Cowley, and H. Luehr (1993), Ionospheric signatures of pulsed reconnection at the earth's magnetopause, *Nature*, *361*, 424–428, doi:10.1038/361424a0.

Lockwood, M., T. G. Onsager, C. J. Davis, M. F. Smith, and W. F. Denig (1994), The characteristic of the magnetopause reconnection X-line deduced from low-altitude satellite observations of cusp ions, *Geophys. Res. Lett.*, *21*, 2757–2760, doi:10.1029/94GL02696.

Lockwood, M., T. G. Onsager, C. J. Davis, M. F. Smith, and W. F. Denig (1995), Correction to "The characteristics of the magnetopause reconnection X-line deduced from low-altitude satellite observations of cusp ions", *Geophys. Res. Lett.*, *22*, 867–867, doi:10.1029/95GL00910.

Lockwood, M., S. E. Milan, T. Onsager, C. H. Perry, J. A. Scudder, C. T. Russell, and M. Brittnacher (2001), Cusp ion steps, field-aligned currents and poleward moving auroral forms, *J. Geophys. Res.*, *106*, 29,555–29,570, doi: 10.1029/2000JA900175.

Lui, A. T. Y. (1987), *Road map to magnetotail domains*, pp. 3–5.

Lyons, L. R., and R. M. Thorne (1973), Equilibrium structure of radiation belt electrons, *J. Geophys. Res.*, *78*, 2142–2149, doi:10.1029/JA078i013p02142.

Markwardt, C. B. (2009), Non-linear Least-squares Fitting in IDL with MPFIT, in *Astronomical Data Analysis Software and Systems XVIII*, *Astronomical Society of the Pacific Conference Series*, vol. 411, edited by D. A. Bohlender, D. Durand, and P. Dowler, p. 251.

Marquardt, D. W. (1963), An algorithm for least-squares estimation of nonlinear parameters, *SIAM Journal on Applied Mathematics*, *11*(2), 431–441, doi:10.1137/0111030.

Masters, A., D. G. Mitchell, A. J. Coates, and M. K. Dougherty (2011a), Saturn's low-latitude boundary layer: 1. Properties and variability, *J. of Geophys. Res.*, *116*, A06210, doi:10.1029/2010JA016421.

Masters, A., A. P. Walsh, A. N. Fazakerley, A. J. Coates, and M. K. Dougherty (2011b), Saturn's low-latitude boundary layer: 2. Electron structure, *J. of Geophys. Research (Space Physics)*, *116*, A06211, doi:10.1029/2010JA016422.

Masters, A., J. P. Eastwood, M. Swisdak, M. F. Thomsen, C. T. Russell, N. Sergis, F. J. Crary, M. K. Dougherty, A. J. Coates, and S. M. Krimigis (2012), The importance of plasma β conditions for magnetic reconnection at Saturn's magnetopause, *Geophys. Res. Lett.*, *39*, L08103, doi:10.1029/2012GL051372.

Masters, A., L. Stawarz, M. Fujimoto, S. J. Schwartz, N. Sergis, M. F. Thomsen, A. Retinò, H. Hasegawa, B. Zieger, G. R. Lewis, A. J. Coates, P. Canu, and M. K. Dougherty (2013), Electron acceleration to relativistic energies at a strong quasi-parallel shock wave, *Nature Physics*, *9*, 164–167, doi:10.1038/nphys2541.

Mauk, B., and F. Bagenal (2012), Comparative Auroral Physics: Earth and Other Planets, *Washington DC American Geophysical Union Geophysical Monograph Series*, *197*, 3–26, doi:10.1029/2011GM001192.

Mauk, B. H., D. C. Hamilton, T. W. Hill, G. B. Hospodarsky, R. E. Johnson, C. Paranicas, E. Roussos, C. T. Russell, D. E. Shemansky, E. C. Sittler, and R. M. Thorne (2009), *Fundamental Plasma Processes in Saturn's Magnetosphere*, p. 281, doi:10.1007/978-1-4020-9217-6_11.

Maurice, S., and I. M. Engle (1995), Idealized saturn magnetosphere shape and field, *J. of Geophys. Res.*, *100*(A9), 17,143–17,151, doi:10.1029/95JA00897.

McAndrews, H. J., C. J. Owen, M. F. Thomsen, B. Lavraud, A. J. Coates, M. K. Dougherty, and D. T. Young (2008), Evidence for reconnection at Saturn's magnetopause, *J. of Geophys. Res.*, *113*, A04210, doi:10.1029/2007JA012581.

McWilliams, K. A., G. J. Sofko, T. K. Yeoman, S. E. Milan, D. G. Sibeck, T. Nagai, T. Mukai, I. J. Coleman, T. Hori, and F. J. Rich (2004), Simultaneous observations of magnetopause flux transfer events and of their associated signatures at ionospheric altitudes, *Annales Geophysicae*, *22*(6), 2181–2199, doi:10.5194/angeo-22-2181-2004.

Meredith, C. J., I. I. Alexeev, S. V. Badman, E. S. Belenkaya, S. W. H. Cowley, M. K. Dougherty, V. V. Kalegaev, G. R. Lewis, and J. D. Nichols (2014), Saturn's dayside ultraviolet auroras: Evidence for morphological dependence on the direction of the upstream interplanetary magnetic field, *J. of Geophys. Res.*, *119*, 1994–2008, doi:10.1002/2013JA019598.

Meurant, M., J.-C. GéRard, C. Blockx, B. Hubert, and V. Coumans (2004), Propagation of electron and proton shock-induced aurora and the role of the interplanetary magnetic field and solar wind, *J. of Geophys. Res.*, *109*, A10210, doi:10.1029/2004JA010453.

Milan, S. E., E. J. Bunce, S. W. H. Cowley, and C. M. Jackman (2005), Implications of rapid planetary rotation for the Dungey magnetotail of Saturn, *J. Geophys. Res.*, *110*, A03209, doi:10.1029/2004JA010716.

Mitchell, D. G., W. S. Kurth, G. B. Hospodarsky, N. Krupp, J. Saur, B. H. Mauk, J. F. Carbary, S. M. Krimigis, M. K. Dougherty, and D. C. Hamilton (2009), Ion conics and electron beams associated with auroral processes on Saturn, *J. of Geophys. Research (Space Physics)*, *114*, A02212, doi:10.1029/2008JA013621.

Moré, J., and S. Wright (1993), *Optimization Software Guide*, Frontiers in Applied Mathematics, Society for Industrial and Applied Mathematics.

Moré, J. J. (1977), The Levenberg-Marquardt algorithm: Implementation and theory, in *Numerical Analysis*, edited by G. A. Watson, pp. 105–116, Springer, Berlin.

Mozer, F. S., and A. Retinò (2007), Quantitative estimates of magnetic field reconnection properties from electric and magnetic field measurements, *J. of Geophys. Res.*, *112*, A10206, doi:10.1029/2007JA012406.

Ness, N. F., M. H. Acuna, R. P. Lepping, J. E. P. Connerney, K. W. Behannon, L. F. Burlaga, and F. M. Neubauer (1981), Magnetic field studies by Voyager 1 - Preliminary results at Saturn, *Science*, *212*, 211–217, doi:10.1126/science.212.4491.211.

Ness, N. F., M. H. Acuna, L. F. Burlaga, J. E. P. Connerney, and R. P. Lepping (1989), Magnetic fields at Neptune, *Science*, *246*, 1473–1478, doi:10.1126/science.246.4936.1473.

Newell, P. T., and C.-I. Meng (1988), The cusp and the cleft/boundary layer - Low-altitude identification and statistical local time variation, *J. Geophys. Res.*, *93*, 14,549–14,556, doi:10.1029/JA093iA12p14549.

Newell, P. T., and C.-I. Meng (1989), On quantifying the distinctions between the cusp and the cleft/LLBL., in *Electromagnetic Coupling in the Polar Clefts and Caps*, edited by P. E. Sandholt and A. Egeland, pp. 87–101.

Newell, P. T., C.-I. Meng, E. R. Sanchez, W. J. Burke, and M. E. Greenspan (1991), Identification and observations of the plasma mantle at low altitude, *J. Geophys. Res.*, *96*, 35–45, doi:10.1029/90JA01760.

Nichols, J. D., J. T. Clarke, S. W. H. Cowley, J. Duval, A. J. Farmer, J.-C. Gérard, D. Grodent, and S. Wannawichian (2008), Oscillation of Saturn's southern auroral oval, *J. Geophys. Res.(Space Physics)*, *113*, A11205, doi:10.1029/2008JA013444.

Nichols, J. D., S. W. H. Cowley, and L. Lamy (2010), Dawn-dusk oscillation of Saturn's conjugate auroral ovals, *Geophys. Res. Lett.*, *37*, L24102, doi:10.1029/2010GL045818.

Niehof, J. T., T. A. Fritz, R. H. W. Friedel, and J. Chen (2008), Interdependence of magnetic field and plasma pressures in cusp diamagnetic cavities, *Geophys. Res. Lett.*, *35*, L11101, doi:10.1029/2008GL033589.

Niehof, J. T., T. A. Fritz, R. H. W. Friedel, and J. Chen (2010), Size and location of cusp diamagnetic cavities observed by Polar, *J. of Geophys. Res.*, *115*, A07201, doi:10.1029/2009JA014827.

Nykyri, K., A. Otto, E. Adamson, E. Dougal, and J. Mumme (2011a), Cluster observations of a cusp diamagnetic cavity: Structure, size, and dynamics, *J. of Geophys. Res.*, *116*, A03228, doi:10.1029/2010JA015897.

Nykyri, K., A. Otto, E. Adamson, and A. Tjulin (2011b), On the origin of fluctuations in the cusp diamagnetic cavity, *J. of Geophys. Res.*, *116*, A06208, doi:10.1029/2010JA015888.

Odstrcil, D. (2003), Modeling 3-D solar wind structure, *Advances in Space Research*, *32*, 497–506, doi:10.1016/S0273-1177(03)00332-6.

Ogilvie, K. W., M. A. Coplan, P. Bochsler, and J. Geiss (1989), Solar wind observations with the ion composition instrument aboard the ISEE-3/ICE spacecraft, *Sol. Phys.*, *124*, 167–183, doi:10.1007/BF00146526.

Øieroset, M., P. E. Sandholt, W. F. Denig, and S. W. H. Cowley (1997), Northward interplanetary magnetic field cusp aurora and high-latitude magnetopause reconnection, *J. Geophys. Res.*, *102*, 11,349–11,362, doi:10.1029/97JA00559.

Onsager, T. G., C. A. Kletzing, J. B. Austin, and H. MacKiernan (1993), Model of magnetosheath plasma in the magnetosphere: Cusp and mantle particles at low-altitudes, *Geophys. Res. Lett.*, *20*(6), 479–482, doi:10.1029/93GL00596.

Onsager, T. G., J. D. Scudder, M. Lockwood, and C. T. Russell (2001), Reconnection at the high-latitude magnetopause during northward interplanetary magnetic field conditions, *J. of Geophys. Res.*, *106*(A11), 25,467–25,488, doi:10.1029/2000JA000444.

Owen, C. J., A. Marchaudon, M. W. Dunlop, A. N. Fazakerley, J.-M. Bosqued, J. P. Dewhurst, R. C. Fear, S. A. Fuselier, A. Balogh, and H. RèMe (2008), Cluster observations of "crater" flux transfer events at the dayside high-latitude magnetopause, *J. of Geophys. Res.*, *113*, A07S04, doi:10.1029/2007JA012701.

Paranicas, C., D. G. Mitchell, S. M. Krimigis, D. C. Hamilton, E. Roussos, N. Krupp, G. H. Jones, R. E. Johnson, J. F. Cooper, and T. P. Armstrong (2008), Sources and losses of energetic protons in Saturn's magnetosphere, *Icarus*, *197*, 519–525, doi:10.1016/j.icarus.2008.05.011.

Parker, E. (1959), Extension of the Solar Corona into Interplanetary Space, *J. Geophys. Res.*, *64*, 1675–1681, doi:10.1029/JZ064i011p01675.

Parker, E. N. (1957), Sweet's Mechanism for Merging Magnetic Fields in Conducting Fluids, *J. Geophys. Res.*, *62*, 509–520, doi:10.1029/JZ062i004p00509.

Paschmann, G., G. Haerendel, N. Sckopke, H. Rosenbauer, and P. C. Hedgecock (1976), Plasma and magnetic field characteristics of the distant polar cusp near local noon: The entry layer, *J. of Geophys. Research*, *81*(16), 2883–2899, doi:10.1029/JA081i016p02883.

Petschek, H. E. (1964), Magnetic Field Annihilation, *NASA Special Publication*, *50*, 425.

Phan, T. D., J. T. Gosling, G. Paschmann, C. Pasma, J. F. Drake, M. Øieroset, D. Larson, R. P. Lin, and M. S. Davis (2010), The Dependence of Magnetic Reconnection on Plasma β and Magnetic Shear: Evidence from Solar Wind Observations, *ApJ*, *719*, L199–L203, doi:10.1088/2041-8205/719/2/L199.

Pilkington, N. M., N. Achilleos, C. S. Arridge, A. Masters, N. Sergis, A. J. Coates, and M. K. Dougherty (2014), Polar confinement of Saturn's magnetosphere revealed by in situ Cassini observations, *J. of Geophys. Res.*, *119*, 2858–2875, doi:10.1002/2014JA019774.

Pitout, F., C. P. Escoubet, B. Klecker, and H. Rème (2006), Cluster survey of the mid-altitude cusp: 1. size, location, and dynamics, *Annales Geophysicae*, *24*, 3011–3026, doi:10.5194/angeo-24-3011-2006.

Pitout, F., C. P. Escoubet, B. Klecker, and I. Dandouras (2009), Cluster survey of the mid-altitude cusp - Part 2: Large-scale morphology, *Annales Geophysicae*, *27*, 1875–1886, doi:10.5194/angeo-27-1875-2009.

Porco, C. C., P. Helfenstein, P. C. Thomas, A. P. Ingersoll, J. Wisdom, R. West, G. Neukum, T. Denk, R. Wagner, T. Roatsch, S. Kieffer, E. Turtle, A. McEwen, T. V. Johnson, J. Rathbun, J. Veverka, D. Wilson, J. Perry, J. Spitale, A. Brahic, J. A. Burns, A. D. Del Genio, L. Dones, C. D. Murray, and S. Squyres (2006), Cassini Observes the Active South Pole of Enceladus, *Science*, *311*, 1393–1401, doi:10.1126/science.1123013.

Priest, E. (2014), *Magnetohydrodynamics of the Sun*.

Quest, K. B., and F. V. Coroniti (1981), Linear theory of tearing in a high-beta plasma, *J. Geophys. Res.*, *86*, 3299–3305, doi:10.1029/JA086iA05p03299.

Radioti, A., D. Grodent, J.-C. Gérard, S. E. Milan, B. Bonfond, J. Gustin, and W. Pryor (2011), Bifurcations of the main auroral ring at Saturn: ionospheric signatures of consecutive reconnection events at the magnetopause, *J. of Geophys. Res.*, *116*, A11209, doi:10.1029/2011JA016661.

Radioti, A., D. Grodent, J.-C. Gérard, B. Bonfond, J. Gustin, W. Pryor, J. M. Jasinski, and C. S. Arridge (2013), Auroral signatures of multiple magnetopause reconnection at Saturn, *Geophys. Res. Lett.*, *40*, 4498–4502, doi:10.1002/grl.50889.

Reiff, P. H., J. L. Burch, and T. W. Hill (1977), Solar wind plasma injection at the dayside magnetospheric cusp, *J. Geophys. Res.*, *82*, 479–491, doi:10.1029/JA082i004p00479.

Reisenfeld, D., J. Williams, R. Baragiola, M. Fama, H. Martens, E. Sittler, H. T. Smith, M. Thomsen, and D. Young (2008), The ion composition of Saturn's magnetosphere, in *37th COSPAR Scientific Assembly*, *COSPAR Meeting*, vol. 37, p. 2593.

Rosenbauer, H., H. Gruenwaldt, M. D. Montgomery, G. Paschmann, and N. Sckopke (1975), Heos 2 plasma observations in the distant polar magnetosphere - The plasma mantle, *J. Geophys. Res.*, *80*, 2723–2737, doi:10.1029/JA080i019p02723.

Roussos, E., N. Krupp, T. P. Armstrong, C. Paranicas, D. G. Mitchell, S. M. Krimigis, G. H. Jones, K. Dialynas, N. Sergis, and D. C. Hamilton (2008), Discovery of a transient radiation belt at Saturn, *Geophys. Res. Lett.*, *35*, L22106, doi:10.1029/2008GL035767.

Roussos, E., N. Krupp, C. P. Paranicas, P. Kollmann, D. G. Mitchell, S. M. Krimigis, T. P. Armstrong, D. R. Went, M. K. Dougherty, and G. H. Jones (2011), Long- and short-term variability of Saturn's ionic radiation belts, *J. of Geophys. Res.*, *116*, A02217, doi:10.1029/2010JA015954.

Roussos, E., N. Krupp, D. Mitchell, C. Paranicas, S. Krimigis, M. Andriopoulou, B. Palmaerts, W. Kurth, S. Badman, A. Masters, and M. Dougherty (2015), Quasi-periodic injections of relativistic electrons in Saturn's outer magnetosphere, *Icarus*, doi:10.1016/j.icarus.2015.04.017.

Russell, C. T. (2003), *The Cassini-Huygens Mission. Overview, Objectives and Huygens Instrumentarium.*

Russell, C. T., and R. C. Elphic (1978), Initial ISEE magnetometer results - Magnetopause observations, *Space Sci. Rev.*, *22*, 681–715, doi:10.1007/BF00212619.

Russell, C. T., and R. C. Elphic (1979), Isee observations of flux transfer events at the dayside magnetopause, *Geophys. Res. Lett.*, *6*(1), 33–36, doi:10.1029/GL006i001p00033.

Russell, C. T., C. R. Chappell, M. D. Montgomery, M. Neugebauer, and F. L. Scarf (1971), OGO 5 observations of the polar cusp on November 1, 1968., *J. Geophys. Res.*, *76*, 6743–6764, doi:10.1029/JA076i028p06743.

Rymer, A. M., A. J. Coates, K. Svenes, G. A. Abel, D. R. Linder, B. Narheim, M. Thomsen, and D. T. Young (2001), Cassini plasma spectrometer electron spectrometer measurements during the Earth swing-by on August 18, 1999, *J. Geophys. Res.*, *106*, 30,177–30,198, doi:10.1029/2001JA900087.

Šafránková, J., Z. Němeček, L. Přech, J. Šimůnek, D. Sibeck, and J.-A. Sauvaud (2007), Variations of the flank LLBL thickness as response to the solar wind dynamic pressure and IMF orientation, *J. of Geophys. Res.*, *112*, A07201, doi:10.1029/2006JA011889.

Sandholt, P. E., C. J. Farrugia, M. ieroset, P. Stauning, and S. W. H. Cowley (1996), Auroral signature of lobe reconnection, *Geophys. Res. Lett.*, *23*(14), 1725–1728, doi:10.1029/96GL01846.

Saur, J., N. Schilling, F. M. Neubauer, D. F. Strobel, S. Simon, M. K. Dougherty, and C. T. Russell (2008), Evidence for temporal variability of Enceladus' gas jets: Modeling of Cassini observations, *AGU Fall Meeting Abstracts*, p. B1376.

Scurry, L., and C. T. Russell (1991), Proxy studies of energy transfer to the magnetosphere, *J. Geophys. Res.*, *96*, 9541–9548, doi:10.1029/91JA00569.

Scurry, L., C. T. Russell, and J. T. Gosling (1994), Geomagnetic activity and the beta dependence of the dayside reconnection rate, *J. of Geophys. Res.*, *99*(A8), 14,811–14,814, doi:10.1029/94JA00794.

Sergis, N., S. M. Krimigis, D. G. Mitchell, D. C. Hamilton, N. Krupp, B. H. Mauk, E. C. Roelof, and M. K. Dougherty (2009), Energetic particle pressure in saturn's magnetosphere measured with the magnetospheric imaging instrument on cassini, *J. of Geophys. Res.*, *114*(A2), doi:10.1029/2008JA013774, a02214.

Shelley, E. G., R. D. Sharp, and R. G. Johnson (1976), He/++/ and H/+/ flux measurements in the day side cusp - Estimates of convection electric field, *J. Geophys. Res.*, *81*, 2363–2370, doi:10.1029/JA081i013p02363.

Shi, Q. Q., Z. Y. Pu, J. Soucek, Q.-G. Zong, S. Y. Fu, L. Xie, Y. Chen, H. Zhang, L. Li, L. D. Xia, Z. X. Liu, E. Lucek, A. N. Fazakerley, and H. Reme (2009a), Spatial structures of magnetic depression in the earth's high-altitude cusp: Cluster multipoint observations, *J. of Geophys. Res.*, *114*(A10), doi:10.1029/2009JA014283, a10202.

Shi, Q. Q., Q.-G. Zong, H. Zhang, Z. Y. Pu, S. Y. Fu, L. Xie, Y. F. Wang, Y. Chen, L. Li, L. D. Xia, Z. X. Liu, A. N. Fazakerley, H. Reme, and E. Lucek (2009b), Cluster observations of the entry layer equatorward of the cusp under northward interplanetary magnetic field, *J. of Geophys. Res.*, *114*(A12), doi:10.1029/2009JA014475, a12219.

Slavin, J. A., R. E. Holzer, J. R. Spreiter, and S. S. Stahara (1984), Planetary

Mach cones - Theory and observation, *J. Geophys. Res.*, *89*, 2708–2714, doi: 10.1029/JA089iA05p02708.

Slavin, J. A., R. P. Lepping, C.-C. Wu, B. J. Anderson, D. N. Baker, M. Benna, S. A. Boardsen, R. M. Killen, H. Korth, S. M. Krimigis, W. E. McClintock, R. L. McNutt, M. Sarantos, D. Schriver, S. C. Solomon, P. Trávníček, and T. H. Zurbuchen (2010), MESSENGER observations of large flux transfer events at Mercury, *Geophys. Res. Lett.*, *37*, L02105, doi:10.1029/2009GL041485.

Slavin, J. A., S. M. Imber, S. A. Boardsen, G. A. DiBraccio, T. Sundberg, M. Sarantos, T. Nieves-Chinchilla, A. Szabo, B. J. Anderson, H. Korth, T. H. Zurbuchen, J. M. Raines, C. L. Johnson, R. M. Winslow, R. M. Killen, R. L. McNutt, Jr., and S. C. Solomon (2012), MESSENGER observations of a flux-transfer-event shower at Mercury, *J. of Geophys. Res.*, *117*, A00M06, doi:10.1029/2012JA017926.

Slavin, J. A., G. A. DiBraccio, D. J. Gershman, S. M. Imber, G. K. Poh, J. M. Raines, T. H. Zurbuchen, X. Jia, D. N. Baker, K.-H. Glassmeier, S. A. Livi, S. A. Boardsen, T. A. Cassidy, M. Sarantos, T. Sundberg, A. Masters, C. L. Johnson, R. M. Winslow, B. J. Anderson, H. Korth, R. L. McNutt, and S. C. Solomon (2014), MESSENGER observations of Mercury's dayside magnetosphere under extreme solar wind conditions, *J. of Geophys. Res.*, *119*, 8087–8116, doi: 10.1002/2014JA020319.

Smith, M. F., and M. Lockwood (1990), The pulsating cusp, *Geophys. Res. Lett.*, *17*, 1069–1072, doi:10.1029/GL017i008p01069.

Smith, M. F., and M. Lockwood (1996), Earth's magnetospheric cusps, *Reviews of Geophysics*, *34*, 233–260, doi:10.1029/96RG00893.

Smith, M. F., M. Lockwood, and S. W. H. Cowley (1992), The statistical cusp - A flux transfer event model, *Planet. Space Sci.*, *40*, 1251–1268, doi:10.1016/ 0032-0633(92)90082-Y.

Spence, H., G. Reeves, D. Baker, J. Blake, M. Bolton, S. Bourdarie, A. Chan, S. Claudepierre, J. Clemmons, J. Cravens, S. Elkington, J. Fennell, R. Friedel, H. Funsten, J. Goldstein, J. Green, A. Guthrie, M. Henderson, R. Horne, M. Hudson, J.-M. Jahn, V. Jordanova, S. Kanekal, B. Klatt, B. Larsen, X. Li, E. MacDon-

ald, I. Mann, J. Niehof, T. OBrien, T. Onsager, D. Salvaggio, R. Skoug, S. Smith, L. Suther, M. Thomsen, and R. Thorne (2013), Science goals and overview of the radiation belt storm probes (rbsp) energetic particle, composition, and thermal plasma (ect) suite on nasas van allen probes mission, *S. Sci. Rev.*, *179*(1-4), 311–336, doi:10.1007/s11214-013-0007-5.

Spencer, J. R., and N. M. Schneider (1996), Io on the Eve of the Galileo Mission, *Annual Review of Earth and Planetary Sciences*, *24*, 125–190, doi:10.1146/annurev.earth.24.1.125.

Stallard, T. S., S. Miller, L. M. Trafton, T. R. Geballe, and R. D. Joseph (2004), Ion winds in Saturn's southern auroral/polar region, *Icarus*, *167*, 204–211, doi:10.1016/j.icarus.2003.09.006.

Swisdak, M., B. N. Rogers, J. F. Drake, and M. A. Shay (2003), Diamagnetic suppression of component magnetic reconnection at the magnetopause, *J. of Geophys. Res.*, *108*, 1218, doi:10.1029/2002JA009726.

Swisdak, M., M. Opher, J. F. Drake, and F. Alouani Bibi (2010), The Vector Direction of the Interstellar Magnetic Field Outside the Heliosphere, *ApJ*, *710*, 1769–1775, doi:10.1088/0004-637X/710/2/1769.

Szabo, A., G. L. Siscoe, A. J. Lazarus, R. L. McNutt, R. P. Lepping, and N. F. Ness (1991), Magnetopause and cusp observations at neptune, *J. of Geophys. Res.*, *96*(S01), 19,149–19,152, doi:10.1029/91JA01600.

Talboys, D. L., C. S. Arridge, E. J. Bunce, A. J. Coates, S. W. H. Cowley, and M. K. Dougherty (2009), Characterization of auroral current systems in Saturn's magnetosphere: High-latitude Cassini observations, *J. of Geophys. Res.*, *114*, A06220, doi:10.1029/2008JA013846.

Talboys, D. L., E. J. Bunce, S. W. H. Cowley, C. S. Arridge, A. J. Coates, and M. K. Dougherty (2011), Statistical characteristics of field-aligned currents in Saturn's nightside magnetosphere, *J. of Geophys. Res.*, *116*, A04213, doi:10.1029/2010JA016102.

Thomsen, M. F., D. B. Reisenfeld, D. M. Delapp, R. L. Tokar, D. T. Young, F. J. Crary, E. C. Sittler, M. A. McGraw, and J. D. Williams (2010), Survey of ion

plasma parameters in Saturn's magnetosphere, *J. of Geophys. Res.*, *115*, A10220, doi:10.1029/2010JA015267.

Tokar, R. L., R. E. Johnson, T. W. Hill, D. H. Pontius, W. S. Kurth, F. J. Crary, D. T. Young, M. F. Thomsen, D. B. Reisenfeld, A. J. Coates, G. R. Lewis, E. C. Sittler, and D. A. Gurnett (2006), The Interaction of the Atmosphere of Enceladus with Saturn's Plasma, *Science*, *311*, 1409–1412, doi:10.1126/science.1121061.

Trattner, K. J., S. A. Fuselier, W. K. Peterson, and S.-W. Chang (1999), Comment on "Correlation of cusp MeV helium with turbulent ULF power spectra and its implications", *Geophys. Res. Lett.*, *26*, 1361–1362, doi:10.1029/1999GL900284.

Trattner, K. J., S. A. Fuselier, W. K. Peterson, S.-W. Chang, R. Friedel, and M. R. Aellig (2001), Origins of energetic ions in the cusp, *J. Geophys. Res.*, *106*, 5967–5976, doi:10.1029/2000JA003005.

Trattner, K. J., S. A. Fuselier, W. K. Peterson, M. Boehm, D. Klumpar, C. W. Carlson, and T. K. Yeoman (2002), Temporal versus spatial interpretation of cusp ion structures observed by two spacecraft, *J. of Geophys. Res.*, *107*, 1287, doi:10.1029/2001JA000181.

Trattner, K. J., S. A. Fuselier, W. K. Peterson, S.-W. Chang, R. Friedel, and M. R. Aellig (2003), Reply to comment on "Origins of energetic ions in the cusp" by R. Sheldon, J. Chen, and T. A. Fritz, *J. of Geophys. Res.*, *108*, 1303, doi:10.1029/2002JA009781.

Trattner, K. J., S. A. Fuselier, T. K. Yeoman, C. Carlson, W. K. Peterson, A. Korth, H. Reme, J. A. Sauvaud, and N. Dubouloz (2005), Spatial and Temporal Cusp Structures Observed by Multiple Spacecraft and Ground Based Observations, *Surveys in Geophysics*, *26*, 281–305, doi:10.1007/s10712-005-1883-3.

Trattner, K. J., S. A. Fuselier, S. M. Petrinec, T. K. Yeoman, C. P. Escoubet, and H. Reme (2008), The reconnection site of temporal cusp structures, *J. of Geophys. Res.*, *113*, A07S14, doi:10.1029/2007JA012776.

Trattner, K. J., S. M. Petrinec, S. A. Fuselier, and R. Friedel (2012), Investigating the relationship between cusp energetic particle events and cusp diamagnetic

cavities, *Journal of Atmospheric and Solar-Terrestrial Physics*, *87*, 56–64, doi: 10.1016/j.jastp.2011.08.004.

Tsyganenko, N. A. (1995), Modeling the Earth's magnetospheric magnetic field confined within a realistic magnetopause, *J. Geophys. Res.*, *100*, 5599–5612, doi: 10.1029/94JA03193.

Tsyganenko, N. A., and C. T. Russell (1999), Magnetic signatures of the distant polar cusps: Observations by polar and quantitative modeling, *J. Geophys. Res.*, *104*, 24,939–24,956, doi:10.1029/1999JA900279.

Vasyliūnas, V. M. (1983), *Plasma distribution and flow*, pp. 395–453.

Vasyliūnas, V. M. (2008), Comparing jupiter and saturn: dimensionless input rates from plasma sources within the magnetosphere, *Annales Geophysicae*, *26*(6), 1341–1343, doi:10.5194/angeo-26-1341-2008.

Waite, J. H., M. R. Combi, W.-H. Ip, T. E. Cravens, R. L. McNutt, W. Kasprzak, R. Yelle, J. Luhmann, H. Niemann, D. Gell, B. Magee, G. Fletcher, J. Lunine, and W.-L. Tseng (2006), Cassini Ion and Neutral Mass Spectrometer: Enceladus Plume Composition and Structure, *Science*, *311*, 1419–1422, doi:10.1126/science. 1121290.

Wang, C.-P. (2008), Penetration of the plasma sheet into the ring current region during a magnetic storm, Available at `http://www.igpp.ucla.edu/public/THEMIS/SCI/Pubs/Nuggets/PS_ring_current/Penetrationofplasmasheet.HTML`(2008).

Wei, H. (2012), Cassini magnetometer planetary data system user's guide, Available at `http://ppi.pds.nasa.gov/ditdos/download?id=pds://PPI/COMAG_0001/DOCUMENT/USER_GUIDE/CASSINI_MAG_USER_GUIDE-131008.PDF`(2012).

Whipple, E. C. (1981), Potentials of surfaces in space, *Reports on Progress in Physics*, *44*, 1197–1250, doi:10.1088/0034-4885/44/11/002.

Wing, S., P. T. Newell, and J. M. Ruohoniemi (2001), Double cusp: Model prediction and observational verification, *J. of Geophys. Res.*, *106*(A11), 25, 571–25, 593, doi:10.1029/2000JA000402.

Wing, S., P. T. Newell, and C.-I. Meng (2005), Cusp Modeling and Observations at Low Altitude, *Surveys in Geophysics*, *26*, 341–367, doi:10.1007/s10712-005-1886-0.

Winslow, R. M., C. L. Johnson, B. J. Anderson, H. Korth, J. A. Slavin, M. E. Purucker, and S. C. Solomon (2012), Observations of Mercury's northern cusp region with MESSENGER's Magnetometer, *Geophys. Res. Lett.*, *39*, L08112, doi:10.1029/2012GL051472.

Woch, J., and R. Lundin (1992), Magnetosheath plasma precipitation in the polar cusp and its control by the interplanetary magnetic field, *J. Geophys. Res.*, *97*, 1421–1430, doi:10.1029/91JA02487.

Young, D. T., J. J. Berthelier, M. Blanc, J. L. Burch, A. J. Coates, R. Goldstein, M. Grande, T. W. Hill, R. E. Johnson, V. Kelha, D. J. McComas, E. C. Sittler, K. R. Svenes, K. Szegö, P. Tanskanen, K. Ahola, D. Anderson, S. Bakshi, R. A. Baragiola, B. L. Barraclough, R. K. Black, S. Bolton, T. Booker, R. Bowman, P. Casey, F. J. Crary, D. Delapp, G. Dirks, N. Eaker, H. Funsten, J. D. Furman, J. T. Gosling, H. Hannula, C. Holmlund, H. Huomo, J. M. Illiano, P. Jensen, M. A. Johnson, D. R. Linder, T. Luntama, S. Maurice, K. P. McCabe, K. Mursula, B. T. Narheim, J. E. Nordholt, A. Preece, J. Rudzki, A. Ruitberg, K. Smith, S. Szalai, M. F. Thomsen, K. Viherkanto, J. Vilppola, T. Vollmer, T. E. Wahl, M. Wüest, T. Ylikorpi, and C. Zinsmeyer (2004), Cassini Plasma Spectrometer Investigation, *Space Sci. Rev.*, *114*, 1–112, doi:10.1007/s11214-004-1406-4.

Zhou, X. W., C. T. Russell, G. Le, S. A. Fuselier, and J. D. Scudder (2000), Solar wind control of the polar cusp at high altitude, *J. Geophys. Res.*, *105*, 245–252, doi:10.1029/1999JA900412.

Zhou, X. W., C. T. Russell, G. Le, S. A. Fuselier, and J. D. Scudder (2001), Factors controlling the diamagnetic pressure in the polar cusp, *Geophys. Res. Lett.*, *28*, 915–918, doi:10.1029/2000GL012306.

Zieger, B., and K. C. Hansen (2008), Statistical validation of a solar wind propagation model from 1 to 10 AU, *J. of Geophys. Res.*, *113*, A08107, doi:10.1029/2008JA013046.

Zong, Q.-G., H. Zhang, T. A. Fritz, M. L. Goldstein, S. Wing, W. Keith, J. D. Winningham, R. Frahm, M. W. Dunlop, A. Korth, P. W. Daly, H. RèMe, A. Balogh, and A. N. Fazakerley (2008), Multiple cusps during an extended northward IMF period with a significant B_y component, *J. of Geophys. Res.*, *113*, A01210, doi: 10.1029/2006JA012188.